

MICRO- AND NANOTECHNOLOGY-BASED
PLATFORMS TO STUDY BIOLOGY AT SMALL
SCALE: FROM DNAs TO SINGLE CELLS

Thesis by

Young Shik Shin

In Partial Fulfillment of the Requirements for the

degree of

Doctor of Philosophy

CALIFORNIA INSTITUTE OF TECHNOLOGY

Pasadena, California

2011

(Defended March 11, 2011)

© 2011

Young Shik Shin

All Rights Reserved

To my family,

Jinha and Seung-Hyuck

Acknowledgements

I have been so fortunate to interact with talented and intelligent people during my stay at Caltech. First of all, I would like to thank my advisor Professor Jim Heath. His passion for science always motivates me to think deeply, and creatively, and to move forward. The academic freedom he gives and the resources he makes available to the group have extended my scientific/engineering experience and skill sets to the scope that I cannot imagine reaching in another place. I was lucky to work with great collaborators through Jim's organization of the Nanosystems Biology Cancer Center (NSBCC) between Caltech, UCLA, and the Institute for Systems Biology (ISB). I would like to thank many senior collaborators within the NSBCC, including Professor Raphael D. Levine, Professor Françoise Remacle, and Professor Paul Mischel. Discussion with them has always been fruitful and intellectually pleasing. I also thank the members of my thesis committee, Professor David Tirrell, Professor Morteza Gharib, and Professor Jack Beauchamp.

I have had the pleasure of working with many talented co-workers. Specifically, I have worked closely with Yuri Bunimovich, Michael Amori, and Heather Agnew on silicon nanowire biosensors, and Kiwook Hwang, Habib Ahmad, Qihui Shi, and Rong Fan on single-cell barcode chips. I have also worked with Hugh Kim in Jack Beauchamp's group and Hyungjun Kim in Bill Goddard's group on the lung surfactant project. Working with them has been a great rewarding and pleasure. I am very grateful to the current and past members of the Heath group. Especially I had wonderful time with Woon-Seok Yeo and Jang Wook Choi (and Tae Hyeon Yoo in Tirrell's lab) by sharing personal lives as well as

scientific ideas. I thank Kevin Kan for his effort to manage our lab facilities. I also must thank many Korean friends at Caltech with whom I could share and enrich my personal life with joy and happiness.

During the past six-and-a-half years at Caltech, I had the most dramatic change in my life. I got married to my beautiful wife, Katherine (Jinha), and my adorable son, Christopher (Seung-Hyuck), joined our family. I owe much to them for their unlimited support with love, understanding, and motivation. I thank my family members on both sides, especially my parents and parents-in-law, for their encouragement and support. Last, but by no means least, I would like to thank God, who has been so sincere and responsive to me all the time.

Abstract

This thesis describes technology platforms for various biological applications at nano- and microscale. The first platform is the silicon nanowire (SiNW) field-effect-transistor (FET)-based biosensor. SiNW FETs have unique features such as label-free, real-time, and electrical measurement, which will be demonstrated with DNA and protein sensing. We further demonstrate that using different surface chemistry can modulate the sensitivity and dynamic range of the sensor. Debye screening, one of the major bottlenecks of the technology, is shown to be circumvented by using electrostatically immobilized capture DNA for DNA sensing and a small synthetic capture agent, peptide, for protein sensing. A model for the detection of analyte by SiNW sensors is also developed and utilized to extract DNA binding kinetic parameters, which shows the potential of the platform as a more sensitive version of surface plasmon resonance (SPR).

The second part of this thesis focuses on a more practical and easily expandable technology, the microfluidics-based platform, to perform a single-cell-based protein analysis. We develop a flow patterning technology to generate highly parallel DNA barcodes that can be further utilized as a handle to immobilize protein capture agents, such as antibodies. As a first step, a protocol to make high-quality DNA micro-barcodes with an excellent uniformity is introduced. The uniform DNA barcode patterns enable us to perform protein detection from single cells in a microfluidic device that spans the whole glass microscope slide. A data set from about thousand experiments can be collected from a single test with the developed microfluidic device, owing to the good quality of DNA

barcodes and DNA Encoded Antibody Libraries (DEAL) technology. This platform further demonstrates that multi-parameter protein detection at the single-cell level presents cellular heterogeneity which leads to new findings in biology. A quantitative version of the Le Chatelier's principle, as derived using information theory, is applied to analyze a large amount of data from this platform. This principle provides a quantitative prediction of the role of perturbations and allows a characterization of a protein–protein interaction network.

Lastly, another application of microfluidics is demonstrated for studying interfacial chemistry on lung surfactant systems under oxidative stress, along with mass spectrometry (MS) and molecular dynamic (MD) simulation results. The findings from the MS and MD simulations provide mechanistic details for the reaction of ozone with unsaturated phospholipids, leading to possible damage of the pulmonary system by ROS or direct ozone exposure. These investigations focus on molecular transformations that occur as a result of oxidative stress. Such molecular transformations can have a strong influence on the physical properties of the pulmonary surfactant (PS) system (i.e., the surface tension and elasticity of the interface), and therefore understanding how chemical transformations influence such physical properties can provide key insights into how the PS system responds to environmental challenges. Thus, we also propose utilizing microbubbles as a model system for investigating the physical transformations of the PS system when exposed to environmental challenges. The chemical composition change, along with physical property change, is analyzed by altered bubble size and oscillatory behavior which can provide an improved understanding of the physics of a PS system when it is subjected to oxidative stress.

Table of Contents

ACKNOWLEDGEMENTS	iii
ABSTRACT.....	vi
TABLE OF CONTENTS.....	viii
LIST OF FIGURES, SCHEMES, AND TABLES	xiii
CHAPTER 1	1
1.1 MICRO- AND NANOTECHNOLOGIES IN BIOLOGY	1
1.2 HOW TO STUDY BIOLOGY: TOP-DOWN VS. BOTTOM-UP	2
1.3 COMPLEXITY OF BIOLOGY AND MULTI-PARAMETER ANALYSIS	4
1.4 THESIS OVERVIEW	7
1.5 REFERENCES	12
CHAPTER 2	19
2.1 INTRODUCTION	19
2.2 EXPERIMENTAL METHODS	24
2.2.1 Nanowire sensor fabrication	24
2.2.2 Surface functionalization and characterization for DNA sensing and antibody-based protein sensing.....	29
2.2.3. Surface functionalization and characterization for peptide-based protein sensing	31
2.2.4 SPR and electronic measurements.....	36

2.3 RESULTS AND DISCUSSION	38
2.3.1 DNA sensing	38
2.3.2 Protein sensing with antibodies	53
2.3.3 Protein sensing with peptide	62
2.4 CONCLUSIONS.....	67
2.5 REFERENCES	69
CHAPTER 3.....	80
3.1 INTRODUCTION	80
3.2 EXPERIMENTAL METHODS	81
3.2.1 Microfluidic chip fabrication for DNA patterning.....	81
3.2.2 Patterning of DNA barcode arrays	82
3.2.3 Microfluidic chip fabrication for multi-protein detection.....	84
3.2.4 Cell culture	85
3.2.5 Multi-protein detection.....	85
3.2.6 On-chip cell lysis and multiplexed intracellular protein profiling from single cells	86
3.2.7 Data analysis.....	88
3.2.8 Molecular dynamic simulation	89
3.2.9 Modeling of electrostatic adsorption of DNA to poly-L-lysine (PLL) surface...	89
3.3 RESULTS AND DISCUSSION	91
3.4 CONCLUSIONS.....	104
3.5 REFERENCES	105
CHAPTER 4.....	111

4.1 INTRODUCTION	111
4.2 EXPERIMENTAL METHODS	113
4.2.1 Patterning of DNA barcode arrays	113
4.2.2 Microfluidic chip fabrication for the detection of protein secretion.....	114
4.2.3 Cell culture	115
4.2.4 On-chip secretion profiling	115
4.2.5 Data analysis.....	116
4.3 RESULTS AND DISCUSSION	117
4.3.1 Multiple-protein secretion profiling from single cells and small cell colonies with integrated microchip.....	117
4.3.2 Secretion profile from integrated barcode chip vs. bulk experiment.....	118
4.3.3 Single-cell protein secretion profiling of GBM cell line: U87 cells.....	120
4.3.4 Cell–cell communication effect	124
4.3.5 PTEN activity on GBM cell line: U87EGFRvIII vs. U87EGFRvIII/PTEN	126
4.3.6 Toward clinical sample: analysis on GBM primary tumor cells	128
4.4 CONCLUSIONS.....	129
4.5 REFERENCES	132
CHAPTER 5	136
5.1 INTRODUCTION	136
5.2 METHODS	138
5.2.1 Experimental Methods	138
5.2.2 Theoretical Methods.....	148
5.3 RESULTS AND DISCUSSION	155

5.3.1 Computing the covariance matrix.....	155
5.3.2 The network.....	156
5.3.3 The composite networks	160
5.3.4 The number-based network.....	162
5.4 CONCLUSIONS.....	165
5.5 REFERENCES	166
5.6 APPENDIX A: SUPPLEMENTARY EXPERIMENTAL METHODS (SI.I)	170
5.6.1 Experimental procedure	170
5.6.2 Experimental data analysis methods.....	174
5.7 APPENDIX B: SUPPLEMENTARY THEORY METHODS (SI.II)	179
5.7.1 Introduction to theoretical supplementary methods	179
5.7.2 The ensemble: A basis for making predictions	180
5.7.3 Fluctuations describe the response to small perturbations.....	182
5.7.4 The principle of Le Chatelier	184
5.7.5 The equation for the direction of change	185
5.7.6 Tiers of the network are eigenvectors of the correlation matrix	187
5.7.7 The spectral representation of the covariance matrix.....	188
5.7.8 The role of the number of cells in the sample	189
5.7.9 Antibody perturbations.....	190
5.8 APPENDIX C: SUPPLEMENTARY TABLES	191
CHAPTER 6.....	198
6.1 INTRODUCTION	198
6.2 EXPERIMENTAL METHODS	204

6.2.1 Chemicals and reagents.....	204
6.2.2 Online FIDI-MS technique and heterogeneous oxidation by O ₃	204
6.2.3 Computational modeling.....	205
6.2.4 Design and fabrication of microfluidic device	207
6.2.5 Bubble formation tests and analysis	207
6.2.6. Analysis and imaging of the ozone effect	209
6.3 RESULTS AND DISCUSSION	209
6.3.1 Probing chemical property changes by FIDI.....	209
6.3.2 Probing physical property changes by microfluidic bubble generator	221
6.4 CONCLUSIONS.....	231
6.5 REFERENCES	233

List of Figures, Schemes, and Tables

Chapter 2

Figure 2.1 A diagram and an SEM image of a single device section containing three groups of SiNWs in a microfluidics channel	25
Figure 2.2 Sensing device and fluidics device for sample handling.....	28
Scheme 2.1/2.2 Surface functionalization schemes.....	30
Figure 2.3 Surface treatment scheme for peptide functionalization on a Si (100) substrate and XPS data	32
Figure 2.4 Experimental setup for biological sensing with silicon nanowires.....	38
Table 2.1 Measured contact angles for various Si(100) surfaces.....	39
Figure 2.5 Surface analysis with XPS and SiNW response to pH.....	40
Figure 2.6 Solution gating of SiNWs functionalized by Scheme 2.1 and by Scheme 2.2	42
Figure 2.7 Real-time response of SiNWs functionalized as in Scheme 2.1	43
Figure 2.8 Concentration-dependent, real-time sensing of complementary DNA by SiNWs and by SPR in 0.165 M electrolyte.....	45
Figure 2.9 Comparison of SPR-derived hybridization kinetic parameters with NW sensing data	48
Table 2.2 Kinetic Parameters estimated from SiNW biosensors for the hybridization of 16-mer DNA.....	52
Scheme 2.3 The binding of proteins to antibodies at a distance ~10 nm from the surface of silicon nanowires	53

Table 2.3 Debye length at different salt concentrations	55
Figure 2.10 XPS of carbon 1s region, followed through the process of nanowire functionalization with antibodies.....	56
Figure 2.11 Solution gating responses of SiNWs.....	57
Figure 2.12 IL-2 sensing with SiNWs	58
Figure 2.13 Schematic of the microfluidic PDMS chip overlaying a nanowire sensor device for differential measurements	59
Figure 2.14 IL-2 sensing with dual channel device.....	61
Figure 2.15 High-resolution XPS spectra of Surfaces 2 and 3, illustrating the coupling of the azide-containing unnatural amino acid and subsequently the FLAG peptide	63
Figure 2.16 Fluorescence-based bioassay with FLAG peptides in microfluidic channels	65
Figure 2.17 Scanning electron micrograph (SEM) image of the NW-FET device and sensing result.....	66

Chapter 3

Figure 3.1 Surface treatment schemes and design of the DNA patterning device and fluorescence image of DNAs filled into the channel	82
Table 3.1 Sequences and terminal functionalization of oligonucleotides.....	84
Table 3.2 Summary of antibodies used for cell lysis experiments.....	87
Figure 3.2 The Single-Cell Barcode Chip (SCBC) utilized for on-chip cell lysis and multiplex intracellular protein detection	88

Figure 3.3 The microfluidic flow-patterning process to form the DNA barcodes	91
Figure 3.4 Line profiles for the DNAs patterned by Scheme 1 to 3	93
Figure 3.5 Electrostatic adsorption of DNAs on PLL surface and DMSO effect	94
Figure 3.6 Results from experiments designed to more fully understand the effect of electrostatic adsorption of DNA within the microchannels during flow patterning	95
Figure 3.7 Molecular simulation result of the influence of DMSO in the Scheme 2 process	96
Figure 3.8 Contrast-enhanced raw data extracted from multi-protein calibration experiments performed on a substrate prepared by Scheme 2 and Scheme 3	100
Figure 3.9 A schematic representation of the single-cell, intracellular protein analysis device and experimental data.....	102
Figure 3.10 Antibody cross-reactivity tests	103
Figure 3.11 Calibration data for proteins in the panel.....	104

Chapter 4

Figure 4.1 Integrated barcode chip for secreted protein profiling from single cells and small cell colonies	119
Figure 4.2 Secretion profiles from GBM cell lines: integrated barcode chip vs. bulk experiment.....	121
Figure 4.3 Single-cell secretion profiles for U87 cells.....	122
Figure 4.4 Distance effect for cell–cell communication	125

Figure 4.5 PTEN activity in U87EGFRvIII cells revealed by protein secretion profiling	126
Figure 4.6 Profiling of tumor-secreted proteins at the single-cell level	128

Chapter 5

Figure 5.1 Single-cell barcode chips for protein secretion profiling	138
Figure 5.2 Design of integrated microchip for single-cell protein secretome analysis	139
Figure 5.3 Cross-reactivity check and calibration curves	140
Figure 5.4 PMA and LPS activation and kinetics of protein secretion from activated macrophage cells.....	141
Figure 5.5 Comparison of two data sets from two experiments performed in parallel	143
Figure 5.6 Experimental and simulation results for extracting the experimental error contribution to the SCBC protein assays.....	144
Figure 5.7 Simulated histograms of average intensity from multiple DNA barcode loctions	146
Figure 5.8 Protein secretion heat maps for different colony sizes of LPS-stimulated macrophages.....	147
Figure 5.9 Fluctuations in the numbers of secreted IL-8 proteins for all single-cell experiments	149
Figure 5.10 The summary network derived from the information theory treatment of the data.....	157

Figure 5.11 Protein–protein interactions via the quantitative Le Chatelier’s theorem.....	158
Figure 5.12 The dependence of the dominant eigenvalues of the covariance matrix on the number of cells in the sample	161
Figure 5.13 Heat map of the covariance matrix and of the contributions to the first two tiers of the network for measurements on chambers containing three cells	162
Figure 5.14 Perturbation of protein networks using neutralizing antibodies	164
Figure 5.15 Morphology change of THP-1 cells upon PMA/LPS activation for 24 hrs	172
Figure 5.16 The eigenvalues of the covariance matrix in order of decreasing magnitude for samples containing $n = 1$ cells	188
Table 5.1 Sequences and terminal functionalization of oligonucleotides.....	191
Table 5.2 Summary of antibodies used for macrophage experiments	192
Table 5.3 Digital data for the fluctuation in protein copy numbers for experiments with single cell in the chamber	192
Table 5.4 Signal-to-noise ratio (S/N) for single cells in SCBC measurements.....	195
Table 5.5 Parameters utilized for the protein assay calibration curve	196
Table 5.6 Values of parameters used in simulation.....	196
Table 5.7 The coefficients of variation for each of the assayed proteins from single cell experiments	196
Table 5.8 Digital representation of the covariance matrix for single-cell measurements	197

Chapter 6

Figure 6.1 Schematic illustration of FIDI-MS setup for heterogeneous reaction study	200
Scheme 6.1 Structures of POPG, DPPG, SOPC, and DPPC investigated in this study	202
Figure 6.2 Design of the microfluidic device for bubble generation	208
Figure 6.3 Heterogeneous reaction of POPG with O ₃ as a function of time	211
Scheme 6.2 Summary of heterogeneous oxidation of POPG with O ₃ at the air-liquid interface	212
Figure 6.4 The FIDI-MS ² spectrum of SOZ	213
Figure 6.5 Heterogeneous reaction of a 1:1 mixture of POPG and DPPG with O ₃ as a function of time	215
Figure 6.6 Heterogeneous reaction of a 1:1 mixture of SOPC and DPPC with O ₃ as a function of time	217
Figure 6.7 MD simulation results of a POPG monolayer	219
Table 6.1 Calculated solvation energies of phospholipids and ozonolysis products	221
Figure 6.8 Experimental setup and device for the bubble generation and ozone effect test	222
Table 6.2 Bubble size and the polydispersity index	223
Figure 6.9 Major force components contributing to bubble generation	223
Figure 6.10 Ozone effect on the chemical composition change in the interface	225
Figure 6.11 Time and frequency for bubble formation	228
Table 6.3 Parameters for the effective elastic modulus calculation	229
Figure 6.12 Bubble size analysis	230

Chapter 1

Introduction

1.1 Micro- and nanotechnologies in biology

Microtechnology or nanotechnology is no longer a scientific jargon used solely in science or engineering society. Now we can easily find examples that utilize such up-to-date technologies everywhere in daily life, and biology is one of the fields actively adapting such a paradigm change originated by the size.^{1, 2} Size, in itself, is an important characteristic factor for us to use to define and describe an object. Viruses, for example, are the smallest living organism. They are so small that they are able to live inside other cells undetected. Thus ‘small’ can be one of the first characteristic descriptions of virus. However, if we think about the ‘small’ in depth, we can easily encounter a lot of interesting questions: How do they move? What would be the resistance (or drag force) that they feel when they move? How about their energy utilization (metabolism)? Is that related to their size? Size indeed relates to functions. The new physical and chemical property changes introduced by accessing the extremely small scale can open up a new angle on things that is related to function.

When it comes to biology or medicine, scaling down of tools introduces advantages in terms of small sample amount, fast reaction, multi-parameter analysis, and integration. Early on, microfluidics brought miniaturization and integration together and such efforts

gave birth to micro devices for PCR,³ capillary electrophoresis (CE),⁴ cell counting/sorting,⁴ protein crystallization,⁵ and integrated devices of multiple functionalities.^{6, 7} CE especially shows the power of scaling by accelerating the human genome project.⁸ Recently, microfluidics has been actively used in sequencing, which is expected to enable personalized medicine at a reasonable price and timescale.⁹ Nanotechnology also shows its potential in multiple applications. Nanovectors such as liposomes¹⁰ or nanoparticles¹¹ for drug-delivery, nanoparticle-based identification labeling like ‘bio-barcode’,¹² or ‘chemical nose’,¹³ and silicon nanowire (SiNW)-based biosensors¹⁴ are good examples of nanotechnology applied to biology.

Scaling is an important as well as interesting topic in physics. It is impressive how much progress we’ve made in understanding new physics at nanoscale since Richard Feynman introduced the concept of nanotechnology in his famous lecture, ‘There’s Plenty of Room at the Bottom’ in 1959. However, it will be more exciting to see how the deep understanding of scale and the wide application of the understandings change the world. Biology and medicine are actively adapting this trend and we will see the outcomes soon in a better quality of life.

1.2 How to study biology: Top-down vs. bottom-up

About two decades ago, there was a huge debate introduced by Eric Drexler in a book entitled *Nanosystems*^{15–17} about whether the molecular nanotechnology (MNT) driven by an ‘assembler’ he proposed can be realized or not. This debate paralleled the discussion on the two major approaches in nanotechnology, top-down or bottom-up (because the concept

of MNT is based on a bottom-up approach). It is still an on-going debate. However, the true meaning of this debate, at least I think, is that people started to think about the way they study and look at things. They started to think about whether they could build up and control at the molecular level. Thus the scope of people's interests has changed. We can find a similar concept in biology as well. Single-cell-based studies are a good example of this. Instead of looking at tissue samples consisting of millions of cells, people become interested in a single cell and its heterogeneous characteristics. Systems biology is also closely related to this paradigm change because it approaches biology with a systemic view, and cells or genes are basic components of the system.^{18, 19} The focus of biology moves toward smaller and smaller components, while maintaining its interest in conventional, bulk targets. Now we can categorize the methodologies for biological study into either top-down or bottom-up approaches. Most clinical studies can be categorized as top-down, while rather recent researches—such as on tumor microenvironment or single cells—can be recognized as bottom-up. Categorizing them might be meaningless in itself. However, if it reflects that people start to adopt new way of thinking and analysis, it becomes very important.

We are already seeing the success of the single-cell-based bottom-up approach in biology and medicine.²⁰⁻²³ Lahav et al. reported that p53 shows pulsed responses to radiation damage at the single-cell level, but not in population measurements.²¹ Cohen and coworkers studied the heterogeneous response of human cancer cells to chemotherapy drug by monitoring the levels and locations of ~ 1000 endogenously tagged proteins.²² Tay et al. also showed that the activation of TNF- α -induced NF- κ B signaling is heterogeneous and has a digital response at the single-cell level, which is different from population-level

studies with bulk assays.²⁰ The most interesting common fact in those studies is that the single-cell-based approaches, which we can call the biological version of the bottom-up approach, illuminate hidden, heterogeneous characteristics of cells that are in contrast to what we have seen in conventional bulk assays. This new set of information will broaden our understanding in biology and will guide us in our fight against diseases in novel and creative ways.

As we have seen from the micro- and nanotechnology fields, there is no reason that either the top-down or the bottom-up approach should lead the studies.²⁴⁻²⁶ Combined together, both approaches will open up new feasibility in biology and medicine through a series of breakthroughs, and the micro- and nanotechnologies will play an important role in that. In this thesis, some of those examples will be presented by introducing new technology, device platforms, and analysis schemes.

1.3 Complexity of biology and multi-parameter analysis

Biological systems are complex.²⁷⁻²⁹ Even a cell, one of the most basic units of life, can be seen to have extremely complex components under microscopy. It is amazing how all the components are packed into a ~ 10-μm-length scale. And those components are functional: moving, binding, pulling, and replicating. Cancer is another good example of the complexity of biology. Difficulties in cancer treatment arise from the complexity of cancer pathophysiology. The concept of cancer is changing from that of a homogeneous disease to that of stratified heterogeneous diseases, each with its own biological

characteristics, each requiring a specified therapeutic approach. Thus, we need a more effective solution to deal with biology, especially cancer diagnosis and treatment.

Multi-parameter analysis is an effective solution for such needs, and systems biology can be a powerful approach towards predictive, preventative, and personalized medical care.^{18, 30} The importance of this approach can be found in many examples. Current clinical treatments are based on monitoring only a few biomarkers, such as prostate-specific antigen (PSA) for prostate cancer, CA125 for ovarian cancer, and HER2 for breast cancer. However, these biomarker tests frequently fail to identify early stages of cancer and allow the tumor to transform to a malignant phenotype before a proper treatment can be instituted. For example, mutation in the KIT receptor tyrosine kinase is the major cause of most gastrointestinal stromal tumors (GISTs). That is why Gleevec, a KIT inhibitor, works well in most patients with GISTs. However Fletcher et al. reported that mutations of KIT or platelet-derived growth factor receptor (PDGFRA) are mutually exclusive oncogenic mechanisms in GISTs and that these mutations induce similar downstream signaling pathways of tumor progression. Actually, about 35% of GISTs have intragenic activation mutations in the PDGFRA, even though they don't have KIT mutations.³¹ The global profiling of the molecular signature at a genomic level^{32, 33} or proteomic level^{34, 35} shows its potential in a number of studies reported in the literature as well. Multi-parameter analysis not only allows a more accurate diagnosis, but also enables early-stage cancer detection. An increased number of biomarkers will lead to a more informative diagnosis, which raises the possibility for the right clinical decision. Earlier disease detection makes proper treatment more likely and improves the survival rate.³⁶

However, there are still challenges before multi-parameter analysis will be practical. The first challenge is non-specific binding. Most multi-parameter analysis for biological applications utilizes fluorescence, absorbance, or electrical signals, and for accurate, sensitive measurement the signal-to-noise ratio should be maximized. Looking at multiple targets means a higher chance of non-specific adsorption of target biomolecules on the surface of sensing component, which is known as biofouling. It makes it difficult to deconvolute the real signal from noise. In making the analysis quantitative, this issue becomes more significant.

Another limiting factor is the need to detect small quantities of biomarkers in a small volume, which requires extremely sensitive and fast sensors.³⁷ This factor has attracted significant interest in rapid measurement of a panel of plasma proteins from quantities of whole blood as small as those obtained by a finger prick.^{38–40}

The third challenge is the capture agent. Currently, the antibody is the most commonly used capture agent.⁴¹ High-quality antibodies show good specificity and affinity for the target protein. However, they are expensive and unstable under various experimental conditions such as pH, dehydration, and temperature.⁴² This makes it difficult to incorporate them into common fabrication steps for microfluidics or micro/nanotechnologies. Thus, it is necessary to refine our approach to finding biomolecule capture agents that exhibit a high level of chemical and biochemical stability.^{43–46}

While there are still challenges to address, the multi-parameter analysis approach shows its potential in new platforms and is creating a new paradigm. The multi-parameter analysis will be one of the major topics discussed throughout this thesis.

1.4 Thesis overview

This thesis presents the development of chip-based test platforms that utilize nano- and microtechnologies and their biological applications. The scope of the technologies introduced here is broad. It covers the fabrication of nano/microscale devices, efforts to perform multi-parameter analysis experimentally, analyzing data in a quantitative manner, and possible new applications of those technologies. In Chapter 2, I will begin with the nanotechnology-based platform silicon nanowire (SiNW) field-effect transistor (FET). In addition to showing the advantages of label-free, real-time, and electrical measurement, the quantitative detection of single-stranded oligonucleotides with SiNWs in physiologically relevant electrolyte solution is demonstrated. The efforts are further extended to protein sensing as well. Debye screening is one of the major bottlenecks of electrical measurement in solution. To circumvent this problem we utilized electrostatically adsorbed primary DNA on an amine-terminated NW surface for DNA detection, and synthetic peptide as a capture agent for protein sensing. The surface state is important when it comes to smaller, nanostructures, and SiNW is not an exception. In order to look into the surface-state effect on the electrical measurement, two surface functionalization chemistries are compared: an amine-terminated siloxane monolayer on the native SiO_2 surface of the SiNW, and an amine-terminated alkyl monolayer grown directly on a hydrogen-terminated SiNW surface. The SiNWs without the native oxide exhibit improved solution-gated field-effect transistor characteristics and a significantly enhanced sensitivity to single-stranded DNA detection, with an accompanying two orders of magnitude improvement in the dynamic range of sensing. A model for the detection of analyte by SiNW sensors is developed and utilized to

extract DNA binding kinetic parameters. Those values are directly compared with values obtained by the standard method of surface plasmon resonance (SPR), and demonstrated to be similar. The nanowires, however, are characterized by higher detection sensitivity. The implication is that SiNWs can be utilized to quantitate the solution phase concentration of biomolecules at low concentrations. This work also demonstrates the importance of surface chemistry for optimizing biomolecular sensing with silicon nanowires. (Chapter 2 has been taken in part from *Journal of the American Chemical Society* **2006**, 128, 16323–16331).

Chapter 3 to 5 introduce a microfluidics-based platform for performing a single-cell-based protein analysis. A SiNW-based biosensor has some advantages, but is complicated to fabricate and difficult to apply to multi-parameter analysis. Thus, these three chapters present a more simple and practical strategy to study biology in a multi-parameter manner. The technologies introduced in these chapters are relatively simple but highly optimized, and still present new biological findings because they enable analysis of multiple proteins at the isolated, single-cell level, which is difficult to achieve with conventional, bulk analysis. As a starting point of this effort, Chapter 3 presents a method to make high-quality DNA micro-barcodes. To detect proteins, we utilize an approach called DNA-Encoded Antibody Libraries (DEAL) developed in our lab several years ago.^{39, 47} DEAL technique is based on orthogonal ssDNAs conjugated to an antibody library where every antibody-specificity is uniquely encoded with a distinct ssDNA sequence. We then can use a more robust biomolecule, as a handle to convert a DNA microarray to a protein microarray. It is a simple but powerful technique, since we can perform multi-parameter protein analysis only if we can find orthogonal DNA pairs (which can be done computationally) and pattern complimentary DNAs on a substrate. We described this in

Chapter 3. We have identified a protocol for generating high-quality, high-density DNA barcode patterns by comparing three microfluidics-based patterning schemes. We find, through both experiment and theory, that the electrostatic attractions between the positively charged PLL substrates and the negatively charged DNA backbone induces significant non-uniformity in the patterning process, but that those electrostatic interactions may be mediated by adding DMSO to the solution, resulting in uniform and highly reproducible barcodes patterned using ~ 55-cm-long channels that template barcodes across an entire 2.5-cm-wide glass slide. Dendrimer-based covalent immobilization also yields good ultimate uniformity, but is hampered by a relatively unstable chemistry that limits run-to-run reproducibility. The potential of this approach has been further demonstrated by assaying cytoplasm proteins from single and lysed U87 model cancer cells. Successful detection of a panel of such proteins represents the potential of our platform to be applied to various biological and, perhaps, clinical applications. (Chapter 3 has been taken in part from *ChemPhysChem* **2010**, 11(14), 3063–3069).

Chapter 4 extends and develops the single cell-based protein detection with DNA micro-barcodes and DEAL technique. We take an approach that integrates microfluidic cell handling and *in situ* protein secretion profiling to assess the functional heterogeneity of single cells, with extensions to small cell colonies. We measured a dozen proteins secreted from cells for the most aggressive type of primary brain tumor, glioblastoma multiforme (GBM). We observed functional phenotypes in terms of secreted proteins with profound cellular heterogeneity but still in a statistically meaningful manner. The unique features that we confirmed from single-cell analysis can present additional useful information to the conventional bulk analysis. Combining physical status of the system (such as cell–cell

distance) and the protein secretion profiles enables study of the tumor microenvironment. We further demonstrate the potential clinical application of this platform by analyzing solid tumor cells derived from a GBM patient. This platform is inexpensive, requires minute amounts of cells and yields a large volume of molecular information, showing great potential for clinical assessment of cellular characteristics in human disease lesions, such as a tumor microenvironment.

One of the challenges that we have noticed from the approach introduced in Chapter 4 is how to analyze the sheer amount of information. By utilizing a microfluidic device with ~ 1000 isolated chambers, we can collect ~ 1000 data sets with a single experiment, and each data set represents highly heterogeneous cellular activity. Thus, we should come up with a good strategy to identify the meaningful information by looking at the heterogeneous data set as a whole. In Chapter 5, I will present an approach that integrates microfluidic cell handling, *in situ* protein secretion profiling, and information theory to determine the extracellular protein-signaling network and the role of perturbations. Protein-signaling networks among cells in a disease lesion play critical roles in a host of pathophysiological processes, from inflammation to tumorigenesis. We assayed 12 proteins secreted from human macrophages that were subjected to lipopolysaccharide challenge, which activates the Toll-like receptor-4 signaling pathway. This process emulates the macrophage-based innate immune responses against Gram-negative bacteria. We characterize the fluctuations in protein secretion of single cells, and of small cell colonies ($n = 2, 3, \dots$), as a function of colony size. Measuring the fluctuations permits a validation of the conditions required for the application of a quantitative version of the Le Chatelier's principle, as derived using information theory. This principle provides a quantitative

prediction of the role of perturbations and allows a characterization of a protein–protein interaction network.

In Chapter 6, another application of microfluidics will be demonstrated in studying interfacial chemistry for a lung surfactant system. The motivation for this study is to understand the interfacial structure and chemistry of a surfactant layer system when subjected to oxidative stress. In order to achieve that, we combined experimental observations based on field-induced droplet ionization mass spectrometry (FIDI-MS) with computational analysis. FIDI-MS comprises a soft ionization method to sample ions from the surface of microliter droplets. A pulsed electric field stretches neutral droplets until they develop dual Taylor cones, emitting streams of positively and negatively charged submicron droplets in opposite directions, with the desired polarity being directed into a mass spectrometer for analysis. This methodology is employed to study the heterogeneous ozonolysis of 1-palmitoyl-2-oleyl-*sn*-phosphatidylglycerol (POPG) at the air-liquid interface in negative ion mode using FIDI mass spectrometry. Our results demonstrate unique characteristics of the heterogeneous reactions at the air-liquid interface. We observe the hydroxyhydroperoxide and the secondary ozonide as major products of POPG ozonolysis in the FIDI-MS spectra. These products are metastable and difficult to observe in the bulk phase using standard electrospray ionization (ESI) for mass spectrometric analysis. We also present studies of the heterogeneous ozonolysis of a mixture of saturated and unsaturated phospholipids at the air-liquid interface. A mixture of the saturated phospholipid 1,2-dipalmitoyl-*sn*-phosphatidylglycerol (DPPG) and unsaturated POPG is investigated in negative ion mode using FIDI-MS, while a mixture of 1,2-dipalmitoyl-*sn*-phosphatidylcholine (DPPC) and 1-stearoyl-2-oleyl-*sn*-phosphatidylcholine (SOPC)

surfactant is studied in positive ion mode. In both cases FIDI-MS shows the saturated and unsaturated pulmonary surfactants form a mixed interfacial layer. Only the unsaturated phospholipid reacts with ozone, forming products that are more hydrophilic than the saturated phospholipid. With extensive ozonolysis only the saturated phospholipid remains at the droplet surface. Later we confirm this finding with a microfluidics-based bubble generator with a model pulmonary surfactant composed of two major phospholipids: DPPC and POPG. With fluorescence imaging, we observe the ozone-induced chemical modification of the unsaturated lipid component of the lipid mixture, POPG. This chemical change due to the oxidative stress was further utilized to study the physical characteristics of the interface through the bubble formation process. The physical property change was evaluated through the oscillatory behavior of the monolayer as well as the bubble size and formation time. Results presented demonstrate the potential of this platform to study interfacial physics of a lung surfactant system under various environmental challenges both qualitatively and quantitatively. (Chapter 6 has been taken in part from *Journal of Physical Chemistry C* **2010**, 114, (29), 9496–9503).

1.5 References

1. Blow, N., Nanotechnology in biology: big collaborations for a small world. *Nature Methods* **2008**, 5, (6), 569–574.
2. Blow, N., Microfluidics: the great divide. *Nature Methods* **2009**, 6, (9), 683–686.
3. Zhang, C.; Xu, J.; Ma, W.; Zheng, W., PCR microfluidic devices for DNA amplification. *Biotechnology advances* **2006**, 24, (3), 243–284.

4. Development of a microfluidic device for fluorescence activated cell sorting. *Journal of Micromechanics and Microengineering* **2002**, 12, 486–494.
5. Hansen, C. L.; Skordalakes, E.; Berger, J. M.; Quake, S. R., A robust and scalable microfluidic metering method that allows protein crystal growth by free interface diffusion. *Proceedings of the National Academy of Sciences of the United States of America* **2002**, 99, (26), 16531–16536.
6. Burns, M. A.; Johnson, B. N.; Brahmasandra, S. N.; Handique, K.; Webster, J. R.; Krishnan, M.; Sammarco, T. S.; Man, P. M.; Jones, D.; Heldsinger, D.; Mastrangelo, C. H.; Burke, D. T., An integrated nanoliter DNA analysis device. *Science* **1998**, 282, (5388), 484–487.
7. Thorsen, T.; Maerkl, S. J.; Quake, S. R., Microfluidic Large-Scale Integration. *Science* **2002**, 298, (5593), 580–584.
8. Collins, F. S.; Morgan, M.; Patrinos, A., The Human Genome Project: lessons from large-scale biology. *Science* **2003**, 300, (5617), 286–290.
9. Pushkarev, D.; Neff, N. F.; Quake, S. R., Single-molecule sequencing of an individual human genome. *Nature Biotechnology* **2009**, 27, (9), 847–850.
10. Park, J. W., Liposome-based drug delivery in breast cancer treatment. *Breast Cancer Research* **2002**, 4, (3), 93–97.
11. Davis, M. E.; Zuckerman, J. E.; Choi, C. H.; Seligson, D.; Tolcher, A.; Alabi, C. A.; Yen, Y.; Heidel, J. D.; Ribas, A., Evidence of RNAi in humans from systemically administered siRNA via targeted nanoparticles. *Nature* **2010**, 464, (7291), 1067–1070.
12. Nam, J. M.; Park, S. J.; Mirkin, C. A., Bio-barcodes based on oligonucleotide-modified nanoparticles. *Journal of the American Chemical Society* **2002**, 124, (15), 3820–3821.

13. You, C. C.; Miranda, O. R.; Gider, B.; Ghosh, P. S.; Kim, I. B.; Erdogan, B.; Krovi, S. A.; Bunz, U. H. F.; Rotello, V. M., Detection and identification of proteins using nanoparticle-fluorescent polymer 'chemical nose' sensors. *Nature Nanotechnology* **2007**, 2, (5), 318–323.
14. Patolsky, F.; Zheng, G. F.; Lieber, C. M., Nanowire-based biosensors. *Analytical Chemistry* **2006**, 78, (13), 4260–4269.
15. Drexler, K. E., *Nanosystems: molecular machinery, manufacturing, and computation*. Wiley: New York, **1992**.
16. Baum, Rudy, NANOTECHNOLOGY: Drexler and Smalley make the case for and against ‘molecular assemblers’. *Chemical & Engineering News* **2003**, 81, (48), 37–42.
17. Drexler, K. E., Toward integrated nanosystems: Fundamental issues in design and modeling. *Journal of Computational and Theoretical Nanoscience* **2006**, 3, (1), 1–10.
18. Hood, L.; Heath, J. R.; Phelps, M. E.; Lin, B. Y., Systems biology and new technologies enable predictive and preventative medicine. *Science* **2004**, 306, (5296), 640–643.
19. Spivey, A., Systems Biology: The Big Picture. *Environmental Health Perspectives* **2004**, 112, (16), A938–A943.
20. Tay, S.; Hughey, J. J.; Lee, T. K.; Lipniacki, T.; Quake, S. R.; Covert, M. W., Single-cell NF- κ B dynamics reveal digital activation and analogue information processing. *Nature* **2010**, 466, (7303), 267–271.
21. Lahav, G.; Rosenfeld, N.; Sigal, A.; Geva-Zatorsky, N.; Levine, A. J.; Elowitz, M. B.; Alon, U., Dynamics of the p53-Mdm2 feedback loop in individual cells. *Nature genetics* **2004**, 36, (2), 147–150.

22. Cohen, A. A.; Geva-Zatorsky, N.; Eden, E.; Frenkel-Morgenstern, M.; Issaeva, I.; Sigal, A.; Milo, R.; Cohen-Saidon, C.; Liron, Y.; Kam, Z.; Cohen, L.; Danon, T.; Perzov, N.; Alon, U., Dynamic proteomics of individual cancer cells in response to a drug. *Science* **2008**, 322, (5907), 1511–1516.
23. Cheong, R.; Paliwal, S.; Levchenko, A., Models at the single cell level. *Wiley Interdisciplinary Reviews—Systems Biology and Medicine* **2010**, 2, (1), 34–48.
24. Wong, T.-S.; Brough, B.; Ho, C.-M., Creation of functional micro/nano systems through top-down and bottom-up approaches. *Molecular & cellular biomechanics: MCB* **2009**, 6, (1), 1–55.
25. Ding, B.; Wu, H.; Xu, W.; Zhao, Z.; Liu, Y.; Yu, H.; Yan, H., Interconnecting Gold Islands with DNA Origami Nanotubes. *Nano letters* **2010**, 10, (12), 5065–5069.
26. Hah, J. H.; Mayya, S.; Hata, M.; Jang, Y.-K.; Kim, H.-W.; Ryoo, M.; Woo, S.-G.; Cho, H.-K.; Moon, J.-T., Converging lithography by combination of electrostatic layer-by-layer self-assembly and 193 nm photolithography: Top-down meets bottom-up. *Journal of Vacuum Science & Technology B: Microelectronics and Nanometer Structures* **2006**, 24, (5), 2209–2213.
27. Mazzocchi, F., Complexity in biology. Exceeding the limits of reductionism and determinism using complexity theory. *EMBO reports* **2008**, 9, (1), 10–14.
28. Carter, G. W.; Rush, C. G.; Uygun, F.; Sakhanenko, N. A.; Galas, D. J.; Galitski, T., A systems-biology approach to modular genetic complexity. *Chaos* **2010**, 20, (2), 026102.
29. Inoki, K.; Guan, K. L., Complexity of the TOR signaling network. *Trends in cell biology* **2006**, 16, (4), 206–212.

30. Feng, Y.; Mitchison, T. J.; Bender, A.; Young, D. W.; Tallarico, J. A., Multi-parameter phenotypic profiling: using cellular effects to characterize small-molecule compounds. *Nature reviews Drug discovery* **2009**, 8, (7), 567–578.
31. Heinrich, M. C., Corless, C. L., Duensing, A., McGreevey, L., Chen, C. J., Joseph, N., Singer, S., Griffith, D. J., Haley, A., Town, A.; Demetri, G. D.; Fletcher, C. D.; Fletcher, J. A., PDGFRA activating mutations in gastrointestinal stromal tumors. *Science* **2003**, 299, (5607), 708–710.
32. The Cancer Genome Atlas Research Network, Comprehensive genomic characterization defines human glioblastoma genes and core pathways. *Nature* **2008**, 455, (7216), 1061–1068.
33. Parsons, D. W.; Jones, S.; Zhang, X.; Lin, J. C.; Leary, R. J.; Angenendt, P.; Mankoo, P.; Carter, H.; Siu, I. M.; Gallia, G. L.; Olivi, A.; McLendon, R.; Rasheed, B. A.; Keir, S.; Nikolskaya, T.; Nikolsky, Y.; Busam, D. A.; Tekleab, H.; Diaz, L. A., Jr.; Hartigan, J.; Smith, D. R.; Strausberg, R. L.; Marie, S. K.; Shinjo, S. M.; Yan, H.; Riggins, G. J.; Bigner, D. D.; Karchin, R.; Papadopoulos, N.; Parmigiani, G.; Vogelstein, B.; Velculescu, V. E.; Kinzler, K. W., An integrated genomic analysis of human glioblastoma multiforme. *Science* **2008**, 321, (5897), 1807–1812.
34. Chen, G.; Gharib, T. G.; Wang, H.; Huang, C. C.; Kuick, R.; Thomas, D. G.; Shedden, K. A.; Misek, D. E.; Taylor, J. M.; Giordano, T. J.; Kardia, S. L.; Iannettoni, M. D.; Yee, J.; Hogg, P. J.; Orringer, M. B.; Hanash, S. M.; Beer, D. G., Protein profiles associated with survival in lung adenocarcinoma. *Proceedings of the National Academy of Sciences of the United States of America* **2003**, 100, (23), 13537–13542.
35. Hanash, S., Disease proteomics. *Nature* **2003**, 422, (6928), 226–232.

36. Etzioni, R., Urban, N., Ramsey, S., McIntosh, M., Schwartz, S., Reid, B., Radich, J., Anderson, G., Hartwell, L., The case for early detection. *Nature Reviews Cancer* **2003**, 3, (4), 243–252.
37. Spinney, L., Cancer: Caught in time. *Nature* **2006**, 442, (7104), 736–738.
38. Feng, Y.; Mitchison, T. J.; Bender, A.; Young, D. W.; Tallarico, J. A., Multi-parameter phenotypic profiling: using cellular effects to characterize small-molecule compounds. *Nature reviews Drug discovery* **2009**, 8, (7), 567–578.
39. Fan, R.; Vermesh, O.; Srivastava, A.; Yen, B. K. H.; Qin, L. D.; Ahmad, H.; Kwong, G. A.; Liu, C. C.; Gould, J.; Hood, L.; Heath, J. R., Integrated barcode chips for rapid, multiplexed analysis of proteins in microliter quantities of blood. *Nature Biotechnology* **2008**, 26, (12), 1373–1378.
40. Wang, J.; Ahmad, H.; Ma, C.; Shi, Q. H.; Vermesh, O.; Vermesh, U.; Heath, J., A self-powered, one-step chip for rapid, quantitative and multiplexed detection of proteins from pinpricks of whole blood. *Lab on a Chip* **2010**, 10, (22), 3157–3162.
41. Borrebaeck, C. A. K., Antibodies in diagnostics—from immunoassays to protein chips. *Immunology Today* **2000**, 21, (8), 379–382.
42. Blow, N., Antibodies: The generation game. *Nature* **2007**, 447, 741–744.
43. Agnew, H. D.; Rohde, R. D.; Millward, S. W.; Nag, A.; Yeo, W. S.; Hein, J. E.; Pitram, S. M.; Tariq, A. A.; Burns, V. M.; Krom, R. J.; Fokin, V. V.; Sharpless, K. B.; Heath, J. R., Iterative In Situ Click Chemistry Creates Antibody-like Protein-Capture Agents. *Angewandte Chemie—International Edition* **2009**, 48, (27), 4944–4948.

44. Proske, D.; Blank, M.; Buhmann, R.; Resch, A., Aptamers—basic research, drug development, and clinical applications. *Applied Microbiology and Biotechnology* **2005**, 69, (4), 367–374.
45. Lam, K. S.; Lebl, M.; Krchnak, V., The "One-Bead-One-Compound" Combinatorial Library Method. *Chemical reviews* **1997**, 97, (2), 411–448.
46. Smith, G. P.; Petrenko, V. A., Phage Display. *Chemical reviews* **1997**, 97, (2), 391–410.
47. Bailey, R. C.; Kwong, G. A.; Radu, C. G.; Witte, O. N.; Heath, J. R., DNA-encoded antibody libraries: A unified platform for multiplexed cell sorting and detection of genes and proteins. *Journal of the American Chemical Society* **2007**, 129, (7), 1959–1967.

Chapter 2

Silicon Nanowires for Real-Time, Label-Free Biological Sensing

2.1 Introduction

Over the past few years a number of new biomolecular sensors have been reported.^{1–5} The development of these devices is in part driven by the emerging needs of both systems biology^{6, 7} and personalized and predictive medicine⁸—both of which are increasingly requiring quantitative, rapid, and multiparameter measurement capabilities on ever smaller amounts of tissues, cells, serum, etc. To meet these needs, many groups have focused their attention on developing real-time, highly sensitive, and potentially scalable tools for detecting nucleic acids and proteins. One-dimensional nanostructures such as nanotubes,^{9–12} semiconductors,^{13–15} metal oxide nanowires (NWs),¹⁶ and conducting polymer nanofilaments¹⁷ have all been demonstrated as capable of the label-free detection of small molecules, nucleic acids, and proteins.

Silicon nanowire (SiNW) biosensors are promising label-free, electronic-based detectors of biomolecules.² However, significant scientific challenges remain before SiNW sensors can be viewed as a realistic technology. One challenge relates to the use of these devices in biologically relevant media, which is typically a 0.14 M electrolyte. NW sensors detect the local change in charge density (and the accompanying change in local chemical potential) that characterizes a target/capture agent binding event. That changing chemical

potential is detected as a ‘gating’ voltage by the NW, and so, at a given voltage, affects the source (S) → drain (D) current value, or I_{SD} . However, that change is screened (via Debye screening) from the NW by the solution in which the sensing takes place.^{18, 19} Debye screening is a function of electrolyte concentration, and in a 0.14 M electrolyte (which represents physiological environments such as serum) the screening length is about 1 nm.²⁰ Because of this, all reports on SiNW sensors for proteins or DNA have been carried out in low-ionic-strength solutions.^{14, 15, 21} In this chapter, we demonstrate that a single-stranded complementary oligonucleotide is able to significantly change the conductance of a group of 20-nm-diameter SiNWs (p-doped at $\sim 10^{19} \text{ cm}^{-3}$) in 0.165 M solution by hybridizing to a primary DNA strand that has been electrostatically adsorbed onto an amine-terminated organic monolayer atop the NWs. This intimate contact of the primary strand with the amine groups of the NW surface brings the binding event close enough to the NW to be electronically detected. In addition, within a 0.165 M ionic-strength solution the DNA hybridization is more efficient.^{10, 22} However, we further demonstrate that the sensing of proteins in physiological conditions is fundamentally limited by the size of the antibodies, which, at the moment, remain the most widely used high-affinity probes for most proteins. This problem may be circumvented by utilizing alternative probes, which have smaller physical size, to circumvent the Debye screening issue. In this chapter, we also propose to use small peptides as a capture agent for protein sensing with NWs.

Synthetic capture agents such as peptides have advantages over macromolecules including antibodies, nucleic acid aptamers, and protein aptamers.^{23, 24} They are robust in terms of maintaining their structure and can be easier to produce and purify in bulk than antibodies or aptamers. Especially for NW-FETs, their small size enables detection of the

presence of target molecules in high-ionic-strength solution which has a short Debye screening length. Synthetic capture agents can also be immobilized on the surface in a defined manner, which means we can control the orientation of the capture agents in solution based on the reaction chemistries implemented. Recently, Heather et al. reported a methodology to find peptide-based protein-capture agents through iterative *in situ* click chemistry and one-bead-one-compound method.²⁵ Their approach has a high impact since it can be expected to create cheap but highly stable synthetic capture agents that have the potential to take the place of the antibodies.

To immobilize the peptide, we utilized the Cu^I-catalyzed alkyne-azide ‘click’ cycloaddition. Thus, we can expect all the peptides to be fully exposed to the solution in the same manner. Since the click reaction is defined by a set of stringent criteria such as selectivity, wide scope, high yields, and inoffensive by-products, it can easily serve as a general chemical method for biological applications.²⁶ As a demonstration of this approach, we used the FLAG system: FLAG peptides and monoclonal anti-FLAG M2 antibodies. The FLAG peptides are modified at the N-terminus with the alkyne and two spacer amino acids, SG, to increase accessibility of the target molecules.²⁴

A second challenge involves demonstrating reproducible and high-throughput nanofabrication methods that can produce nearly identical NW sensors time and time again, and that allow for multiple measurements to be executed in parallel. Based on electrostatic considerations, it is well known that nanowires are more sensitive to surface charges than planar ion-sensitive field-effect transistors (ISFET) or chemical field-effect transistors (CHEMFET). Such dimensional arguments²⁷ imply that nontraditional methods must be utilized to fabricate the NWs.^{28, 29} While biological sensing with silicon produced by wet

etch³⁰ or dry oxidation³¹ was reported, to date, most reports of NW sensors have utilized semiconductor NWs grown as bulk materials³² using the vapor-liquid-solid (VLS) technique.³³ This method produces high quality NWs, but they are characterized by a distribution of lengths and diameters, and they also must be assembled into the appropriate device structure (or the device structure must be constructed around the nanowire³⁴). In this study we utilize the Superlattice Nanowire Pattern Transfer (SNAP) method³⁵ to produce highly aligned array of 400 SiNWs, each 20 nm wide and ~ 2 millimeters long. Standard semiconductor processing techniques are utilized to control the NW doping level,³⁶ to section the NWs into several individual sensor arrays, to establish electrical contacts to the NW sensors, and to integrate each array into a microfluidic channel. Such integration is rather challenging in itself;³⁷ however, it is extremely important for obtaining low-noise, reproducible measurements. The resulting NWs exhibit excellent, controllable, and reproducible electrical characteristics from device to device and across fabrication runs. The sensor platforms may also be fabricated in reasonably high throughput. A key advantage, which is provided by the top-down approach of SNAP vs. the bottom-up VLS technique, is the precise control of doping level of the nanowires. We utilize diffusion doping technique to create nanowires with well-characterized doping levels ranging from 10^{17} to 10^{20} cm⁻³. We demonstrate that the doping level profoundly affects the limit of detection of both DNA and protein; therefore, nanowires can be tuned to a specific dynamic range window with an appropriate concentration of impurities.

A third challenge involves the SiNW surface. The effectiveness of SiNWs for biomolecular sensing arises in part because of their high surface-to-volume ratio. The native (1–2 nm thick) surface oxide on a SiNW may limit sensor performance due to the

presence of interfacial electronic states.^{38,39} In addition, the oxide surface of SiNWs acts as a dielectric which can screen the NW from the chemical event to be sensed. Covalent alkyl passivation of Si(111) surfaces can render those surfaces resistant to oxidation in air⁴⁰ and under oxidative potentials.^{41,42} Recently, methyl-passivated SiNWs were shown to exhibit improved field-effect transistor characteristics.⁴³ More complex molecules, such as amine-terminated alkyl groups, can be covalently attached to H-terminated Si surfaces (including SiNWs) via UV-initiated radical chemistry.⁴⁴⁻⁴⁷ Such chemistry has been used for a covalent attachment of DNA to VLS-grown SiNWs.⁴⁸ DNA may also be immobilized on amine-terminated surfaces via electrostatic interactions. In this work, we explore how the characteristics of SiNW sensors vary as the nature of the inorganic/organic interface is varied. We find that SiNW sensors in which the native oxide provides the interface for organic functionalization are significantly inferior in terms of both sensitivity and dynamic range when compared with SiNW sensors that are directly passivated with an alkyl monolayer.

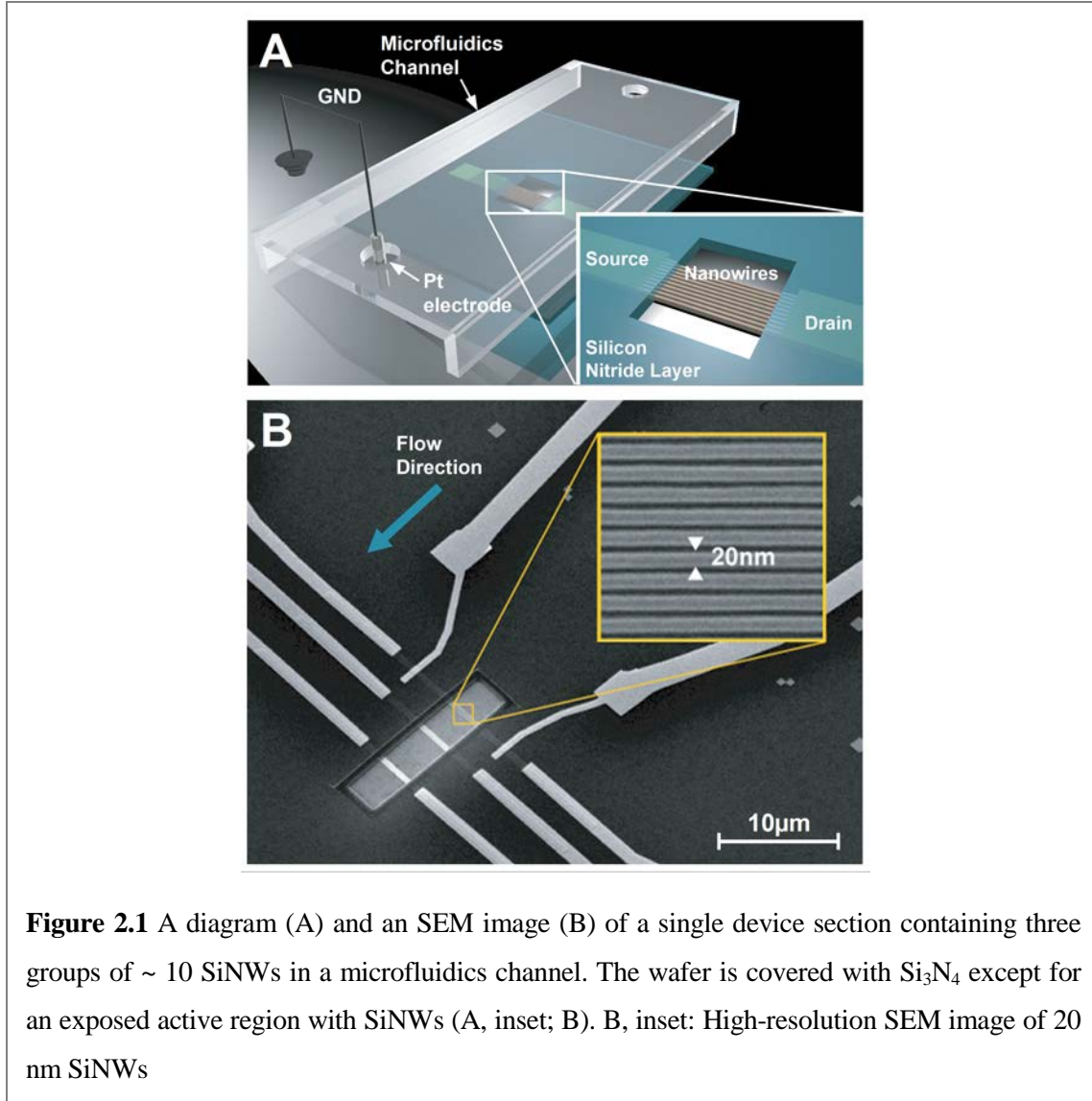
A final challenge is actually an opportunity that is provided by the intrinsic nature of a label-free, real-time sensor. The standard such sensing technique is surface plasmon resonance (SPR).⁴⁹ SPR is utilized to determine the κ_{on} and κ_{off} rates, and hence the equilibrium binding affinities, of complementary DNA strands or antibody–protein pairs. The capture agent (single stranded DNA or an antibody) is typically surface-bound, and so the key experimental variables are the analyte (complementary DNA strand or a protein), concentration, and time. If k_{on} and k_{off} are both known, then SPR can be utilized to quantitate the analyte concentration. Very few biomolecular sensing techniques are quantitative. In this work, we dope the NW sensors so that their sensing dynamic range is

optimized to match that of SPR for the detection of DNA hybridization or protein binding to an antibody. We demonstrate the equivalence of these two methods, and thus demonstrate the potential use of SiNW sensors for quantitating analyte concentrations. SiNW sensors can be optimized for significantly higher sensitivity than SPR by an appropriate surface modification and doping, and thus can potentially be utilized to quantitate the concentrations of specific biomolecules at very low concentrations. That would constitute a unique application of these devices.

2.2 Experimental Methods

2.2.1 Nanowire sensor fabrication

The SiNW arrays were fabricated as previously described,⁵⁰ and all fabrication was done within a class 1000 or class 100 clean room environment. A typical NW sensor device employed in this work for DNA sensing is shown in Fig. 2.1. The starting material for the SNAP process was an intrinsic, 320 Å thick silicon-on-insulator (SOI) substrate with (100) orientation (Ibis Technology Inc., Danvers, MA) and a 1500 Å buried oxide. Cleaned substrates were coated with either p-type (Boron A, Filmtronics, Inc. Butler, PA) or n-type (Phosphorosilica, Emulsitone, Inc., Whippany, NJ) spin-on-dopants (SODs). SODs were thermally diffused into the SOI film. We reproducibly controlled the resulting substrate doping concentration, as quantified by 4-point resistivity measurements on the SOI film, by varying the diffusion temperature. For this study, a 3 min, 850°C (875°C) rapid thermal anneal was used to generate p (n) dopant levels of $\sim 8 \times 10^{18}/\text{cm}^3$. The p-type substrates



were thermally oxidized in O_2 for 1 min at 850°C, which was necessary to remove the organic SOD residue. The SOD films were removed by brief immersion in piranha (70% H_2SO_4 , 30% H_2O_2), followed by a water rinse, and immersion in buffered oxide etchant (BOE; General Chemical, Parcipppany, NJ).

The SNAP method for NW array fabrication translates the atomic control achievable over the individual layer thicknesses within an MBE-grown $\text{GaAs}/\text{Al}_x\text{Ga}_{(1-x)}\text{As}$ superlattice into an identical level of control over NW width, length, and spacing. This method has been described in some detail elsewhere,^{35, 50} and will not be described here. We utilized

the SNAP process to produce a 2-mm-long array of 400 SiNWs, each of 20 nm width and patterned at 35 nm pitch (Fig. 2.1B, inset).

The SiNWs were sectioned into \sim 30- μm -long segments using e-beam lithography (EBL) and SF₆ RIE etching, producing groups of \sim 10 SiNWs with a diameter of 20 nm. Six identical sections from a single imprint, each containing 3 NW segments, were produced. One such section is shown in Fig. 2.1. When fully integrated with the microfluidics channels, this allowed for six separate measurements, with three independent NW segments per measurement. Source (S) and drain (D) electrical contacts, \sim 500 nm wide and separated by 10–15 μm , were patterned using electron beam lithography (EBL) on each section of SiNWs. Prior to metallization, the native oxide of the SiNWs over the contacts was removed with BOE to promote the formation of ohmic contacts. Finally, 400 \AA Ti and 500 \AA Pt were evaporated to form S/D contacts. Immediately after the lift-off, the devices were annealed in 95% N₂, 5% H₂ at 475°C for 5 min. This step greatly improves the characteristics of SNAP SiNW FETs. To provide room for a 1 cm by 1.5 cm PDMS chip with microchannels for analyte delivery to each section of the SiNWs (Fig. 2.1A and 2.2), the electrical contacts were extended to the edges of the substrate using standard photolithography techniques followed by evaporation of 200 \AA Ti and 1500 \AA Au. To eliminate parasitic current between metal contacts in solution, approximately 70 nm of Si₃N₄ was deposited using plasma-enhanced chemical vapor deposition (PECVD) everywhere on the chip except in 5 μm by 20 μm regions over the NWs and the outer tips of the Au contacts. Briefly, 100 nm of chromium was deposited over an active region of the NWs. PECVD was used to deposit Si₃N₄ film at 300°C (900 mT, 20 W, 13.5 MHz) from N₂ (1960 sccm), NH₃ (55 sccm), and SiH₄ (40 sccm) gases. The nitride film was selectively

etched with CHF₃/O₂ plasma over the protected NW region using PMMA as a mask, followed by the removal of chromium with CR-7C (Cyantek Corp., Fremont, CA).

Microfluidics Fabrication. The soft lithography microfluidics chips were fabricated as described by others.⁵¹ We observed that manual introduction/changing of solutions caused serious noise, capacitive currents, and baseline shifts in real-time recordings. Thus, for low noise, stable, real-time electronic measurements, we found it necessary to automate fluid injection and solution switching by using PDMS multilayer, integrated elastomeric microfluidics chips of the type developed by the Quake and Scherer groups.⁵² The size of the wafer containing SiNWs did not permit the inclusion of all necessary flow and control lines necessary for the fluidic handling chip, and so that was fabricated as a separate chip. Such PDMS chip was fabricated using a standard photolithography: mixed PDMS (Dow Corning, Inc., Midland, MI) was applied over a pre-made photoresist (Shipley SPR 220-7) molding on silicon wafer and incompletely cured at 80°C for 30 min. The chip containing microchannels was cut out of the PDMS layer and 0.5-mm-diameter holes were punctured to serve as microchannel inlets and outlets. The fluidic chip and the device containing SiNWs were then brought into contact, with the 100-μm-wide microchannels aligned over the individual nanowire sections. The assembled device was cured to completion overnight at 80°C.

To automate an injection/changing of analyte solutions, we also introduced a second PDMS chip which can sequentially inject four different solutions into one of six microchannels on the silicon wafer. Such sample injection chip is composed of two layers,

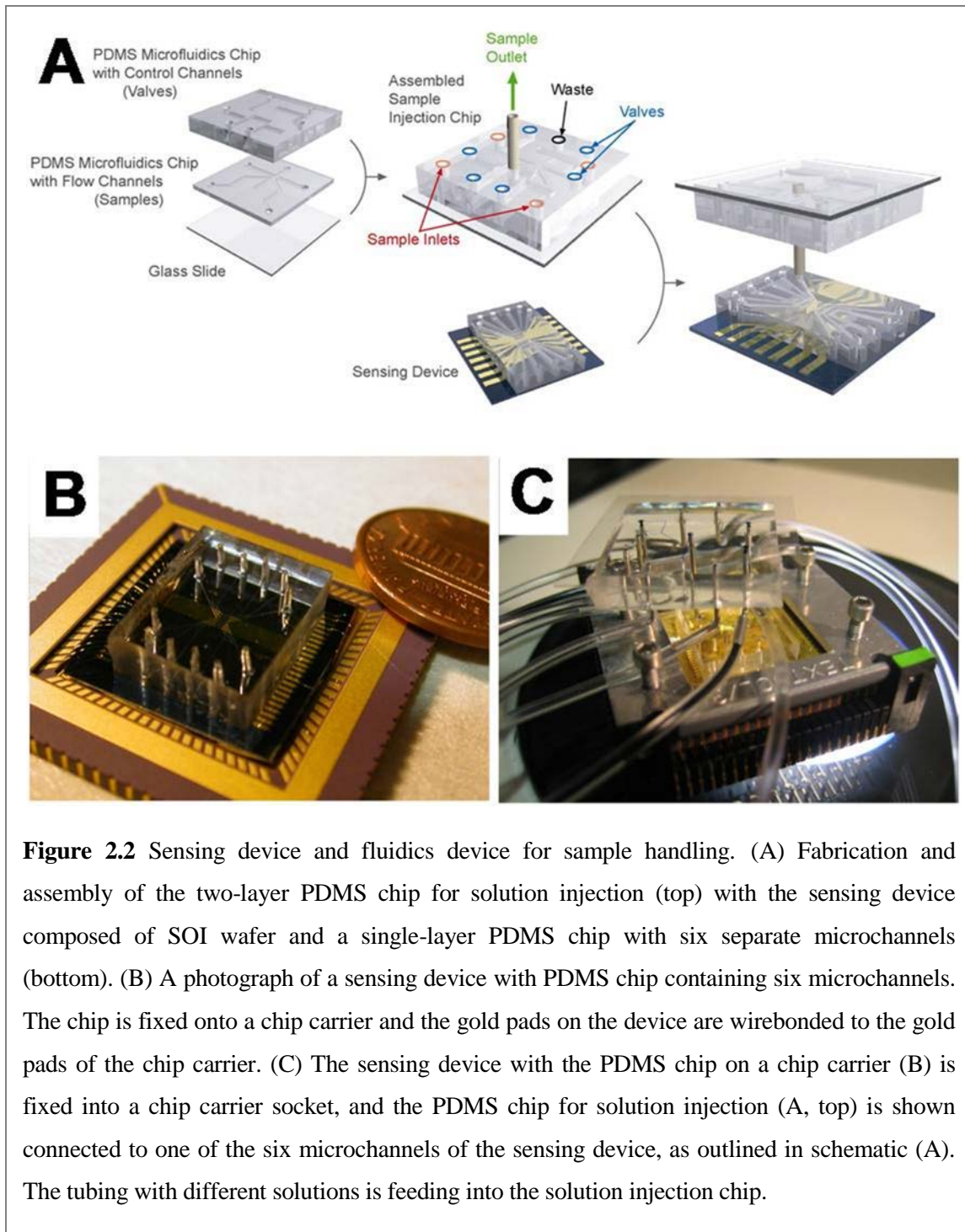


Figure 2.2 Sensing device and fluidics device for sample handling. (A) Fabrication and assembly of the two-layer PDMS chip for solution injection (top) with the sensing device composed of SOI wafer and a single-layer PDMS chip with six separate microchannels (bottom). (B) A photograph of a sensing device with PDMS chip containing six microchannels. The chip is fixed onto a chip carrier and the gold pads on the device are wirebonded to the gold pads of the chip carrier. (C) The sensing device with the PDMS chip on a chip carrier (B) is fixed into a chip carrier socket, and the PDMS chip for solution injection (A, top) is shown connected to one of the six microchannels of the sensing device, as outlined in schematic (A). The tubing with different solutions is feeding into the solution injection chip.

a control layer and a flow layer (Fig. 2.2A). For the fabrication of the flow layer, mixed PDMS was spin coated on a photoresist mold at 2500 rpm for 50 sec and incompletely cured at 80°C for 30 min. The control layer was fabricated by applying mixed PDMS over a photoresist mold directly and incompletely curing at 80°C, followed by the puncturing of

holes for inlets and outlets. The two layers were aligned together and the inlets/outlets for the flow layer were created. After two hours at 80°C, the two-layer PDMS chip was bonded to a glass slide via an O₂ plasma treatment. By utilizing such sample injection chip, we were able to control the injection and solution changing processes without disturbing the measurement, while maintaining the sensing device in an electrically isolated chamber at all times. The valves of the sample injection chip were actuated with the Labview program by means of the BOB3 Microfluidic Valve Manifold Controller and solenoid cluster manifolds (Fluidigm, Inc.). By introducing a waste outlet into the sample injection chip, we were able to remove any bubbles arising from switching between different solutions, which also helped in maintaining a stable baseline reading.

2.2.2 Surface functionalization and characterization for DNA sensing and antibody-based protein sensing

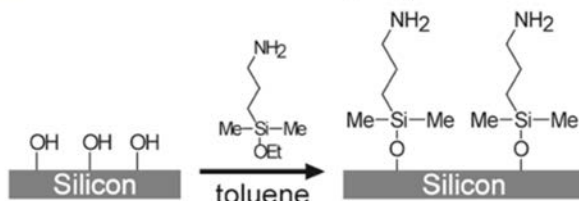
Synthesis of *tert*-Butyl allylcarbamate. To a solution of allylamine (2.27 g, 39.8 mmol) in THF (20 ml) was added *N,N*-diisopropylethylamine (13 ml, 80.0 mmol) followed by di-*tert*-butyl dicarbonate (8.7 g, 39.9 mmol). After 1 hr, the organic solvent was evaporated under reduced pressure, and the residue was purified by silica gel chromatography (Hex : EtOAc = 9 : 1) to give 6.6 g (93%) of a product as a clear oil. ¹H NMR 300 MHz (CDCl₃) δ 5.82 (m, 1H), 5.12 (m, 2H), 3.74 (bm, 2H), 1.45 (s, 9H).

Surface Functionalization. The two procedures used to functionalize SiNWs with and without oxide layer are shown in Schemes 2.1 and 2.2, respectively. Both procedures resulted in an amine terminated organic monolayer atop SiNWs. For the oxide surface functionalization, cleaned SiNWs were treated with 2% (v/v) 3-

aminopropyldimethylmethoxysilane (Gelest, Inc., Morrisville, PA) in toluene for 2 hr. The wafers were then rinsed in toluene and methanol and incubated at 100°C for 1 hr.

The procedure described previously^{42, 48} was used to functionalize hydrogen-terminated SiNWs with *tert*-Butyl allylcarbamate (Scheme 2.2). SiNWs were immersed in 2% HF solution for 3 s, washed with Millipore water and blow dried under N₂ stream. The wafer was immediately placed in a custom-made quartz container which was then pumped down to ~ 2×10⁻⁵ Torr, followed by an argon purge. Under positive argon pressure, a mixture of 1:2 *tert*-Butyl allylcarbamate:methanol (v/v) was applied to the wafer, completely covering the SiNWs. The wafer was illuminated with UV (254 nm, 9 mW/cm² at 10 cm) for 3 h. SiNWs were then rinsed in methylene chloride and methanol. The deprotection of t-Boc amine was carried out in a solution of TFA in methanol (1:4 v/v) for 4 h, followed by extensive methanol washing. In the case of antibody attachment, the amine-terminated surfaces were reacted with water-soluble homobifunctional N-hydroxysuccinimide ester (NHS ester), followed by the introduction of 50 µg/ml of

Scheme 2.1 Functionalization of Si (100) Oxide Surface with Amine



Scheme 2.2 Functionalization of Si (100) Surface with Amine



Schemes 2.1 and 2.2 Surface functionalization schemes

monoclonal anti-human IL-2 antibodies. The unreacted amines were quenched with ethanolamine (100 mM in 1×PBS).

X-ray photoelectron spectroscopy. X-ray photoelectron spectroscopy (XPS) was utilized to quantify the amount of oxide on Si(100) wafers after surface treatments outlined in Schemes 2.1 and 2.2. XPS was also used to follow the attachment of antibodies to silicon surfaces. All XPS measurements were performed in an ultrahigh vacuum chamber of an M-probe surface spectrometer that has been previously described.⁵³ Experiments were performed at room temperature, with 1486.6 eV X-ray from the Al K α line and a 35° incident angle measured from the sample surface. ESCA-2000 software was used to collect the data. An approach described elsewhere^{40,53} was used to fit the Si 2p peaks and quantify the amount of surface SiO_x, assuming that the oxide layer was very thin. Any peak between 100 eV and 104 eV was assigned to Si⁺-Si⁴⁺ and fitted as described in the literature.⁵⁴ SiO_x:Si 2p peak ratio was divided by a normalization constant of 0.17 for Si(100) surfaces.

Contact Angle Measurements. The sessile contact angle of water on the functionalized Si(100) surface was used to check the fidelity of surface chemistry as described in Schemes 2.1 and 2.2. Contact angle measurements were obtained with an NRL C.A. Goniometer Model #100-00 (Rame-Hart, Inc., Netcong, NJ) at room temperature. All measurements were repeated three times and averaged to obtain the contact angle θ for the surface.

2.2.3. Surface functionalization and characterization for peptide-based protein sensing

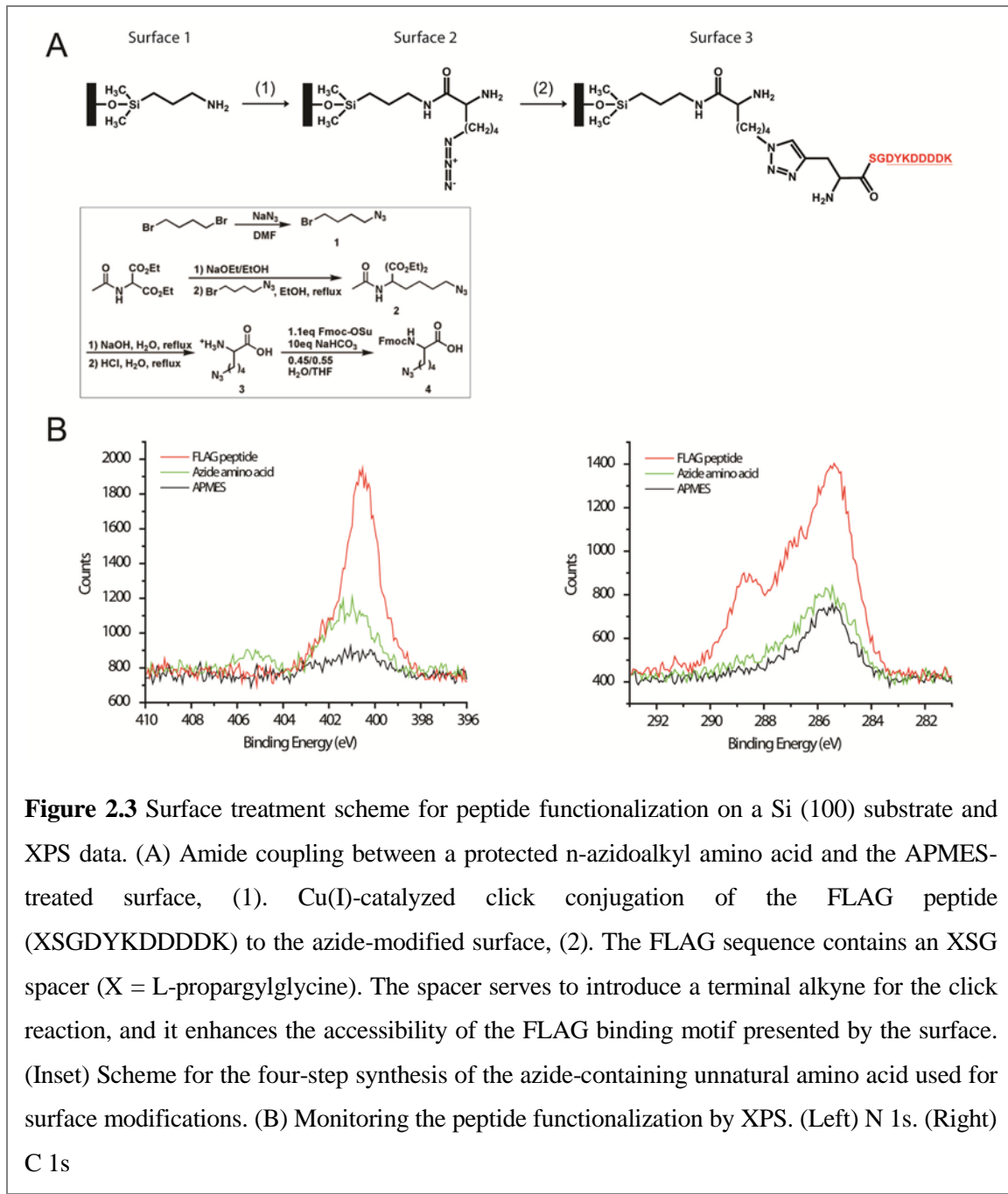


Figure 2.3 Surface treatment scheme for peptide functionalization on a Si (100) substrate and XPS data. (A) Amide coupling between a protected n-azidoalkyl amino acid and the APMES-treated surface, (1). Cu(I)-catalyzed click conjugation of the FLAG peptide (XSGDYKDDDDK) to the azide-modified surface, (2). The FLAG sequence contains an XSG spacer ($X = L$ -propargylglycine). The spacer serves to introduce a terminal alkyne for the click reaction, and it enhances the accessibility of the FLAG binding motif presented by the surface. (Inset) Scheme for the four-step synthesis of the azide-containing unnatural amino acid used for surface modifications. (B) Monitoring the peptide functionalization by XPS. (Left) N 1s. (Right) C 1s

Peptide Synthesis and Purification. The FLAG peptide was synthesized on Fmoc-Rink Amide MBHA resin (0.67 mmol/g, Anaspec, San Jose, CA) using conventional solid-phase synthesis strategy with Fmoc protection chemistry. To prepare the peptide for click conjugation, a terminal alkyne was introduced by adding Fmoc-L-propargylglycine (ChemImpex International, Wood Dale, IL), X, to the N-terminus to yield the sequence

XSGDYKDDDDK. The FLAG sequence also contains an SG spacer, to enhance the accessibility of the FLAG binding motif. The deprotected FLAG peptide was purified by HPLC on a C18 reversed phase column (Varian Dynamax semi-preparative column, 25 cm × 2.15 cm). The column was eluted with 0.1% trifluoroacetic acid and a two-step linear gradient of acetonitrile/water (3/2), rising from 0–25% over 30 min and 25–100% over 30 min. The pure FLAG peptide eluted at 41 min. The purified peptide product was verified to have the correct molecular weight as determined by mass spectrometry.

Synthesis of Azide-Containing Unnatural Amino Acid. The azide-containing unnatural amino acid used for surface modifications is synthesized by the following four steps.

Azidobutylbromide (1). To a solution of 1,4-dibromobutane (123 mmol), sodium azide (61.5 mmol) was added. The reaction mixture was stirred overnight at 50 °C, washed with water and brine, and dried over MgSO₄. The organic layer was concentrated and purified by silica gel chromatography (100% Hex) to give a product (80%) as clear oil.

Diethyl 2-acetamido-2-(4-azidobutyl)malonate (2). To a solution of 0.598 g (0.026 mol) sodium metal in 25 ml absolute EtOH was added 5.65 g diethyl acetamidomalonate (0.026 mol), following previously described procedures.⁵⁵ The mixture was stirred for 30 min at room temperature. By dropwise addition, azidobutylbromide **1** (4.82 g, 0.027 mol) was added with stirring. The reaction mixture was stirred for 2 h at room temperature and for 6 h at reflux. After cooling and standing for 14 h, the reaction mixture was concentrated to dryness, and the residue was extracted with ether. The combined ether extracts were washed with water, sat. NaHCO₃, and water, and were dried over MgSO₄ and then

concentrated. Silica gel chromatography (Hex:EtOAc = 1:1) gave a product (63%) as a clear oil.

2-Azidobutyl Amino Acid (3). Following standard methods,⁵⁶ the diester **2** (2.8 mmol) in 25 ml of 10% NaOH solution was heated to reflux for 4 h. The solution was then neutralized with concentrated HCl and evaporated. The residue was dissolved in 25 ml of 1 M HCl and heated to reflux for 3 h. The solvent was reduced and extraction with MeOH afforded amino acid **3** as a foamy solid (85%).

Fmoc-2-Azidobutyl Amino Acid (4). The amino acid **3** (26.3 mmol) was dissolved in 0.45:0.55 H₂O/THF (150 ml), and NaHCO₃ (22.1 g, 263 mmol) was added, following published methods.⁵⁷ After the mixture was cooled to 0°C, Fmoc-OSu (9.7 g, 28.9 mmol) was added dropwise over 5 min. The reaction mixture was allowed to come to room temperature and stirred overnight. The THF was evaporated *in vacuo* and the aqueous residue was washed with ether (2 x 200 ml). The aqueous layer was collected, acidified with concentrated HCl to pH 2 and extracted with ethyl acetate (4 x 100 ml). The combined organic layers were washed with brine, dried over MgSO₄, filtered, and concentrated. The organic residue was purified by column chromatography (2% MeOH in dichloromethane) to give a foamy solid. After recrystallization from EtOAc/Hex, a pure white powder was obtained (25% yield).

Surface Treatment. The cleaned silicon (100) surface was treated with 2% (v/v) 3-aminopropyltrimethylethoxysilane (Gelest, Inc., Morrisville, PA) in toluene for 2 h followed by rinsing with toluene and isopropanol (IPA). The wafer was then incubated at 120°C for 15 min (APMES-treated surface in Fig. 2.3A). The amine-terminated surface was converted into an azide-terminated one through the conjugation of the azide-containing

unnatural amino acid (synthesized following the scheme in Fig. 2.3A, inset). A solution of 20 mM azide-containing unnatural amino acid in DMF was prepared to contain 8 equiv HATU, 4 equiv HOAt, and 24 equiv DIEA (relative to the azide). This coupling solution was incubated with the surface for 2 h at room temperature, followed by rinsing with IPA and water. The N-terminal Fmoc protecting group was removed by treatment with 20% piperidine in DMF for 30 min. After cleaning the device with IPA and water, a PDMS chip with microfluidics channel was bonded to the device. The PDMS chip was fabricated by the soft lithography technique described by others.⁵¹ The channel was 150 μm wide and 20 μm high. The Cu(I)-catalyzed click conjugation of the FLAG peptide (XSGDYKDDDDK) to the azide-modified surface was performed. 20 equiv CuSO₄·5H₂O and 40 equiv sodium ascorbate (relative to the peptide) were mixed with a solution of 1 mM FLAG peptide in water and incubated over the device for 12 h in the prepared solution. Unreacted peptides and catalysts were rinsed away by flowing water through the channels. The FLAG sequence contains an XSG spacer (X = L-propargylglycine). The spacer serves to introduce a terminal alkyne for the click reaction, and it enhances the accessibility of the FLAG binding motif presented by the surface.

X-Ray Photoelectron Spectroscopy. X-ray photoelectron spectroscopy (XPS) was utilized to evaluate the surfaces at each step of the functionalization on Si (100) wafers. All XPS measurements were performed in an ultra-high vacuum chamber of an M-probe surface spectrometer that has been previously described.⁵³ Monochromatic Al K α X-rays (1486.6 eV) were used to irradiate the sample incident at 35° from the surface. ESCA-2000 software was used to collect and analyze the data. To gain an overview of the species present in the sample, survey scans were run from 0 to 1000 binding eV (BeV). The Si 2p

(95.5–107.5 BeV), C 1s (281–293 BeV), and N 1s (396–410 BeV) regions were investigated in detail.

Contact Angle Measurements. The sessile contact angle of water on the functionalized Si(100) surface was used to check the fidelity of surface chemistry. Contact angle measurements were obtained with an NRL C.A. Goniometer Model #100-00 (Rame-Hart, Inc., Netcong, NJ) at room temperature. All measurements were repeated ten times and averaged to obtain the contact angle for the surface.

2.2.4 SPR and electronic measurements

Surface Plasmon Resonance (SPR). All SPR experiments were performed on the Biacore 3000 with carboxylic-acid-terminated Biacore CM5 chips. The active flow cells were first primed in 1×SSC (15 mM NaCitrate, 150 mM NaCl, pH 7.5). To generate an amine surface, the carboxylic acid groups were converted to succinimide esters by flowing EDC/NHS prior to exposure of a 1 mg/ml solution of polylysine (Sigma-Aldrich, St. Louis, MO). Single-stranded DNA (5' TGGACGCATTGCACAT3', Midland Certified, Ind., Midland, TX) was electrostatically absorbed unto the polylysine matrix. Complementary DNA was then immediately introduced and allowed to hybridize to the active surface. The flow cell was regenerated with two 1-min pulses of 50 mM NaOH, after which ssDNA was reabsorbed electrostatically before another cDNA pulse was introduced for hybridization. The antibodies in acetate buffer (pH 5.5) were attached directly immediately following the surface treatment with EDC/NHS, and the remaining esters were reacted with ethanolamine. The antigen was introduced at various concentrations in 1×PBS buffer at the flow rate of 30

$\mu\text{l}/\text{min}$. Between each addition, the surface was regenerated with glycine/HCl buffer (pH 3.0).

Electronic Measurements. The 4-point resistivity of silicon film as well as SiNW resistances and solution gating were measured with a Keithley 2400 Source Meter (Keithley Instruments, Inc., Cleveland, OH). The sensing experiments were performed with a SR830 DSP Lock-in Amplifier (Stanford Research Systems, Inc., Sunnyvale, CA). Fig. 2.4 shows the experimental setup for the electronic measurements. A 50 mVrms at 13 Hz voltage source (V_{SD}) was applied to one terminal of the nanowire, with the amplifier input operating in the current-measure mode. For the DNA sensing experiments, platinum wire was inserted into the microchannel and used as a solution gate, while it was kept at a ground potential throughout the real-time measurements to reduce the noise in the system (Fig. 2.1A). In the case of protein sensing, the handle of the wafer (backside Si) was held at a ground potential instead of the platinum electrode in solution. The devices were functionalized and assembled as described above. Single-stranded 10 μM DNA (same as in SPR experiments) in 1 \times SSC buffer was flowed through the microchannel for 1 hr and allowed to electrostatically adsorb to the amine-terminated surface of SiNWs. The non-bound DNA was washed thoroughly with 1 \times SSC buffer. Complementary DNA (5'ATGTGCAATGCGTCCA3', Midland Certified, Ind., Midland, TX) of varying concentrations in 1 \times SSC buffer was sequentially injected from the injection PDMS chip into the microchannel containing SiNWs at a flow rate of 2.0 $\mu\text{l}/\text{min}$ as the resistance of the NWs was recorded in real time. Noncomplementary DNA (noncomp. DNA) (5'CATGCATGATGTCACG3') was used as a control. In general, a different SiNW sensor

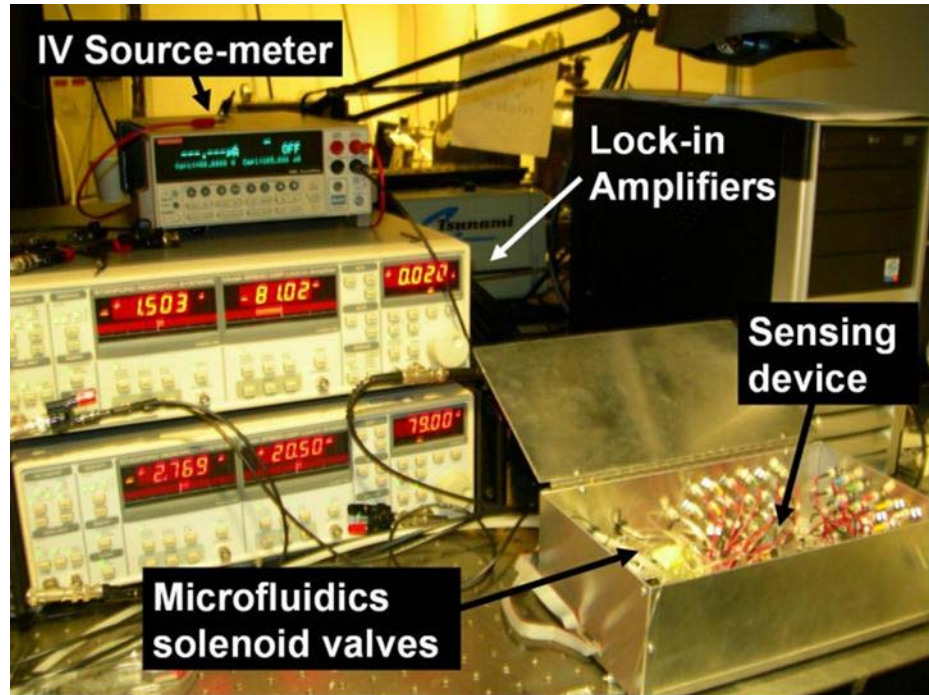


Figure 2.4 Experimental setup for biological sensing with silicon nanowires. The sensing devices (Figure 2.2C) are placed inside an electrically isolated box, which also contains solenoid manifolds that actuate microfluidic valves. The nanowire resistance is recorded in real-time with lock-in amplifiers.

was utilized for each of the measurements described here. Similar procedure was followed for protein sensing. The surface functionalized with capture antibodies was subjected to the 10 μM PBS solution containing various antigen concentrations (1 pM to 100 nM). After the introduction of a particular concentration, the surface was completely regenerated with 10 μM PBS, followed by the introduction of the next antigen concentration in the same microchannel.

2.3 Results and Discussion

2.3.1 DNA sensing

Surface Characterization. We used contact angle measurements to follow the functionalization processes of various surfaces. Table 2.1 presents the data for both Schemes 2.1 and 2.2. The procedure in Scheme 2.1 generates a large increase in contact angle. Similarly, large changes in contact angles are observed for photochemically treated Si surface before and after t-Boc deprotection. The resulting contact angle of $\sim 60^\circ$ is observed for surfaces prepared by Scheme 2.1 and 2.2, arguing for the existence of chemically similar, amine-terminated monolayers on these surfaces.

Quantifying the amount of oxide on the SOI NWs is extremely challenging. Therefore, we used Si(100) bulk surfaces to approximate the amount of surface oxide remaining after photochemical functionalization. Fig. 2.5A shows XPS scan in the Si/SiO_x region. The Si(100) surface with native oxide exhibited approximately 1.9 equivalent monolayers of

Table 2.1 Measured contact angles for various Si(100) surfaces

<i>Si(100) surface</i>	<i>contact angle</i>
With nonfunctionalized oxide	11 ± 1
Scheme 2.1: amine terminated	61 ± 1
Scheme 2.2: t-Boc protected	81 ± 1
Scheme 2.2: deprotected, amine terminated	60 ± 1

SiO_x. In contrast, the Si(100) surface treated according to Scheme 2.2 contained 0.08 equivalent monolayers of SiO_x prior to TFA deprotection and 0.3 monolayers of SiO_x after the deprotection step and a 10 h exposure to 1×SSC buffer. The roughness of a SiNW surface may cause a more extensive oxidation than the one observed on the bulk surface, but the data in Fig. 2.5A does demonstrate a significant reduction in oxide thickness after photochemical treatment. Furthermore, we used XPS to determine the presence of amine-terminated monolayer on bulk Si(100) surfaces post functionalization with two different

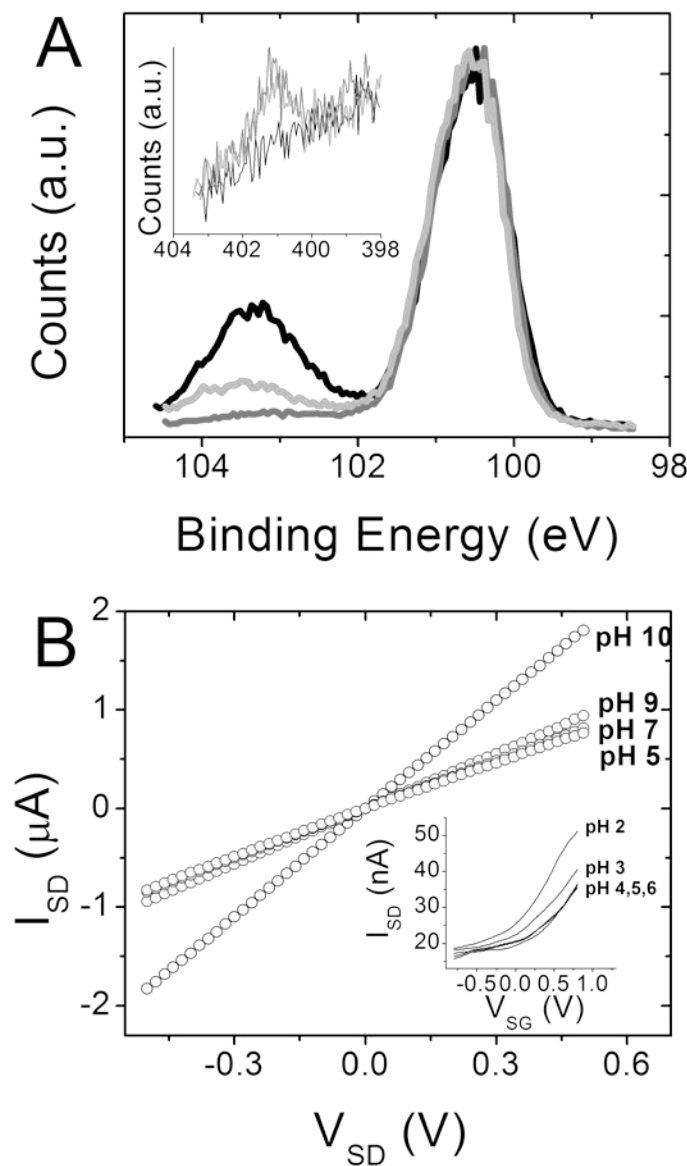
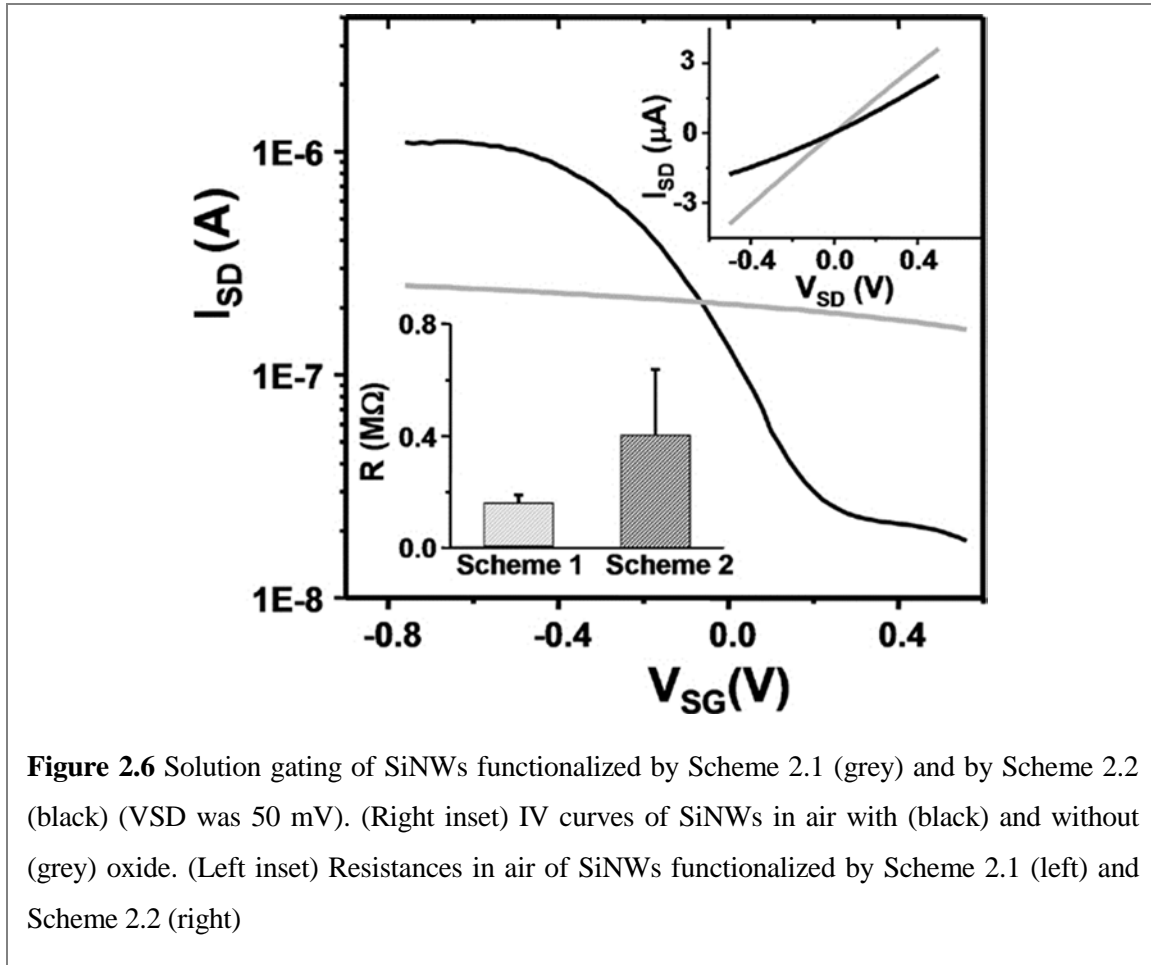


Figure 2.5 Surface analysis with XPS and SiNW response to pH. (A) XPS of Si 2p region of Si(100) surface functionalized as in Scheme 2.2 before (dark grey) and after (light grey) TFA deprotection and 10 hrs in 1×SSC buffer. Nonfunctionalized Si(100) surface with native oxide (black). Inset: N 1s region of nonfunctionalized Si(100) surface (black), Si(100) functionalized by Scheme 2.1 (light grey) and Scheme 2.2 (dark grey). (B) Current-voltage (IV) graphs of SiNWs functionalized by Scheme 2.1 in solutions of varying pH. Inset: Solution-gated (V_{SG}) n-type hydroxyl terminated SiNW in solutions of varying pH

schemes. The Fig. 2.5A inset demonstrates the XPS scans of N 1s region. Nitrogen peak is clearly visible for surfaces functionalized by Schemes 2.1 and 2.2, while no peak is present for the nonfunctionalized Si.

Scheme 2.1 functionalized SiNWs demonstrate a sensitivity to pH which is different than for native oxide-passivated NWs.¹³ The isoelectric point of silica is ~ 2 ,⁵⁸ implying that for hydroxyl-terminated, non-functionalized SiNWs at low pH, the SiOH groups are largely protonated. At high pH, negative charges on SiO⁻ should deplete carriers in the n-type SiNWs, causing a decrease in I_{DS} (Fig. 2.5B, inset). Above pH 4 the conductance is no longer modulated by increasing the pH, as most of the hydroxyl groups are deprotonated. When the surface is functionalized with amine ($pK_a \sim 9\text{--}10$), the opposite trend is expected. At low pH, the amine is protonated, causing carrier depletion or increased resistance in p-type SiNW. This trend is observed in Fig. 2.5B, where the sharpest transition in resistance occurs between pH 9 and 10. The observation of the correct pH effects on the resistance of the SiNWs serves as a confirmation of the presence of surface functional groups: amine in this case.

As shown in Fig. 2.6, oxide-covered SiNWs in 1×SSC buffer (0.165 M, pH 7.2) respond weakly to the applied solution gate voltage, V_{SG} , showing no significant on–off current transition between 0.8 and -0.8 volts. In contrast, directly passivated SiNWs (Scheme 2.2) exhibit on–off current ratios of $\sim 10^2$. Fig. 2.6 strongly suggests that directly passivated SiNWs exhibit an enhanced response to surface charges and should therefore serve as superior NW sensors compared with similarly functionalized, but oxide-passivated SiNWs.



The Scheme 2.2 procedure does involve an HF etch step, which can be potentially detrimental to the device conductance. We thus checked the conductivity of SiNWs before and after photochemical treatment. Lightly doped SiNWs provide for superior FET properties,⁵⁹ and, in fact, we have reported that lightly doped (10^{17} cm⁻³) p- or n-type SiNWs are more sensitive biomolecular sensors than those reported here.⁶⁰ Our doping process preferentially dopes the top few nanometers of the SiNWs.⁶¹ Thus, if the HF etching of the Si surface was extensive enough, we could expect an enhancement in SiNW current modulation by V_{SG} to be entirely due to the decrease in carrier concentration and not the removal of surface oxide. The Fig. 2.6 insets demonstrate that the NW resistance

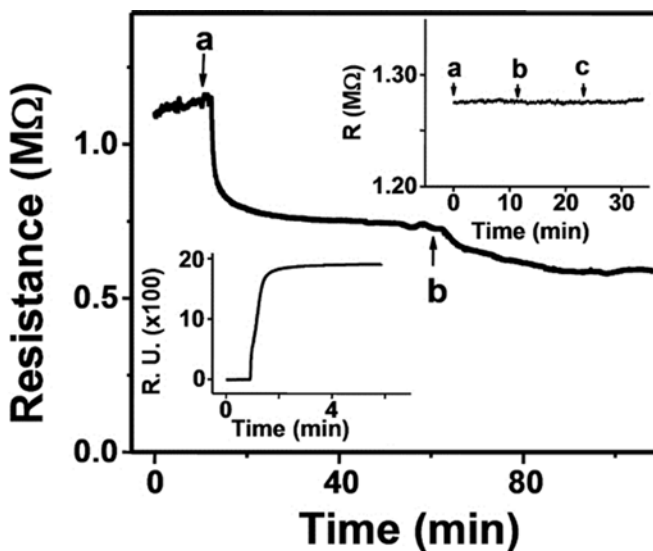


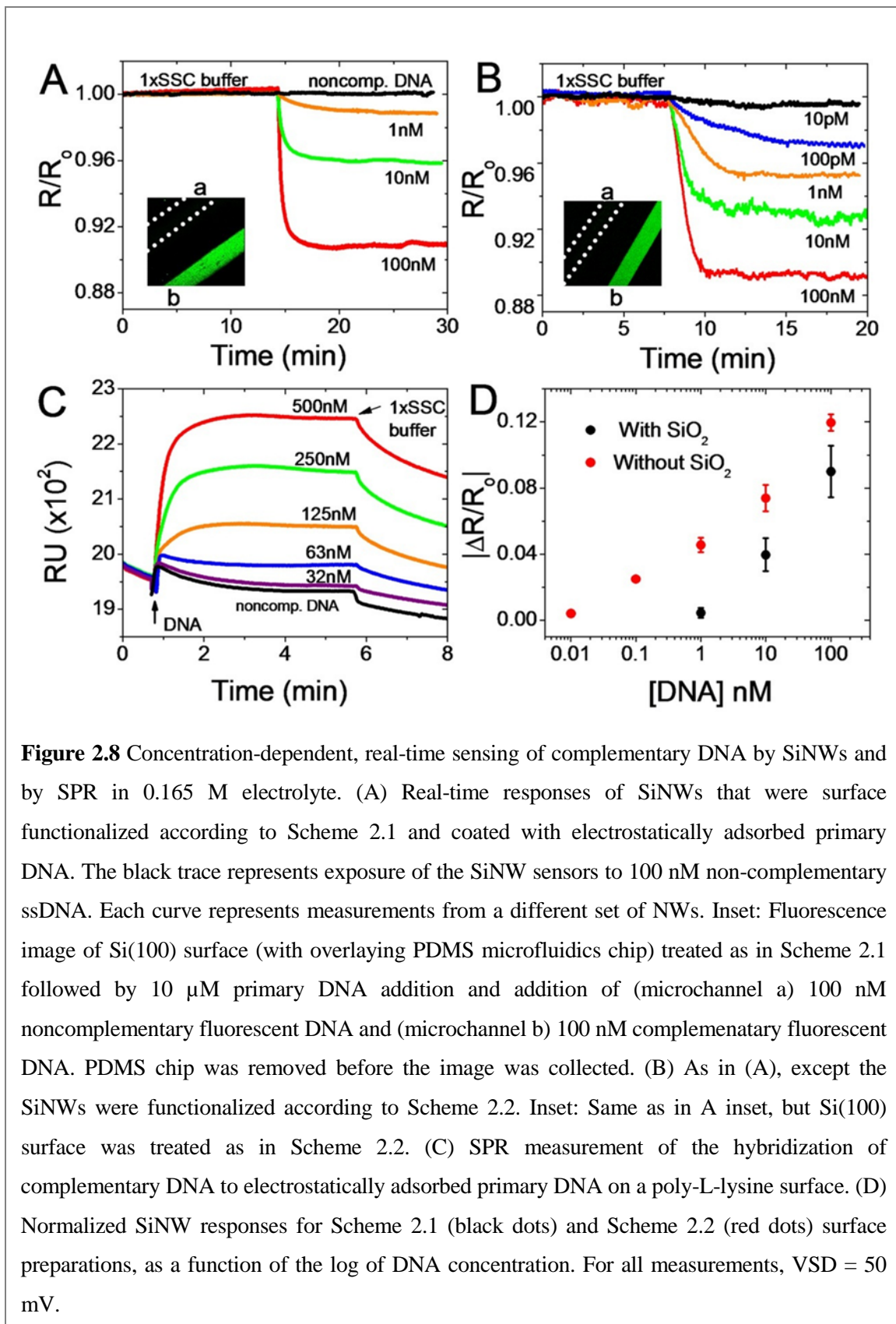
Figure 2.7 Real-time response of SiNWs functionalized as in Scheme 2.1 to the addition of (a) 10 μ M ssDNA and (b) 100 nM complementary DNA. Right top inset: Real-time SiNW response to the sequential addition of (a) 0.165 M SSC, (b) 0.0165 M SSC, and (c) 0.00165 M SSC buffers. Left inset: SPR measurement demonstrating the addition of 10 μ M ssDNA to poly-L-lysine coated CM5 sensor chip. VSD = 50 mV.

increased only, on average, by a factor of 2 following the HF treatment. This relatively negligible resistance increase indicates that the major reason that the SiNWs prepared by Scheme 2.2 exhibit an improved solution FET performance originates from the elimination of oxide via direct silicon passivation. This result is consistent with the recent demonstration that, for VLS-grown SiNWs, direct methylation of the SiNW surface leads to a 10^3 – 10^4 -fold enhancement in the on–off conductance of the FETs made from those nanowires.⁴³

Nanowire Sensing Measurements. Fig. 2.7 shows SiNW real-time detection of the electrostatic adsorption of 10 μ M ssDNA, followed by the hybridization in 1×SSC buffer of 100 nM complementary DNA strand. As expected, the resistance of p-type SiNWs is decreased with the addition of negative surface charges. The metal contacts to NWs have

been covered with a Si₃N₄ layer, and there is no background conductance through the solution. We have observed an insignificant change in the resistance of the NWs upon switching from dry environment to buffer solution (data not shown). Moreover, as Fig. 2.7 (right inset) shows, changing the ionic strength of the solution does not affect the resistance. In addition, the automated solution injection removes any baseline shifts or transient changes in the resistance. SPR was also utilized in parallel to SiNWs in order to validate the surface chemistry and to obtain kinetic parameters such as k_{on} , k_{off} , and affinity constant K_A for this particular DNA pair. Poly-L-lysine was covalently attached to the SPR sensor chips, mimicking the amine-terminated monolayer of SiNWs. Fig. 2.7 (left inset) shows the SPR response to the electrostatic adsorption of a 10 μM primary DNA strand. The surface density of adsorbed DNA was estimated as $2.5 \times 10^{13} \text{ cm}^{-2}$, using the conversion factor of 1000 RU = 100 ng cm⁻² from the literature.⁶² The surface density is approximately an order of magnitude higher than the average surface density of 10^{12} cm^{-2} obtained when localizing biotinylated DNA on a streptavidin-covered surface.⁶³ Such high surface density of primary DNA is expected because the poly-L-lysine-treated surface is positively charged. It is likely that the amine-terminated SiNW surface has less surface charge than the poly-L-lysine-covered surface and thus contains fewer sites for electrostatic adsorption of oligonucleotides.

Fig. 2.8 demonstrates real-time label-free detection of ssDNA by SiNWs and by SPR. In either case, the primary DNA strand was electrostatically immobilized on the sensor surface. Known DNA concentrations were injected after a stable reading with 1×SSC buffer was obtained and the flow was maintained throughout the experiment. Different concentrations were detected with different groups of SiNWs. We observed that the



hybridization on SiNWs is essentially irreversible on the relevant time scales when the analyte DNA was being washed away with the buffer solution. Such behavior is in contrast to SPR measurements, where the slow reversal of hybridization was observed (Fig. 2.8C). The performance of the NWs surface functionalized according to Scheme 2.1 (Fig. 2.8A) was compared to SiNW sensors prepared according to Scheme 2.2 (Fig. 2.8B). The SPR experiments, although carried out on Au substrates, also utilized primary ssDNA that was electrostatically adsorbed onto an amine-terminated surface. The intention here was to find experimental conditions that could serve to validate the NW experiments by obtaining kinetic parameters for these particular DNA strands under specific experimental conditions. Control experiments with non-complementary DNA yielded no response for either SiNWs or SPR measurements (black traces of Figs. 2.8A and 2.8C). These negative controls were also independently validated via fluorescent detection in microfluidic channels on two different (Schemes 2.1 and 2.2) Si surfaces (Figs. 2.8A and 2.8B, insets). Fig. 2.8D demonstrates that the NW response ($\Delta R/R_0$) varies as $\log[\text{DNA}]$. Such a logarithmic dependence has been previously reported.²¹ As demonstrated in Fig. 2.8D, the dynamic range of SiNWs is increased by 100 after the removal of oxide and UV-initiated chemical passivation; the limit of detection (LOD) increased from 1 nM to 10 pM.

Nanowires as Quantitative Biomolecular Sensors. SiNW sensors can potentially be utilized to quantitate analyte concentration and binding constants. In order to explore this possibility, the SiNW sensing response must be compared with other label-free, real-time methods such as SPR. It is also critical to design experimental parameters for both sensing modalities that are as similar as possible, as was described above. In this section, we first discuss the use of electrostatically adsorbed primary DNA for detecting complementary

DNA analyte. We then discuss the development of a self-consistent model that allows for the direct comparison of SPR measurements with nanowire sensing data. Finally, we test that model by utilizing the nanowire sensing data to calculate 16-mer DNA binding constants and analyte concentrations.

Previous studies have demonstrated that the Langmuir model can be applied for parameterization of the hybridization processes of short oligonucleotides.^{22, 63} We used the Langmuir model to calculate kinetic parameters from the SPR hybridization measurements (Fig. 2.8C) and obtained $k_{\text{on}}=1\times10^5$, $k_{\text{off}}=2\times10^{-2}$, $K_A=5\times10^6$ (Table 2.2). This K_A value is between 10 and 100 times smaller than that reported for similar length DNA measured with a quartz crystal microbalance, SPR,²² and surface plasmon diffraction sensors (SPDS).⁶³ The average primary DNA surface coverage in those studies was $\sim 5\times10^{12}$ molecules/cm². As stated above, the electrostatically adsorbed DNA coverage in our SPR experiments was approximately 10 times higher, at 2.5×10^{13} cm⁻². This difference in coverage likely arises from the differing methods of DNA immobilization; while in our system the DNA is electrostatically adsorbed, other studies utilized a streptavidin-biotinylated DNA linkage for surface immobilization.^{22, 63} High surface coverage of primary DNA significantly reduces the efficiency of hybridization.^{63, 64} In addition, the hybridized duplex of electrostatically adsorbed and covalently bound DNA may be structurally and energetically different. It has been proposed that a preferred structural isomer of an oligonucleotide pair on a positively charged surface is a highly asymmetrical and unwound duplex.⁶⁵ We believe that such non-helical nature of DNA duplex, together with steric effects of highly packed surface play major roles in the reduced affinity for the 15mer pair used in this study.

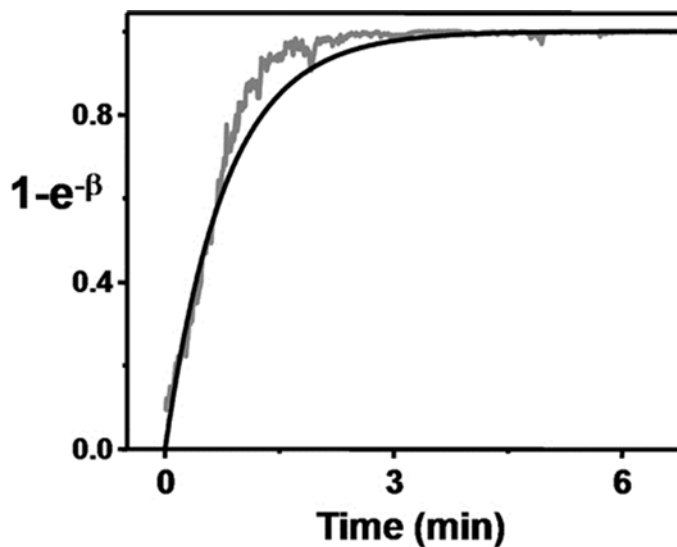


Figure 2.9 Comparison of SPR-derived hybridization kinetic parameters with NW sensing data. The black line represents eq. 5 plotted using k_{on} and k_{off} obtained from SPR measurements, $\beta = (k_{on}C + k_{off})t$. The grey trace is obtained from SiNW resistance vs. time data, $\beta = \frac{\Delta R}{R_{max} - R}$. C = 10 nM.

We now turn toward developing a model for using SiNW sensors to quantitate complementary DNA pair-binding constants, and, if those numbers are known, to determine the solution concentration of the analyte. A discussion of the kinetics of a surface binding assay, as measured within flowing microfluidics environments, is required. Zimmermann and coworkers modeled the kinetics of surface immunoassays in microfluidics environments.⁶⁶ Their model was based on four differential equations: the two Navier-Stokes partial differential equations, the Convection-Diffusion equation, and the ordinary differential equation resulting from the Langmuir binding model (i.e., the binding/hybridization equilibrium). A key result was that in the limit of high analyte flow speeds (> 0.5 mm/sec) (which is the case for all the experiments here) the amount of

analyte that is captured and ready for detection can be described by the ordinary differential equation resulting from the Langmuir binding model:

$$\frac{d\Theta_t}{dt} = k_{on} C (\Theta_{max} - \Theta_t) - k_{off} \Theta_t . \quad (2.1)$$

Here, Θ_t = surface density of bound analyte molecules; k_{on} = rate constant for association; k_{off} = rate constant for dissociation; C = solution concentration of analyte (a constant under flowing conditions); Θ_{max} = maximum number of binding sites available per surface area. Eq. 2.1 can be solved analytically:

$$\Theta_t = \frac{k_{on} \Theta_{max} C}{k_{on} C + k_{off}} \left(1 - e^{-(k_{on} C + k_{off}) t} \right) . \quad (2.2)$$

The challenge is to translate from the resistance change of a SiNW sensor to the analyte concentration, C . However, the exact relationship between a measured resistance change and the surface density of bound analyte molecules is not intuitively clear. Here we attempt to determine the nature of that relationship.

We demonstrated above (Fig. 2.8D) that the cumulative change in SiNW sensor resistance arising from the binding of a charged analyte (ssDNA) at a concentration-dependent saturation was linearly proportional to the $\log[DNA]$, similar to what has been reported for VLS SiNW detection of prostate-specific antigen (PSA).²¹ In mathematical terms, this means that as we approach saturation for a given concentration:

$$\frac{\Delta R}{R_0} = \alpha \ln C \quad (2.3)$$

where α is a constant, $\Delta R = R - R_0$, R is resistance at time t , and R_0 is the resistance at $t = 0$.

At saturation levels eq. 2.2 reduces to $\Theta_t = \frac{k_{on} \Theta_{max} C}{k_{on} C + k_{off}} = \frac{K_A \Theta_{max} C}{K_A C + 1}$ (where the binding

affinity $K_A = \frac{k_{on}}{k_{off}}$). In the limit where $K_A C \ll 1$ (which is usually the case with values of

$C \leq 10^{-9}$ and values of $K_A < 10^8$), this reduces to $\Theta_t = K_A \Theta_{\max} C$. Therefore, at saturation,

and with $K_A C \ll 1$, Θ_t scales linearly with C . From our previous discussion, this implies

that at saturation $\frac{\Delta R}{R_0}$ scales logarithmically with Θ_t (or equivalently that Θ_t is an

exponential function of $\frac{\Delta R}{R_0}$ at saturation). In estimating the relationship between resistance

changes at all times (not just at saturation) and the surface density of bound analyte

molecules at all corresponding times, we start by assuming the same functional relationship

that we experimentally observe at saturation. We also impose two boundary conditions. (1)

When the measured resistance reaches its saturation level we would expect the maximum

number of binding events to have taken place and for that number to be consistent with the

prediction from the Langmuir binding model (eq. 2.2). (2) When the measured resistance is

unchanged from its starting level we expect zero binding events (again consistent with the

Langmuir model at time = 0). Based on these assumptions and boundary conditions we can

thus estimate that the surface density of bound analyte molecules as a function of resistance

change has the form:

$$\Theta_t = \frac{k_{on} \Theta_{\max} C}{k_{on} C + k_{off}} \left(1 - e^{\frac{-\Delta R}{R_{\max} - R}} \right); (R_{\max} = R \text{ at saturation}). \quad (2.4)$$

The validity of eq. 2.4 can be tested by considering the following expression that is

derived from eq. 2.4 and comparing it to the same expression derived from eq. 2.2:

$$\frac{\Theta_t}{\frac{k_{on}\Theta_{max}C}{k_{on}C + k_{off}}} = [1 - e^{\frac{-\Delta R}{R_{max} - R}}] = [1 - e^{-(k_{on}C + k_{off})t}] \quad (2.5)$$

Note that eq. 2.5 is expressing the fraction of bound analyte molecules at time t relative to the level at saturation in terms of ΔR (first term in brackets) and in terms of binding constants (second term in brackets). Time appears explicitly in the second term in brackets, while it is implicit in the first term in brackets (i.e., at a given time t there is a given R and ΔR). If we plot the first term in brackets in eq. 2.5 (the term containing ΔR) against the second term in brackets (using k_{on} and k_{off} values from an SPR analysis), we find that the two curves are similar (Fig. 2.9).

A second test of eq. 2.4 is to utilize it to extract binding kinetics. As we can infer from eq. 2.5, if eq. 2.4 is equivalent to the Langmuir binding model (eq. 2.2), then:

$$\frac{\Delta R}{R_{max} - R} = (k_{on}C + k_{off})t \quad (2.6)$$

We can thus extract k_{on} and k_{off} values from measured resistance data. We can select R vs. time traces at any two concentration values. Taking R and ΔR at an arbitrary point in time and noting R_{max} (the resistance at saturation), we have two equations (one for each concentration C) and two unknowns. We thus solve for k_{on} and k_{off} and compare directly with kinetic parameters obtained from SPR experiments. The k_{on} , k_{off} , and K_A values are summarized in Table 2.2. The k_{on} constants determined from the SiNW experiments are 3–5 times larger than k_{on} obtained with SPR experiments. The nanowire-measured k_{off} values, however, are consistently quite close to those measured with SPR. As stated above, the variation in k_{on} values may be a reflection of steric affects that arise from the unusually high surface density of primary DNA adsorbed onto the poly-L-lysine surfaces that were

	SiNWs-concentration pair:			SPR (this work) (poly-L-lysine surface, 16-mer DNA)	SPDS (ref. 63) (avidin-biotin linkage, 15-mer DNA)
	10 nM 100 nM	1 nM 100 nM	1 nM 10 nM		
k_{on} (M ⁻¹ s ⁻¹)	3.5(3.4) × 10 ⁵	4.2(2.4) × 10 ⁵	6.2(9.6) × 10 ⁵	1.01 × 10 ⁵	6.58 × 10 ⁴
k_{off} (s ⁻¹)	3.1 (0.5) × 10 ⁻²	2.4 (0.8) × 10 ⁻²	2.4 (0.9) × 10 ⁻²	2.01 × 10 ⁻²	1.32 × 10 ⁻⁴
K_A (M ⁻¹)	1.1 × 10 ⁷	1.8 × 10 ⁷	2.6 × 10 ⁷	5.02 × 10 ⁶	4.98 × 10 ⁸
[DNA]	100 nM (actual); 68(52) nM calculated 10 nM (actual); 14(9) nM calculated				

Table 2.2 Kinetic parameters estimated from SiNW biosensors for the hybridization of 16-mer DNA and corresponding comparisons with analogous SPR and SPDS (surface plasmon diffraction sensor).⁶³ The calculated concentrations (bottom row) were estimated with eq. 6, by using the pair of SiNW measurements that did not include the concentration to be determined. For example, the 1 nM and 100 nM measurements were used to determine the concentration at 10 nM. Standard deviations are given in parentheses.

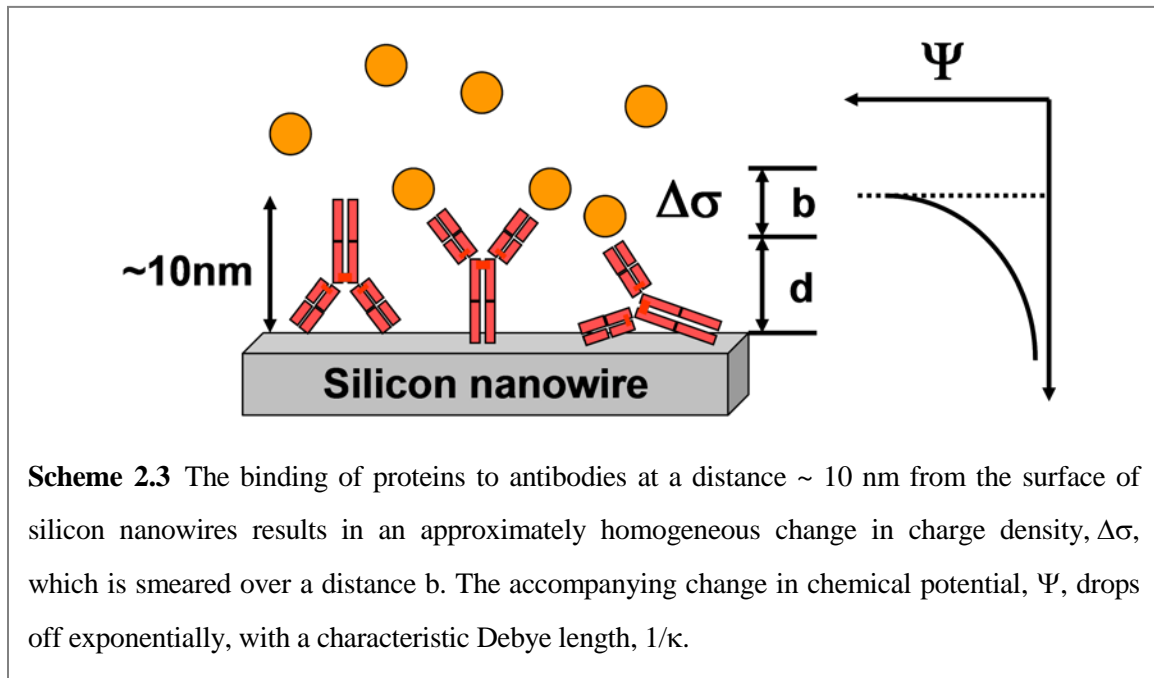
used for the SPR experiments.^{63, 64}

Further work has to be done to ground this translation from nanowire-resistant readings to the Langmuir binding model (or equivalently from resistance readings to number of bound analyte molecules) on firm theoretical grounds. It is encouraging, however, that with our resistance data we can extract useful binding kinetics. The most useful application of our model would be in extracting otherwise unknown concentration values once k_{on} and k_{off} values are known. As demonstrated here and elsewhere, SiNW sensors can be used for label-free biomolecule detection at concentrations significantly below the limits of detection for SPR. Thus, the potential for SiNW sensors to quantitate analyte concentrations when the concentrations are below 10 nM represents a nontrivial application. The consistency of the SiNW measurements that is reflected in the Table 2.2 values is worth noting, especially since each measurement was carried out using a different SiNW

sensor. This provides validation that the nanofabrication techniques that were utilized to prepare the NW sensing devices are highly reproducible.

2.3.2 Protein sensing with antibodies

Robust label-free detection of proteins below the concentration of ~ 10 pM is of considerable importance in rapid clinical evaluation, cancer marker detection, disease staging, etc. The real-time nature of electronic label-free detection also offers additional



benefits such as characterization of new affinity probes, drug screening, and could, therefore, be potentially useful in basic research as well as in clinical practice. For these reasons, we have extended the above study to the detection of proteins. Such endeavor, however, faces a fundamental challenge, owing to the significant charge screening in the solution of high ionic strength. The extent of such screening may be characterized by the Debye length, $1/\kappa$,²⁰ which describes a distance from a point charge at which the potential

due to that charge drops off to $\sim e^{-1}$ of its value. Scheme 2.3 demonstrates the relevance of Debye screening to the electrical detection of biomolecules in solution. Here, we assume that the antibodies, which serve as capture probes for proteins, are approximately 10 nm long, and are randomly oriented on the surface of the nanowire. The change in charge density, $\Delta\sigma$, due to the equilibrium binding of proteins is smeared over a distance b , which is a distance d away from the NW surface. The change in chemical potential per area at the surface of the nanowire may be described by the Debye-Hückel equation,^{18, 20}

$$\Delta\Psi = \frac{\Delta\sigma}{b} \frac{[e^{-\kappa d} - e^{-\kappa(d+b)}]}{\epsilon_0 \epsilon_w \kappa^2} \quad (2.7)$$

where ϵ_0 is the dielectric constant, ϵ_w is the permittivity of water and κ^{-1} is the Debye screening length. As is readily noticeable from eq. 2.7, the larger the $1/\kappa$ (smaller κ), the more pronounced will be the surface potential change for a given change in the charge density. Surface potential and the distance from the surface at which the binding takes place are intimately coupled. If the screening length is much smaller than d , $\kappa^{-1} \ll d$, then the potential due to protein binding will be completely screened from the surface of the nanowire. Therefore, the condition $\kappa^{-1} \geq d$ must be met in order to detect charged species in the solution a distance d away from the surface. In the case of DNA sensing (Section 2.3.1), the capture probe single-stranded DNA was electrostatically adsorbed on the NW surface, and the hybridization was taking place very close, ~ 1 nm from the surface, allowing us to carry out sensing in high ionic strength conditions of 0.165 M. The antibodies, however, are fairly large biomolecules (Scheme 2.3). At 25°C the Debye length of aqueous solution is²⁰

$$\frac{1}{\kappa} = \frac{0.304}{\sqrt{[NaCl]}} nm \quad (2.8)$$

for 1:1 electrolytes such as NaCl.

As Table 2.3 demonstrates, the size of the antibodies dictates the ionic strength of the solution in which the electronic detection may take place. This is a serious limitation if the physiological medium such as serum (0.14 M) must be used to detect low abundance proteins, without the possibility of appropriate dilutions. To circumvent this problem, new high-affinity probes, such as aptamers, small molecules, and short peptides, must be developed, all of which are significantly smaller than the antibodies.

[NaCl]	$1/\kappa$
100 mM	1 nm
1 mM	10 nm
10 μ M	100 nm

Table 2.3 Debye length at different salt concentrations

SiNW surfaces for protein sensing were functionalized in a similar manner to the experiments with DNA. Native oxide of silicon was functionalized with an amine-terminating monolayer. A bifunctional crosslinker, with an NHS ester on either end, was coupled to the primary amines on the surface, followed by the coupling of antibodies to the other end of the linker. This chemistry may potentially involve any of the primary amines of the antibody, and, therefore, probably results in a random orientation of the antibodies on the surface (Scheme 2.3). Since the surface area of a nanowire is rather small, $\sim 10^{-13} m^2$, this may result in the broadening of the distribution of the responses from the identical

nanowires. Measuring the response of a larger array of nanowires, therefore, may lead to a smaller variance in the response.

XPS scans of the carbon 1s region from the silicon surface treated as described above are presented in Fig. 2.10. Clear emergence of the C=O and C-O/C-N bonds is visible, suggesting that the antibodies are successfully attached to the surface. The doping level was chosen as the one which reproducibly yields wires with resistances of $\sim 1 \text{ M}\Omega$, ohmic contacts, and good solution transconductance behavior (Fig. 2.11A). Wires with higher doping are not as sensitive to proteins and those with lower doping yield fewer functional devices.

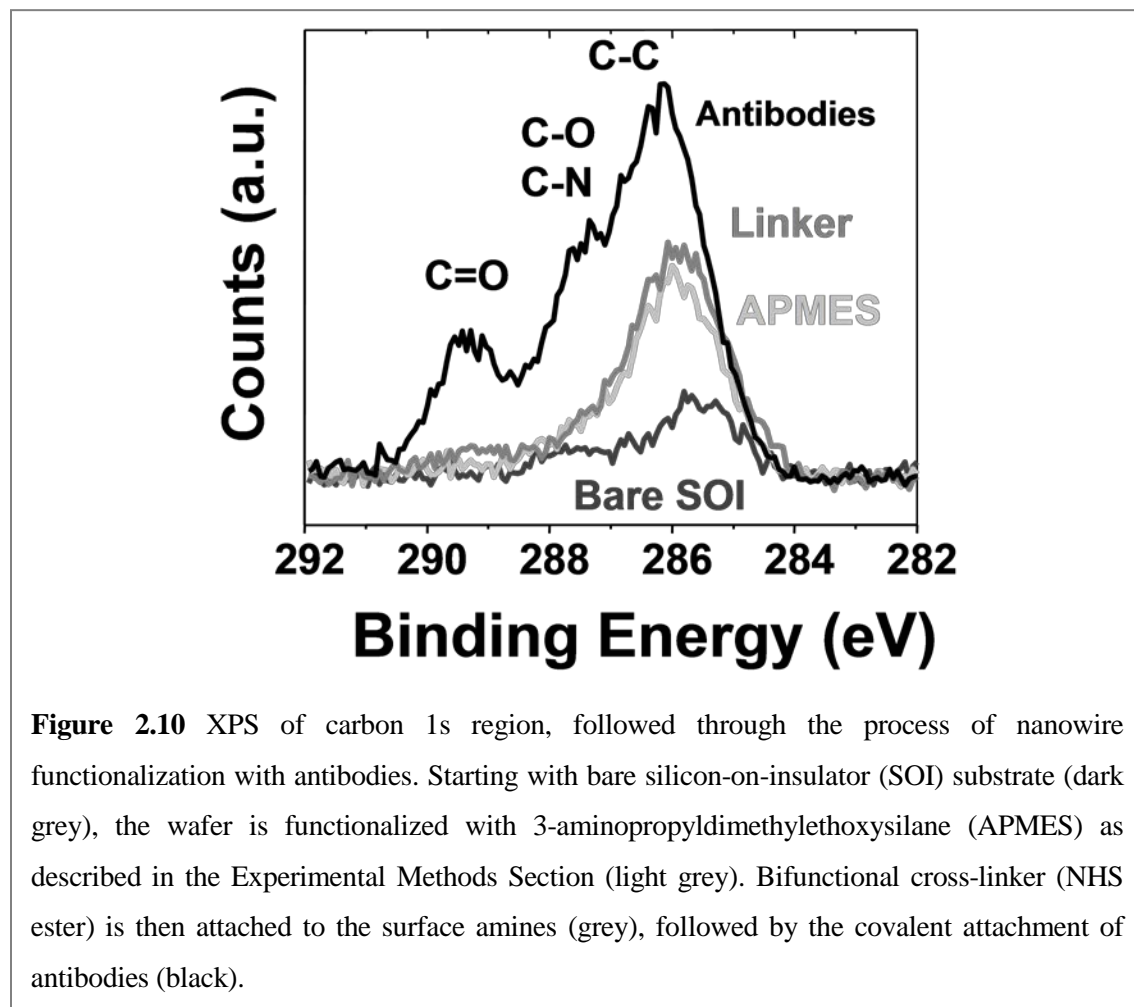
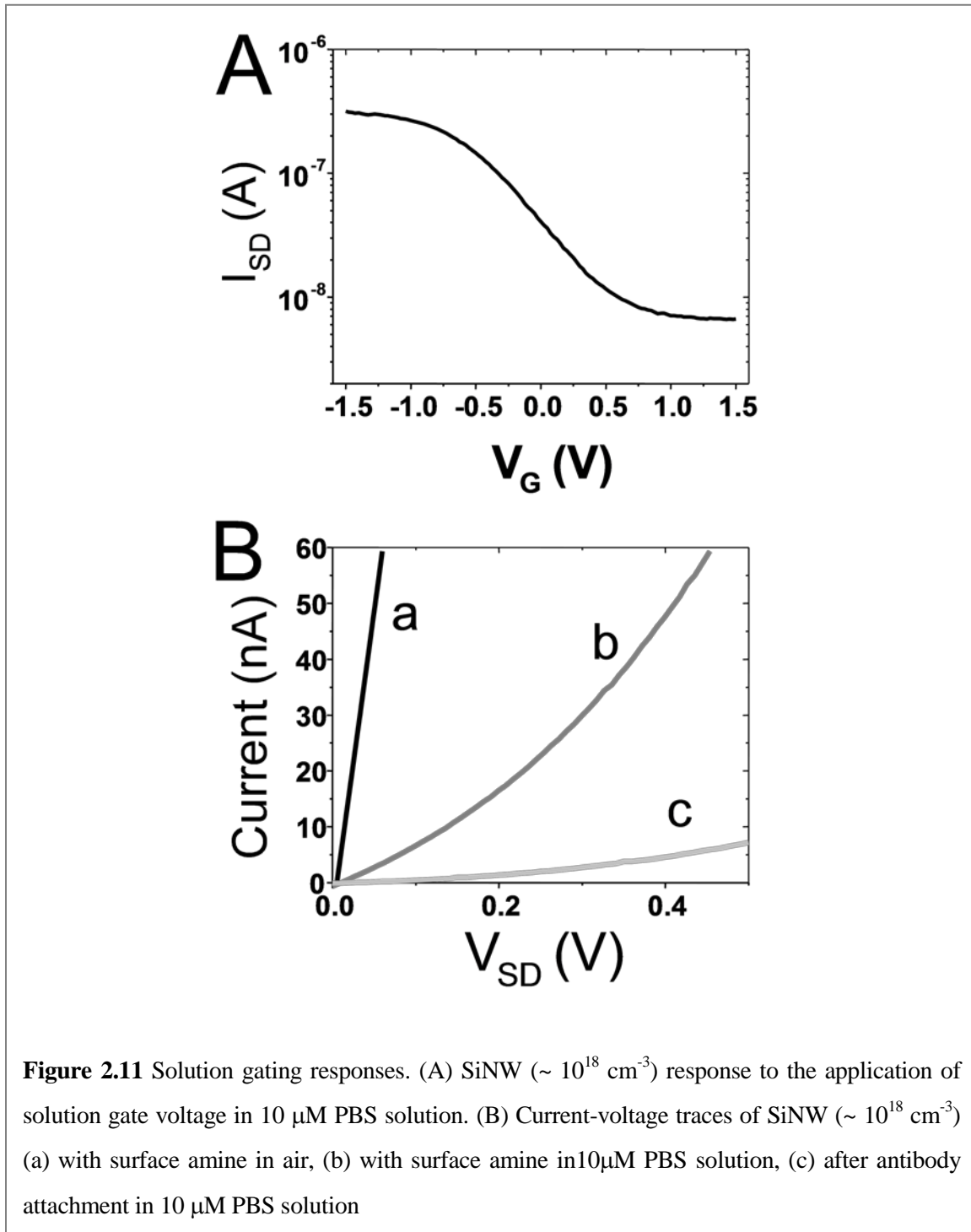


Figure 2.10 XPS of carbon 1s region, followed through the process of nanowire functionalization with antibodies. Starting with bare silicon-on-insulator (SOI) substrate (dark grey), the wafer is functionalized with 3-aminopropyltrimethoxysilane (APMES) as described in the Experimental Methods Section (light grey). Bifunctional cross-linker (NHS ester) is then attached to the surface amines (grey), followed by the covalent attachment of antibodies (black).

The attachment of antibodies was further verified by monitoring the resistance of the nanowires during the functionalization process. Fig. 2.11B shows IV curves of the nanowires in air, in solution, and after the attachment of the antibodies. The resistance of



the amine-terminated nanowires drops significantly after immersion in solution and yet further after the attachment of the antibodies. The pH of the 10 μM PBS is approximately 6.0, which may account for the increase in the resistance in the solution. It is also possible that pH 6.0 is below the isoelectric point of the particular antibody used here, and the excess positive charges on the antibody surface lead to the further increase in the resistance.

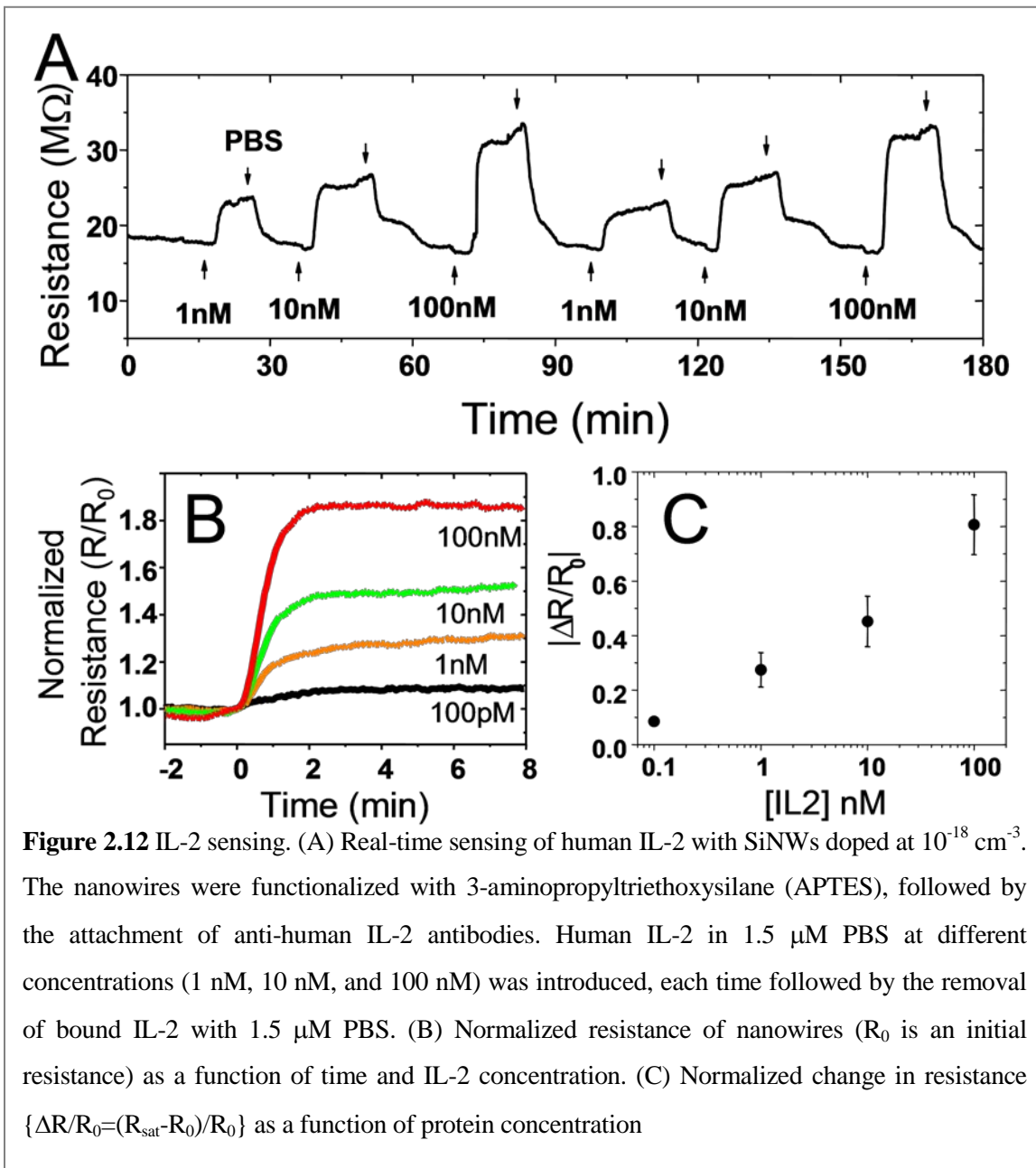


Figure 2.12 IL-2 sensing. (A) Real-time sensing of human IL-2 with SiNWs doped at 10^{-18} cm^{-3} . The nanowires were functionalized with 3-aminopropyltriethoxysilane (APTES), followed by the attachment of anti-human IL-2 antibodies. Human IL-2 in 1.5 μM PBS at different concentrations (1 nM, 10 nM, and 100 nM) was introduced, each time followed by the removal of bound IL-2 with 1.5 μM PBS. (B) Normalized resistance of nanowires (R_0 is an initial resistance) as a function of time and IL-2 concentration. (C) Normalized change in resistance $\{\Delta R/R_0 = (R_{\text{sat}} - R_0)/R_0\}$ as a function of protein concentration

Real-time detection of proteins with SiNWs is demonstrated in Figs. 2.13 and 2.15. In each case, the same microchannel (the same SiNWs) was used for introducing antigen at various concentrations. After the saturation of the signal, phosphate buffer was used to remove bound human interleukin-2 (IL-2). This process was repeated several times with different IL-2 concentrations, and as Figs. 2.12A and 2.14A demonstrate, the antigen-antibody binding is fully reversible. SiNWs can, therefore, similarly to the SPR chip, be reused multiple times for protein detection. The data in Fig. 2.12 was collected in 1.5 μM PBS using the chip which was functionalized with 3-aminopropyltriethoxysilane (APTES).

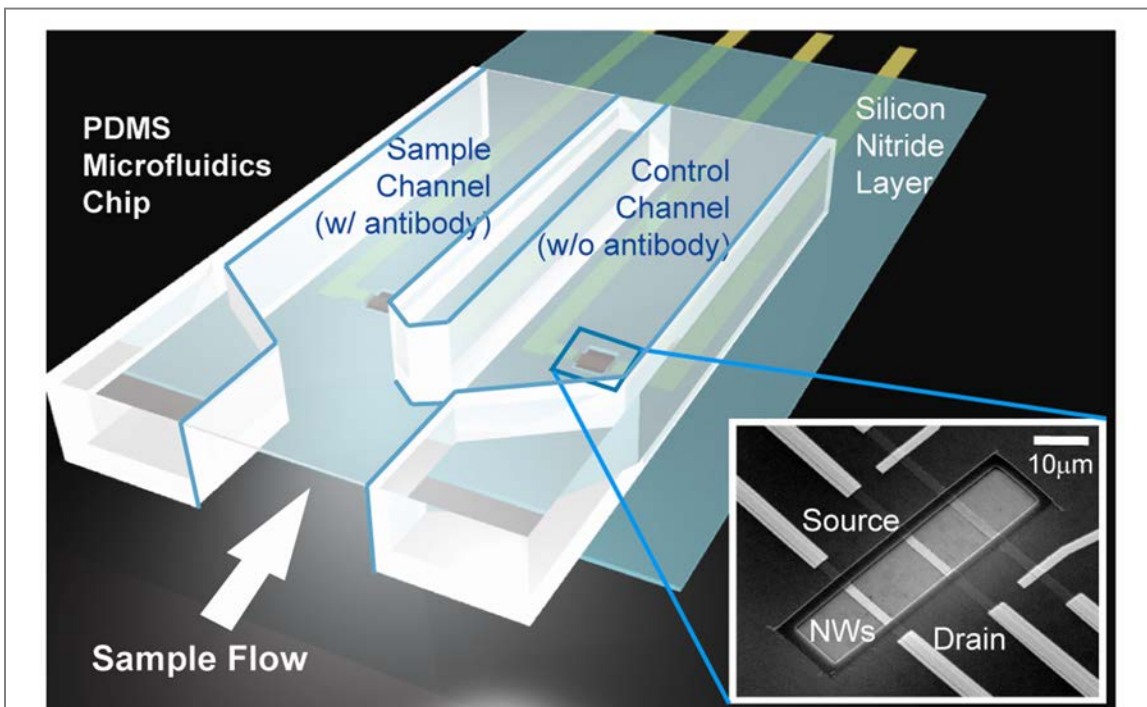
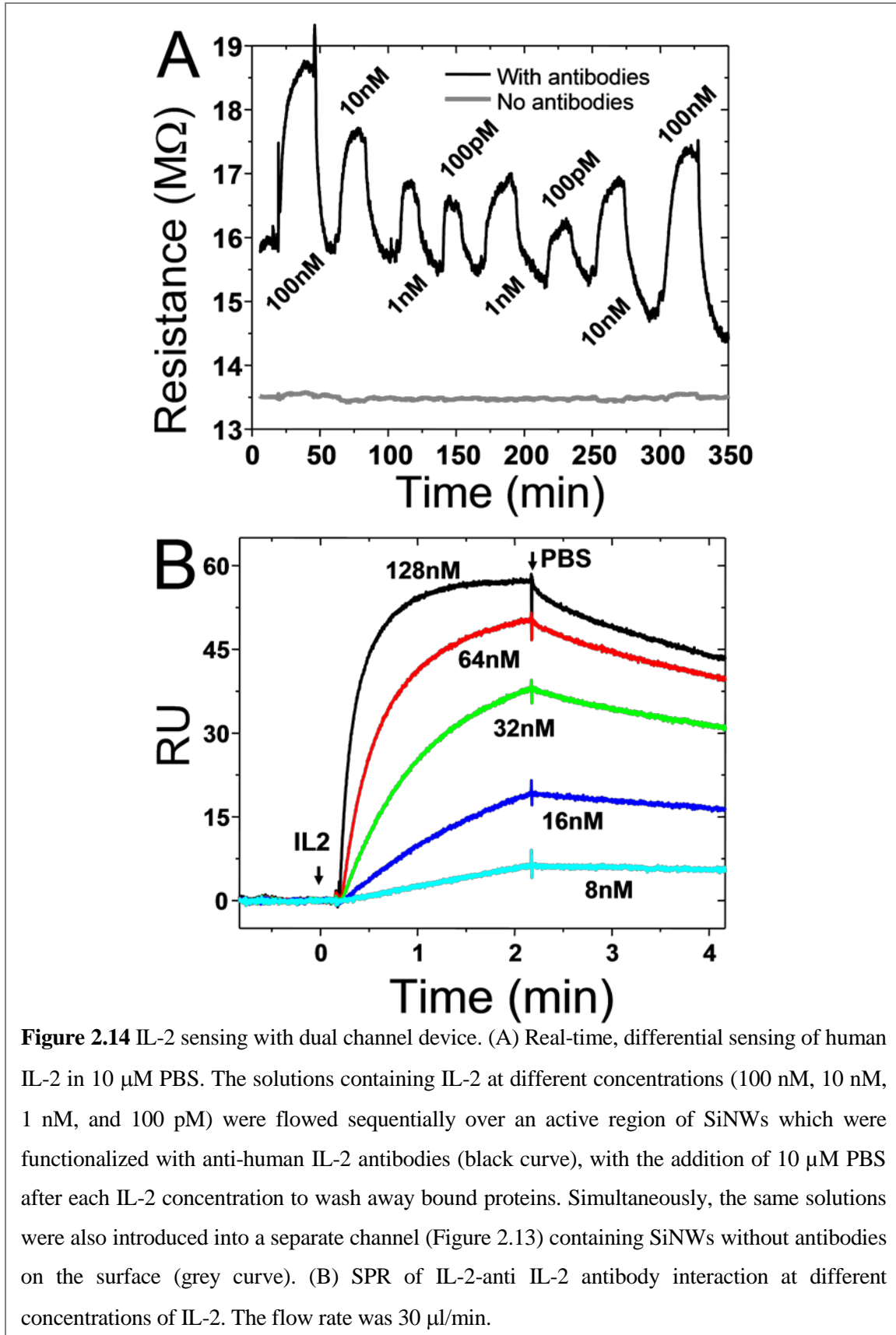


Figure 2.13 Schematic of the microfluidic PDMS chip overlaying a nanowire sensor device for differential measurements. A single microchannel bifurcates into two channels, each delivering solution to a separate sensor region with SiNWs (inset). One of the two sensor regions is functionalized with antibodies (left channel), while the other serves as a reference (right channel), accounting for the signal due to non-specific binding. The analyte solution is flown over both regions simultaneously (arrow), and the real-time resistance of the two regions is subtracted.

APTES forms multilayers on the surface due to intermolecular polymerization. After the data in Fig. 2.12 was collected, the chip was cleaned in organic solvents and briefly in O₂ plasma. The surface of the SiNWs was then functionalized with 3-aminopropyltrimethoxysilane (APMES), which forms a monolayer on silicon oxide surface. Subsequent protein sensing was carried out in 10 µM PBS. For this time, devices were modified (original devices as in Fig. 2.1) to include a control channel for each measurement (Fig. 2.13), which contained nonfunctionalized SiNWs. It is expected that such bare SiNWs provide a measure of nonspecific protein binding to the surface; therefore, a differential measurement taking biofouling and random drift into account is more accurate.

As evident from comparing Figs. 2.12 and 2.14, while the same SiNW device was used for protein sensing, the changes in resistance corresponding to the same concentrations of IL-2 are markedly different. The reason for this difference is difficult to pinpoint exactly. In Fig. 2.12, the functionalization with APTES may have resulted in a higher density of surface amines, which translated to a higher surface density of anti-IL-2 antibodies, and, therefore, to a larger saturation signal. Also, longer Debye screening length, corresponding to the detection in 1.5 µM PBS (Fig. 2.12), vs. 10 µM PBS (Fig. 2.14), may have also contributed to higher signals. Finally, O₂ treatment may have oxidized the surface, leading to a drop in sensitivity. Regardless of the exact reason, it is evident that the sensing devices may be reused multiple times for protein detection. Fig. 2.14 demonstrates that the increase in resistance is specific to antibody-IL-2 binding. When the antibodies are absent from the SiNW surface, no changes in the resistance are observed, meaning that the nonspecific binding of the antigen is below the detection threshold. In addition, the response of the



nanowires to the binding of IL-2 is consistent with the majority surface charge of the protein. The isoelectric point of recombinant human IL-2 is between pH 6.5 and 7.5. Therefore in dilute PBS, pH ~ 6.0, there should be a prevalence of positive surface charges on the protein, leading to an increase in resistance of p-type silicon nanowires (Figs. 2.12 and 2.14).

The above protein-sensing experiments demonstrate that it is possible to engineer silicon nanowires to detect protein concentrations below the detection limit of other label-free methods, such as SPR (Fig. 2.14B). The detection of IL-2, which is a crucial cytokine of the immune system, is demonstrated. For more practical application of this technique, such as detecting low levels of cancer markers in the serum, it is necessary to address the Debye length issue. In the next section, we will discuss a method of utilizing peptides to detect proteins in higher ionic strength solution.

2.3.3 Protein sensing with peptide

As a first step, we showed the efficient immobilization of the FLAG peptide on the bulk silicon (100) surface by using X-ray photoelectron spectroscopy (XPS) (Fig. 2.3). A cleaned silicon (100) surface was treated with 2% (v/v) APMES to generate the amine-terminated surface (Surface 1 in Fig. 2.3A). Surface 1 was converted into an azide-terminated one through the coupling between an azide-containing unnatural amino acid and the amine on the surface (Surface 2 in Fig. 2.3A). Finally, the FLAG peptide was immobilized by alkyne-azide “click” cycloaddition (Surface 3 in Fig. 2.3A). The contact angles for amine, azide, and FLAG peptide surfaces were 72°, 73°, and 35° respectively. The significant decrease in contact angle after the click reaction suggests efficient peptide coupling to the surface. The presence of the azide group on Surface 2 can be identified

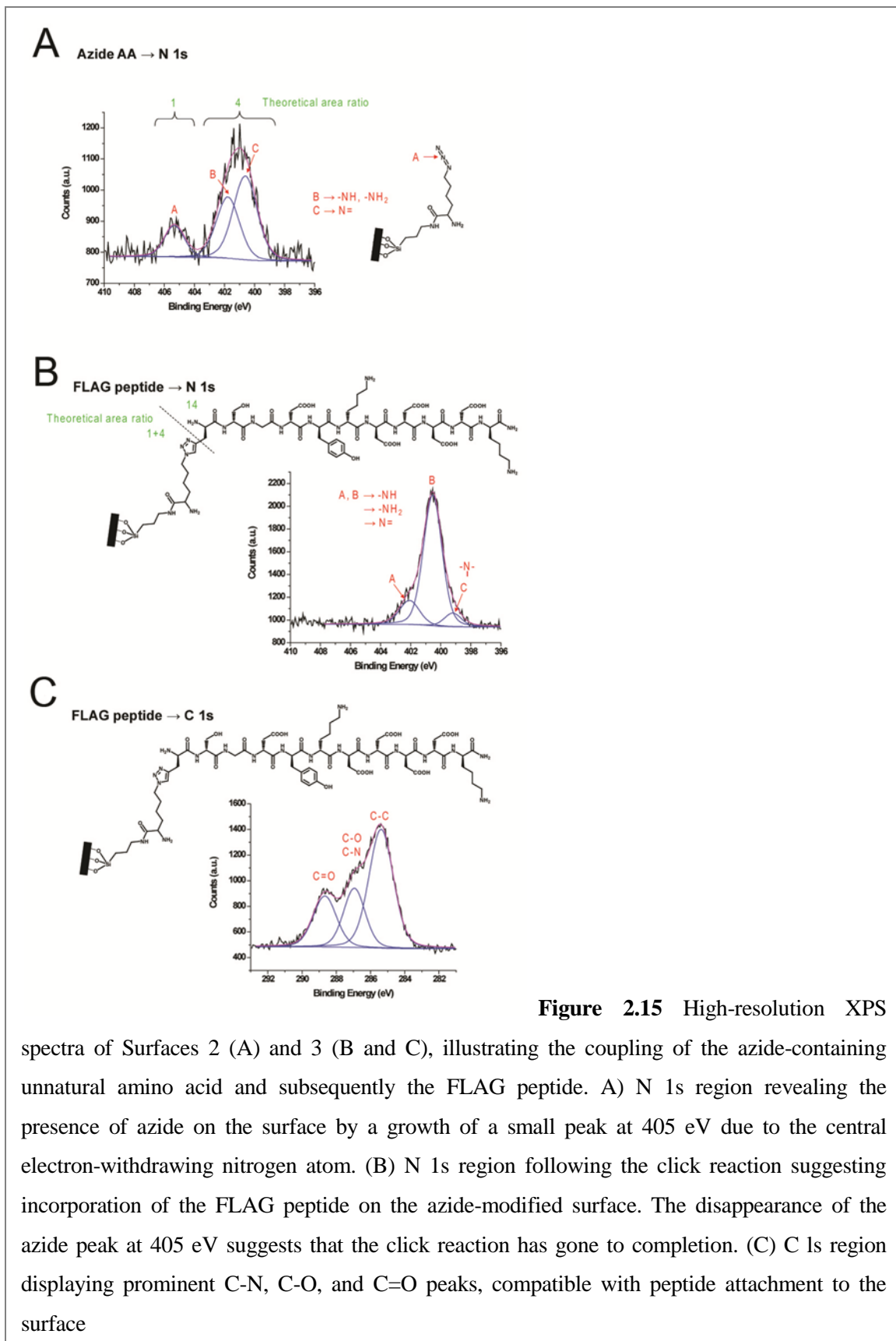
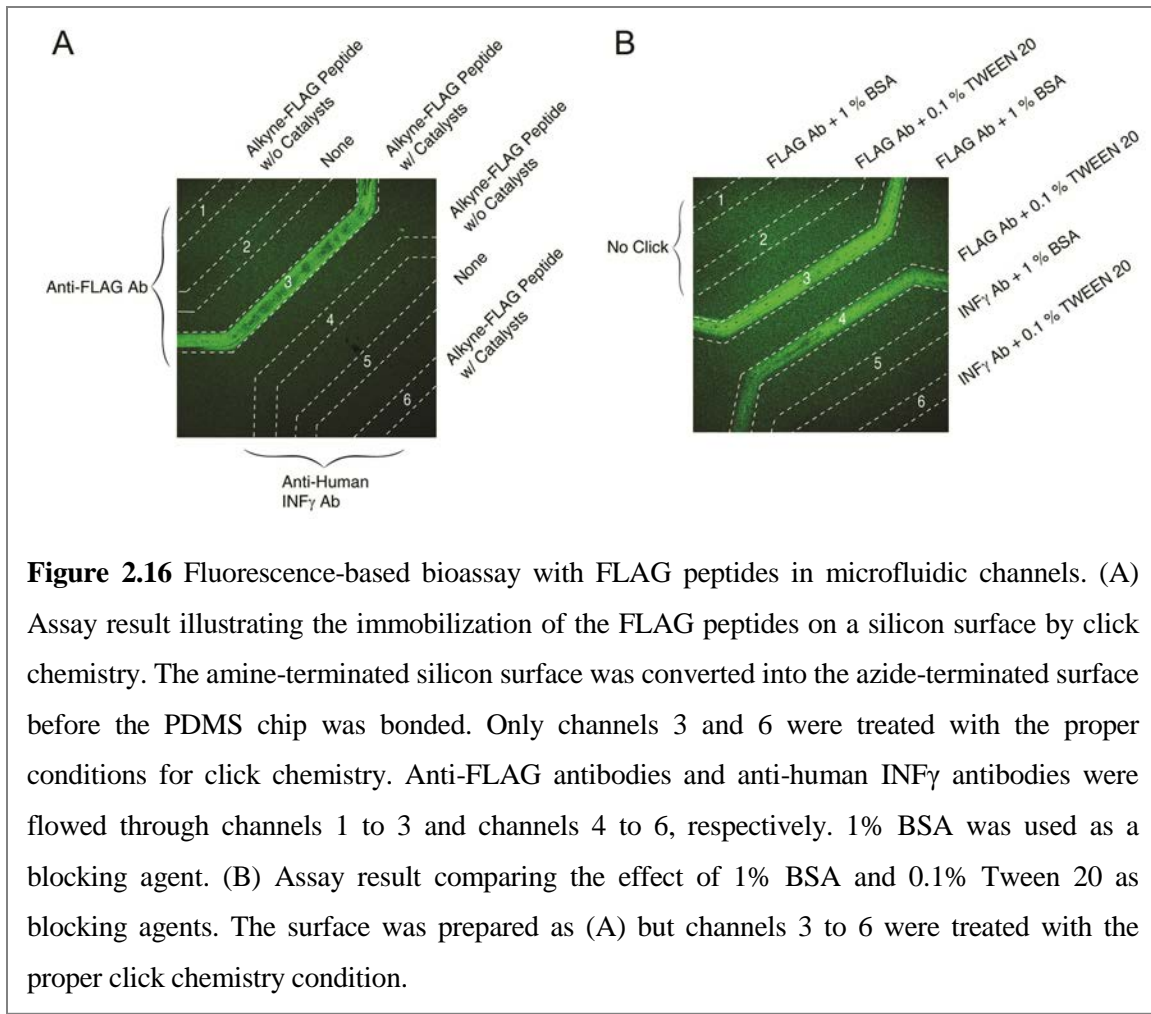


Figure 2.15 High-resolution XPS

spectra of Surfaces 2 (A) and 3 (B and C), illustrating the coupling of the azide-containing unnatural amino acid and subsequently the FLAG peptide. A) N 1s region revealing the presence of azide on the surface by a growth of a small peak at 405 eV due to the central electron-withdrawing nitrogen atom. (B) N 1s region following the click reaction suggesting incorporation of the FLAG peptide on the azide-modified surface. The disappearance of the azide peak at 405 eV suggests that the click reaction has gone to completion. (C) C 1s region displaying prominent C-N, C-O, and C=O peaks, compatible with peptide attachment to the surface

from the peak at 405 eV in the N 1s spectra of XPS, which is attributed to the central, electron-deficient nitrogen in the azide group (Fig. 2.3B). The disappearance of the same peak on Surface 3 explains ~ 100% conversion to the peptide-modified surface (Fig. 2.3B). By analyzing the ratio of the 400 eV and 405 eV peak areas in N 1s spectra, azide amino acid coverage in Surface 2 can be estimated as 73%, assuming 100% of APMES coverage, and the conversion to the peptide can be estimated as 100%⁶⁷ (Fig. 2.15). The growth of the 289 eV peak in C 1s spectra, which corresponds to C=O, a signature of peptides by XPS, also proves that the click reaction has proceeded (Fig. 2.15C).

To demonstrate the functionality of the peptide immobilized by click chemistry on silicon, a fluorescence-based bioassay in microfluidic channels was performed (Fig. 2.15). The amine-terminated surface was treated with azide-containing amino acid. Then a PDMS chip was bonded, and click reaction with the FLAG peptide was allowed to proceed in the microfluidic channel. As a control, channels 1 and 4 were filled with peptide solution without Cu^I catalyst and channels 2 and 5 were left as the azide-terminated surface. Channels 3 and 6 were treated with the FLAG peptide in the presence of the Cu^I catalysts. After the surface treatment in the microfluidic channels, anti-FLAG M2 antibodies and anti-human INF γ antibodies were filled into channels 1 to 3 and channels 4 to 6, respectively. After 1 h of incubation, secondary anti-mouse antibodies tagged with biotin were introduced into all channels and incubated for 1 hour. Then streptavidin conjugated with a Cy-5 fluorescence tag was reacted with the bound secondary anti-mouse antibodies. For all solutions containing antibodies, 1% BSA was included to prevent non-specific binding. Only channel 3, which was treated with FLAG peptide under the proper click condition and reacted with anti-FLAG M2 antibodies, showed fluorescence (Fig. 2.15A).



From this result, it can be noticed that the presented surface treatment scheme works for efficient immobilization of synthetic capture agents on a silicon surface. Although the size of the FLAG peptide is small enough for the SiNW-FETs sensing in high ionic strength solution, non-specific binding of the large BSA molecules can significantly lower the accessibility of binding antibodies to the peptide on the surface of NWs due to steric effects. To prevent that problem, 0.1% Tween 20 was tested as an alternative blocking agent. The surface was treated as described above but only channels 1 and 2 were left as azide-terminated surface whereas all the other channels were treated with FLAG peptide. The result shows that Tween 20 can also minimize the non-specific binding as effectively as BSA (Fig. 2.15B).

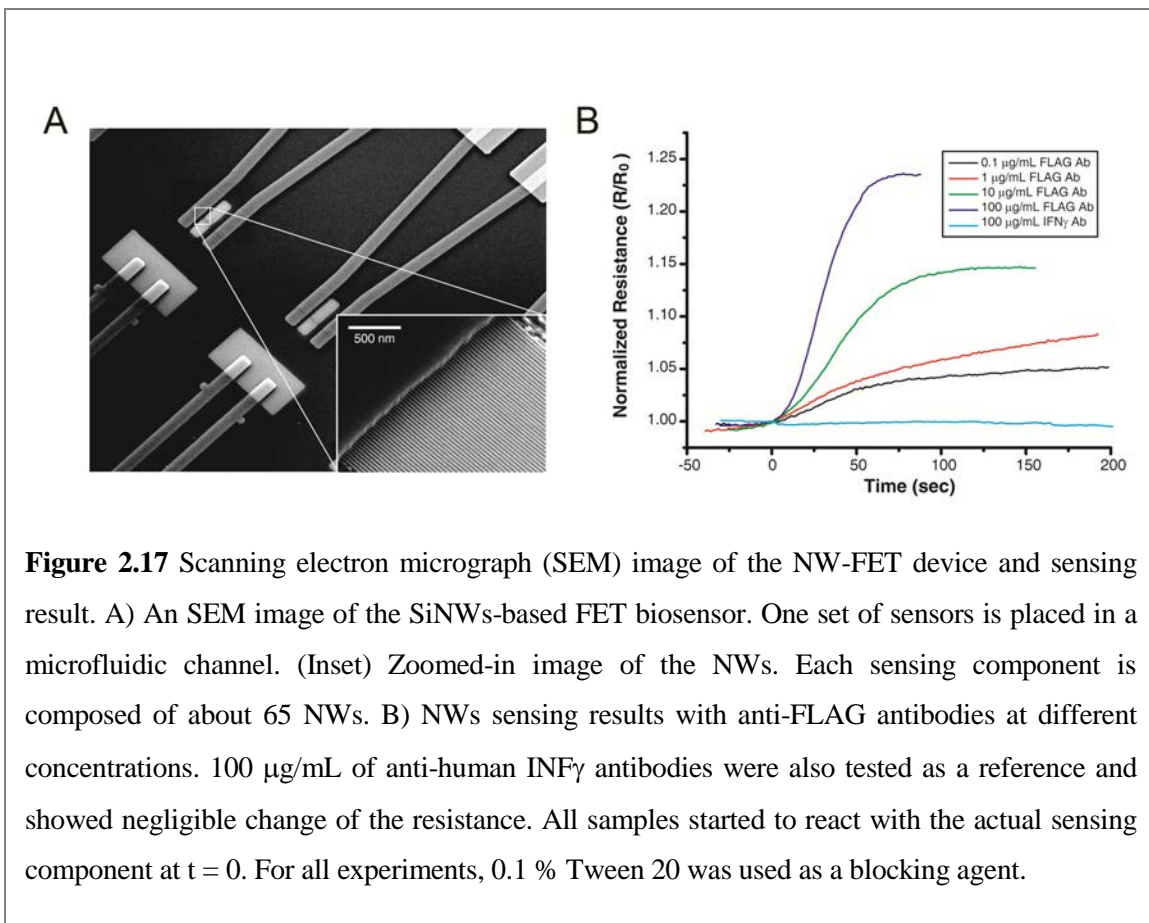


Figure 2.17 Scanning electron micrograph (SEM) image of the NW-FET device and sensing result. A) An SEM image of the SiNWs-based FET biosensor. One set of sensors is placed in a microfluidic channel. (Inset) Zoomed-in image of the NWs. Each sensing component is composed of about 65 NWs. B) NWs sensing results with anti-FLAG antibodies at different concentrations. 100 µg/mL of anti-human INF γ antibodies were also tested as a reference and showed negligible change of the resistance. All samples started to react with the actual sensing component at $t = 0$. For all experiments, 0.1 % Tween 20 was used as a blocking agent.

By utilizing peptides as a capture agent and click chemistry as a surface treatment method, we can sense anti-FLAG antibodies with SiNW-FETs in 0.1×PBS, which is 15 mM solution (Fig. 2.17). The Debye screening length of this high ionic strength solution is about 2.3 nm.⁶⁸ The SiNWs were fabricated by the superlattice nanowire pattern transfer (SNAP) method.³⁵ Then the SiNWs were sectioned into about 65 NWs and metal electrodes were patterned by photolithography technique (Fig. 2.17A). Up to 0.1 µg/mL (~ 666 pM) of anti-FLAG M2 antibody was clearly sensed whereas 100 µg/mL (~ 666 nM) of anti-human INF γ antibody did not give any noticeable signal (Fig. 2.17B). Although the sensitivity of the device was not that high, it can be enhanced by optimizing fabrication

conditions such as the doping concentration. Detection of target proteins in fM sensitivity is reported from other groups^{21,30} and further work is in progress to achieve high sensitivity.

Because high-salt buffer solution provides a better condition for the activity of biomolecules, and considering the efforts on developing synthetic capture agents such as peptides, peptoid and small molecules,^{25, 69–71} these data suggest that the peptide immobilization via click chemistry may offer more practical applications of the SiNW-FETs in basic studies of biological reaction as well as detection.

2.4 Conclusions

Real-time label-free detection of DNA and proteins with SiNWs was performed. Primary DNA was electrostatically adsorbed onto an amine-terminated SiNW surface and hybridized to the complementary strand in a microfluidics channel under flow. Electrostatic adsorption of single-stranded DNA to poly-L-lysine-coated surface has previously been electronically detected at nanomolar concentrations with capacitive methods on lowly doped Si electrodes in 0.015 M solution.⁷² The ability to detect DNA under physiological conditions, as demonstrated in this work, is of significance, as it may allow the direct use of biological samples such as serum or tissue culture media. It is likely that because the primary DNA is electrostatically bound and hybridization occurs very close to NW surface, Debye screening does not prevent SiNW-based detection.

SiNWs with significantly reduced oxide coverage exhibited enhanced solution FET characteristics (Fig. 2.6) when compared to SiNWs characterized by a native SiO₂ surface passivation. Oxide-covered, highly doped SiNWs were designed to exhibit a similar

dynamic range of DNA detection as the best near-infrared imaging SPR technique⁷³(~10 nM for 18 mer, corresponding to ~ 10^{11} molecules/cm²). When identical nanowires were functionalized by the UV-initiated radical chemistry method, resulting in near-elimination of the Si-SiO₂ interface, the limit of detection was increased by two orders of magnitude, with an accompanying increase in the dynamic range. This result highlights the importance of controlling surface chemistry of SiNWs for their optimization as biological sensors. In the future, surface chemistries yielding higher coverage than UV-initiated alkylation may be utilized to passivate and electrochemically convert SiNWs into arrays for multiparameter analysis.^{42, 74}

Sensing of an important cytokine, interleukin-2, has also been performed. Protein detection is significantly limited by the size of the capture agent. Using antibodies poses a limitation on the ionic strength of the buffer containing the analyte. To circumvent this limitation, we propose using peptide as alternative high-affinity protein probes. The application demonstrated in this chapter, detecting FLAG antibody with FLAG peptide, is a well-known system and just shows the feasibility for now. Thus a general scheme to screen and make synthetic capture agents on demand must be developed.²⁵ However, a combination of an appropriate doping level and surface chemistry will undoubtedly allow the detection down to a sub-picomolar regime, which is more than sufficient for most relevant clinical applications.

A model that is consistent with both the standard Langmuir binding model and with the fundamentals of semiconductor physics is developed. Kinetic parameters and analyte concentrations that are consistent with SPR values may be extracted from the silicon nanowire experiments. The potential for SiNW sensors to quantitate the concentrations of

low-abundance biomolecules within physiologically relevant environments is an intriguing one, and it is worth vigorously pursuing this possibility. The most useful application of our model would be in extracting otherwise unknown concentration values once k_{on} and k_{off} values are known. As demonstrated here, SiNW sensors can be used for label-free biomolecule detection at concentrations significantly below the limits of detection for SPR. The robustness of the fabrication technique (SNAP) employed here, which yields nanowire sensors that exhibit reproducible and highly tunable behavior, holds a promise for the future integration of this technology within the clinical setting.

2.5 References

1. Kong, J.; Franklin, N. R.; Zhou, C. W.; Chapline, M. G.; Peng, S.; Cho, K. J.; Dai, H. J., Nanotube molecular wires as chemical sensors. *Science* **2000**, 287, (5453), 622–625.
2. Patolsky, F.; Timko, B. P.; Zheng, G. F.; Lieber, C. M., Nanowire-based nanoelectronic devices in the life sciences. *MRS Bulletin* **2007**, 32, (2), 142–149.
3. Park, S. J.; Taton, T. A.; Mirkin, C. A., Array-based electrical detection of DNA with nanoparticle probes. *Science* **2002**, 295, (5559), 1503–1506.
4. Ziegler, C., Nanotechnologies for the biosciences. *Analytical and Bioanalytical Chemistry* **2004**, 379, (7–8), 903–903.
5. Lasseter, T. L.; Cai, W.; Hamers, R. J., Frequency-dependent electrical detection of protein binding events. *Analyst* **2004**, 129, (1), 3–8.
6. Davidson, E. H.; Rast, J. P.; Oliveri, P.; Ransick, A.; Calestani, C.; Yuh, C. H.; Minokawa, T.; Amore, G.; Hinman, V.; Arenas-Mena, C.; Otim, O.; Brown, C. T.; Livi, C. B.; Lee, P. Y.; Revilla, R.; Rust, A. G.; Pan, Z. J.; Schilstra, M. J.; Clarke, P. J. C.;

- Arnone, M. I.; Rowen, L.; Cameron, R. A.; McClay, D. R.; Hood, L.; Bolouri, H., A genomic regulatory network for development. *Science* **2002**, 295, (5560), 1669–1678.
7. Kitano, H., Systems biology: A brief overview. *Science* **2002**, 295, (5560), 1662–1664.
8. Hood, L.; Heath, J. R.; Phelps, M. E.; Lin, B. Y., Systems biology and new technologies enable predictive and preventative medicine. *Science* **2004**, 306, (5696), 640–643.
9. Chen, R. J.; Bangsaruntip, S.; Drouvalakis, K. A.; Kam, N. W. S.; Shim, M.; Li, Y. M.; Kim, W.; Utz, P. J.; Dai, H. J., Noncovalent functionalization of carbon nanotubes for highly specific electronic biosensors. *Proceedings of the National Academy of Sciences of the United States of America* **2003**, 100, (9), 4984–4989.
10. Star, A.; Tu, E.; Niemann, J.; Gabriel, J. C. P.; Joiner, C. S.; Valcke, C., Label-free detection of DNA hybridization using carbon nanotube network field-effect transistors. *Proceedings of the National Academy of Sciences of the United States of America* **2006**, 103, (4), 921–926.
11. Besteman, K.; Lee, J. O.; Wiertz, F. G. M.; Heering, H. A.; Dekker, C., Enzyme-coated carbon nanotubes as single-molecule biosensors. *Nano Letters* **2003**, 3, (6), 727–730.
12. Maehashi, K.; Katsura, T.; Kerman, K.; Takamura, Y.; Matsumoto, K.; Tamiya, E., Label-free protein biosensor based on aptamer-modified carbon nanotube field-effect transistors. *Analytical Chemistry* **2007**, 79, (2), 782–787.
13. Cui, Y.; Wei, Q. Q.; Park, H. K.; Lieber, C. M., Nanowire nanosensors for highly sensitive and selective detection of biological and chemical species. *Science* **2001**, 293, (5533), 1289–1292.
14. Hahm, J.; Lieber, C. M., Direct ultrasensitive electrical detection of DNA and DNA sequence variations using nanowire nanosensors. *Nano Letters* **2004**, 4, (1), 51–54.

15. Li, Z.; Chen, Y.; Li, X.; Kamins, T. I.; Nauka, K.; Williams, R. S., Sequence-specific label-free DNA sensors based on silicon nanowires. *Nano Letters* **2004**, 4, (2), 245–247.
16. Li, C.; Curreli, M.; Lin, H.; Lei, B.; Ishikawa, F. N.; Datar, R.; Cote, R. J.; Thompson, M. E.; Zhou, C. W., Complementary detection of prostate-specific antigen using In₂O₃ nanowires and carbon nanotubes. *Journal of the American Chemical Society* **2005**, 127, (36), 12484–12485.
17. Ramanathan, K.; Bangar, M. A.; Yun, M.; Chen, W.; Myung, N. V.; Mulchandani, A., Bioaffinity sensing using biologically functionalized conducting-polymer nanowire. *Journal of the American Chemical Society* **2005**, 127, (2), 496–497.
18. Lud, S. Q.; Nikolaides, M. G.; Haase, I.; Fischer, M.; Bausch, A. R., Field effect of screened charges: Electrical detection of peptides and proteins by a thin-film resistor. *Chemphyschem* **2006**, 7, (2), 379–384.
19. Neff, P. A.; Wunderlich, B. K.; Lud, S. Q.; Bausch, A. R., Silicon-on-insulator based thin film resistors for quantitative biosensing applications. *Physica Status Solidi A—Applications and Materials Science* **2006**, 203, (14), 3417–3423.
20. Israelachvilli, J., *Intermolecular and Surface Forces*. Academic Press: London, 1985.
21. Zheng, G. F.; Patolsky, F.; Cui, Y.; Wang, W. U.; Lieber, C. M., Multiplexed electrical detection of cancer markers with nanowire sensor arrays. *Nature Biotechnology* **2005**, 23, (10), 1294–1301.
22. Okahata, Y.; Kawase, M.; Niikura, K.; Ohtake, F.; Furusawa, H.; Ebara, Y., Kinetic measurements of DNA hybridisation an an oligonucleotide-immobilized 27-MHz quartz crystal microbalance. *Analytical Chemistry* **1998**, 70, (7), 1288–1296.

23. Naffin, J. L.; Han, Y.; Olivos, H. J.; Reddy, M. M.; Sun, T.; Kodadek, T., Immobilized peptides as high-affinity capture agents for self-associating proteins. *Chemical Biology* **2003**, 10, (3), 251–259.
24. Wegner, G. J.; Lee, H. J.; Corn, R. M., Characterization and optimization of peptide arrays for the study of epitope-antibody interactions using surface plasmon resonance imaging. *Analytical Chemistry* **2002**, 74, (20), 5161–5168.
25. Agnew, H. D.; Rohde, R. D.; Millward, S. W.; Nag, A.; Yeo, W. S.; Hein, J. E.; Pitram, S. M.; Tariq, A. A.; Burns, V. M.; Krom, R. J.; Fokin, V. V.; Sharpless, K. B.; Heath, J. R., Iterative in situ click chemistry creates antibody-like protein-capture agents. *Angewandte Chemie International Edition* **2009**, 48, (27), 4944–4948.
26. Kolb, H. C.; Finn, M. G.; Sharpless, K. B., Click Chemistry: Diverse Chemical Function from a Few Good Reactions. *Angewandte Chemie International Edition* **2001**, 40, (11), 2004–2021.
27. Li, Z.; Rajendran, B.; Kamins, T. I.; Li, X.; Chen, Y.; Williams, R. S., Silicon nanowires for sequence-specific DNA sensing: device fabrication and simulation. *Applied Physics A—Materials Science & Processing* **2005**, 80, (6), 1257–1263.
28. Vieu, C.; Carcenac, F.; Pepin, A.; Chen, Y.; Mejias, M.; Lebib, A.; Manin-Ferlazzo, L.; Couraud, L.; Launois, H., Electron beam lithography: resolution limits and applications. *Applied Surface Science* **2000**, 164, 111–117.
29. Yang, P. D., The chemistry and physics of semiconductor nanowires. *MRS Bulletin* **2005**, 30, (2), 85–91.
30. Stern, E.; Klemic, J. F.; Routenberg, D. A.; Wyrembak, P. N.; Turner-Evans, D. B.; Hamilton, A. D.; LaVan, D. A.; Fahmy, T. M.; Reed, M. A., Label-free

- immunodetection with CMOS-compatible semiconducting nanowires. *Nature* **2007**, *445*, (7127), 519–522.
31. Gao, Z.; Agarwal, A.; Trigg, A. D.; Singh, N.; Fang, C.; Tung, C. H.; Fan, Y.; Buddharaju, K. D.; Kong, J., Silicon Nanowire Arrays for Label-Free Detection of DNA. *Analytical Chemistry* **2007**, *79* (9), 3291–3297.
32. Heath, J. R.; Legoues, F. K., A Liquid Solution Synthesis of Single-Crystal Germanium Quantum Wires. *Chemical Physics Letters* **1993**, *208*, (3–4), 263–268.
33. Morales, A. M.; Lieber, C. M., A laser ablation method for the synthesis of crystalline semiconductor nanowires. *Science* **1998**, *279*, (5348), 208–211.
34. Chung, S. W.; Yu, J. Y.; Heath, J. R., Silicon nanowire devices. *Applied Physics Letters* **2000**, *76*, (15), 2068–2070.
35. Melosh, N. A.; Boukai, A.; Diana, F.; Gerardot, B.; Badolato, A.; Petroff, P. M.; Heath, J. R., Ultrahigh-density nanowire lattices and circuits. *Science* **2003**, *300*, (5616), 112–115.
36. Beckman, R. A.; Johnston-Halperin, E.; Melosh, N. A.; Luo, Y.; Green, J. E.; Heath, J. R., Fabrication of conducting Si nanowire arrays. *Journal of Applied Physics* **2004**, *96*, (10), 5921–5923.
37. Wikswo, J. P.; Prokop, A.; Baudenbacher, F.; Cliffel, D.; Csukas, B.; Velkovsky, M., Engineering challenges of BioNEMS: the integration of microfluidics, micro- and nanodevices, models and external control for systems biology. *IEEE Proceedings—Nanobiotechnology* **2006**, *153*, (4), 81–101.

38. Yablonovitch, E.; Allara, D. L.; Chang, C. C.; Gmitter, T.; Bright, T. B., Unusually Low Surface-Recombination Velocity on Silicon and Germanium Surfaces. *Physical Review Letters* **1986**, *57*, (2), 249–252.
39. Sham, T. K.; Naftel, S. J.; Kim, P. S. G.; Sammynaiken, R.; Tang, Y. H.; Coulthard, I.; Moewes, A.; Freeland, J. W.; Hu, Y. F.; Lee, S. T., Electronic structure and optical properties of silicon nanowires: A study using X-ray excited optical luminescence and X-ray emission spectroscopy. *Physical Review B* **2004**, *70*, 045313.
40. Webb, L. J.; Lewis, N. S., Comparison of the electrical properties and chemical stability of crystalline silicon(111) surfaces alkylated using grignard reagents or olefins with Lewis acid catalysts. *Journal of Physical Chemistry B* **2003**, *107*, (23), 5404–5412.
41. Bansal, A.; Lewis, N. S., Stabilization of Si photoanodes in aqueous electrolytes through surface alkylation. *Journal of Physical Chemistry B* **1998**, *102*, (21), 4058–4060.
42. Bunimovich, Y. L.; Ge, G. L.; Beverly, K. C.; Ries, R. S.; Hood, L.; Heath, J. R., Electrochemically programmed, spatially selective biofunctionalization of silicon wires. *Langmuir* **2004**, *20*, (24), 10630–10638.
43. Haick, H.; Hurley, P. T.; Hochbaum, A. I.; Yang, P. D.; Lewis, N. S., Electrical characteristics and chemical stability of non-oxidized, methyl-terminated silicon nanowires. *Journal of the American Chemical Society* **2006**, *128*, (28), 8990–8991.
44. Terry, J.; Mo, R.; Wigren, C.; Cao, R. Y.; Mount, G.; Pianetta, P.; Linford, M. R.; Chidsey, C. E. D., Reactivity of the H-Si (111) surface. *Nuclear Instruments & Methods in Physics Research Section B—Beam Interactions with Materials and Atoms* **1997**, *133*, (1–4), 94–101.

45. Effenberger, F.; Gotz, G.; Bidlingmaier, B.; Wezstein, M., Photoactivated preparation and patterning of self-assembled monolayers with 1-alkenes and aldehydes on silicon hydride surfaces. *Angewandte Chemie International Edition* **1998**, 37, (18), 2462–2464.
46. Boukherroub, R.; Wayner, D. D. M., Controlled functionalization and multistep chemical manipulation of covalently modified Si(111) surfaces. *Journal of the American Chemical Society* **1999**, 121, (49), 11513–11515.
47. Cicero, R. L.; Linford, M. R.; Chidsey, C. E. D., Photoreactivity of unsaturated compounds with hydrogen-terminated silicon(111). *Langmuir* **2000**, 16, (13), 5688–5695.
48. Streifer, J. A.; Kim, H.; Nichols, B. M.; Hamers, R. J., Covalent functionalization and biomolecular recognition properties of DNA-modified silicon nanowires. *Nanotechnology* **2005**, 16, (9), 1868–1873.
49. Jonsson, U.; Fagerstam, L.; Ivarsson, B.; Johnsson, B.; Karlsson, R.; Lundh, K.; Lofas, S.; Persson, B.; Roos, H.; Ronnberg, I.; Sjolander, S.; Stenberg, E.; Stahlberg, R.; Urbaniczky, C.; Ostlin, H.; Malmqvist, M., Real-Time Biospecific Interaction Analysis Using Surface-Plasmon Resonance and a Sensor Chip Technology. *Biotechniques* **1991**, 11, (5), 620–&.
50. Wang, D. W.; Sheriff, B. A.; Heath, J. R., Silicon p-FETs from ultrahigh density nanowire arrays. *Nano Letters* **2006**, 6, (6), 1096–1100.
51. Duffy, D. C.; McDonald, J. C.; Schueller, O. J. A.; Whitesides, G. M., Rapid prototyping of microfluidic systems in poly(dimethylsiloxane). *Analytical Chemistry* **1998**, 70, (23), 4974–4984.

52. Unger, M. A.; Chou, H. P.; Thorsen, T.; Scherer, A.; Quake, S. R., Monolithic microfabricated valves and pumps by multilayer soft lithography. *Science* **2000**, 288, (5463), 113–116.
53. Haber, J. A.; Lewis, N. S., Infrared and X-ray photoelectron spectroscopic studies of the reactions of hydrogen-terminated crystalline Si(111) and Si(100) surfaces with Br-2, I-2, and ferrocenium in alcohol solvents. *Journal of Physical Chemistry B* **2002**, 106, (14), 3639–3656.
54. Himpsel, F. J.; McFeely, F. R.; Talebibrahimi, A.; Yarmoff, J. A.; Hollinger, G., Microscopic Structure of the SiO₂/Si Interface. *Physical Review B* **1988**, 38, (9), 6084–6096.
55. Chenault, H. K., Dahmer, J. and Whitesides, G.M., Kinetic resolution of unnatural and rarely occurring amino acids: enantioselective hydrolysis of N-acyl amino acids catalyzed by acylase I. *Journal of the American Chemical Society* **1989**, 111.
56. van Hest, J. C. M., Kiick, K.L. and Tirrell, D.A., Efficient incorporation of unsaturated methionine analogues into proteins in vivo. *Journal of the American Chemical Society* **2000**, 122.
57. Lee, H.-S., Park, J.-S., Kim, B.M. and Gellman, S.H. , Efficient synthesis of enantiomerically pure δ -2-amino acids via chiral isoxazolidinones. *Journal of Organic Chemistry* **2003**, 68.
58. Hu, K.; Fan, F. R. F.; Bard, A. J.; Hillier, A. C., Direct measurement of diffuse double-layer forces at the semiconductor/electrolyte interface using an atomic force microscope. *Journal of Physical Chemistry B* **1997**, 101, (41), 8298–8303.

59. Cui, Y.; Duan, X. F.; Hu, J. T.; Lieber, C. M., Doping and electrical transport in silicon nanowires. *Journal of Physical Chemistry B* **2000**, 104, (22), 5213–5216.
60. Cheng, M. M.-C.; Cuda, G.; Bunimovich, Y. L.; Gaspari, M.; Heath, J. R.; Hill, H. D.; Mirkin, C. A.; Nijdam, A. J.; Terracciano, R.; Thundat, T.; Ferrari, M., Nanotechnologies for biomolecular detection and medical diagnostics. *Current Opinion in Chemical Biology* **2006**, 10, (1), 11–19.
61. Beckman, R.; Johnston-Halperin, E.; Luo, Y.; Green, J. E.; Heath, J. R., Bridging dimensions: Demultiplexing ultrahigh-density nanowire circuits. *Science* **2005**, 310, (5747), 465–468.
62. Stenberg, E.; Persson, B.; Roos, H.; Urbaniczky, C., Quantitative-Determination of Surface Concentration of Protein with Surface-Plasmon Resonance Using Radiolabeled Proteins. *Journal of Colloid and Interface Science* **1991**, 143, (2), 513–526.
63. Yu, F.; Yao, D. F.; Knoll, W., Oligonucleotide hybridization studied by a surface plasmon diffraction sensor (SPDS). *Nucleic Acids Research* **2004**, 32, (9).
64. Peterson, A. W.; Heaton, R. J.; Georgiadis, R. M., The effect of surface probe density on DNA hybridization. *Nucleic Acids Research* **2001**, 29, (24), 5163–5168.
65. Lemeshko, S. V.; Powdrill, T.; Belosludtsev, Y. Y.; Hogan, M., Oligonucleotides form a duplex with non-helical properties on a positively charged surface. *Nucleic Acids Research* **2001**, 29, (14), 3051–3058.
66. Zimmermann, M.; Delamarche, E.; Wolf, M.; Hunziker, P., Modeling and optimization of high-sensitivity, low-volume microfluidic-based surface immunoassays. *Biomedical Microdevices* **2005**, 7, (2), 99–110.

67. Collman, J. P.; Devaraj, N. K.; Eberspacher, T. P.; Chidsey, C. E., Mixed azide-terminated monolayers: a platform for modifying electrode surfaces. *Langmuir* **2006**, *22*, (6), 2457–2464.
68. Stern, E.; Wagner, R.; Sigworth, F. J.; Breaker, R.; Fahmy, T. M.; Reed, M. A., Importance of the debye screening length on nanowire field effect transistor sensors. *Nano Letters* **2007**, *7*, (11), 3405–9.
69. Alluri, P. G.; Reddy, M. M.; Bachhawat-Sikder, K.; Olivos, H. J.; Kodadek, T., Isolation of Protein Ligands from Large Peptoid Libraries. *Journal of the American Chemical Society* **2003**, *125*, (46), 13995–14004.
70. Bachhawat-Sikder, K.; Kodadek, T., Mixed-Element Capture Agents: A Simple Strategy for the Construction of Synthetic, High-Affinity Protein Capture Ligands. *Journal of the American Chemical Society* **2003**, *125*, (32), 9550–9551.
71. Enander, K., Dolphin, G.T., Liedberg, B., Lundström, I., Baltzer, L., A Versatile Polypeptide Platform for Integrated Recognition and Reporting: Affinity Arrays for Protein-Ligand Interaction Analysis. *Chemistry—A European Journal* **2004**, *10*, (10), 2375–2385.
72. Fritz, J.; Cooper, E. B.; Gaudet, S.; Sorger, P. K.; Manalis, S. R., Electronic detection of DNA by its intrinsic molecular charge. *Proceedings of the National Academy of Sciences of the United States of America* **2002**, *99*, (22), 14142–14146.
73. Nelson, B. P.; Grimsrud, T. E.; Liles, M. R.; Goodman, R. M.; Corn, R. M., Surface plasmon resonance imaging measurements of DNA and RNA hybridization adsorption onto DNA microarrays. *Analytical Chemistry* **2001**, *73*, (1), 1–7.

74. Rohde, R. D.; Agnew, H. D.; Yeo, W. S.; Bailey, R. C.; Heath, J. R., A non-oxidative approach toward chemically and electrochemically functionalizing Si(111). *Journal of the American Chemical Society* **2006**, 128, (29), 9518–9525.

Chapter 3

Chemistries for Patterning Robust DNA Microbarcodes Enable Multiplex Assays of Cytoplasm Proteins from Single Cancer Cells

3.1 Introduction

The demand for parallel, multiplex analysis of protein biomarkers from ever smaller biospecimens is an increasing trend for both fundamental biology and clinical diagnostics.^{1–3} The most highly multiplex protein assays rely on spatially encoded antibody microarrays,^{4–6} and small biospecimen samples are now routinely manipulated using microfluidics approaches. The integration of antibody microarray techniques with microfluidic chips has only been explored relatively recently. One challenge arises from the relative instability of antibodies to microfluidics fabrication conditions. In recent years, several groups have devised methods to transform standard DNA microarrays *in situ* into protein microarrays and cell-capture platforms.^{7–13} These approaches capitalize on the chemical robustness of DNA oligomers, and the reliable assembly of DNA-labeled structures via complementary hybridization. Recently, Fan et al. utilized a microfluidics-based flow patterning technique to generate DNA barcode-type arrays at 10× higher density than standard, spotted microarrays.¹⁵ The DNA barcodes were converted into antibody arrays using the DNA-Encoded Antibody Library (DEAL) technique, and then applied towards the measurement of a highly multiplex panel of proteins from a pinprick of whole blood.

A second challenge involves scaling such miniaturized DNA microarrays so that a large surface area can be encoded. This problem is non-trivial, as it involves identifying chemistries for patterning 10^{-5} -m-wide, 1-m-long strips of biomolecules with a uniformity that permits those patterns to be utilized in hundreds to thousands of quantitative protein assays per chip. Here, we explore the surface chemistry associated with a microfluidics-based flow patterning of DNA barcodes, with an eye towards producing highly reproducible and robust barcodes. We then apply the optimized chemistry towards assaying a panel of cytoplasmic proteins from single cells.

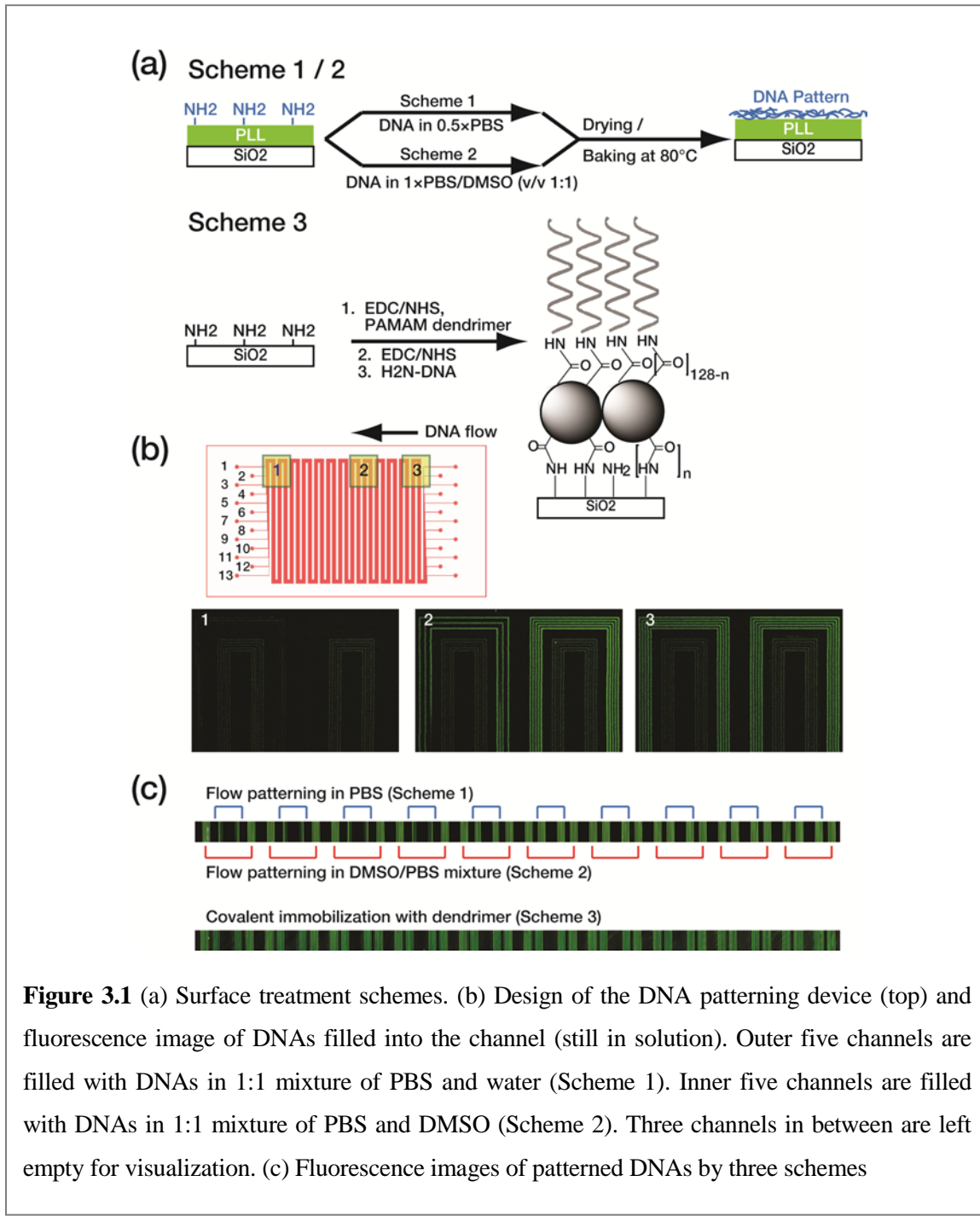
3.2 Experimental Methods

3.2.1 Microfluidic chip fabrication for DNA patterning

Microfluidic-patterning PDMS chips were fabricated by soft lithography. The master mold was prepared using either a negative photoresist, SU8 2010, with photolithography, or an etched silicon mold generated by a deep reactive ion etching (DRIE) process. The mold has long meandering channels with a 20×20 μm cross section. The distance from channel to channel is also 20 μm , which generates $10\times$ higher density than standard, spotted microarrays. Sylgard PDMS (Corning) prepolymer and curing agent were mixed in a 10:1 ratio (w/w), poured onto the mold, and cured (80° , 1 h). The cured PDMS slab was released from the mold, inlet/outlet holes were punched, and the device was bonded onto a PLL coated (C40-5257-M20, Thermo scientific) or aminated glass slide (48382-220, VWR) to form enclosed channels. The number of microfluidic channels determines the size of the microarray; 13 parallel microchannels were used in this study.

3.2.2 Patterning of DNA barcode arrays

For the DNA filling test, a 30 mer DNA oligomer labeled with Cy3 fluorescence tag on the 5' end (5'-/Cy3/-AAA AAA AAA ATA CGG ACT TAG CTC CAG GAT - 3') in a 1:1



mixture (v/v) of 1×PBS buffer and DMSO or a 1:1 mixture (v/v) of 1×PBS buffer and deionized (DI) water was used. The final DNA concentration was 2.5 μM. DNA solution was pushed into the channel under a constant pressure (2.5 psi). Immediately after the channels were fully filled, fluorescence images were obtained by confocal microscopy.

Dendrimer-based microarrays were prepared using aminated substrates. Generation 4.5 Poly(amidoamine) (PAMAM) dendrimers (470457-2.5G, Aldrich), 5% wt in MeOH, were mixed 1:1 (v/v) with EDC/NHS (0.2 M) in MES buffer (0.1 M, pH 6.0). After 5 minutes of incubation, the activated dendrimers were introduced to the microfluidic channels, and allowed to flow (2 h). Following a brief MeOH rinse to remove unbound dendrimers, the channels were filled with EDC/NHS (0.2 M) in MES (0.1 M, pH 5.3) with NaCl (0.5 M). After 0.5 h, 5' aminated DNA sequences in 1×PBS (200 μM) were introduced to the channels and allowed to flow (2 h). Thereafter, the microfluidic device was removed from the substrate, and the latter was rinsed copiously with DI water. Prepared substrates that were not used immediately were stored in a desiccator.

To generate the DNA barcode array for multi-protein detection and single cell lysis test, 13 orthogonal DNA oligomer solutions (sequences are provided in Table 3.1) in 1×PBS buffer (400 μM) were mixed with DMSO (in 1:2 ratio, v/v) and flowed into each of the microfluidic channels (Scheme 3.2). For Scheme 3.1, DNA solutions in 1×PBS buffer were used. The DNA-filled chip was placed in a desiccator until the solvent evaporated completely, leaving only DNA molecules behind. Finally, the PDMS elastomer was removed from the glass substrate and the microarray-patterned DNAs were cross-linked to the PLL by thermal treatment (80 °C, 4 h). The slide was gently rinsed with DI water prior to use in order to remove salt crystals remaining from the solution evaporation step.

Table 3.1 Sequences and terminal functionalization of oligonucleotides: All oligonucleotides were synthesized by Integrated DNA Technology (IDT) and purified via high-performance liquid chromatography (HPLC). The DNA coding oligomers were pre-tested for orthogonality to ensure that cross-hybridization between non-complementary oligomer strands was negligible (< 1% in photon counts).

Name	Sequence	Melting Point
A	5'- AAA AAA AAA AAA AAT CCT GGA GCT AAG TCC GTA-3'	57.9
A'	5' NH3- AAA AAA AAA ATA CGG ACT TAG CTC CAG GAT-3'	57.2
B	5'-AAA AAA AAA AAA AGC CTC ATT GAA TCA TGC CTA -3'	57.4
B'	5' NH3AAA AAA AAA ATA GGC ATG ATT CAA TGA GGC -3'	55.9
C	5'- AAA AAA AAA AAA AGC ACT CGT CTA CTA TCG CTA -3'	57.6
C'	5' NH3-AAA AAA AAA ATA GCG ATA GTA GAC GAG TGC -3'	56.2
D	5'-AAA AAA AAA AAA AAT GGT CGA GAT GTC AGA GTA -3'	56.5
D'	5' NH3-AAA AAA AAA ATA CTC TGA CAT CTC GAC CAT -3'	55.7
E	5'-AAA AAA AAA AAA AAT GTG AAG TGG CAG TAT CTA -3'	55.7
E'	5' NH3-AAA AAA AAA ATA GAT ACT GCC ACT TCA CAT -3'	54.7
F	5'-AAA AAA AAA AAA AAT CAG GTA AGG TTC ACG GTA -3'	56.9
F'	5' NH3-AAA AAA AAA ATA CCG TGA ACC TTA CCT GAT -3'	56.1
G	5'-AAA AAA AAA AGA GTA GCC TTC CCG AGC ATT-3'	59.3
G'	5' NH3-AAA AAA AAA AAA TGC TCG GGA AGG CTA CTC-3'	58.6
H	5'-AAA AAA AAA AAT TGA CCA AAC TGC GGT GCG-3'	59.9
H'	5' NH3-AAA AAA AAA ACG CAC CGC AGT TTG GTC AAT-3'	60.8
I	5'-AAA AAA AAA ATG CCC TAT TGT TGC GTC GGA-3'	60.1
I'	5' NH3-AAA AAA AAA ATC CGA CGC AAC AAT AGG GCA-3'	60.1
J	5'-AAA AAA AAA ATC TTC TAG TTG TCG AGC AGG-3'	56.5
J'	5' NH3-AAA AAA AAA ACC TGC TCG ACA ACT AGA AGA-3'	57.5
K	5'-AAA AAA AAA ATA ATC TAA TTC TGG TCG CGG-3'	55.4
K'	5' NH3-AAA AAA AAA ACC GCG ACC AGA ATT AGA TTA-3'	56.3
L	5'-AAA AAA AAA AGT GAT TAA GTC TGC TTC GGC-3'	57.2
L'	5' NH3-AAA AAA AAA AGC CGA AGC AGA CTT AAT CAC-3'	57.2
M	5'-Cy3-AAA AAA AAA AGT CGA GGA TTC TGA ACC TGT-3'	57.6
M'	5' NH3-AAA AAA AAA AAC AGG TTC AGA ATC CTC GAC-3'	56.9

3.2.3 Microfluidic chip fabrication for multi-protein detection

The PDMS microfluidic chip for the cell experiment was fabricated by two-layer soft lithography.¹⁶ A push-down valve configuration was utilized with a thick control layer bonded together with a thin flow layer. The molds for the control layer and the flow layer were fabricated with SU8 2010 negative photoresist (~ 20 µm thickness) and SPR 220

positive photoresist ($\sim 18 \mu\text{m}$), respectively. The photoresist patterns for the flow layer were rounded via thermal treatment. The thick control layer was molded with a 5:1 mixture of GE RTV 615 PDMS prepolymer part A and part B (w/w) and the flow layer was formed by spin-coating a 20:1 mixture of GE RTV 615 part A and part B (w/w) on the flow layer mold (2000 rpm, 60 sec). Both layers were cured (80°C, 1 h), whereupon the control layer was cut from its mold and aligned to the flow layer. An additional thermal treatment (80°C, 1 h) ensured that the two layers bonded into a monolithic device, which was then peeled from its mold and punched to create appropriate access holes. Finally, the PDMS chip was thermally bonded to the DNA microbarcodes-patterned glass slide to form the working device.

3.2.4 Cell culture

The human GBM cell line U87 was cultured in DMEM (American Type Culture Collection, ATCC) supplemented with 10% fetal bovine serum (FBS, Sigma-Aldrich). U87 cells were serum-starved for 1 day and then stimulated by EGF (50 ng/ml, 10 min) before they were introduced into the device.

3.2.5 Multi-protein detection

Protein detection assays were initiated by blocking the chip with 3% bovine serum albumin (BSA) in PBS to prevent non-specific binding. This 3% BSA/PBS solution was used as a working buffer for most subsequent steps. After blocking, a cocktail containing all 11 (Scheme 3.2) or 3 (Scheme 3.3) DNA-antibody conjugates ($\sim 0.5 \mu\text{g/ml}$, 100 μl) in working buffer was flowed through the micro channels for 1 h. The unbound DNA-

antibody conjugates were washed away with fresh buffer. Then, target proteins were flowed through the microfluidic channels for 1 h. These were followed by a 200 μ l cocktail containing biotin-labeled detection antibodies ($\sim 0.5 \text{ }\mu\text{g/ml}$) in working buffer, and thereafter a 200 μ l mixture of 1 $\mu\text{g/ml}$ Cy5-labeled streptavidin and 25 nM Cy3-labeled M' ssDNA in working buffer to complete the immune sandwich assay. DNA sequence M is used for a location reference. The microchannels were rinsed with working buffer once more before the PDMS chip was removed; the bare microarray slide was rinsed sequentially with 1 \times PBS, 0.5 \times PBS, DI water, and was finally subjected to spin-drying.

3.2.6 On-chip cell lysis and multiplexed intracellular protein profiling from single cells

The multi-protein detection procedure described above was slightly modified for intracellular protein profiling experiments. Again, the chip was initially blocked with a 3% BSA/PBS working buffer, followed by a 200 μ l cocktail containing all 11 DNA-antibody conjugates ($\sim 0.5 \text{ }\mu\text{g/ml}$, Table 3.2) in working buffer (continuously flowed for 1 h). Unbound DNA-antibody conjugates were washed off with fresh buffer. The lysis buffer (Cell Signaling) was loaded into the lysis buffer channels while the valve 1 (V1 in Fig. 3.9a) was kept closed by applying 15–20 psi constant pressure. Then cells were introduced to the cell loading channels and microfluidic valves (V2 in Fig. 3.9a) were closed by applying 15–20 psi constant pressure; this converts the 8 channels into 120 isolated microchamber sets. After cell numbers were counted under microscope, V1 valves were released to allow diffusion of lysis buffer to the neighboring microchamber containing different numbers of cells. The cell lysis was performed on ice for two h. After that, the V2 valves were

Table 3.2 Summary of antibodies used for cell lysis experiments: All antibody pairs except p-VEGFR2 were purchased as ELISA kits of R&D systems (DuoSet® Elisa Development Reagents) containing capture antibodies, biotinylated detection antibodies, and standard proteins. Capture antibodies bind both phosphorylated and unphosphorylated proteins. The biotinylated detection antibodies detect only the phosphorylated variants of the proteins. VEGFR2 capture antibody, and p-VEGFR2 (Y1214) detection antibodies were purchased from Abcam.

DNA label	Antibody	Source
A'	Human p-PDGFR□ (Y751) kit	R&D DYC3096
B'	Human p-Src (Y419) kit	R&D DYC2685
C'	Human p-mTOR (S2448) kit	R&D DYC1665
D'	Human p-p70S6K (T389) kit	R&D DYC896
E'	Human p-GSK3α/β (S21/S9) kit	R&D DYC2630
G'	Human p-p38 α (T180/Y182) kit	R&D DYC869
H'	Human p-ERK (T202/Y204) kit	R&D DYC1825
I'	Human p-JNK2 (T183/Y185) kit	R&D DYC2236
K'	Human total EGFR kit	R&D DYC1854
L'	Human total P53 kit	R&D DYC1043
J'	Capture antibody: rabbit anti-human p-VEGFR2 (Y1214)	Abcam ab31480
	Detection antibody: biotin-labeled mouse anti-human VEGFR2	Abcam ab10975

released and the unbound cell lysate was quickly removed by flowing the fresh buffer.

Then, a cocktail containing biotin-labeled detection antibodies (~ 0.5 µg/ml, 200 µl) in working buffer was flowed into the chip for 1 h on ice, followed by flowing a 200 µl mixture of Cy5-labeled streptavidin (1 µg/ml) and Cy3-labeled M' ssDNA (25 nM) in working buffer to complete the sandwich immunoassay. Finally, the microchannels were

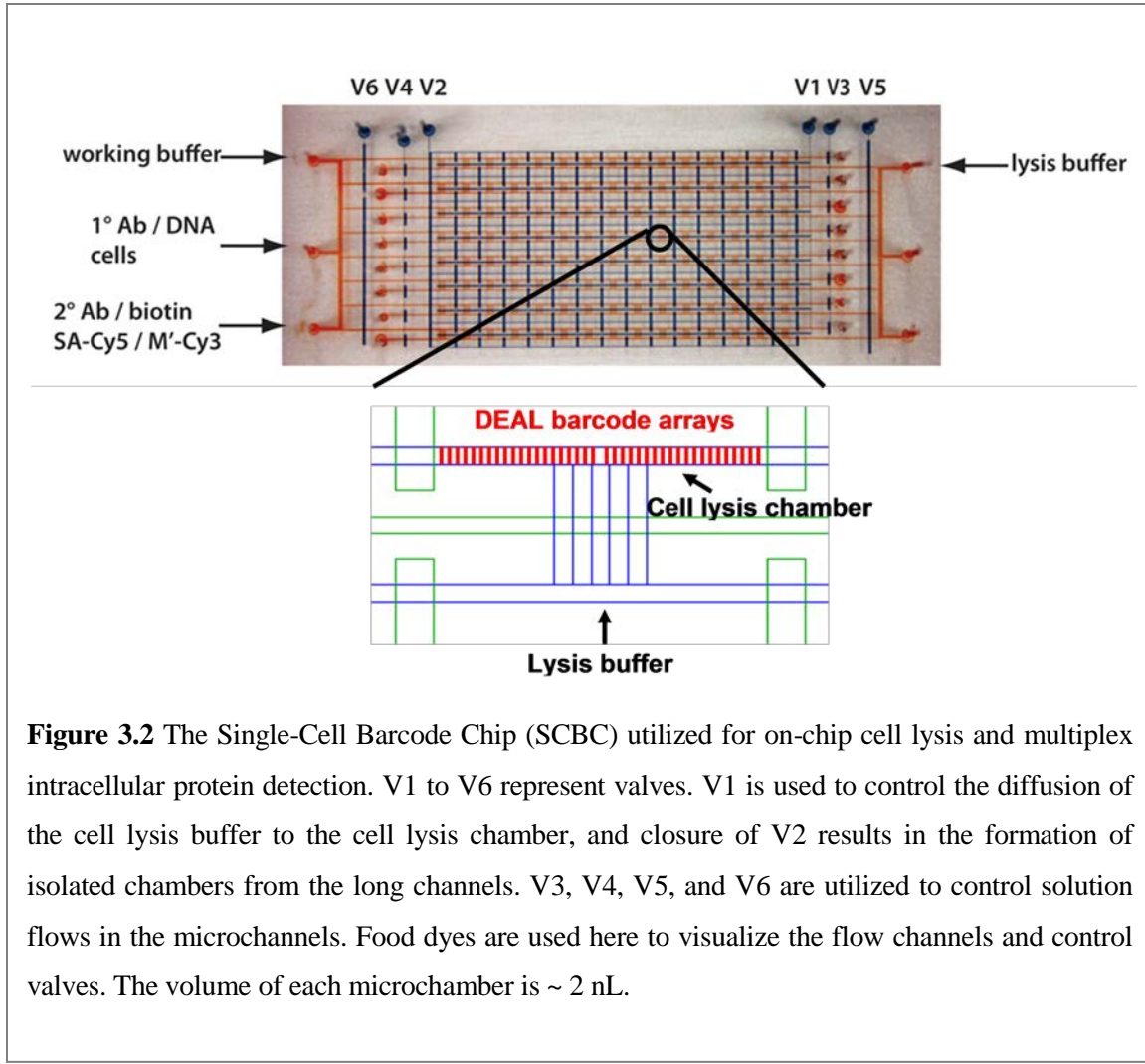


Figure 3.2 The Single-Cell Barcode Chip (SCBC) utilized for on-chip cell lysis and multiplex intracellular protein detection. V1 to V6 represent valves. V1 is used to control the diffusion of the cell lysis buffer to the cell lysis chamber, and closure of V2 results in the formation of isolated chambers from the long channels. V3, V4, V5, and V6 are utilized to control solution flows in the microchannels. Food dyes are used here to visualize the flow channels and control valves. The volume of each microchamber is ~ 2 nL.

rinsed with working buffer, the PDMS chip was removed, and the bare microarray slide was rinsed sequentially with 1×PBS, 0.5×PBS, and DI water, before spin-drying. The layout of the chip and used inlets for different solutions are described in Fig. 3.2.

3.2.7 Data analysis

The microarray slide was scanned with the GenePix 200B (Axon Instruments) to obtain a fluorescence image of both Cy3 and Cy5 channels. All scans were performed with the same setting of 50% (635 nm) and 15% (532 nm) laser power, 500 (635 nm) and 450 (532

nm) optical gain. The averaged fluorescence intensities for all barcodes in each chamber were obtained and matched to the cell number by custom-developed Excel or MATLAB codes.

3.2.8 Molecular dynamic simulation

The MD simulations were performed with the all-atom AMBER2003 force field^{17, 18} using the Large-scale Atomic/Molecular Massively Parallel Simulator (LAMMPS) code.¹⁹ As an initial structure, a single-strand DNA (5'-ACCCATGGAGCATTCCGGG-3') whose base pairs are randomly chosen was built using the Namot2 program.²⁰ Near the DNA strand, 19 sodium counter ions were included to neutralize the negatively charged 19 phosphate groups on the DNA backbone. Then this was immersed in a solvation box composed of either 1) 5206 water molecules + 106 DMSO molecules or 2) only 5206 water molecules. We used a TIP4P model to describe the water interactions.²¹ We performed 3 ns NPT MD simulations using Nose-Hoover thermostat with a damping relaxation time of 0.1 ps and Andersen-Hoover barostat with a dimensionless cell mass factor of 1.0. The last 1 ns trajectory is employed for the analysis. To compute the electrostatic interactions, the particle-particle particle-mesh method²² was employed using an accuracy criterion of 10^{-4} .

3.2.9 Modeling of electrostatic adsorption of DNA to poly-L-lysine (PLL) surface

This modeling follows the approach used in reference 22.²³

The following assumptions are used for the simulation:

- Nonspecific DNA adhesion to the PDMS surface is insignificant compared with the adhesion to the PLL surface

—DNAs are instantaneously and irreversibly captured to the PLL surface when they are transported to the surface.

We start with the following mass transport equation,

$$v_x \frac{\partial C}{\partial x} = D \frac{\partial^2 C}{\partial y^2}$$

where v_x is the fluid velocity along the channel and y is the channel height. We can apply boundary conditions such that at the top and side walls, there are no concentration gradients.

In a rectangular channel the mass diffusion coefficient can be approximated by

$$h_{\text{diff}} = 3.81 \frac{D}{d_h}$$

where h_{diff} is the hydraulic channel diameter, $\frac{4 \text{ [cross-section area]}}{\text{[perimeter]}}$.

As DNA flows down the channel during the initial filling step, DNA is electrostatically captured by PLL on the surface, causing a concentration gradient. Thus, the mean concentration of the sample at position x , C_x can be expressed as

$$C_x = C_i e^{-h_{\text{diff}} w x / Q}$$

where C_i is the sample concentration at the channel entrance.

We are interested in how C_x changes as the sample flows along the channel and we can simply apply the parameters of our system.

It has been reported that the diffusion coefficients of labeled single-strand DNA are predicted by:

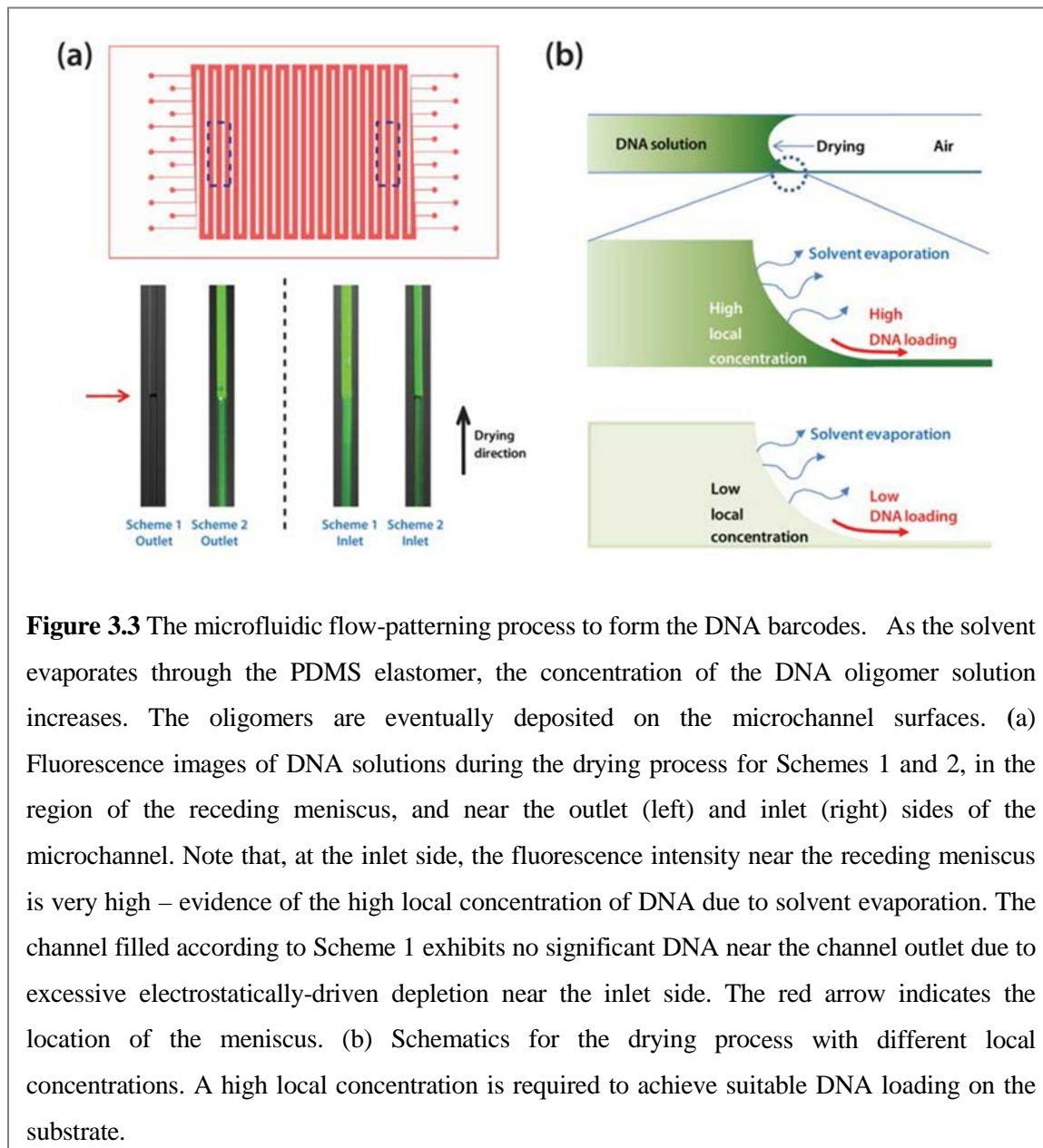
$$D_{\text{label}} = 4 \times 10^{-6} B^{-0.539}$$

where B is the number of bases.^{24, 25}

In order to calculate C_x , we need the flow velocity. We measured the DNA sample filling speed (Fig. 3.6a) and used 536 $\mu\text{m/sec}$ for simulation.

3.3 Results and Discussion

The microfluidics flow patterning chip is comprised of a patterned polydimethylsiloxane (PDMS) layer adhered to an aminated or PLL-coated glass substrate that provides the base surface for the microchannels. The microchannels are long (about 55 cm), meandering channels that span ~ 1.5 in² of our substrate, and are used to pattern a



DNA barcode over most of the glass surface (Fig. 3.1b). After the flow patterning is completed, the PDMS layer is replaced with a second micropatterned PDMS layer that is designed to support a biological assay, such as the previously reported blood proteomics chip,¹⁵ or the single-cell proteomics chips utilized here. For the microfluidic patterning method to be useful, it must generate a DNA barcode that exhibits high and uniform DNA loading over the entire substrate. We evaluated the patterning chemistries illustrated in Fig. 3.1a, Schemes 1-3. Schemes 3.1 and 3.2 are drawn from the conventional protocol for pin-spotted microarrays— a solution containing the DNA is introduced, the solvent is evaporated, and subsequent thermal or UV treatment is employed to cross-link the deposited DNA to the substrate. Scheme 3.1 utilizes ssDNA oligomers dissolved in phosphate buffered saline (PBS), whereas Scheme 3.2 employs ssDNAs in a 1:1 mixture of 1×PBS and dimethyl sulfoxide (DMSO). DMSO is used in conventional microarray preparation to improve feature consistency by reducing the rate of solvent evaporation and by denaturing the DNA²⁶ although, as described below, its role in this process is different. Scheme 3.3 utilizes a covalent immobilization method based upon a dendrimer scaffold.²⁷ Poly(amidoamine) (PAMAM) dendrimers (generation 4.5, carboxylate surface) have previously shown promise as DNA and protein microarray substrates. Dendrimers do not form entangled chains²⁸ and because harsh crosslinking procedures are avoided, dendrimer-immobilized DNA retains high accessibility and activity in microarray applications. Moreover, the highly branched structure of the dendrimers provides a high density of reactive sites for surface attachment and for DNA coupling, thus leading to a high overall binding capacity. For all cases, a high level of DNA loading has been shown to decrease non-specific binding when compared to standard microarray substrates.^{11, 29–31}

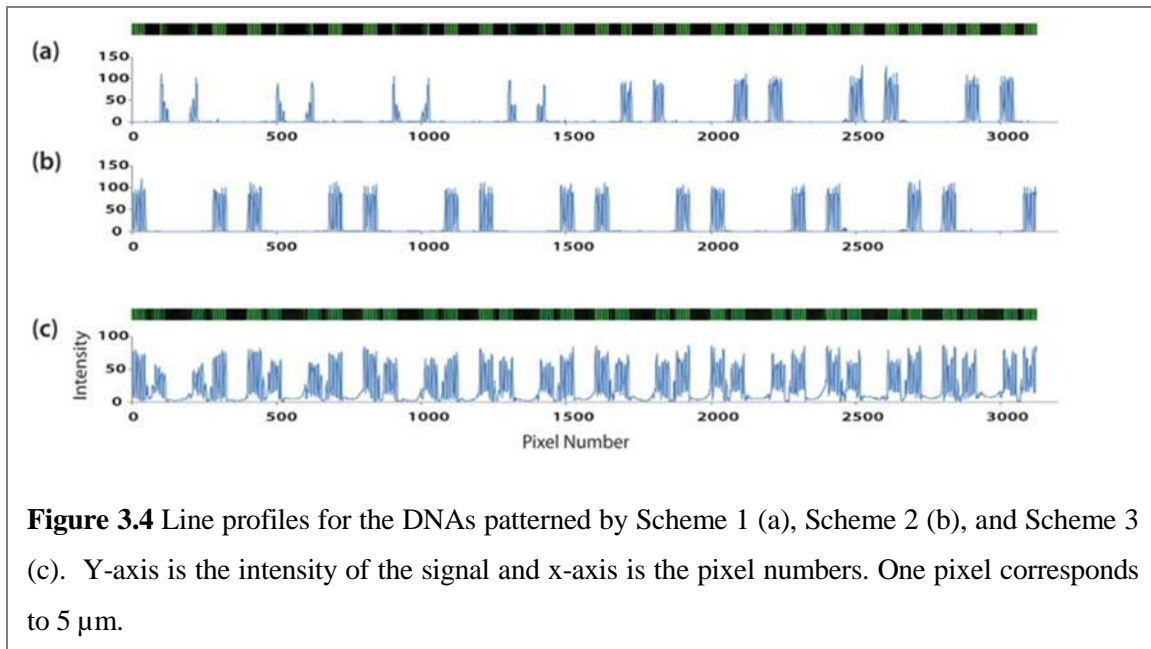


Figure 3.4 Line profiles for the DNAs patterned by Scheme 1 (a), Scheme 2 (b), and Scheme 3 (c). Y-axis is the intensity of the signal and x-axis is the pixel numbers. One pixel corresponds to 5 μm .

Fig. 3.1b (top) shows the PDMS chip design used for barcode patterning; 13 discrete channels (for a 13-element barcode) allow for a multiplex microarray. We loaded five adjacent channels according to Scheme 3.1, skipped three channels, and then loaded the remaining five channels according to Scheme 3.2. The use of fluorescently-tagged DNA permitted measurements of the DNA distribution within each individual channel immediately after introducing the solutions. Fig. 3.1b demonstrates a clear difference in aqueous DNA distribution across the chip: DNA loaded according to Scheme 3.1 (outer 5 channels) is notably lower in concentration near the middle of the chip (Fig. 3.1b, Region 2) and is barely detectable near the channel exit (Fig. 3.1b, Region 1). Conversely, DNA loaded according to Scheme 3.2 (inner 5 channels) presents an even, consistent distribution across the entire chip. Notably, Scheme 3.1 yields a relatively higher fluorescence intensity at the input side of the chip. These results clearly indicate that, for Scheme 3.1, the ssDNA oligomers are accumulating upstream during the early stages of flow, and so are depleted from the advancing solution by the time it reaches mid-chip. The actual patterning of the

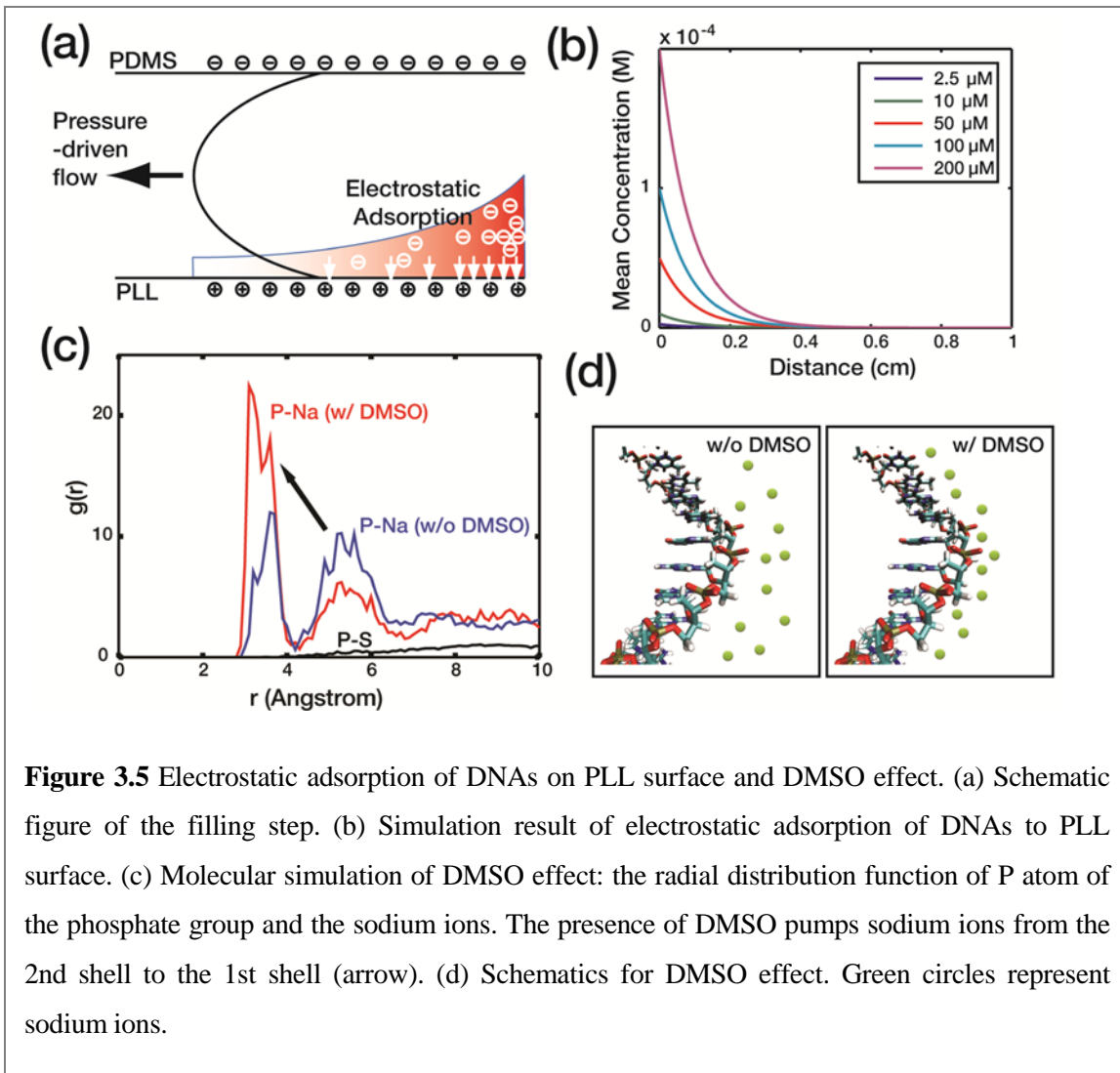


Figure 3.5 Electrostatic adsorption of DNAs on PLL surface and DMSO effect. (a) Schematic figure of the filling step. (b) Simulation result of electrostatic adsorption of DNAs to PLL surface. (c) Molecular simulation of DMSO effect: the radial distribution function of P atom of the phosphate group and the sodium ions. The presence of DMSO pumps sodium ions from the 2nd shell to the 1st shell (arrow). (d) Schematics for DMSO effect. Green circles represent sodium ions.

glass substrate occurs when solvent is evaporated (Fig. 3.3). Indeed, the final patterning results after solvent evaporation and cross-linking (Fig. 3.1c, top) reflect the trend established by the aqueous fluorescence images; Scheme 3.2 produces uniform DNA barcodes across the substrate, while Scheme 3.1 does not. Line profiles corresponding to Fig 3.1c. can be found in Fig. 3.4

In order to understand the difference in patterning uniformity between Schemes 3.1 and 3.2, we considered the electrostatic environment for each case. As depicted in Fig. 3.5a, the PDMS side walls carry a slightly negative zeta potential, whereas the PLL surface has a strong positive zeta potential.³² When the ssDNA solution in Scheme 3.1 is introduced to

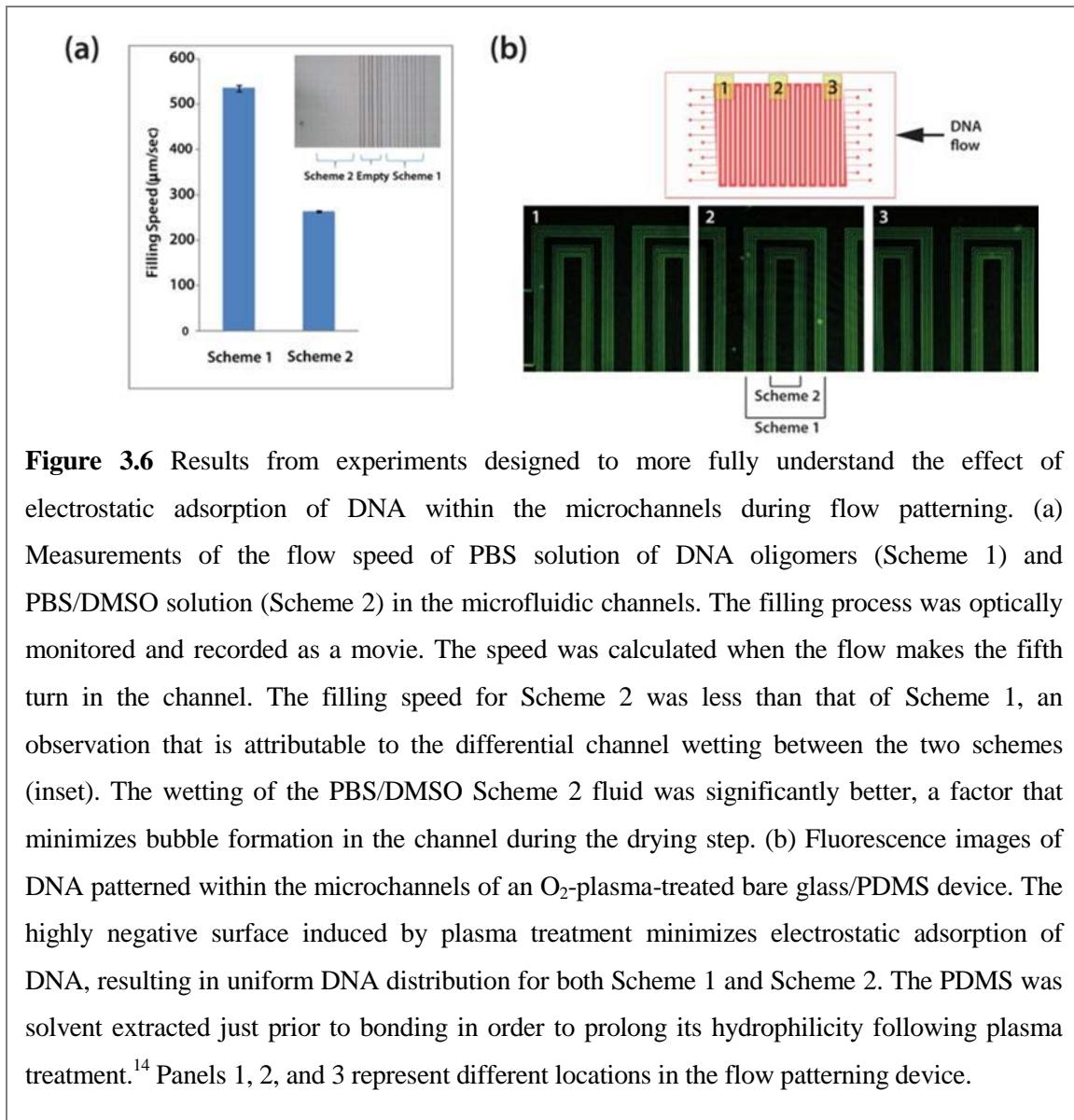


Figure 3.6 Results from experiments designed to more fully understand the effect of electrostatic adsorption of DNA within the microchannels during flow patterning. (a) Measurements of the flow speed of PBS solution of DNA oligomers (Scheme 1) and PBS/DMSO solution (Scheme 2) in the microfluidic channels. The filling process was optically monitored and recorded as a movie. The speed was calculated when the flow makes the fifth turn in the channel. The filling speed for Scheme 2 was less than that of Scheme 1, an observation that is attributable to the differential channel wetting between the two schemes (inset). The wetting of the PBS/DMSO Scheme 2 fluid was significantly better, a factor that minimizes bubble formation in the channel during the drying step. (b) Fluorescence images of DNA patterned within the microchannels of an O₂-plasma-treated bare glass/PDMS device. The highly negative surface induced by plasma treatment minimizes electrostatic adsorption of DNA, resulting in uniform DNA distribution for both Scheme 1 and Scheme 2. The PDMS was solvent extracted just prior to bonding in order to prolong its hydrophilicity following plasma treatment.¹⁴ Panels 1, 2, and 3 represent different locations in the flow patterning device.

the channel, ssDNA near the PLL matrix is electrostatically immobilized, thereby generating a concentration gradient.²³ As the solution flows towards the channel exit, the ssDNA oligomers are continually depleted via deposition onto the PLL surface. Fig. 3.5b shows the results from a rough simulation designed to capture the mean concentration of aqueous ssDNA as the solution traverses a channel. The simulation implies that the effect of electrostatic adsorption proves dominant even at high DNA concentration, a result that agrees well with the observed behavior for Scheme 3.1 in Fig. 3.1b. A detailed description

of the model and assumptions employed can be found in Section 3.2.9. We tested this model via the strong negative charging of all four channel surfaces via O₂ plasma treatment. Consistent with the model, both Scheme 3.1 and Scheme 3.2 exhibited equivalently uniform distribution of fluorescence intensity across the chip (Fig. 3.6b). We note that lack of the positive charges on the bottom surface failed to hold DNAs during the drying procedure and the plasma treatment induces the irreversible bonding of PDMS and glass, which limits further use beyond this experimental test.

Scheme 3.1 and 3.2 results imply that DMSO alleviates the electrostatic adsorption effect. In order to more fully understand this, we performed molecular dynamics (MD) simulations of DNA in PBS and PBS/DMSO solutions; 3 ns of NPT (NPT is a simulation in which moles (N), pressure and temperature are held constant) MD simulations were performed, with the last 1 ns trajectory being employed for analysis. We examined the

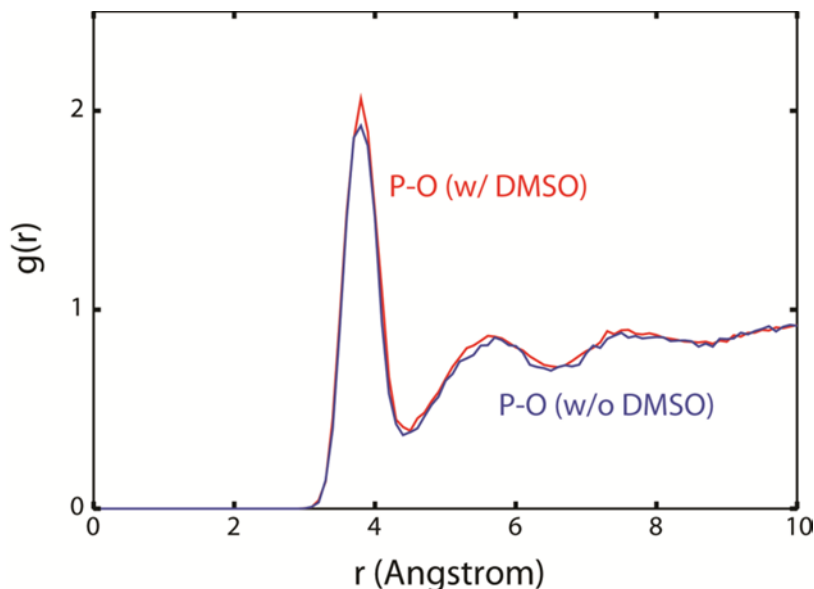


Figure 3.7 Molecular simulation resulting from the influence of DMSO in the Scheme 3.2 process. The radial distribution function of the P atom of the phosphate group of the DNA backbone and O atom of the water molecule is not influenced by the presence of DMSO.

radial distribution function of phosphorous atoms in the DNA backbone with respect to various elements of the surrounding solvent. For example, the radial distribution function of P and the O atom of a water molecule is virtually unperturbed by the addition of DMSO (Fig. 3.7). Consequently, it is unsurprising that the radial distribution function of P and the S atom of DMSO (Fig. 3.5c, black solid line) reveals that DMSO is not forming a solvation structure with the DNA backbone. However, Figure 3.5c demonstrates a clear interaction between P and Na⁺ ions which delineates into two well-defined shell structures: the first is located at $r < 4.3\text{\AA}$ while the second is located at $4.3\text{\AA} < r < 6.6\text{\AA}$; these are similar to the locations of the first and the second water solvation structures. By integrating the radial distribution functions, we determined the number of molecules per phosphate in the first and second shells for both PBS and PBS/DMSO solutions. Although the number of H₂O^s per shell is virtually independent of DMSO, DMSO does significantly increase the number of Na⁺ ions in the first shell (from 0.14 to 0.24), and it decreases the number of Na⁺ ions in the second shell (from 0.61 to 0.34). Conversely, the number of DMSO molecules is almost zero in the first shell (0.01) but becomes significant in the second shell (0.20). Thus, we conclude that DMSO, with a lower dielectric constant relative to water (47.2 vs. 80), destabilizes the solvation energy of Na⁺ in the second shell. This thermodynamic change prompts the sodium ions to move to the first shell where they are stabilized by electrostatic interactions with the negatively charged phosphate groups. The increased number of sodium ions near the DNA backbone more efficiently screens the negative charges of phosphate groups, thereby reducing electrostatic interactions of the DNA with the PLL surface, resulting in uniform DNA distribution throughout the channels. Although the addition of DMSO to DNA patterning solutions yields the same ultimate effect for both

traditional spotted arrays and microfluidics-patterned barcodes, the underlying mechanisms are completely different. We conclude that Scheme 3.2 is intrinsically superior relative to Scheme 3.1.

We now turn towards analyzing Scheme 3.3, and comparing it against Scheme 3.2. For this scheme, the PAMAM dendrimers are first covalently attached to the aminated glass surface, and then (aminated) ssDNA oligomers are covalently attached to the dendrimers. The lack of a solvent evaporation step makes Scheme 3.3 significantly more rapid than Scheme 3.2. We flowed activated PAMAM dendrimers, followed by aminated ssDNA, through ten microfluidic channels (Fig. 3.1b). Note that the aqueous DNA distribution is expected to be uniform because the substrate surface is comprised of charge-neutral N-hydroxysuccinimide (NHS)-modified carboxylates which minimize electrostatic interactions. The resulting DNA microarray was assayed for uniformity with complementary DNAs labeled with Cy3-fluorophores. Visual analysis indicates good uniformity across the chip (Fig. 3.1c, bottom). In order to quantitate the patterning quality for all three schemes, we obtained signal intensities for each channel at sixteen locations within the patterning region and calculated the coefficient of variation (CV). CV is defined as the standard deviation divided by the mean and expressed as a percentage. CVs for Schemes 3.1, 3.2, and 3.3 registered 69.8%, 10.5%, and 10.9%, respectively. Thus, we conclude that Schemes 3.2 and 3.3 offer consistent DNA loading across the entire substrate.

Having established that Scheme 2 and 3 produce consistent, large-scale DNA barcodes, we then extended our analysis of array consistency to protein measurements. We previously demonstrated that, when using the DEAL platform for multiplex protein sensing in microfluidics channels, the sensitivities of the assays directly correlate with the amount

of immobilized DNA,¹⁵ up to the point where the DNA coverage is saturated. We performed multiple protein assays along the length of our DNA stripes to ensure that the above described results would translate into stable and sensitive barcodes for protein sensing. All protein assays were performed in microfluidic channels that were oriented perpendicular to the patterned barcodes (five channels for Scheme 3.2 and four channels for Scheme 3.3). This allowed us to test distal microarray repeats with a single small analyte volume. For barcodes prepared using Scheme 3.2, we utilized the DEAL technique to convert them into antibody barcodes designed to assay the following proteins: phosphorylated (phospho)-steroid receptor coactivator (Src), phospho-mammalian target of rapamycin (mTOR), phospho-p70 S6 kinase (S6K), phospho-glycogen synthase kinase (GSK)-3 α/β , phospho-p38 α , phospho-extracellular signal-regulated kinase (ERK), and total epidermal growth factor receptor (EGFR) at 10 ng/ml and 1 ng/ml concentrations. This panel samples key nodes of the phosphoinositide 3-kinase (PI3K) signaling pathway within GBM, and are used below for single-cell assays.³³ For barcodes prepared using Scheme 3.3, we similarly converted the DNA barcodes into antibody barcodes designed to detect the three proteins (interferon (IFN)- γ , tumor necrosis factor (TNF) α , and interleukin (IL)-2) at 100 ng/ml and 10 ng/ml. All the DNAs used were pre-validated for the orthogonality in order to avoid cross-hybridization and the sequences can be found in Table 3.1. The detection scheme is similar to a sandwich immunoassay. Captured proteins from primary antibodies were fluorescently visualized by biotin-labeled secondary antibodies and Cy5-labeled streptavidin. For both cases, data averaged from multiple DNA repeats across the chip yielded CVs that were commensurate with those of the underlying DNA barcodes (from 10 ng/ml concentration, 7% for Scheme 3.2 and 17% for Scheme 3.3, respectively).

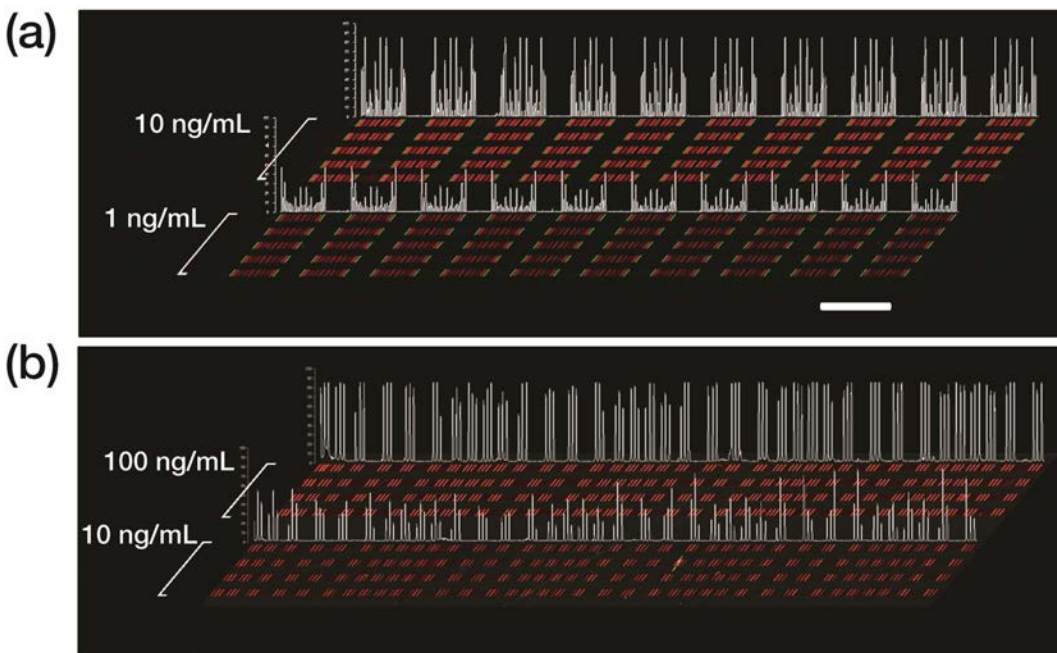


Figure 3.8 Contrast-enhanced raw data extracted from multi-protein calibration experiments performed on a substrate prepared by Scheme 2 (a) and Scheme 3 (b). Each red bar represents a unique protein measurement, and is clustered with up to ten additional proteins (for Scheme 2). The clusters become symmetrical due to the winding nature of the barcode pattern, so that each cluster actually contains two measurements of each protein. Clustering is less evident in (b) because a lower-density barcode pattern was employed. Recombinant proteins were analyzed across five discrete channels per concentration for (a) and four discrete channels per concentration for (b); quantitative data for statistical analysis was extracted from all the repeats in each of the channels. By utilizing identical DEAL cocktails followed by identical standard protein cocktails, the reproducibility was also checked. The identical signal patterns within individual channels and between channels of similar concentrations demonstrate the good uniformity and quality of DNA barcodes. Signal intensity profiles sampled from one analysis channel per concentration are quantified in white. Scale bar: 2 mm

Fig. 3.8 shows line profiles of the signal intensities along with the raw data, and demonstrate a better uniformity for barcodes prepared according to Scheme 3.2. While we found that Scheme 3.3 could produce barcodes that were close in quality to those of Scheme 3.2, the absolute (chip-to-chip) consistency of Scheme 3.3 is hard to guarantee due to its use of the unstable coupling reagents 1-ethyl-3-(3-dimethylaminopropyl)

carbodiimide (EDC) and NHS.³⁴ Moreover, although Scheme 3.3 is faster, the detailed procedure itself is more labor intensive; Scheme 3.2 can potentially be automated. Thus, we chose Scheme 3.2 as the preferred barcode patterning method. With Scheme 3.2, over 90% of the patterned slides showed good quality for the test.

We validated the use of the antibody barcodes by applying them towards the multiplex assay of cytoplasmic proteins from single cells. There is a significant body of evidence which demonstrates that genetically identical cells can exhibit significant functional heterogeneity—behavior that cannot be captured by proteomics techniques that average data across a population.³⁵ We therefore designed a highly parallel microfluidic device capable of isolating single/few numbers of cells in chambers with a full complement of antibody barcodes designed to detect intracellular proteins (Fig. 3.2). Fig. 3.9a shows a schematic of the device and the DEAL-based protein detection scheme. The small chamber size keeps the finite number of protein molecules concentrated, thereby enhancing sensitivity. Assaying such a panel of proteins would not be possible without a high-density antibody array, such as the barcodes utilized here, for the following reasons: First, all the barcodes should fit into such a small chamber for multiplexing. Second, since data averaging in such a spatially-constrained scheme is impractical, it is critical to have consistent DNA loading across the microrarray if data comparisons are to be meaningful.

We chose the U87 GBM cell line as a model system for our platform. GBM is the most common malignant brain tumor found in adults, and is the most lethal of all cancers. As the name implies, GBM exhibits extensive biological variability and heterogeneous clinical behavior.³⁶ EGFR is an important GBM oncogene and therapeutic target.³⁷ Thus, we assayed for eleven intracellular proteins associated with the EGFR-activated PI3K

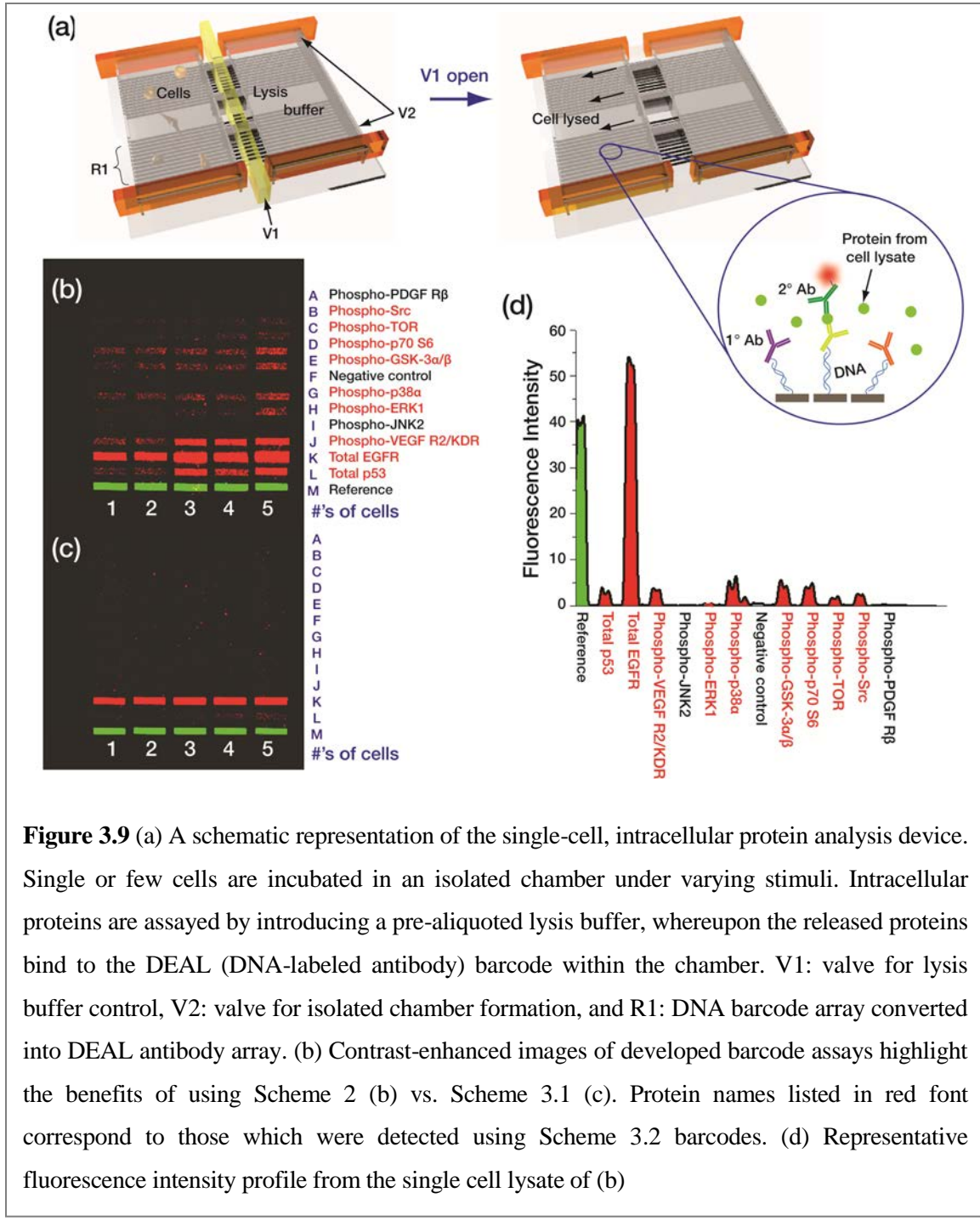


Figure 3.9 (a) A schematic representation of the single-cell, intracellular protein analysis device. Single or few cells are incubated in an isolated chamber under varying stimuli. Intracellular proteins are assayed by introducing a pre-aliquoted lysis buffer, whereupon the released proteins bind to the DEAL (DNA-labeled antibody) barcode within the chamber. V1: valve for lysis buffer control, V2: valve for isolated chamber formation, and R1: DNA barcode array converted into DEAL antibody array. (b) Contrast-enhanced images of developed barcode assays highlight the benefits of using Scheme 2 (b) vs. Scheme 3.1 (c). Protein names listed in red font correspond to those which were detected using Scheme 3.2 barcodes. (d) Representative fluorescence intensity profile from the single cell lysate of (b)

signaling pathway. We provide representative sets of data for protein detection from the lysate of 1 to 5 cells (Fig. 3.9b and 3.9c). Eight proteins were detected from single-cell lysate and up to nine proteins were detected from five cells when using barcodes patterned by Scheme 3.2 (Fig. 3.9b and Fig. 3.9d), whereas only one protein could be detected from

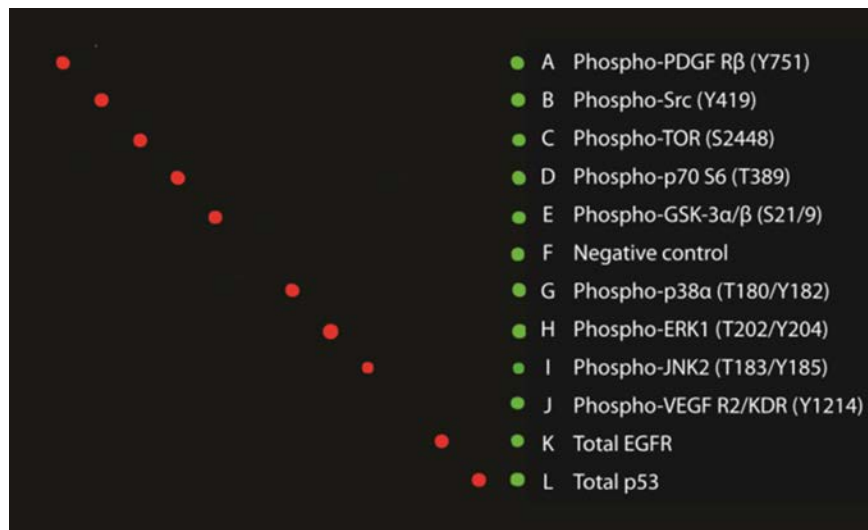
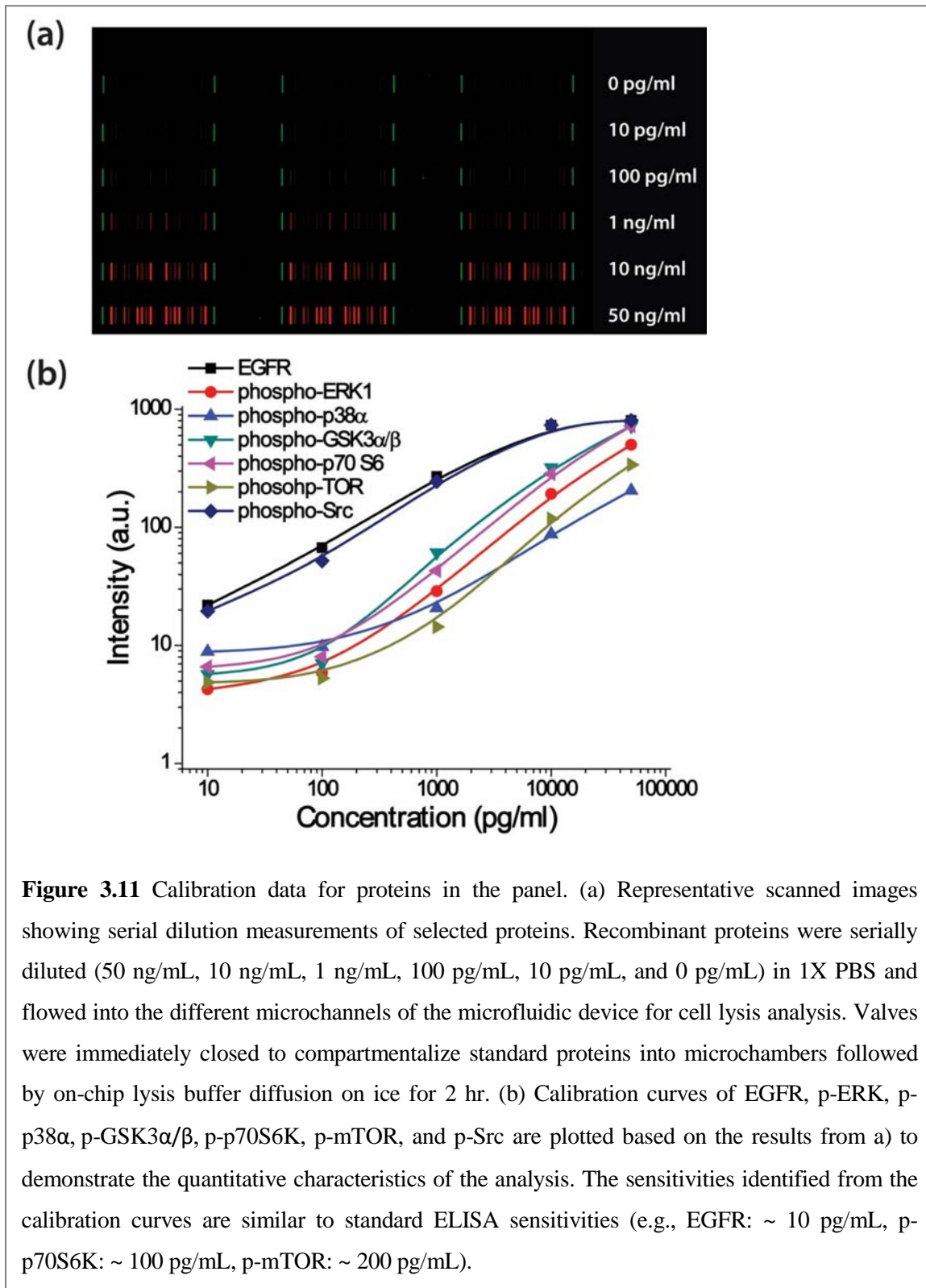


Figure 3.10 Antibody cross-reactivity tests. All antibodies were pre-selected based on such cross-reactivity tests. A pin-spotted DNA microarray was used for a DEAL-based protein detection approach—similar to the assays used within the SCBC microfluidic devices for single-cell proteomics. Each row shows the results from different conditions. For all conditions, the same cocktail of DEAL conjugates was used, and included one conjugate for each of the 11 proteins assayed. For each row, only one target recombinant protein was tested. The target proteins were introduced at concentrations between 5–50 ng/mL, depending on the sensitivity of each antibody pair. Red spots are signals from the target proteins and the green spots are reference signals from Cy3-labeled DNA sequence M'. Phospho-VEGFR2 was not validated because the recombinant protein is not commercially available.

barcodes prepared by Scheme 3.1 (Fig. 3.9c). All the separate protein assays were screened for cross-reactivity (Fig. 3.10), and, for the cases where recombinant proteins were available, quantitation curves for each protein assay were measured (Fig. 3.11). More detailed statistical analysis of these cells, as well as genetic variants thereof, is currently being investigated.



3.4 Conclusions

We have identified a protocol for generating high-quality, high-density DNA barcode patterns by comparing three microfluidics-based patterning schemes. We find, through both experiment and theory, that the electrostatic attractions between positively charged PLL substrates and the negatively-charged DNA backbone induces significant non-uniformity in the patterning process, but that those electrostatic interactions may be mediated by adding DMSO to the solution, resulting in uniform and highly reproducible barcodes patterned using ~ 55-cm-long channels that template barcodes across an entire 2.5-cm-wide glass slide. Dendrimer-based covalent immobilization also yields good ultimate uniformity, but is hampered by a relatively unstable chemistry that limits run-to-run reproducibility. DNA barcodes were coupled with the DEAL technique to generate antibody barcodes, and then integrated into specifically designed microfluidic chips for assaying cytoplasm proteins from single and few lysed U87 model cancer cells. Successful detection of a panel of such proteins represents the potential of our platform to be applied to various biological and, perhaps, clinical applications.

3.5 References

1. Heath, J. R.; Davis, M. E., Nanotechnology and cancer. *Annual Review of Medicine* **2008**, 59, 251–265.
2. Heath, J. R.; Phelps, M. E.; Hood, L., NanoSystems biology. *Molecular Imaging and Biology* **2003**, 5, (5), 312–325.

3. Khalil, I. G.; Hill, C., Systems biology for cancer. *Current Opinion in Oncology* **2005**, 17, (1), 44–48.
4. Zheng, G.; Patolsky, F.; Cui, Y.; Wang, W. U.; Lieber, C. M., Multiplexed electrical detection of cancer markers with nanowire sensor arrays. *Nature Biotechnology* **2005**, 23, (10), 1294–1301.
5. Niemeyer, C. M., Functional devices from DNA and proteins. *Nano Today* **2007**, 2, (2), 42–52.
6. Boozer, C.; Ladd, J.; Chen, S.; Jiang, S., DNA-directed protein immobilization for simultaneous detection of multiple analytes by surface plasmon resonance biosensor. *Analytical Chemistry* **2006**, 78, (5), 1515–1519.
7. Wacker, R.; Niemeyer, C. M., DDI-microFIA—A readily configurable microarray-fluorescence immunoassay based on DNA-directed immobilization of proteins. *Chembiochem* **2004**, 5, (4), 453–459.
8. Schroeder, H.; Adler, M.; Gerigk, K.; Muller-Chorus, B.; Gotz, F.; Niemeyer, C. M., User configurable microfluidic device for multiplexed immunoassays based on DNA-directed assembly. *Analytical Chemistry* **2009**, 81, (3), 1275–1279.
9. Wacker, R.; Schröder, H.; Niemeyer, C. M., Performance of antibody microarrays fabricated by either DNA-directed immobilization, direct spotting, or streptavidin-biotin attachment: a comparative study. *Analytical Biochemistry* **2004**, 330, (2), 281–287.
10. Douglas, E. S.; Chandra, R. A.; Bertozzi, C. R.; Mathies, R. A.; Francis, M. B., Self-assembled cellular microarrays patterned using DNA barcodes. *Lab on a chip* **2007**, 7, (11), 1442–1448.

11. Bailey, R. C.; Kwong, G. A.; Radu, C. G.; Witte, O. N.; Heath, J. R., DNA-encoded antibody libraries: a unified platform for multiplexed cell sorting and detection of genes and proteins. *Journal of the American Chemical Society* **2007**, 129, (7), 1959–1967.
12. Niemeyer, C. M.; Sano, T.; Smith, C. L.; Cantor, C. R., Oligonucleotide-Directed Self-Assembly of Proteins—Semisynthetic DNA Streptavidin Hybrid Molecules as Connectors for the Generation of Macroscopic Arrays and the Construction of Supramolecular Bioconjugates. *Nucleic Acids Research* **1994**, 22, (25), 5530–5539.
13. Sano, T.; Smith, C.; Cantor, C., Immuno-PCR: very sensitive antigen detection by means of specific antibody-DNA conjugates. *Science* **1992**, 258, (5079), 120–122.
14. Vickers, J. A.; Caulum, M. M.; Henry, C. S., Generation of Hydrophilic Poly(dimethylsiloxane) for High-Performance Microchip Electrophoresis. *Analytical Chemistry* **2006**, 78, (21), 7446–7452.
15. Fan, R.; Vermesh, O.; Srivastava, A.; Yen, B. K.; Qin, L.; Ahmad, H.; Kwong, G. A.; Liu, C. C.; Gould, J.; Hood, L.; Heath, J. R., Integrated barcode chips for rapid, multiplexed analysis of proteins in microliter quantities of blood. *Nature Biotechnology* **2008**, 26, (12), 1373–1378.
16. Thorsen, T.; Maerkl, S. J.; Quake, S. R., Microfluidic large-scale integration. *Science* **2002**, 298, (5593), 580–584.
17. Duan, Y.; Wu, C.; Chowdhury, S.; Lee, M. C.; Xiong, G.; Zhang, W.; Yang, R.; Cieplak, P.; Luo, R.; Lee, T.; Caldwell, J.; Wang, J.; Kollman, P., A point-charge force field for molecular mechanics simulations of proteins based on condensed-phase quantum mechanical calculations. *Journal of Computational Chemistry* **2003**, 24, (16), 1999–2012.

18. Cornell, W. D.; Cieplak, P.; Bayly, C. I.; Gould, I. R.; Merz, K. M.; Ferguson, D. M.; Spellmeyer, D. C.; Fox, T.; Caldwell, J. W.; Kollman, P. A., A Second Generation Force Field for the Simulation of Proteins, Nucleic Acids, and Organic Molecules. *Journal of the American Chemical Society* **1995**, 117, (19), 5179–5197.
19. Plimpton, S., Fast Parallel Algorithms for Short-Range Molecular Dynamics. *Journal of Computational Physics* **1995**, 117, (1), 1–19.
20. Tung, C. S.; Carter, E. S., 2nd, Nucleic acid modeling tool (NAMOT): an interactive graphic tool for modeling nucleic acid structures. *Computer Applications in the Biosciences* **1994**, 10, (4), 427–433.
21. Jorgensen, W. L.; Chandrasekhar, J.; Madura, J. D.; Impey, R. W.; Klein, M. L., Comparison of Simple Potential Functions for Simulating Liquid Water. *Journal of Chemical Physics* **1983**, 79, (2), 926–935.
22. Hockney, R. W.; Eastwood, J. W., Computer Simulation Using Particles. *McGraw-Hill: New York*, **1981**.
23. Benn, J. A.; Hu, J.; Hogan, B. J.; Fry, R. C.; Samson, L. D.; Thorsen, T., Comparative modeling and analysis of microfluidic and conventional DNA microarrays. *Analytical Biochemistry* **2006**, 348, (2), 284–293.
24. Tinland, B.; Pluen, A.; Sturm, J.; Weill, G., Persistence Length of Single-Stranded DNA. *Macromolecules* **1997**, 30, (19), 5763–5765.
25. Nkodo, A. E.; Garnier, J. M.; Tinland, B.; Ren, H.; Desruisseaux, C.; McCormick, L. C.; Drouin, G.; Slater, G. W., Diffusion coefficient of DNA molecules during free solution electrophoresis. *Electrophoresis* **2001**, 22, (12), 2424–2432.

26. Dufva, M., Fabrication of high quality microarrays. *Biomolecular Engineering* **2005**, 22, (5–6), 173–184.
27. Le Berre, V.; Trevisiol, E.; Dagkessamanskaia, A.; Sokol, S.; Caminade, A. M.; Majoral, J. P.; Meunier, B.; Francois, J., Dendrimeric coating of glass slides for sensitive DNA microarrays analysis. *Nucleic Acids Research* **2003**, 31, (16), e88.
28. Bosman, A. W.; Janssen, H. M.; Meijer, E. W., About Dendrimers: Structure, Physical Properties, and Applications. *Chemical Reviews* **1999**, 99, (7), 1665–1688.
29. Benters, R.; Niemeyer, C. M.; Drutschmann, D.; Blohm, D.; Wohrle, D., DNA microarrays with PAMAM dendritic linker systems. *Nucleic Acids Research* **2002**, 30, (2), E10.
30. Angenendt, P.; Glokler, J.; Sobek, J.; Lehrach, H.; Cahill, D. J., Next generation of protein microarray support materials: evaluation for protein and antibody microarray applications. *Journal of Chromatography A* **2003**, 1009, (1–2), 97–104.
31. Ajikumar, P. K.; Ng, J. K.; Tang, Y. C.; Lee, J. Y.; Stephanopoulos, G.; Too, H. P., Carboxyl-terminated dendrimer-coated bioactive interface for protein microarray: high-sensitivity detection of antigen in complex biological samples. *Langmuir* **2007**, 23, (10), 5670–5677.
32. Kuo, A.-T.; Chang, C.-H.; Wei, H.-H., Transient currents in electrolyte displacement by asymmetric electro-osmosis and determination of surface zeta potentials of composite microchannels. *Applied Physics Letters* **2008**, 92, (24), 244102–244103.
33. Network, C. G. A. R., Comprehensive genomic characterization defines human glioblastoma genes and core pathways. *Nature* **2008**, 455, (7216), 1061–1068.

34. Kausaite, A.; Dijk, M. v.; Castrop, J.; Ramanaviciene, A.; Baltrus, J. P.; Acaite, J.; Ramanavicius, A., Surface plasmon resonance label-free monitoring of antibody antigen interactions in real time. *Biochemistry and Molecular Biology Education* **2007**, 35, (1), 57–63.
35. Krutzik, P. O.; Irish, J. M.; Nolan, G. P.; Perez, O. D., Analysis of protein phosphorylation and cellular signaling events by flow cytometry: techniques and clinical applications. *Clinical Immunology* **2004**, 110, (3), 206–221.
36. Liang, Y.; Diehn, M.; Watson, N.; Bollen, A. W.; Aldape, K. D.; Nicholas, M. K.; Lamborn, K. R.; Berger, M. S.; Botstein, D.; Brown, P. O.; Israel, M. A., Gene expression profiling reveals molecularly and clinically distinct subtypes of glioblastoma multiforme. *Proceedings of the National Academy of Sciences of the United States of America* **2005**, 102, (16), 5814–5819.
37. Lee, J. C.; Vivanco, I.; Beroukhim, R.; Huang, J. H. Y.; Feng, W. L.; DeBiasi, R. M.; Yoshimoto, K.; King, J. C.; Nghiempahu, P.; Yuza, Y.; Xu, Q.; Greulich, H.; Thomas, R. K.; Paez, J. G.; Peck, T. C.; Linhart, D. J.; Glatt, K. A.; Getz, G.; Onofrio, R.; Ziaugra, L.; Levine, R. L.; Gabriel, S.; Kawaguchi, T.; O'Neill, K.; Khan, H.; Liau, L. M.; Nelson, S. F.; Rao, P. N.; Mischel, P.; Pieper, R. O.; Cloughesy, T.; Leahy, D. J.; Sellers, W. R.; Sawyers, C. L.; Meyerson, M.; Mellinghoff, I. K., Epidermal growth factor receptor activation in glioblastoma through novel missense mutations in the extracellular domain. *PLoS Medicine* **2006**, 3, (12), e485.

Chapter 4

Multiple Protein Secretion Profiling Analysis of Single Cells and Small Cell Colonies with Integrated Barcode Chip

4.1 Introduction

One of the major barriers in cancer research is the complexity. All cancers such as breast, prostate, lung, and brain cancer, etc., can be identified as multiple diseases with different genetic and environmental mutations. The complexity and heterogeneity of cancer require a systemic approach for diagnosis as well as treatment, aiming to find key elements responsible for the emergent properties of cancer.^{1–3} Those elements include individual biomolecules such as DNAs, RNAs, and proteins with specific mutations and networks modulating a series of biological process that leads to cancerous properties such as metastatic potential, immortality, and resistance to therapies. Especially, secreted proteins are an attractive target for cancer research because they can define cell characteristics and they are active agents to interact with the environment including other cells, the so-called tumor microenvironment. Cancer cells can induce adjacent stroma cells and extracellular matrix (ECM) to form a supportive microenvironment by producing stroma-modulating growth factors.⁴ Immune cells such as macrophages and neutrophils can also contribute to tumor progression by expressing proteases or pro-angiogenic factors. Thus, monitoring secreted proteins in a multiplexed manner from individual cells is a useful tool for the basic

research as well as the clinical diagnosis and treatment. Heterogeneity of tumor microenvironment also requires comprehensive characterization of functional phenotypes at the single cell level.

Representative techniques for single-cell functional assay are fluorescence-activated cell sorting (FACS)⁵ and ELISpot,⁶ a variant of the Enzyme-Linked Immunosorbent Assay (ELISA). FACS is commonly utilized to detect and sort cells via their surface markers. However, by blocking vesicle transport followed by staining of proteins in the cytoplasm, FACS can extend its use for the detection of protein secretion. An ELISpot test can indicate the footprint of single-cell secretion by capturing secreted proteins located proximal to the cells. Both of the techniques are currently used in clinical application but sensitivity, limited multiplexing capability, high cost, and the requirement of a large amount of sample limits their widespread use. Therefore, a new platform for the multiplexed protein detection is needed which is simple, fast, and easily expandable, at low cost.

Here, we report on an integrated barcode chip that enables high-content assessment of glioblastoma (GBM) brain tumor cells. GBM is the most common malignant brain tumor in adults, and is the most lethal of all cancers. As the name of the tumor indicates, GBM has extensive genetic and biological variability, heterogeneous clinical behavior, and accordingly unpredictable, poor prognostics⁷. Thus, studying GBM requires dealing with the heterogeneous and complex characteristics, which is a good target for our platform equipped with the capability of multiplexing analysis. The integrated barcode chip is comprised of 360 microchambers in which an antibody barcode array for the measurement of a dozen proteins is patterned. In this study, we measured protein secretion profiles from four GBM cell lines, each with specific mutation, and observed profound cellular

heterogeneity, along with unique features only available at the single-cell level. We found anti-correlations between two proteins, MIF and VEGF, which couldn't be identified with conventional, bulk analysis. We also confirmed the tumor-suppressing activity of PTEN in GBM cell lines by comparing the protein secretion profiles of two cell lines, one with PTEN and the other without PTEN. The optical transparency of our platform enabled us to monitor the physical characteristics of the system, which were matched up with the secretion profile later and presented the cell–cell communication effect through epithermal growth factor receptor (EGFR). We further demonstrate that this platform can be extended to the analysis of solid tumors by measuring secreted proteins from single cells and small cell colonies derived from the tumor of a patient. Even though there is heterogeneity in cellular functions, as we confirmed with our platform, we can also attain statistically meaningful analysis owing to the large amount of data sets that we can obtain from a single experiment.

4.2 Experimental Methods

4.2.1 Patterning of DNA barcode arrays

The DNA barcode array was prepared by microfluidic flow patterning and the microfluidic-patterning PDMS chips were fabricated by soft lithography. The master mold for the PDMS was prepared by either a negative photoresist, SU8 2010 with photolithography or a silicon hard mold with a deep reactive ion etching (DRIE) process. The mold has long meandering channel lines with 20 μm in width and height, respectively. The mixture of Sylgard PDMS (Corning) prepolymer and curing agent in 10:1 ratio (v/v)

was poured onto the mold and cured at 80°C for 1 h. The cured PDMS slab was released from the mold, inlet/outlet holes punched, and bonded onto a poly-L-lysine-(PLL)-coated glass slide (Thermo scientific) to form enclosed channels. The number of microfluidic channels determines the size of the barcode array and 13 parallel microchannels were used in this study.

Once the channels are formed, 13 orthogonal DNA oligomer solutions (sequences are provided in Table 3.1) in a 1:2 mixture (v/v) of 1xPBS buffer and dimethyl sulfoxide (DMSO) were flowed into each of the microfluidic channels. Then the DNA-solution-filled chip was placed in desiccators until the solvent was evaporated completely, leaving the DNA molecules behind. As the last step, the PDMS elastomer was removed from the glass substrate, and the barcode-patterned DNAs were cross-linked to the PLL by thermal treatment at 80 °C for 4 hours. The slide was gently rinsed with deionized water right before use in order to remove salt crystals formed during the solution evaporation step.

4.2.2 Microfluidic chip fabrication for the detection of protein secretion

The PDMS microfluidic chip for the cell experiment was fabricated by two-layer soft lithography⁸. The push-down valve configuration was utilized with a thick control layer bonded together with a thin flow layer. The molds for the control layer and the flow layer were fabricated with SU8 2010 negative photoresist (~ 20 µm thickness) and SPR 220 positive photoresist (~ 18 µm), respectively. The photoresist patterns for the flow layer were rounded via thermal treatment. The thick control layer was molded with a 5:1 mixture of GE RTV 615 PDMS prepolymer part A and part B (w/w) and the flow layer was formed by spin-coating a 20:1 mixture of GE RTV 615 part A and part B (w/w) on the flow layer

mold at 2000 rpm for 60 sec. Both layers were cured at 80°C for 1 h, followed by aligning the control layer to the flow layer, which was still on its silicon mold. Through an additional 60 min of thermal treatment at 80°C, the two layers were bonded. Afterward, the two-layer PDMS chip was peeled off, cut, and access holes punched. As a final step, the two-layer PDMS chip was thermally bonded to the barcode-patterned glass slide, forming the working device.

4.2.3 Cell culture

Human GBM cell lines were cultured in DMEM (American Type Culture Collection, ATCC) supplemented with 10% fetal bovine serum (FBS, Sigma-Aldrich). Human U87MG (U87) GBM cells were purchased from ATCC. The U87EGFR and U87EGFRvIII cell lines were kindly provided by Dr. Paul Mischel (Department of Pathology, University of California at Los Angeles, Los Angeles, CA). For the GBM1600 cell experiments, a low passage primary cell line was established from tumor tissue obtained from a GBM patient. Briefly, the tumor was diagnosed intraoperatively by a board-certified neuropathologist, finely minced with scalpels and resuspended in complete Iscove's modified Dulbecco's medium, supplemented with 20% FBS, 2 mM glutamine, 5 micrograms/ml of insulin and transferrin and 5 ng/ml selenium and a cell line was established in accordance with UCLA-IRB approved human subjects protocol 04-07-020-11.

4.2.4 On-chip secretion profiling

As a first step, the DNA barcode array was transformed into an antibody microarray. The chip was treated with fibronectin (1 µg/mL in phosphate buffered saline (PBS)) by

flow, followed by blocking with 1% bovine serum albumin (BSA) in PBS to prevent non-specific binding. This 1% BSA/PBS solution was used as a working buffer for most of the steps. After blocking, a 200 μ l cocktail containing all 12 DNA-antibody conjugates at 30 ng/ml in working buffer was flowed through the micro channels for 1 h. The unbound DNA-antibody conjugates were washed off with 100 μ l of fresh buffer. Then, cells were introduced to the microfluidic channels and microfluidic valves were closed by applying 15–20 psi constant pressure to convert 30 microfluidic channels to the 360 isolated microchambers. The chip was incubated in a cell incubator (37°C, 5% CO₂) for 24 h. After the incubation, the chip was removed from the incubator, valves were released, and a 200 μ l cocktail containing all biotin-labeled detection antibodies (~ 30 ng/ml) in working buffer was flowed through the microchannels. Next, a 200 μ l mixture of 100 ng/ml Cy5-labeled streptavidin and 20 ng/ml Cy3-labeled M' ss DNA in working buffer were flowed through the microchannels, which completed the immune-sandwich assay. Finally, the microchannels were rinsed by flowing working buffer, followed by peeling off the PDMS chip, rinsing the microarray slide with 1×PBS, 0.5×PBS, and deionized water, sequentially, and spin-drying.

4.2.5 Data analysis

The microarray slide was scanned with the GenePix 200B (Axon Instruments) for the fluorescence image of both Cy3 and Cy5 channels. All scans were performed with the same setting of 50% (635 nm) and 15% (532 nm) laser power, 500 (635 nm) and 450 (532 nm) optical gain. Line profiles for the fluorescence intensity of each channel were obtained with the ImageJ software (NIH) and a home-developed Excel macro was employed to

match averaged fluorescence signals for all the barcodes in each chamber to the cell number. The collected data were clustered by Cluster 3.0 and all the heat maps were generated by Java Treeview (<http://rana.lbl.gov/EisenSoftware.htm>). The bulk secretion data were analyzed by ImageJ.

4.3 Results and Discussion

4.3.1 Multiple-protein secretion profiling from single cells and small cell colonies with integrated microchip

We developed an integrated microfluidic chip to measure proteins from single cells or small cell colonies. The chip is composed of two layers. The lower layer (flow layer) has 30 parallel channels 200 μm in width and 18 μm in height. The top layer (control layer) also has 12 channels perpendicular to the channels in the lower layer which function as valves. When pressure is applied to the channels in the control layer, 360 isolated chambers are formed from the 30 parallel channels. The length of each chamber is 1.8 mm, yielding ~ 6.5 nl of volume per chamber. Owing to this small volume, the secreted protein concentration built up during the incubation time reaches a high enough level to be quantitatively measured even from a single cell.

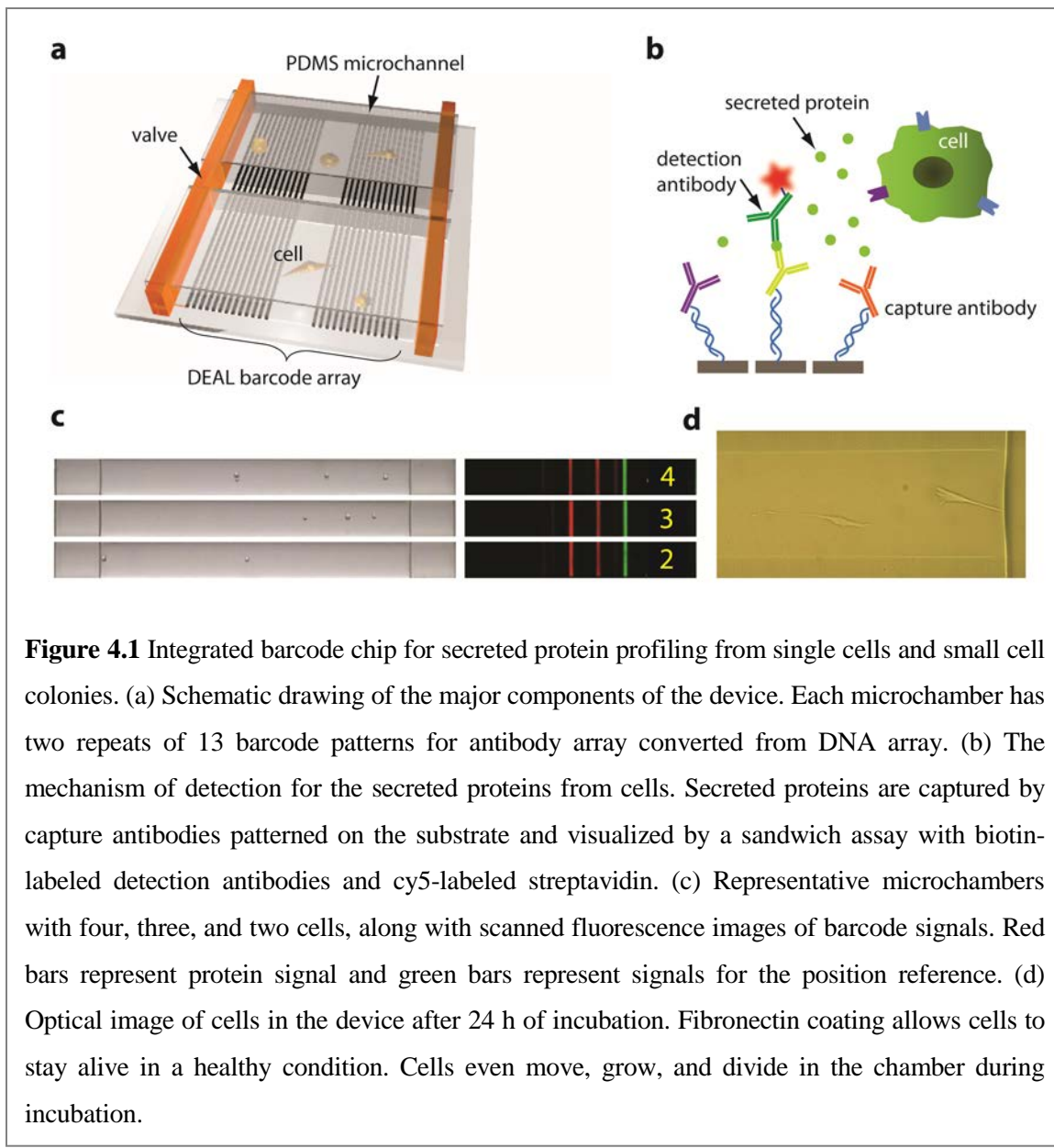
We utilized a miniaturized antibody barcode array based on the DNA-encoded antibody library (DEAL) approach⁹ to detect secreted proteins. First, DNA barcode array in the form of parallel stripes with 20 μm and 40 μm in width and pitch, respectively, is generated based on the microchannel-guided flow patterning technology. The DNA barcode array is transformed to the antibody barcode array by hybridizing DEAL conjugates (antibodies

conjugated to the complementary DNAs)¹⁰. The array for this study is designed for 13 stripes: 12 stripes for proteins and 1 stripe for an alignment reference.

Cells are randomly loaded into the large array of microchambers, which results in one or a small number of cells per chamber. The loaded cells can be imaged owing to the transparency of the chip. The schematics of the chip platform and the protein detection scheme are illustrated in Figs. 4.1a and 4.1b, respectively. The 12 proteins used for this study are as follows: interleukin (IL)-2, monocyte chemotactic protein (MCP)-1, IL-6, granulocyte-colony stimulating factor (G-CSF), macrophage inhibitory factor (MIF), epidermal growth factor (EGF), vascular endothelial growth factor (VEGF), platelet-derived growth factor (PDGF-AB), transforming growth factor (TGF)- α , IL-8, IL-1ra, and hepatocyte growth factor (HGF). For some experiments EGF and PDGF-AB are replaced with matrix metallo-proteases (MMP) 3 and IL-1 β . Fig. 4.1c shows representative microchambers loaded with four, three, and two U87 cells, along with the scanned images. The device presents a good signal-to-noise ratio for the detection of multiple secreted proteins.

4.3.2 Secretion profile from integrated barcode chip vs. bulk experiment

Our integrated barcode chip platform allows high-content analysis on many cell secretion events per chip. Fig. 4.2a shows three heat maps generated from on-chip experiments with U87, U87EGFR, and U87EGFRvIII GBM cell lines, respectively. Signals from single cells to ~ 20 cells were obtained and the secretion of 6 proteins was clearly identified from all cell lines. There are slightly different trends in terms of secretion profile among the three cell lines, even though they are from the same lineage. The major

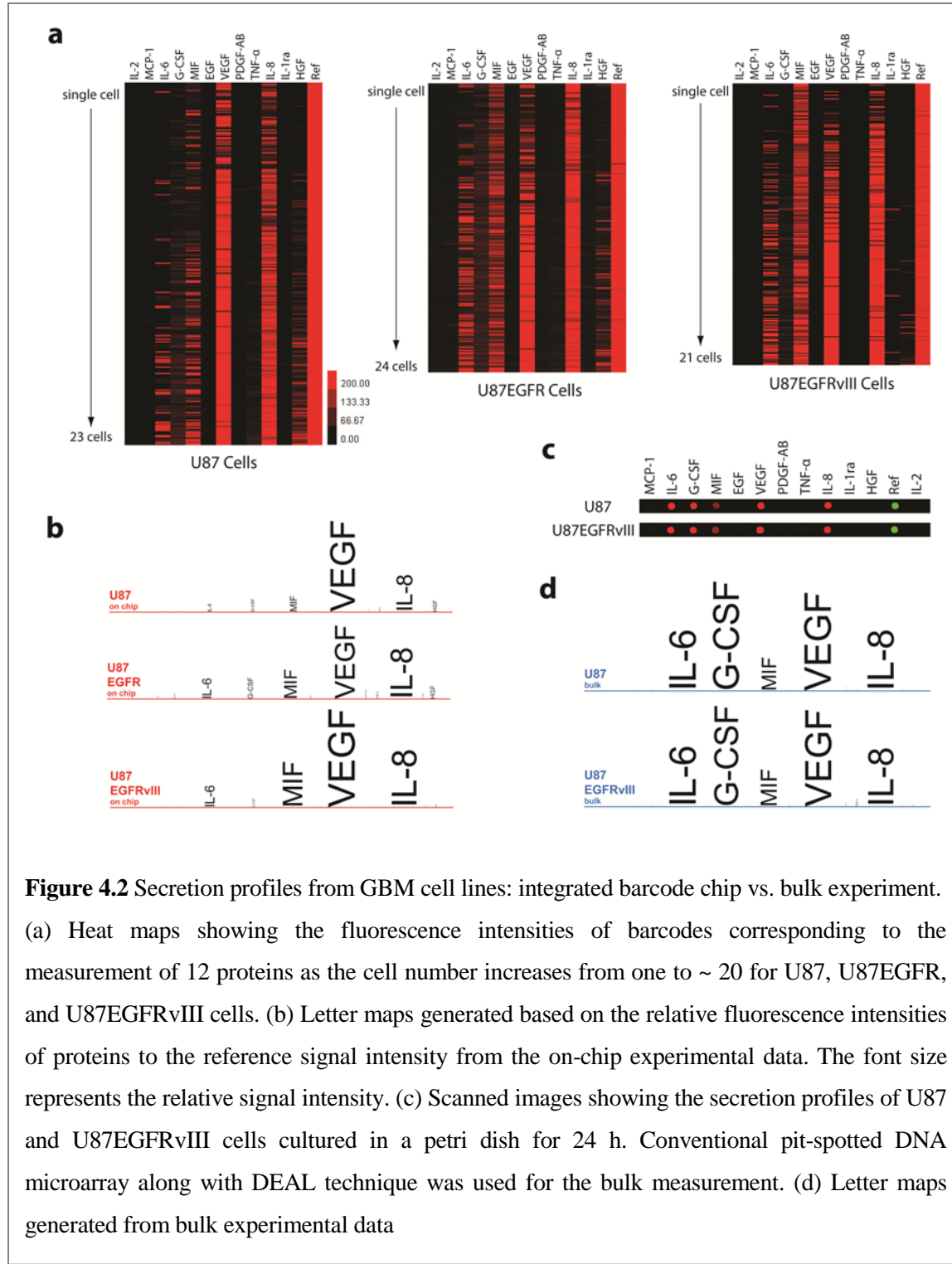


difference among the three cell lines is the epidermal growth factor receptor (EGFR) activity; U87EGFR cells have amplified EGFRs and U87EGFRvIII cells have ligand-independent, constitutively activated EGFR. Thus, different secretion profiles may reflect the effect of EGFR activity on these cells. The bulk secretion measurements for U87 and U87EGFRvIII cells were also performed with a conventional microarray. Similar profiles of secreted proteins to the on-chip experiments were obtained (Fig. 4.2c). However, it was difficult to resolve the difference between two cell types. In order to quantitatively compare

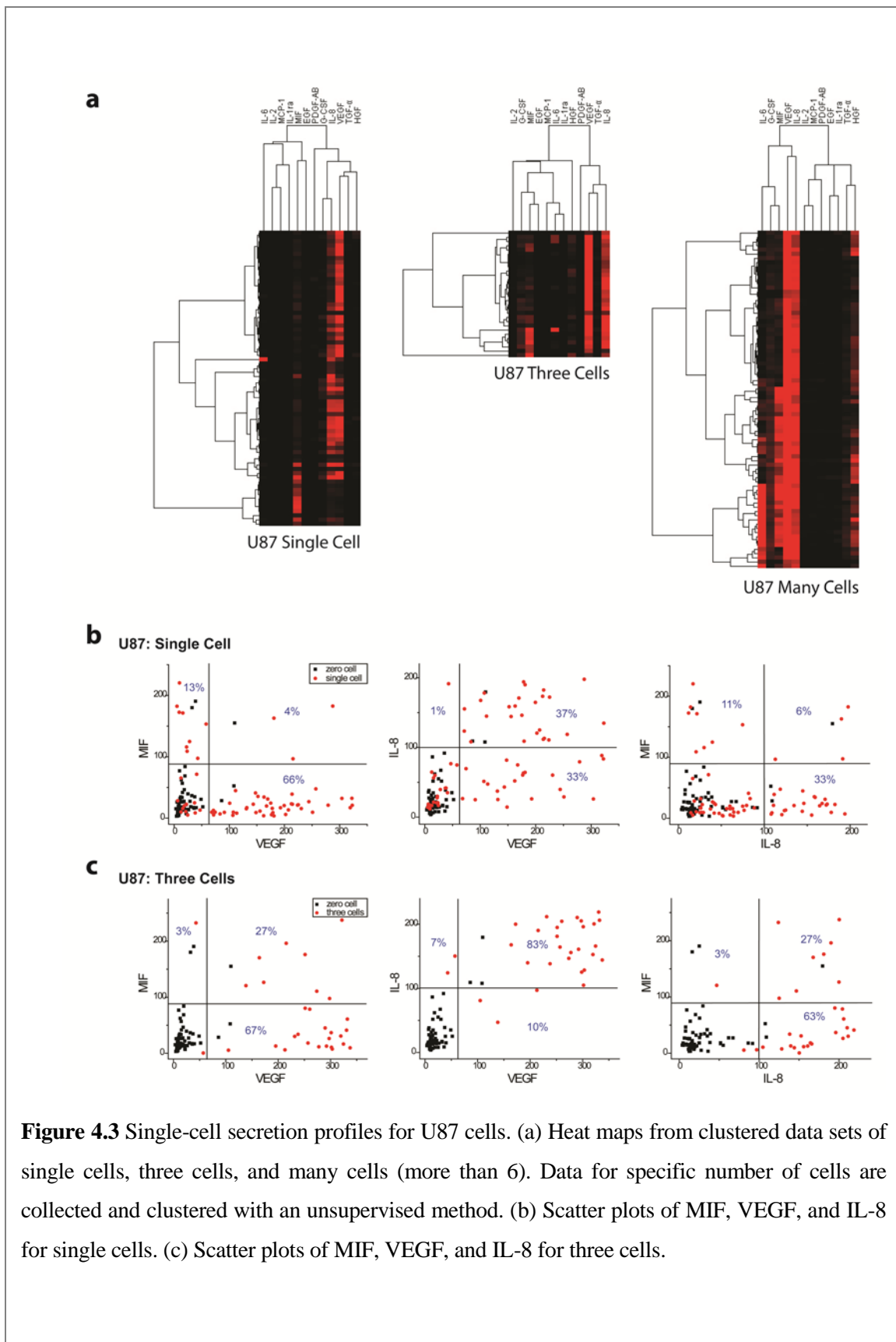
the differences, letter maps based on the signal intensities were generated in Fig. 4.2b and 4.2d. The relative signal intensities of each protein to the reference signal were calculated and the values were used as a font size. In Fig. 4.2d, U87 and U87EGFRvIII from the bulk experiments show almost identical letter maps. In contrast, letter maps of three cell lines from on-chip experiments show differences in terms of signal intensities for major proteins secreted. Most proteins including IL-6, MIF, VEGF, and IL-8 tend to be secreted more as the EGFR activity is stronger. HGF signal was weaker for U87EGFRvIII cells than others. This letter map analysis reveals that we can get more information from the on-chip experiment, information that is difficult to resolve from the conventional bulk experiment. The information from single cells or small colonies of cells, when combined together with the bulk experimental results, can lead us to understand the biology of cells more clearly.

4.3.3 Single-cell protein secretion profiling of GBM cell line: U87 cells

For comparison, the data from a single cell, three cells, and many cells (more than 6 cells) were extracted and analyzed with an unsupervised clustering by Cluster 3.0 software (Fig. 4.3a). Each row in the heat map represents the data from a single chamber. Here 70 single cell data sets were collected and several notable features can be extracted from this analysis. The most striking observation is the anti-correlation between MIF and VEGF / IL-8. This anti-correlation can be found from the single-cell data and the effect becomes weaker as the cell number increases (Fig. 4.3a). It is difficult to identify this relationship from even three-cell data. To quantitatively analyze this, we plotted the scattered plots for single cell and three cells which show the correlation among MIF, VEGF, and IL-



8. The data from the chambers with zero cells were used as a gate for the background reference (black rectangles) and the data from the single cell or three cells were plotted with red circles in Figs. 4.3b and 4.3c. The circles in each quadrant were counted and



represented to quantitatively identify the relationships between two proteins. We found 13% MIF⁺|VEGF⁻ and 66% MIF⁻|VEGF⁺ events from the single cell and only 4% of single-cell events showed MIF⁺|VEGF⁺, which confirms the anti-correlations between MIF and VEGF. Interestingly, from three-cell data, only 3% MIF⁺|VEGF⁻ events were found and 27% of the events showed MIF⁺|VEGF⁺. Thus, we can identify the transition from the anti-correlation to the positive correlation as the cell number increases. This is an interesting observation because it was reported that there is a positive correlation between MIF and VEGF expression with a bulk scale analysis in GBM¹¹ and we also noticed a similar trend in the bulk analysis. The unique feature of an anti-correlation at the single-cell level can offer us another opportunity to find out unknown pathways related to the two potent angiogenic factors in GBM, VEGF and MIF.^{11, 12} IL-8 shows positive correlation with VEGF and thus anti-correlation with MIF.

Another interesting feature can be found from the columns of the heat map. For the clustering, we also included the correlations among proteins, which clusters the proteins as well. In the single-cell heat map, there are two major clusters, one with MIF and the other with VEGF and IL-8, and this can represent the anti-correlation among them again. However, in the heat map for many cells, they are in the same cluster, which represents the transition from the anti-correlation to the positive correlation. IL-6 can also be found in the heat map for many cells and this may reflect a possible paracrine signal for IL-6 secretion, which will be discussed below.

4.3.4 Cell-cell communication effect

Owing to the transparency of PDMS, we can monitor the experimental process optically and this feature also enables us to connect physical properties of cells or microenvironment to the cell physiology. Many different factors such as oxygen level¹³, cell morphology including size and shape,¹⁴ temperature,¹⁵ and cell-cell interaction¹⁶ are correlated to cell behavior. Therefore it is useful to be able to monitor the cell morphology or the environment and to match them with the protein-secretion profiles. As an example, we measured the distance between two cells and analyzed the protein-secretion profiles based on the information. In Fig. 4.4a, representative data sets from the U87EGFR experiment for the chambers with two cells and three cells are presented. Cells secrete more proteins as they are located closer. It can be easily seen that IL-6 and VEGF signals are stronger for the chambers with closely located cells. To analyze this effect quantitatively, scatter plots for protein-secretion level and cell-cell distance were generated based on 34 data sets and 52 data sets from U87 and U87EGFR cells, respectively (Figs. 4.4b and 4.4c). U87EGFR cells show stronger secretion levels for IL-6 and VEGF when cells are closely located, which represents a possible paracrine effect for the secretion of these two proteins. Interestingly, the cell-cell communication effect is not seen in the case of U87 cells. Based on this observation, we can conclude that there exists a paracrine signaling for IL-6 and VEGF secretion and it is related to the EGFR activity. This cell-cell communication effect presents another useful application of this device to study tumor microenvironment systemically. Even though we used the cell-cell distance as a representative parameter in this study, we can also monitor the cell morphology,

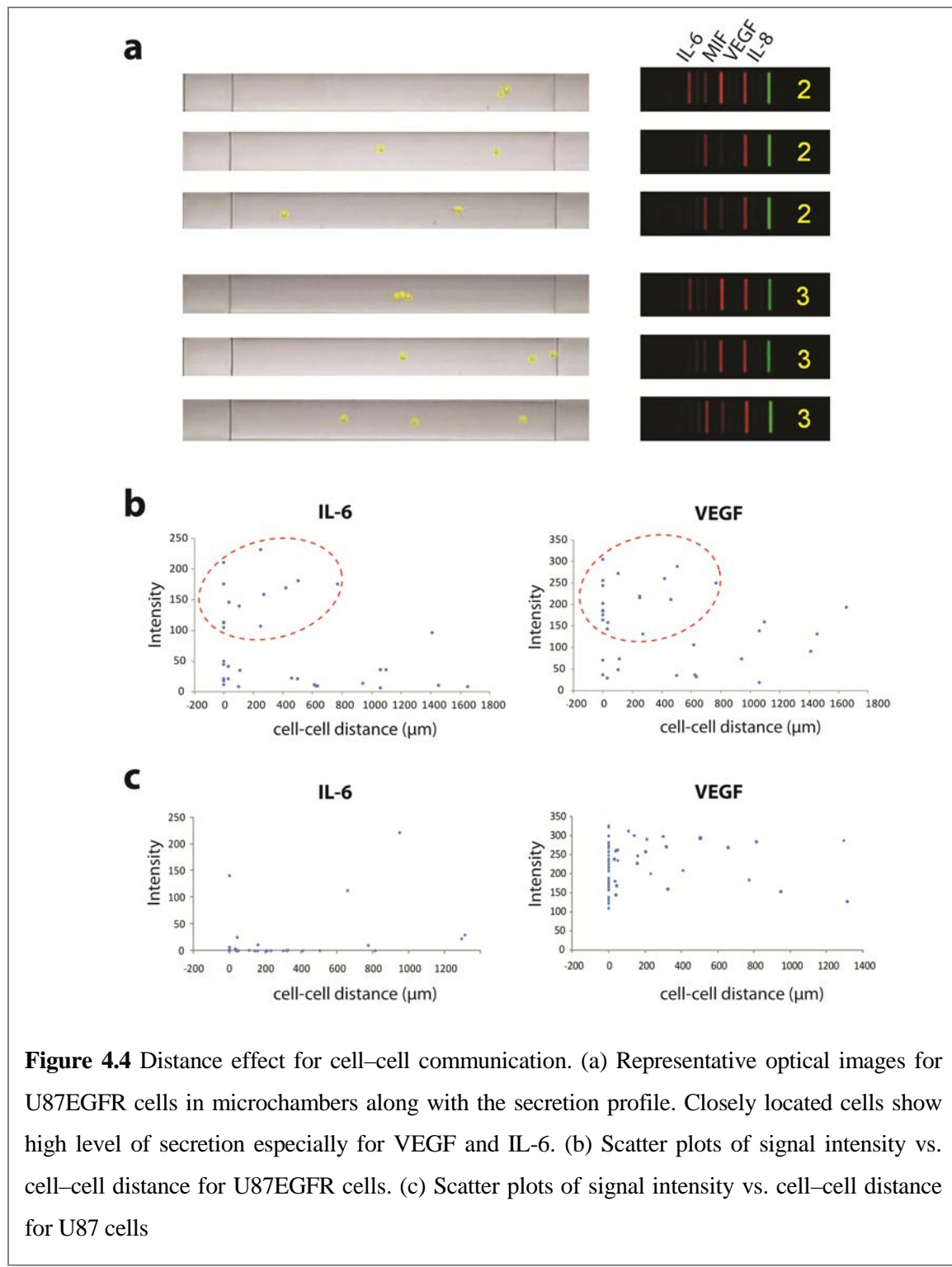
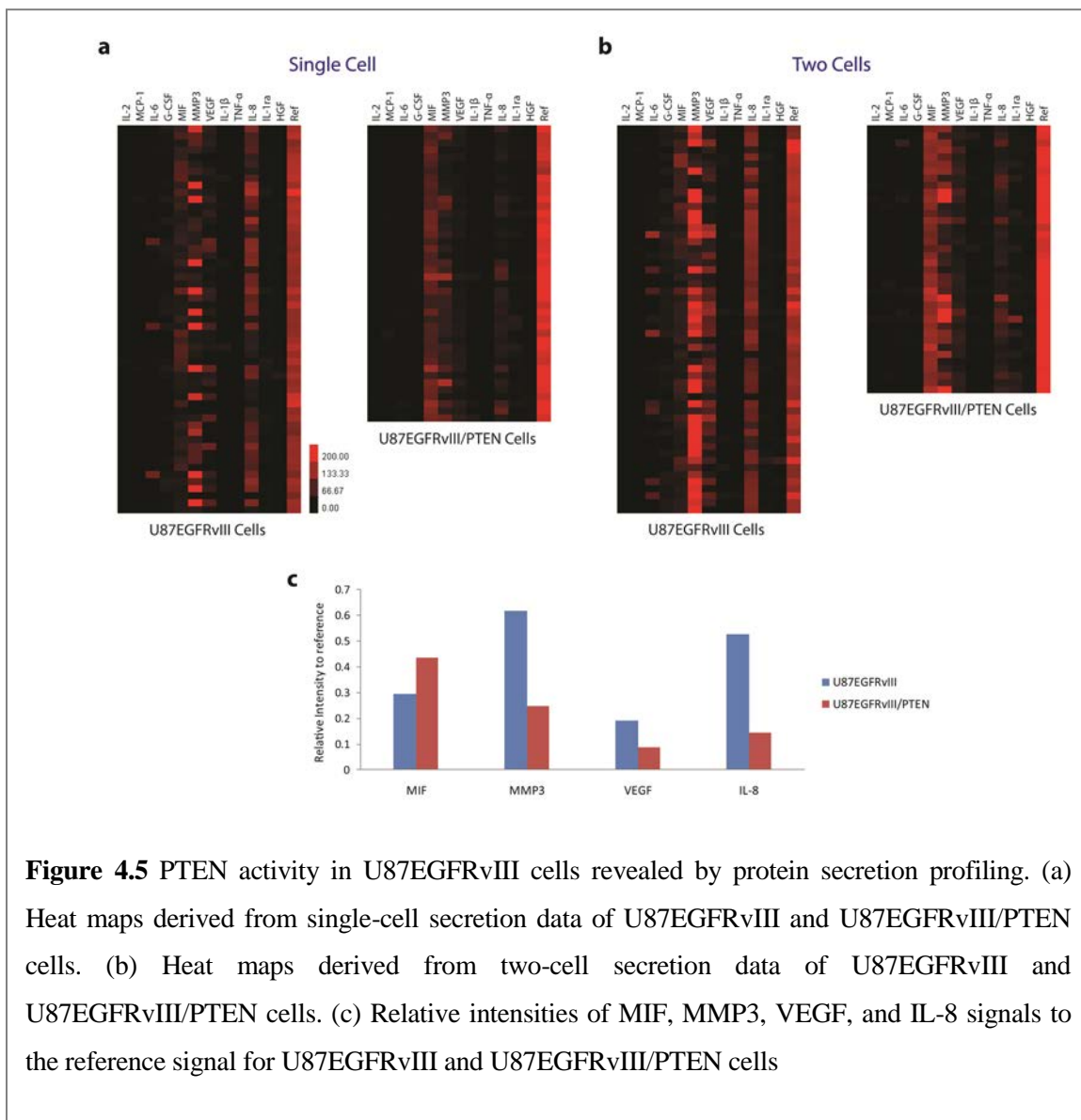


Figure 4.4 Distance effect for cell-cell communication. (a) Representative optical images for U87EGFR cells in microchambers along with the secretion profile. Closely located cells show high level of secretion especially for VEGF and IL-6. (b) Scatter plots of signal intensity vs. cell-cell distance for U87EGFR cells. (c) Scatter plots of signal intensity vs. cell-cell distance for U87 cells

proliferation rate, motility, and size, etc., with the current design or a slightly modified design.

4.3.5 PTEN activity on GBM cell line: U87EGFRvIII vs. U87EGFRvIII/PTEN

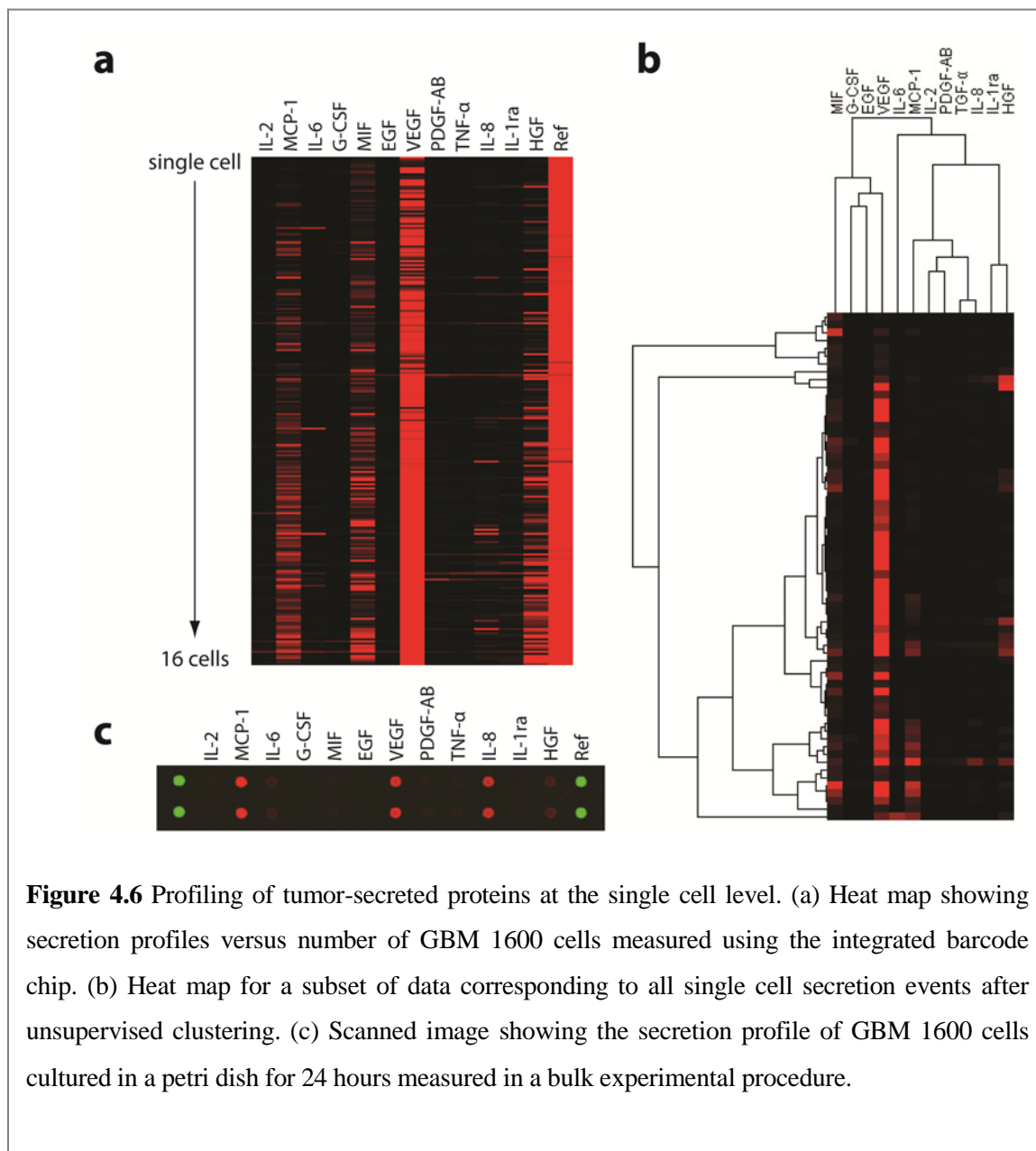
Studying major pathways related to cancer is useful in understanding basic cancer biology as well as in finding new treatment of the disease. Many drugs are inhibitors of specific proteins that play important roles to maintain unique features of cancer such as angiogenesis, immortality, and metastasis. Therefore monitoring secreted proteins, combined with the knowledge of the related signaling pathways, can offer another way of understanding cancer and finding treatment. We further interrogate PTEN, a protein



encoded by a tumor-suppressor gene, *PTEN*, and its effect on U87EGFRvIII cells as an example. *PTEN* is known to negatively regulate intracellular levels of phosphatidylinositol-3,4,5-triphosphate which is in upstream of Akt/PKB signaling pathway. Also in GBM cells, it was reported that *PTEN* mutation can cooperate with EGFR activation to increase VEGF mRNA levels via PI3K/AKT pathway.¹⁷ U87 cells have a *PTEN* mutation¹⁷ and so do U87EGFRvIII cells, because they have been derived by retroviral transduction of U87 cells with pLPCX constructs that contain EGFRvIII cDNA.¹⁸ Thus, U87EGFRvIII cells have a sufficient condition for the up-regulation of VEGF, which can be identified from Figs. 4.5a and 4.5b. Figs. 4.5a and 4.5b show heat maps for secreted proteins from U87EGFRvIII and U87EGFRvIII/*PTEN*, respectively, at the single-cell and two-cell level. Here the protein panel is slightly modified by replacing EGF and PDGF-AB with MMP3 and IL-1 β , respectively. U87EGFRvIII/*PTEN* cells show very weak VEGF signal, as expected. In Fig. 4.5c, the relative signal intensities to the reference signal for the four major proteins, including VEGF, are plotted. It can be easily seen that VEGF, MMP3, and IL-8 are positively correlated and U87EGFRvIII/*PTEN* cells show a much lower signal intensity of them. On the other hand, the MIF signal is stronger for U87EGFRvIII/*PTEN* cells, and this observation is supported by the anti-correlation between MIF and VEGF found in Figs. 4.3a and 4.3b. The results obtained from U87EGFRvIII and U87EGFRvIII/*PTEN* reveal the tumor suppressing effect of *PTEN* by down-regulating pro-angiogenic factors, including VEGF, MMP3, and IL-8, which might be related to the PI3K/Akt pathway.

4.3.6 Toward clinical sample: analysis on GBM primary tumor cells

To demonstrate the utility of our device for analyzing clinical specimens and for probing the molecular heterogeneity of pathogenesis, we performed an on-chip secretion profiling of solid tumor cells at the single-cell level. A low-passage primary GBM culture (GBM 1600 cells) was established from a surgically resected GBM tumor.¹⁹ (The tumor was diagnosed intraoperatively by a board-certified neuropathologist.) Tumor-secreted



soluble factors play a critical role in shaping the tumor microenvironment and inducing metastasis.²⁰ Thus, analysis of protein-secretion profiles at the single-cell level from small amounts of clinical specimens, e.g., tumor tissues, has important implication in cancer diagnosis and sub-typing.

Results from a single microchip (Fig. 4.6a) revealed the secretion of at least six proteins (MCP-1, IL-6, MIF, VEGF, IL-8, and HGF), while the negative control, IL-2, did not show any appreciable signal. We further analyzed the single-cell secretion events with clustering (Fig. 4.6b). It is interesting that the major secreted proteins are very similar to those from U87 cell lines. The GBM 1600 cells displayed highly heterogeneous activities, which can provide insight into the heterotypic nature of tumor cells, as we also noticed from the cell line. This experiment demonstrated the utility of this approach for the multifunctional profiling of cells harvested from clinical specimens such as tumor tissues.

4.4 Conclusions

Traditional assays for cellular functions provide averaged information from a large population of cells. This information alone, however, cannot represent the real biology of a complex, heterogeneous system such as a tumor. Most of time we can miss the hidden players or pathways that are critical to understanding the phenomena. The anti-correlation between MIF and VEGF that we observed with our integrated barcode chip is a good example of that. Previous reports based on a conventional approach showed only a positive correlation. We further identified the transition from the anti-correlation to the positive correlation as the cell number increases. More in-depth study is required to find the mechanism for the anti-correlation. This observation, however, still reflects that there might

be some facts that we are missing by making conclusions solely based on the conventional, bulk experimental data. We noticed highly heterogeneous functions even from the same lineage of cells at the single-cell level. This might be just an intrinsic complexity of biological processes such as cell–cell interaction and stochastic gene expression. But it is also true that the heterogeneity plays important roles in human health, whose outcome is the collective phenomena that we can observe with the bulk analysis. By analyzing heterogeneous but large amounts of data from single cells or small cell colonies, we can add an additional technique that can change our way of looking at diseases or basic biology. Our integrated barcode chip platform can help to disentangle at least some aspects of heterogeneous cellular responses.

Complexity is the major bottleneck for attacking cancer. That is why we need to use a tool for multi-parameter analysis and an approach to systematically study the collected information.² However, the single-parameter assay is still used in clinics because of the lack of a simple and inexpensive multi-parameter analysis tool. The recent failure of an HIV vaccine clinical trial by Merck can be a good example of the importance of a multi-parameter-based approach. Furthermore, the examination of cellular functions in a heterogeneous lesion is critical for the accurate diagnosis of complex human diseases such as cancer.²¹ Our integrated barcode chip platform offers a functionality of multi-parameter analysis not only from the secreted protein profiling but also from the combined analysis of physical characteristics of cells and the environment. Through the cell–cell interaction study, we confirmed that VEGF and IL-6 are secreted in a paracrine manner through EGFR. This is a simple example of what we can find out by adding information from a different angle. By utilizing small chambers with status that we can easily track during the

experiment, we can study the effect of physical, environmental factors such as temperature, geometry, oxygen level, and drugs on cells. Ease of fabrication is a major advantage of a PDMS-based platform, as is the optical transparency. Therefore we can easily modify the design and expand the scope of what we can study, especially for the tumor microenvironment.

From the experiments with U87 cell lines, we noticed the heterogeneity of cell behavior at the single-cell level, which might present clues for understanding deep biology. Through perturbation tests, such as neutralization of specific cytokines or growth factors and drug treatment, we can study the network of signaling pathways and apply the findings to disease diagnostics or treatment. Studying cell lines with a different set of mutations or characteristics enables us to build up an informative database as well. As an example, we confirmed PI3K/Akt-dependent PTEN activity by testing U87EGFRvIII cells and U87EGFRvIII/PTEN cells with our platform. If we collect data sets from many different cell lines for a specific cancer, it can provide a good reference for systemic analysis towards personalized diagnostics and treatments. We also applied the integrated barcode chip platform to perform multiplexed secreted-protein profiling of primary tumor cells. The response was also heterogeneous and complex. However, by combining these results with conventional diagnostic tests, we can use our platform for clinical applications, especially when we have a library of data sets for specific mutations related to cancer. Kotecha et al. showed the existence of unique cellular signatures of tumors that are useful for patient stratification with flow cytometry as well.²² Recently Kwong et al. reported cell sorting with DEAL and Nucleic Acid Cell Sorting (NACS) technologies.²³ If we combine these technologies with our platform, we can sort specific cell types from a cancer patient's

tissue sample and characterize them based on protein-secretion profiling. The integrated barcode chip represents a highly multiplexed, sensitive, and inexpensive platform that offers potential use in assessing functional heterogeneity of cells in complex disease lesions by examining clinical samples (e.g., skinny-needle-biopsied tissue). It also has the potential to analyze a disease-associated signaling network from individual patients for use in differential diagnosis and personalized treatment.

4.5 References

1. Heath, J. R.; Davis, M. E., Nanotechnology and cancer. *Annual Review of Medicine* **2008**, *59*, 251–265.
2. Heath, J. R.; Phelps, M. E.; Hood, L., NanoSystems biology. *Molecular Imaging and Biology* **2003**, *5*, (5), 312–325.
3. Khalil, I. G.; Hill, C., Systems biology for cancer. *Current Opinion in Oncology* **2005**, *17*, (1), 44–48.
4. Mueller, M. M.; Fusenig, N. E., Friends or foes - bipolar effects of the tumour stroma in cancer. *Nature Reviews Cancer* **2004**, *4*, (11), 839–849.
5. Sachs, K.; Perez, O.; Pe'er, D.; Lauffenburger, D. A.; Nolan, G. P., Causal protein-signaling networks derived from multiparameter single-cell data. *Science* **2005**, *308*, (5721), 523–529.
6. Cox, J. H.; Ferrari, G.; Janetzki, S., Measurement of cytokine release at the single cell level using the ELISPOT assay. *Methods* **2006**, *38*, (4), 274–282.

7. Liang, Y.; Diehn, M.; Watson, N.; Bollen, A. W.; Aldape, K. D.; Nicholas, M. K.; Lamborn, K. R.; Berger, M. S.; Botstein, D.; Brown, P. O.; Israel, M. A., Gene expression profiling reveals molecularly and clinically distinct subtypes of glioblastoma multiforme. *Proceedings of the National Academy of Sciences of the United States of America* **2005**, 102, (16), 5814–5819.
8. Thorsen, T.; Maerkl, S. J.; Quake, S. R., Microfluidic large-scale integration. *Science* **2002**, 298, (5593), 580–584.
9. Bailey, R. C.; Kwong, G. A.; Radu, C. G.; Witte, O. N.; Heath, J. R., DNA-encoded antibody libraries: a unified platform for multiplexed cell sorting and detection of genes and proteins. *Journal of the American Chemical Society* **2007**, 129, (7), 1959–1967.
10. Fan, R.; Vermesh, O.; Srivastava, A.; Yen, B. K.; Qin, L.; Ahmad, H.; Kwong, G. A.; Liu, C. C.; Gould, J.; Hood, L.; Heath, J. R., Integrated barcode chips for rapid, multiplexed analysis of proteins in microliter quantities of blood. *Nature Biotechnology* **2008**, 26, (12), 1373–1378.
11. Munaut, C.; Boniver, J.; Foidart, J. M.; Deprez, M., Macrophage migration inhibitory factor (MIF) expression in human glioblastomas correlates with vascular endothelial growth factor (VEGF) expression. *Neuropathology and Applied Neurobiology* **2002**, 28, (6), 452–460.
12. Bacher, M.; Schrader, J.; Thompson, N.; Kuschela, K.; Gemsa, D.; Waeber, G.; Schlegel, J., Up-regulation of macrophage migration inhibitory factor gene and protein expression in glial tumor cells during hypoxic and hypoglycemic stress indicates a critical role for angiogenesis in glioblastoma multiforme. *American Journal of Pathology* **2003**, 162, (1), 11–17.

13. Brown, J. M.; Wilson, W. R., Exploiting tumour hypoxia in cancer treatment. *Nature Reviews Cancer* **2004**, 4, (6), 437–447.
14. Behnam-Motlagh, P.; Grankvist, K.; Henriksson, R.; Engstrom, K. G., Response in shape and size of individual p31 cancer cells to cisplatin and ouabain: a computerized image analysis of cell halo characteristics during continuous perfusion. *Cytometry* **2000**, 40, (3), 198–208.
15. Levine, E. M.; Robbins, E. B., Differential temperature sensitivity of normal and cancer cells in culture. *Journal of Cellular Physiology* **1970**, 76, (3), 373–379.
16. Goswami, S.; Sahai, E.; Wyckoff, J. B.; Cammer, M.; Cox, D.; Pixley, F. J.; Stanley, E. R.; Segall, J. E.; Condeelis, J. S., Macrophages promote the invasion of breast carcinoma cells via a colony-stimulating factor-1/epidermal growth factor paracrine loop. *Cancer Research* **2005**, 65, (12), 5278–5283.
17. Pore, N.; Liu, S.; Haas-Kogan, D. A.; O'Rourke, D. M.; Maity, A., PTEN mutation and epidermal growth factor receptor activation regulate vascular endothelial growth factor (VEGF) mRNA expression in human glioblastoma cells by transactivating the proximal VEGF promoter. *Cancer Research* **2003**, 63, (1), 236–241.
18. Wang, M. Y.; Lu, K. V.; Zhu, S.; Dia, E. Q.; Vivanco, I.; Shackleford, G. M.; Cavenee, W. K.; Mellinghoff, I. K.; Cloughesy, T. F.; Sawyers, C. L.; Mischel, P. S., Mammalian target of rapamycin inhibition promotes response to epidermal growth factor receptor kinase inhibitors in PTEN-deficient and PTEN-intact glioblastoma cells. *Cancer Research* **2006**, 66, (16), 7864–7869.

19. Wang, Y.; Zhu, S.; Cloughesy, T. F.; Liau, L. M.; Mischel, P. S., p53 disruption profoundly alters the response of human glioblastoma cells to DNA topoisomerase I inhibition. *Oncogene* **2004**, *23*, (6), 1283–1290.
20. Kim, S.; Takahashi, H.; Lin, W. W.; Descargues, P.; Grivennikov, S.; Kim, Y.; Luo, J. L.; Karin, M., Carcinoma-produced factors activate myeloid cells through TLR2 to stimulate metastasis. *Nature* **2009**, *457*, (7225), 102–106.
21. Visvader, J. E.; Lindeman, G. J., Cancer stem cells in solid tumours: accumulating evidence and unresolved questions. *Nature Reviews Cancer* **2008**, *8*, (10), 755–768.
22. Kotecha, N.; Flores, N. J.; Irish, J. M.; Simonds, E. F.; Sakai, D. S.; Archambeault, S.; Diaz-Flores, E.; Coram, M.; Shannon, K. M.; Nolan, G. P.; Loh, M. L., Single-cell profiling identifies aberrant STAT5 activation in myeloid malignancies with specific clinical and biologic correlates. *Cancer Cell* **2008**, *14*, (4), 335–343.
23. Kwong, G. A.; Radu, C. G.; Hwang, K.; Shu, C. J.; Ma, C.; Koya, R. C.; Comin-Anduix, B.; Hadrup, S. R.; Bailey, R. C.; Witte, O. N.; Schumacher, T. N.; Ribas, A.; Heath, J. R., Modular nucleic acid assembled p/MHC microarrays for multiplexed sorting of antigen-specific T cells. *Journal of the American Chemical Society* **2009**, *131*, (28), 9695–9703.

Chapter 5

Protein Signaling Networks from Single-Cell Fluctuations and Information Theory Profiling

5.1 Introduction

Protein signaling pathways play important roles in tissue processes ranging from tumorigenesis to wound healing.¹⁻⁵ Elucidation of these signaling pathways is challenging, in large part, because of the heterogeneous nature of tissues.⁶ Such heterogeneity makes it difficult to separate cell-autonomous alterations in function from alterations that are triggered via paracrine signaling, and it can mask the cellular origins of paracrine signaling. Intracellular signaling pathways can be resolved via multiplex protein measurements at the single-cell level.⁷ For secreted protein signaling, there are additional experimental challenges. Intracellular staining flow cytometry (ICS-FC) requires the use of protein transport inhibitors which can influence the measurements.⁸ In addition, the largest number of cytokines simultaneously assayed in single cells by ICS-FC is only 5.⁹ Finally, certain biological perturbations, such as the influence of one cell on another, are difficult to decipher using ICS-FC. Other methods, such as multiplex fluorospot assays,¹⁰ have even more significant limitations.

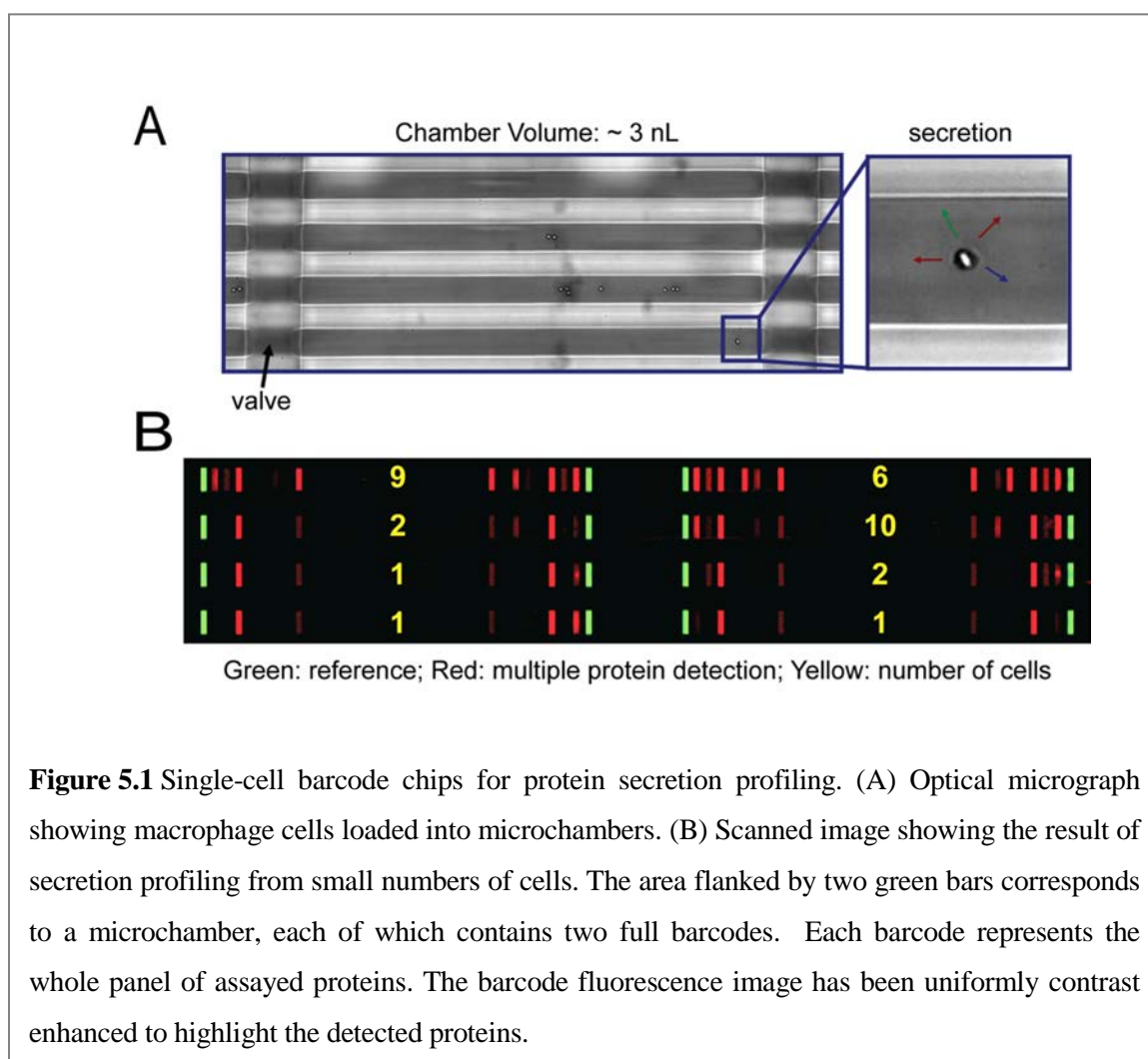
We describe here an experimental/theoretical approach designed to unravel the coordinated relationships between secreted proteins, and to understand how molecular and cellular perturbations can influence those relationships. Our starting points are single,

lipopolysaccharide-(LPS)-stimulated, human macrophage cells.^{11, 12} LPS stimulation activates the toll-like receptor-4 (TLR-4), and emulates the innate immune response to Gram-negative bacteria. We characterize the secretome, at the single-cell level, through the use of a microchip platform in which single, stimulated macrophage cells are isolated into 3 nanoliter (nl) volume microchambers, with ~ 1000 microchambers per chip. Each microchamber permits duplicate assays for each of a dozen proteins that are secreted over the course of a several-hour incubation period following cell stimulation. The barcode assays are developed using detection antibodies and fluorescent labels, and then converted into numbers of molecules detected. We demonstrate that the observed spread in protein levels is dominated by the cellular behaviors (the biological fluctuations), rather than the experimental error. These fluctuations are utilized to compute a covariance matrix linking the different proteins. This matrix is analyzed at both coarse and fine levels to extract the protein–protein interactions. We demonstrate that our system has the stability properties requisite for the application of a quantitative version of a Le Chatelier-like principle, which permits a description of the response of the system to a perturbation. This is a prediction in the strict thermodynamic sense. The fluctuations, as assessed from the multiplexed protein assays from unperturbed single cells, are used to predict the results when the cells are perturbed by the presence of other cells, or through molecular (antibody) perturbations.

5.2 Methods

5.2.1 Experimental Methods

The experimental platform is the single-cell barcode chip (SCBC) (Fig. 5.1). A SCBC contains 80 microchannels into which cells are introduced. Valves¹³ are closed to separate each microchannel into 12 individual (for 960 total) ~ 3-nanoliter-volume microchambers, each of which contains between 0 and a few cells. Cell numbers are recorded by imaging through the transparent chip. Each microchamber contains two copies of an antibody barcode array. Each barcode stripe corresponds to a given antibody; a full barcode



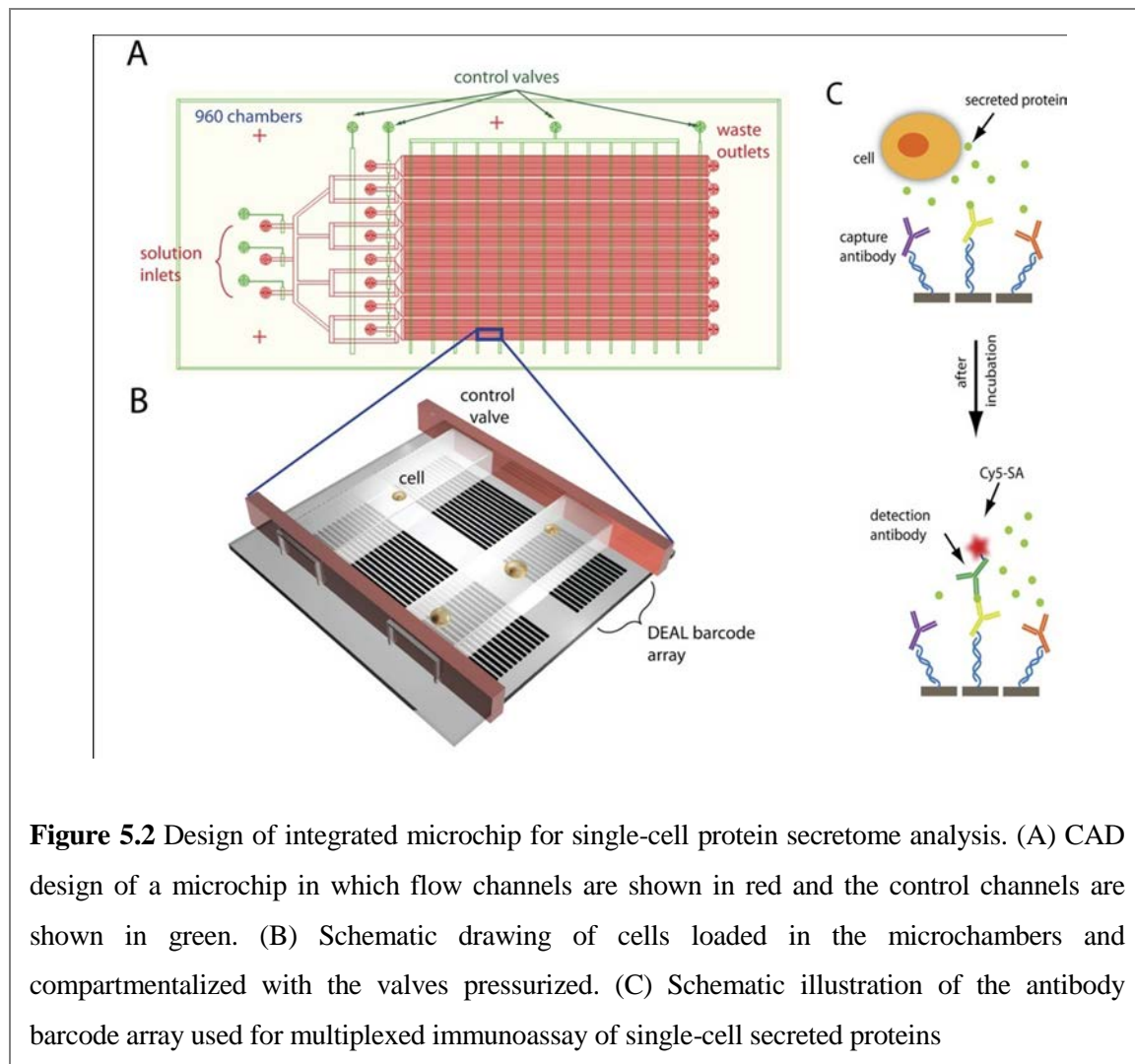


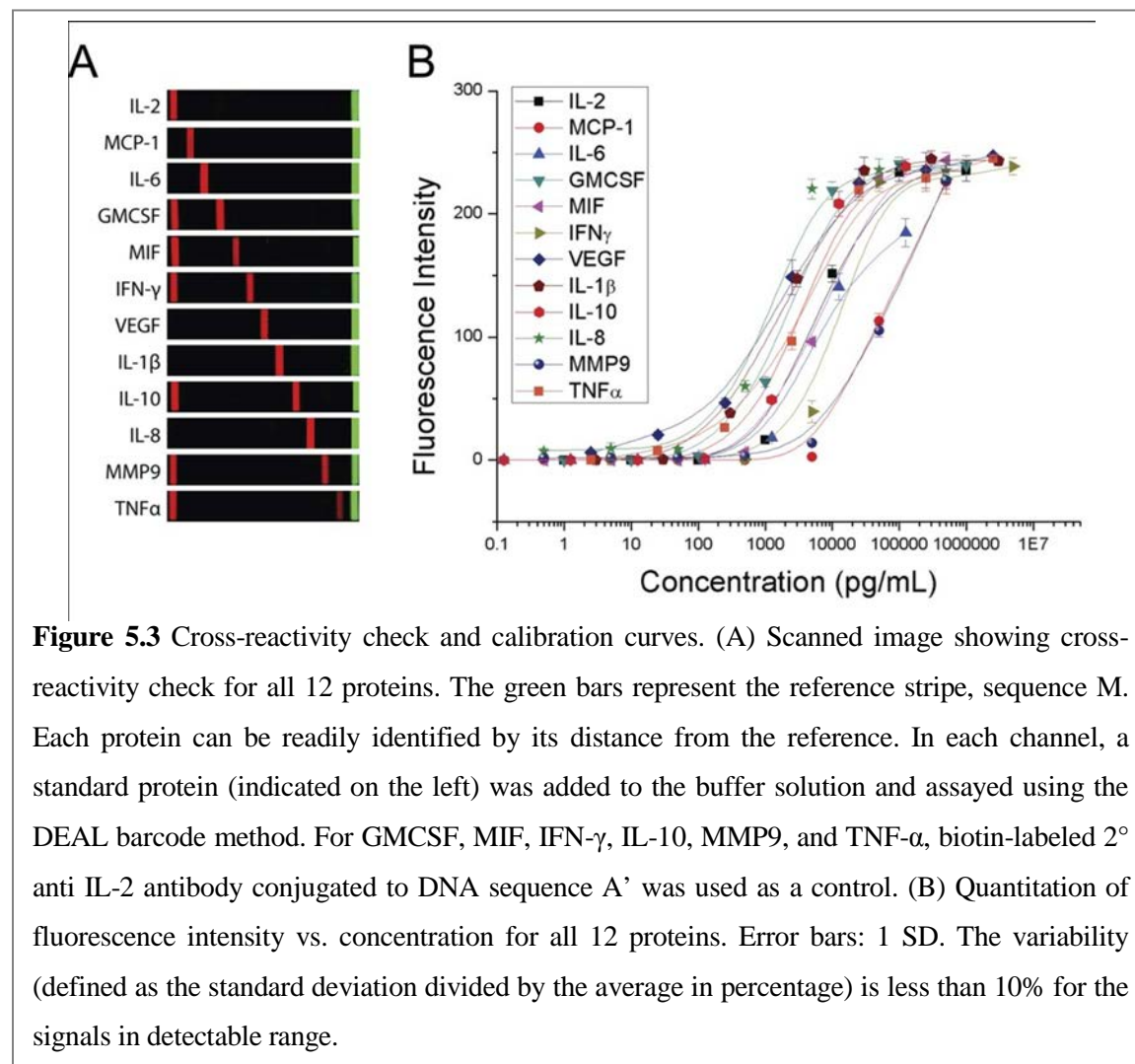
Figure 5.2 Design of integrated microchip for single-cell protein secretome analysis. (A) CAD design of a microchip in which flow channels are shown in red and the control channels are shown in green. (B) Schematic drawing of cells loaded in the microchambers and compartmentalized with the valves pressurized. (C) Schematic illustration of the antibody barcode array used for multiplexed immunoassay of single-cell secreted proteins

represents the panel of assayed proteins. Once the cells are loaded, the chip is placed into a CO₂ incubator for 24 h, during which secreted proteins are captured at the barcode stripes by their cognate antibodies. The cells are removed, and the antibody barcodes are developed using secondary antibodies and fluorophore labels. The fluorescence levels are quantified, and then converted into numbers of molecules detected using calibration curves.

We reported on a related SCBC device for assaying phosphoproteins from single lysed cancer cells (see Chapter 3).¹⁴ In that work, we described the flow patterning approach for the production of the high-quality antibody barcode arrays used here. Each barcode array contains 13 20-μm-wide stripes, at a pitch of 50 μm. The barcodes are initially patterned as

DNA stripes. Following SCBC assembly, the DNA array is converted, using DNA-hybridization, into an antibody array using a DNA-encoded antibody library^{15, 16} (Fig. 5.2). All DNA oligomers and antibody reagents are listed in Tables 5.1 and 5.2. The 12 proteins assayed were: interleukin (IL)-2, monocyte chemotactic protein (MCP)-1, IL-6, granulocyte-macrophage colony stimulating factor (GMCSF), macrophage migration inhibitory factor (MIF), interferon (IFN)- γ , vascular endothelial growth factor (VEGF), IL-1 β , IL-10, IL-8, matrix metallopeptidase (MMP) 9, and tumor necrosis factor (TNF)- α .

The barcode assays were calibrated through the use of standard proteins spiked in buffer



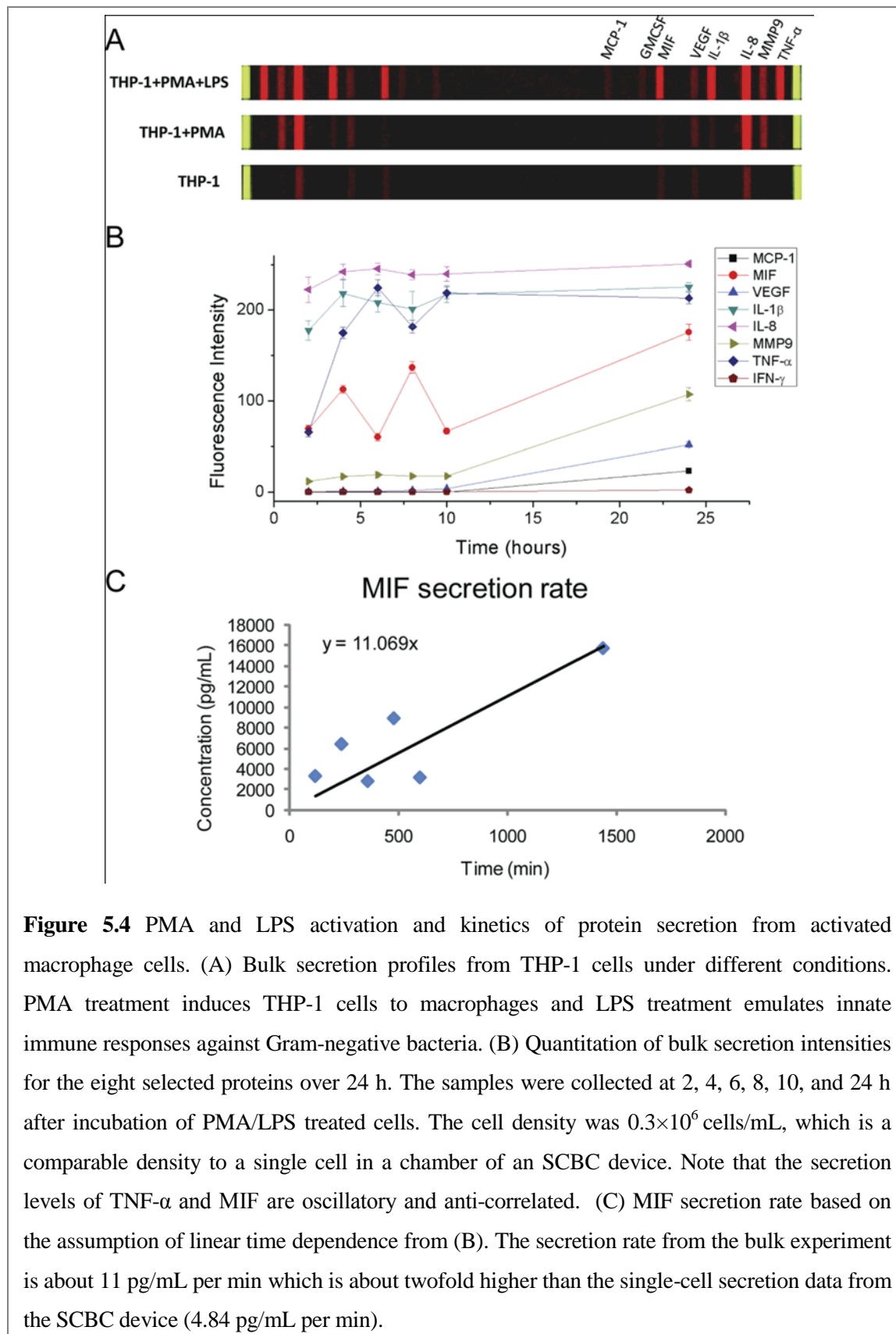


(Fig. 5.3). IL-2 is not expected to be secreted by macrophages, and so the anti-IL-2 barcode stripe was utilized to measure the background.

For the macrophage secretome experiments, cells from the human monocyte cell line, THP-1 were differentiated into macrophage lineage using phorbol 12-myristate 13-acetate (PMA), stimulated with LPS and then loaded into the device. LPS activates the TLR-4 on the cell surface^{17, 18} and stimulates the secretion of a spectrum of cytokines (Fig. 5.4).

Signal-to-noise Calculations and Experimental Error. An Axon GenePix 4400A scanner coupled with a custom algorithm was used to quantify the fluorescence intensities of each protein from each microchamber (Fig 5.1B). Certain proteins were positively detected based upon signal-to-noise ($S/N > 4$). S/N was calculated as follows: Each protein was measured twice per microchamber. The averaged fluorescence values from the two barcode stripes for all proteins were used as signals from each chamber. The ratio of the averaged signal over all single-cell experiments for a specific protein to IL-2 yields the S/N . The following eight proteins were detected (S/N is indicated after the protein name): MCP-1 (4.7), MIF (1380), IFN- γ (4.3), VEGF (77), IL-1 β (95), IL-8 (2620), MMP9 (120), and TNF- α (411).

Macrophages are highly responsive to their environment, and so experimental conditions can influence macrophage behavior. Thus, we sought confirmation that our protocols could lead to reproducible results. We executed identical sets of experiments on different SCBCs and showed that the distributions of the unambiguously detected proteins (Fig. 5.5) were effectively identical (p -value > 0.25). The results presented here do depend on the amount of PMA or LPS used and, to a lesser extent, the passage number of THP-1

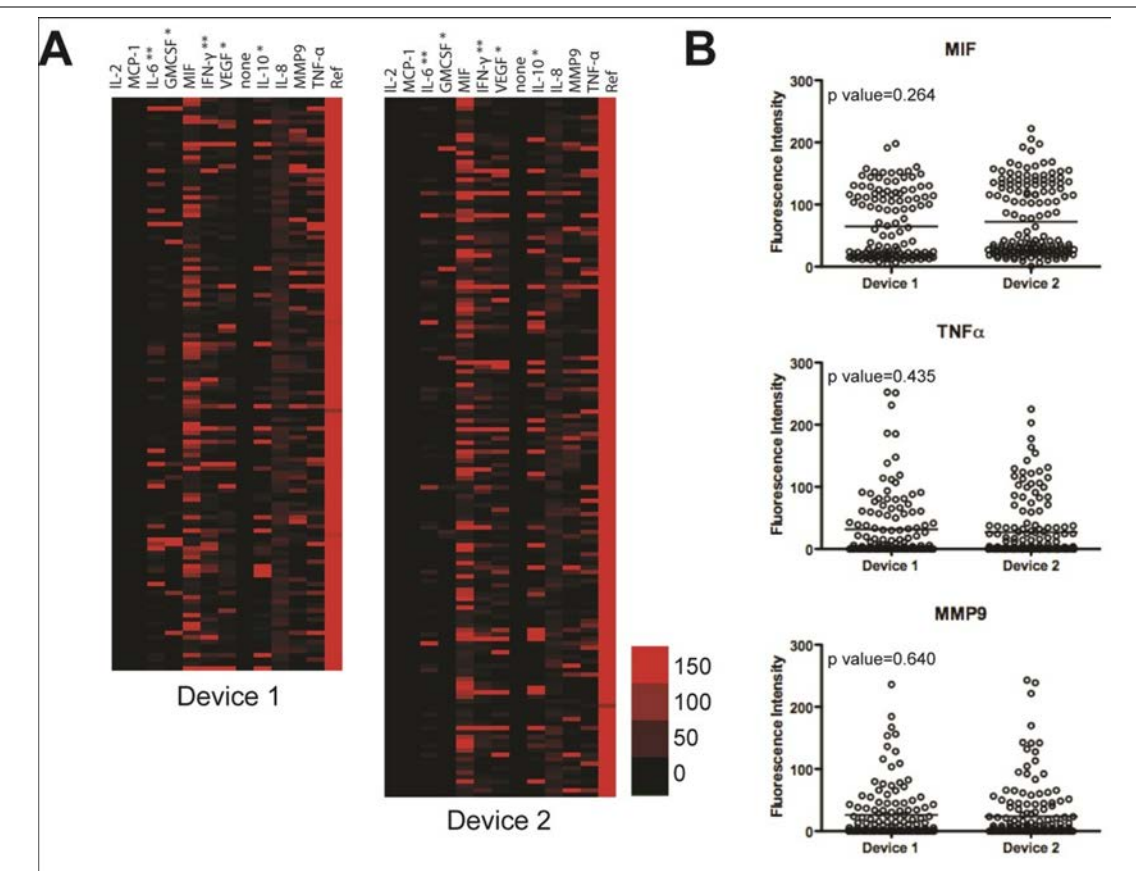


Figure 5.5 Comparison of two data sets from two experiments performed in parallel. All the conditions such as barcode patterning, PDMS-based microfluidic device fabrication, and cell preparation, etc., for the two devices were the same. (A) Heat maps of the single-cell data sets from two devices. Based on the same S/N ratio (4), 9 proteins were detected. It should be noted that the protein profiles are different from the data set used in the main text, which originated from the non-extracted PDMS device. PDMS is known to leach out toxic material to the solution and this can affect the cell condition or protein secretion because macrophages are, by nature, highly responsive to their environment. For the main experiment, solvent-extracted PDMS was used to avoid such effects. For some proteins, the signal values are multiplied by 10 (*) and 100 (**) for the visualization. (B) Dot plots for three major proteins. Based on p-values, both experimental data sets are statistically close to each other.

cells. In addition, a solvent extraction of the PDMS improves the SCBC biocompatibility and the assay reproducibility.¹⁹

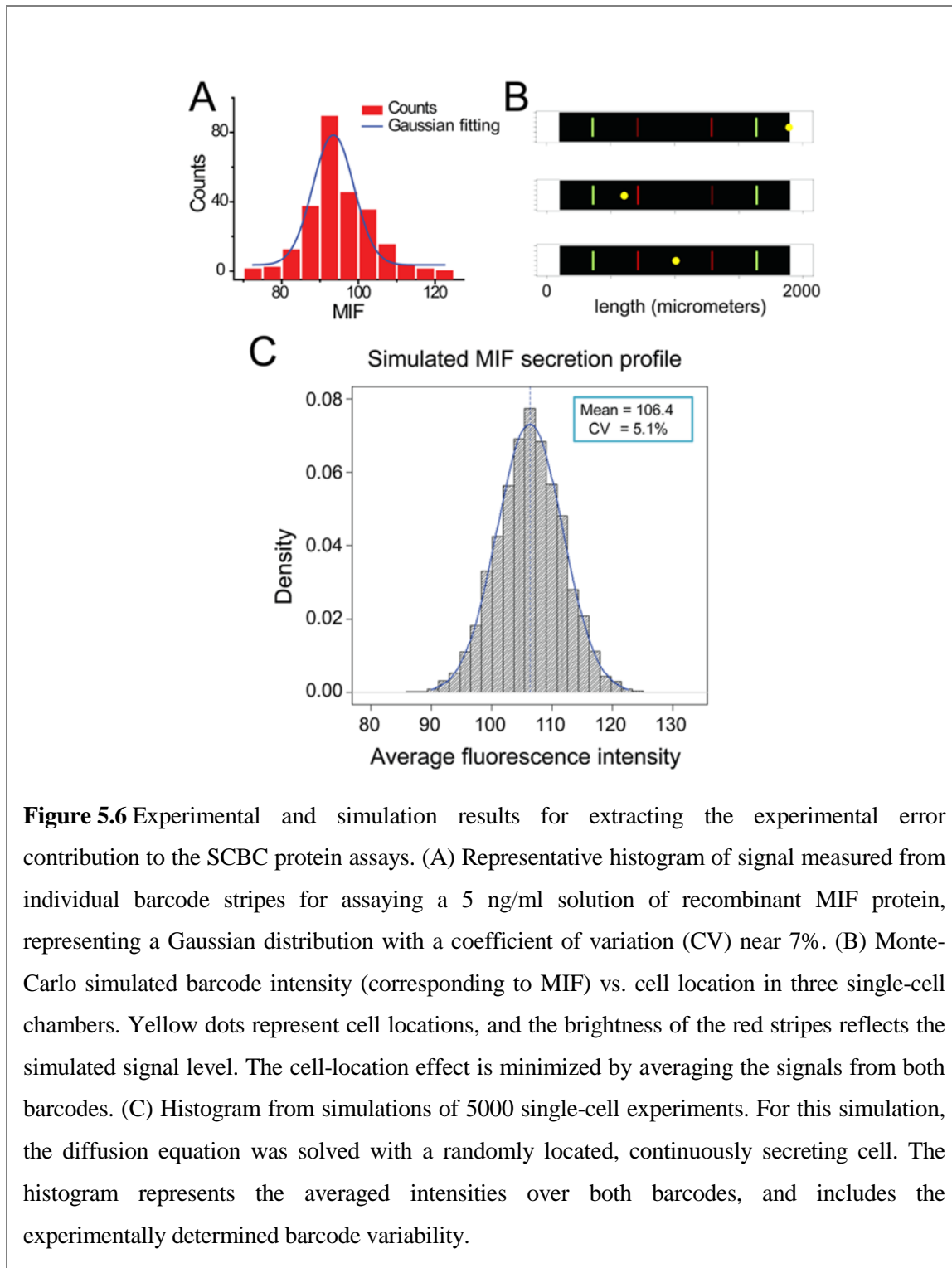
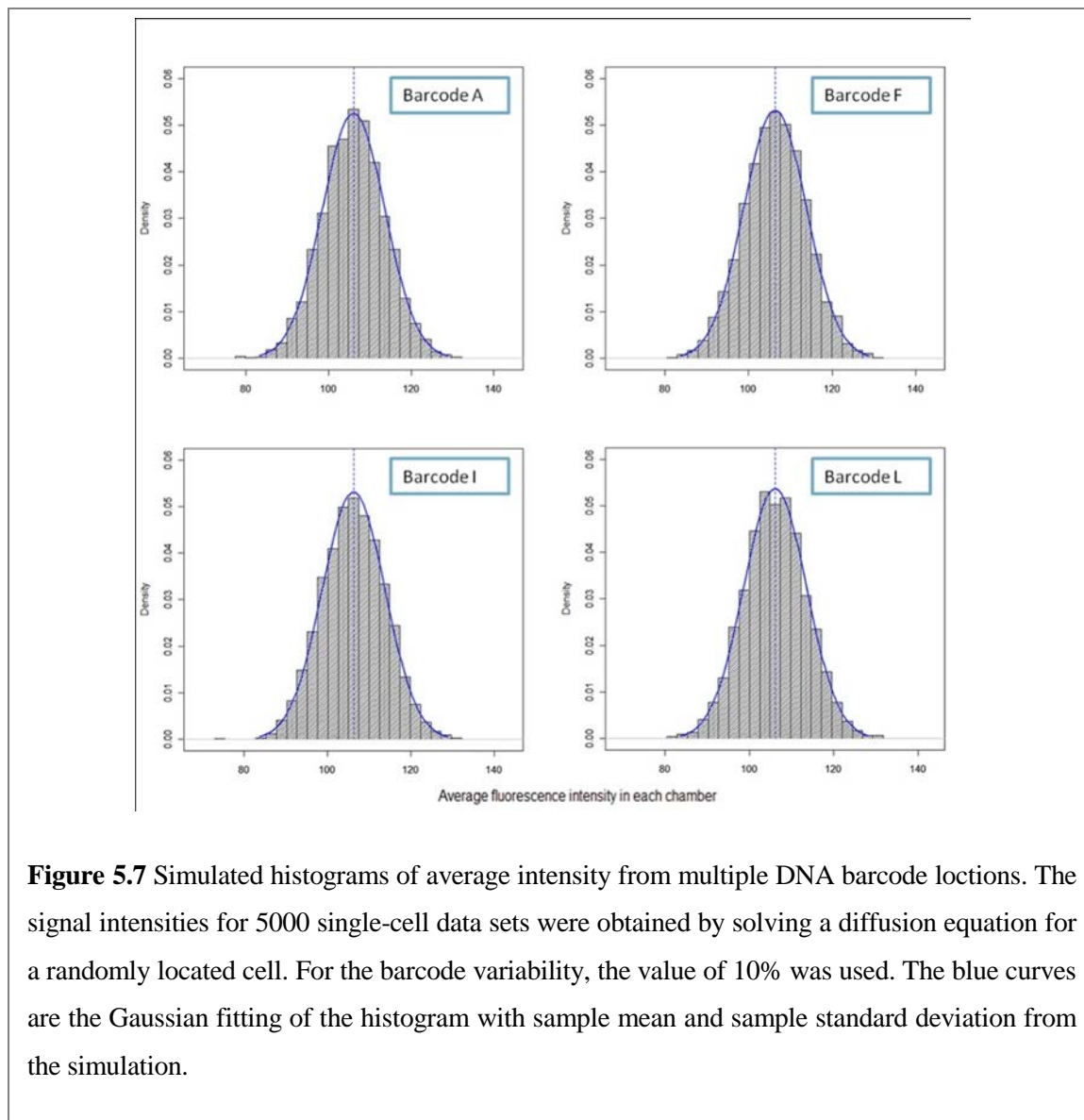


Figure 5.6 Experimental and simulation results for extracting the experimental error contribution to the SCBC protein assays. (A) Representative histogram of signal measured from individual barcode stripes for assaying a 5 ng/ml solution of recombinant MIF protein, representing a Gaussian distribution with a coefficient of variation (CV) near 7%. (B) Monte-Carlo simulated barcode intensity (corresponding to MIF) vs. cell location in three single-cell chambers. Yellow dots represent cell locations, and the brightness of the red stripes reflects the simulated signal level. The cell-location effect is minimized by averaging the signals from both barcodes. (C) Histogram from simulations of 5000 single-cell experiments. For this simulation, the diffusion equation was solved with a randomly located, continuously secreting cell. The histogram represents the averaged intensities over both barcodes, and includes the experimentally determined barcode variability.

Levels of proteins secreted from single cells can exhibit a variability that reflects the stochastic nature of biology²⁰ and, in fact, represents biological fluctuations. The SCBC

experimental error must be compared against the measured variations for extracting the true macrophage fluctuations. One contribution to the experimental error arises from the variability of the flow-patterned antibody barcodes. We characterized that variability via protein assays executed within a complex biological environment (serum), and within the microchambers of an SCBC, but using cocktails spiked with known quantities of standard proteins. In both cases, we found a variability of $< 10\%$ ²¹ (reference 21 and Fig. 5.3), depending upon the protein. Averaging the two identical protein assays per microchamber lowers the variability within a microchamber by a factor of $2^{1/2}$. A second experimental error arises from the competition between protein capture by surface-bound antibody, and protein diffusion. When a cell is proximal to a barcode, that barcode may exhibit higher signal intensity than a more distant barcode. A Monte Carlo calculation allowed for an estimation of the total system error by simulating the location-dependent experimental variation. Using MIF as a representative protein for the simulation (it has a barcode variability of 7.3%; Fig 5.6A) the experimental error of the system is estimated to be 5.1% (Fig. 5.6B,C and Data Analysis Methods in Appendix A, Section 5.6.2). For the worst case of a 10% barcode variability, the total experimental error is estimated to be $\sim 7\%$ (Table 5.7 and Fig. 5.7). Based upon these results, we can calculate the biological coefficient of variation ($CV_{biological}$) from $CV_{assay} = (CV_{system}^2 + CV_{biological}^2)^{1/2}$, where CV_{assay} is the measured spread in secretion levels for a given protein across all measurements for a given number of cells. For IL-8, the biological CV was only \sim twofold larger than the experimental CV, but for the other 7 detected proteins, the biological CV was $7\text{--}50\times$ larger than the experimental CV (Table 5.7). Thus, the fluctuation extracted from our single-cell experiments reflects the cellular behaviors.

The individual protein assays were evaluated for cross-reactivity and calibrated using standard proteins (Fig. 5.3). Calibration curves were fitted by a four-parameter logistic model.²² The SCBC assay sensitivities are comparable to commercial ELISAs (e.g., a few measured limits-of-detection are MIF ~ 100 pg/ml, IL-8 ~ 50 pg/ml, IL-1 β ~ 20 pg/ml, and VEGF ~ 2.5 pg/ml), with each exhibiting a $\sim 10^3$ linear detection range. The SCBC barcode assay results can be translated into numbers of detected molecules using the molecular weight of the standard proteins and the microchamber volume (Fig. 5.3 and



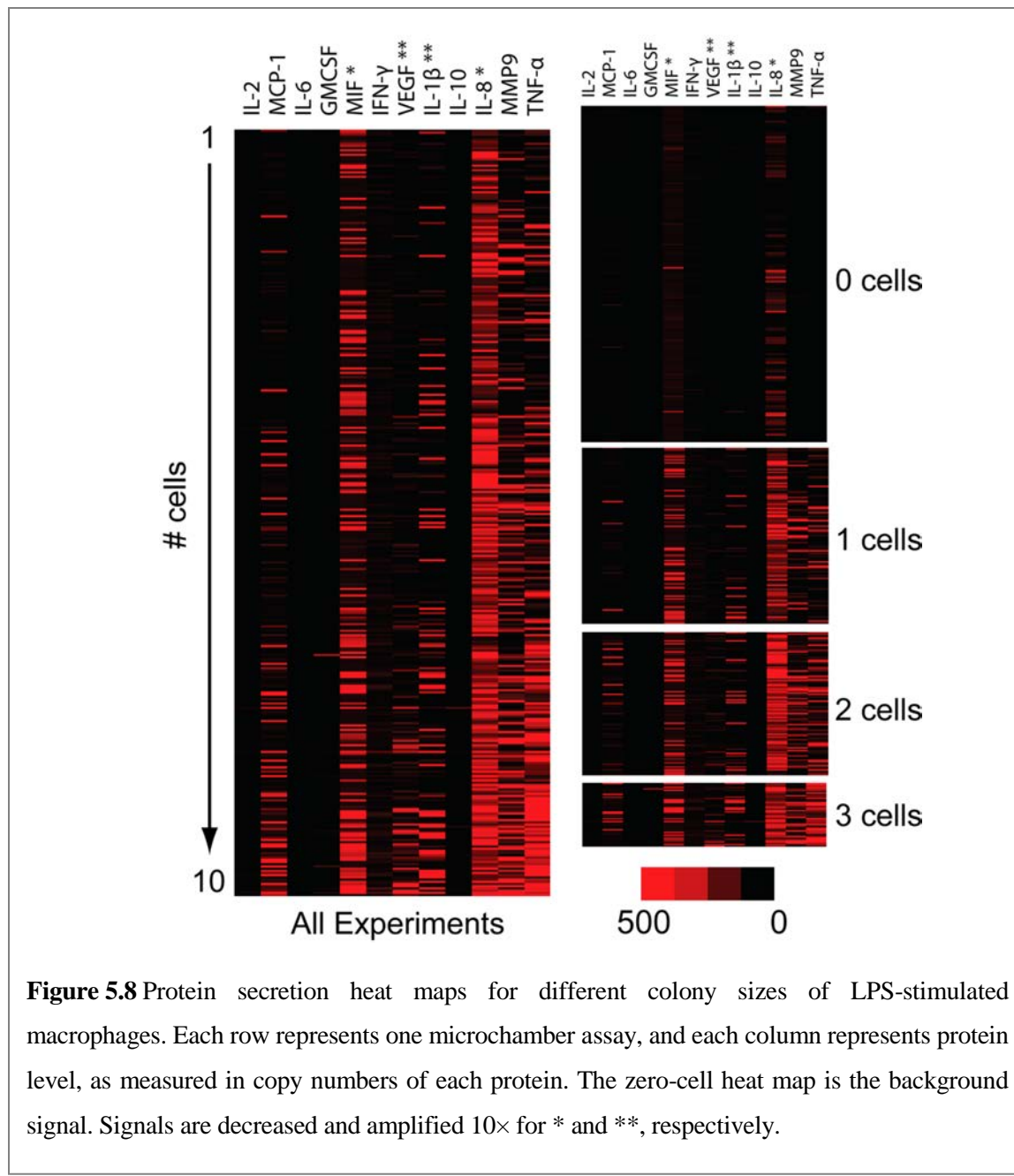


Table 5.4). This quantitative representation of the data is used for the calculations described below. However, the standard proteins may differ from the proteins secreted by the macrophages (for example, glycosylation patterns may vary). Such variations can translate into differences in molecular weight, as well as differences in assay sensitivity.

The experimental results, presented as the number of cells per experiment, are shown in the heat maps of Fig. 5.8, and reveal the transition from single-cell characteristics to bulk behavior (see Fig. 5.4A for protein assay results from large numbers of cells). The experimental methods and results are further discussed in Appendix A: Supplementary Experimental Methods (SI.I).

5.2.2 Theoretical Methods

The Fluctuations in the Secretome. The calibrated experimental data can be organized into digital tables of twelve columns, each representing a different protein, with different tables representing different numbers of cells in the microchamber. For a given table, each row represents the copy numbers of the twelve proteins for a single cell or small cell colony. For a given table, if the number of measurements is large enough we can bin the data for each individual protein into a histogram, with each bin representing a defined range of measured levels (Fig. 5.9). With even more measurements one could generate joint distributions between two proteins, etc. However, we first confine our attention to the individual protein histograms because they provide a natural meeting place for experiment and theory. The theoretical prediction is made by seeking that distribution of copy numbers that is of maximal entropy, meaning that the distribution is as uniform as possible, subject to a given mean number of copies.^{23–26} As discussed in detail in Appendix B: Supplementary Theory Methods (SI.II), we use the distribution of maximal *physical* entropy. This means that at the very global maximum of the entropy, the probabilities of the different proteins are not equal. Rather, as in any multi-component system at thermal equilibrium, each protein will be present in proportion to its partition function,²⁷ where the

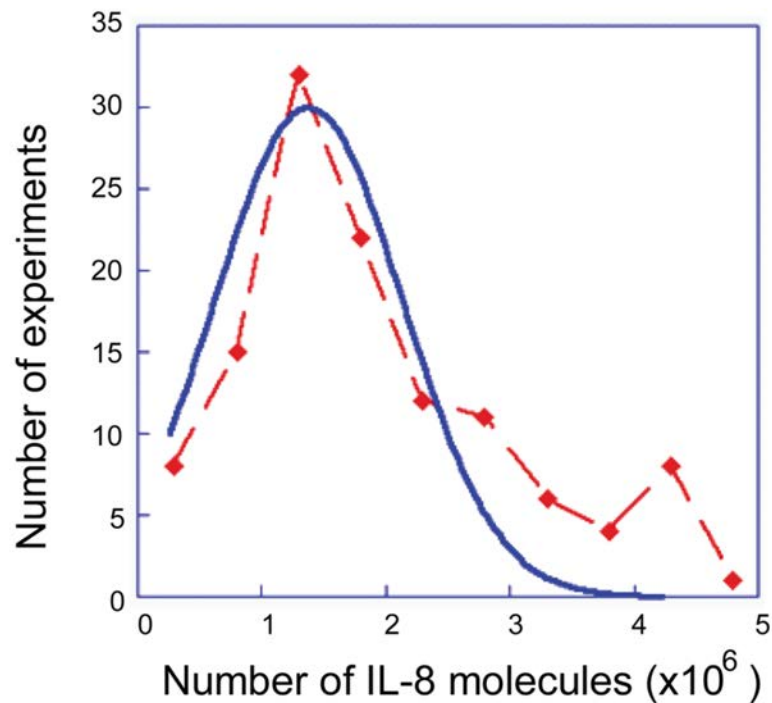


Figure 5.9 Fluctuations in the numbers of secreted IL-8 proteins for all single-cell experiments. The fit to the theoretical distribution is shown as the continuous curve. Even for one cell there can be deviations from the bell-shaped theoretical functional form in the higher tail of the histogram due to autocrine signaling.

partition function is the effective thermodynamic weight of a species at thermal equilibrium. We show below that in our system there is a network structure that imposes (at least) two overriding constraints that preclude the system from being in thermal equilibrium.

The Theoretical Approach. The essence of our approach is to regard the system, a single cell (or a small colony), as not being in an equilibrium state because it is under the action of constraints. When the constraints are present the system is in that state of equilibrium that is possible under the constraints. This allows us to derive a quantitative version of the principle of Le Chatelier. Thereby we can quantitatively predict the response

of the system to a (small) perturbation. Early on, mathematical biologists expressed caution about the application of the Le Chatelier's principle to biological systems.²⁸ It is possible to directly use the measured experimental results to validate our point of view. The qualitative reasoning is straightforward and so we give it here. It is valid to apply the principle of Le Chatelier when the system is in a stable equilibrium. When is the system in a stable equilibrium? when under a small perturbation it returns to its equilibrium state. In Appendix B, we make a quantitative version of this statement. Here we simply state that if the observed fluctuations in protein copy number are about a stable state then we can apply the principle of Le Chatelier. The stability of the state is decided by the experimental measurements. Both the notion of stability and the response to perturbations, as quantified in the principle of Le Chatelier, require that the departure from equilibrium be small. Neither textbook equilibrium thermodynamics applied to a macroscopic system nor the extended theory used here to describe one or a few cells implies that under a 'large' perturbation it should be possible to displace a cell to a new stable state that is distinct from its unperturbed state. For a single cell or small cell colony the experiments reveal that cell-cell perturbations are indeed small. For larger cell colonies the statistics are not secure enough to make a clear-cut statement. We have, however, numerical indications that the unperturbed state of the single cell is possibly unstable in the presence of many other cells.

Theory of Fluctuations. We begin by considering a compartment containing a single cell secreting different proteins. For different compartments the experiment shows a possibly different number of secreted proteins of a given type. We denote the experimentally measured copy number of protein i in a given microchamber by N_i . We

impose the constraints that the distribution for each protein is characterized by the mean number of its molecules. Then the distribution, $P(N_i)$ of copy number fluctuations of a protein i that is of maximal physical entropy (= the distribution at physical equilibrium subject to constraints) is derived in Appendix B, eq. S5.2. It is a bell-shaped function of N_i with a single maximum.

In seeking the maximum of the entropy we require that the energy is conserved. This constraint is imposed by the method discussed in Appendix B. This method introduces parameters into the distribution. β is determined by the constraint of conservation of energy and, as usual, is related to the temperature T as $\beta = 1/kT$, where k is Boltzmann's constant. The μ_i 's are analogs of the chemical potentials as introduced in the thermodynamics of systems of more than one component. Here, however, we are dealing with many replicas of a single cell isolated within a microchamber. Even though we deal with just a single cell, the μ_i 's will be shown in eq. 5.1 below to also play the role of potentials. This means, for example, that the mean copy number \bar{N}_i of protein i increases when its potential μ_i is increased. The mean number, $\bar{N}_i = \sum_i N_i P(N_i)$, is the average computed over the distribution. In operational terms this is an average computed over the different microchamber assays of protein i . We take it that the copy number distribution is normalized, meaning that $\sum_i P(N_i) = 1$.

We next discuss the effect of perturbations on the distribution for a single cell in the compartment. The regime of small perturbations is one in which the distribution, although perhaps distorted from a simple bell-shaped curve, still exhibits only a single maximum.

The signature of large perturbations is that secondary maxima appear. When these become dominant, a new state of the cell is prevailing.

To theoretically characterize the response of the cellular secretion to a perturbation we compute first the change in the distribution for the special case in which a perturbation changes the potential of protein i from μ_i to $\mu_i + \delta\mu_i$, where $\delta\mu_i$ is a small increment. We show (eq. S5.2 in Appendix B, Section 5.7.3) that, to first order in the change of the potential, the distribution changes by $\delta P(N_i) = \beta(\bar{N}_i - N_i)P(N_i)\delta\mu_i$. The result for δP has two immediate implications. One is that a perturbation will distort the shape of the distribution of the copy numbers of a given protein. Specifically, the change is proportional to the unperturbed distribution but its magnitude is weighted by the factor $(\bar{N}_i - N_i)$ so as to favor higher values of protein numbers. Thus, it is the high-end tail of the distribution that is most strongly influenced by the perturbation (see Fig. 5.9, for example).

The other immediate implication of the change in the distribution is that the mean values will change. Specifically the updated mean value of the copy number of protein i , when we change from μ_i to $\mu_i + \delta\mu_i$, is $\bar{N}_i + \delta\bar{N}_i = \sum_i N_i [P(N_i) + \delta P(N_i)]$. A technical point is that because the distribution needs to be normalized we must have $\sum_i \delta P(N_i) = 0$. Using the result above, that the change $\delta P(N_i)$ in the distribution is proportional to the unperturbed distribution and the normalization, we arrive at the explicit result for the change in the mean copy number under a small disturbance.

$$\delta\bar{N}_i = \sum_i N_i \delta P(N_i) = \beta \delta\mu_i \sum_i N_i (\bar{N}_i - N_i) P(N_i) = \beta \delta\mu_i \overline{(\bar{N}_i - N_i)^2} \quad (5.1)$$

This equality states that because the variance is positive, a change in the mean copy number of protein i when its own potential is changed from μ_i to $\mu_i + \delta\mu_i$ is always in the

same direction (positive or negative) as $\delta\mu_i$ itself. It is in this sense that we refer to μ_i as the potential of protein i .

The key point that carries into the general case, is that, to linear order in the perturbation, the change in the mean number of proteins due to a perturbation can be computed as an average over the unperturbed distribution of copy numbers. The change in the mean is the variance of the distribution of fluctuations. Therefore, the lesser the fluctuations (i.e., the narrower the histogram), the more resilient to change is the distribution. As an example, IL-8 (Fig. 5.9) will be shown below to be a very strongly coupled protein. IL-8 also has a particularly large variance as compared to the other proteins. Therefore there is some perturbation via autocrine signaling, as seen in the hump in the higher tail of the histogram.

A Quantitative Le Chatelier Equation. With good measurement statistics one can examine the histogram for a joint distribution of two proteins and verify that pairs of proteins are correlated. Therefore the mean value (and other averages) of a protein i will change when protein j is perturbed. In the linear regime the result (see Appendix B, section 5.7.4) is

$$\delta\bar{N}_i = \beta\sum_j \left[\overline{(\bar{N}_i - N_i)(\bar{N}_j - N_j)} \right] \delta\mu_j \quad (5.2)$$

where the covariance is computed over the unperturbed distribution. eq. 5.2 is valid in the linear regime of small perturbations, and indicates that the contributions of different perturbations add up. The covariance matrix Σ , whose elements are

$\Sigma_{ij} = \overline{(N_j - \bar{N}_j)(N_i - \bar{N}_i)}$, is what is called in matrix algebra a positive matrix.²⁹ The implications of positivity are explored in Section 5.7.5.

We prove in Section 5.7.4 that eq. 5.2 is a quantitative statement of the principle of Le Chatelier in the sense that a response to a perturbation changes the system in the direction of restoring a stable equilibrium. This is the analogue of the observation that when we add energy (i.e., heat the system) the temperature goes up (rather than down). By equilibrium we mean a state of maximal entropy subject to the current value of all the constraints operating on the system. A system can therefore be maintained at equilibrium by imposing constraints such as keeping a gas under higher pressure at a fraction of the available volume of a cylinder. When these constraints are changed the system can move to a new equilibrium.

The covariance matrix is used in statistics as input in such methods of data analysis as principal component analysis.^{30, 31} We emphasize that for us the covariance matrix is derived by physical considerations leading to eq. 5.2. We can thereby state that Σ_{ij} is quantitatively the change in the number of copies of protein i when protein j is perturbed. Note that while the covariance is a positive matrix, individual off-diagonal elements can be negative, signifying inhibition. The covariance matrix in digital form is provided in Appendix C (Table 5.8).

To summarize, the result for the distribution of protein copy numbers for the strongly interacting protein IL-8 (Fig. 5.9) has just one maximum. The noticeable deviations in the tail of the distribution are likely due to autocrine signaling, because the correlation of IL-8 with itself is only comparable in magnitude to the correlation of MIF with itself. Those two correlations are larger than any other variance or covariance. As discussed below, IL-8

is also strongly correlated with other proteins. For $n \geq 3$ cells in the microchamber, there is numerical evidence for a second maximum in the distribution of IL-8 fluctuations. For other proteins, six or more cells per chamber are required before a second maximum is resolved.

We can draw two conclusions from the fit of Fig. 5.9, between observed fluctuations and the theoretical result. First, the experimental distribution has but one maximum, and so the state is stable. Second, the theory accounts for the shape of the experimental distribution. This implies that we have correctly identified the important constraints on the system. Therefore we have Eq. 5.1 for the change of the distribution and eq. 5.2 as the quantitative statement of the Le Chatelier's theorem. If there are additional constraints one can still derive a quantitative Le Chatelier's theorem, but there will be additional terms beyond those shown explicitly in eq. 5.2. We reiterate that eq. 5.2 is the covariance computed from the experiments for an unperturbed cell. In our work below we use eq. 5.2 to predict the effect of perturbation (see Fig. 5.14 in particular).

5.3 Results and Discussion

5.3.1 Computing the covariance matrix

The single-cell data (the heat map of Fig. 5.8) can be regarded as a rectangular matrix \mathbf{X} where each row is a separate measurement and each column contains the copy number of a particular protein. For our convenience we mean center each column. When the number of measurements (= number of rows of \mathbf{X}) is not small (and is \geq than the number of columns) the covariance matrix can be immediately computed as $\Sigma_{ij} = \sum_{k=1}^K X_{ki}X_{kj}/K$

where k runs over all measurements, $k = 1, 2, \dots, K$. By construction of the matrix \mathbf{X} , the matrix element X_{ki} is the number recorded in the k th measurement for protein i minus the mean number \bar{N}_i for that protein. We divide $\mathbf{X}^T \mathbf{X}$ by the number, K , of measurements so that the covariance is the mean value. The covariance is a product of the measured numbers, so the coefficient of variation of the covariance is, for small variations, twice the coefficient of variation of the measurements. An upper estimate, see Table 5.7 and Fig. 5.7, is 14% when the covariance is computed from the fluorescence intensities. The conversion from the fluorescence intensity to the number of molecules does not change the coefficient of variation when we are in the linear regime of the calibration curve (see Fig. 5.3). However at very low or high intensities the calibration curve is non-linear, so that small changes in fluorescence intensity are amplified to larger differences in the number of molecules, and thus large values of the variance. Out of $K = 129$ single-cell experiments, we therefore eliminated four outliers. These corresponded to one instance each for which the fluorescence levels of TNF- α , IL-1 β , MIF, or IL-6 were very high. We thus used $K = 125$ values to compute the covariance matrix. The elimination of these four outliers brings the error of reading the number of molecules to be more comparable to the error in reading the fluorescence intensity.

5.3.2 The network

We analyze the covariance matrix in two stages. The first stage yields a quick (but correct and reliable) ‘global’ summary of the network, meaning which protein is coupled with which other proteins. There is finer structure, discussed below, that is not resolved in this first stage. To obtain the global network we begin by noting that the covariance matrix

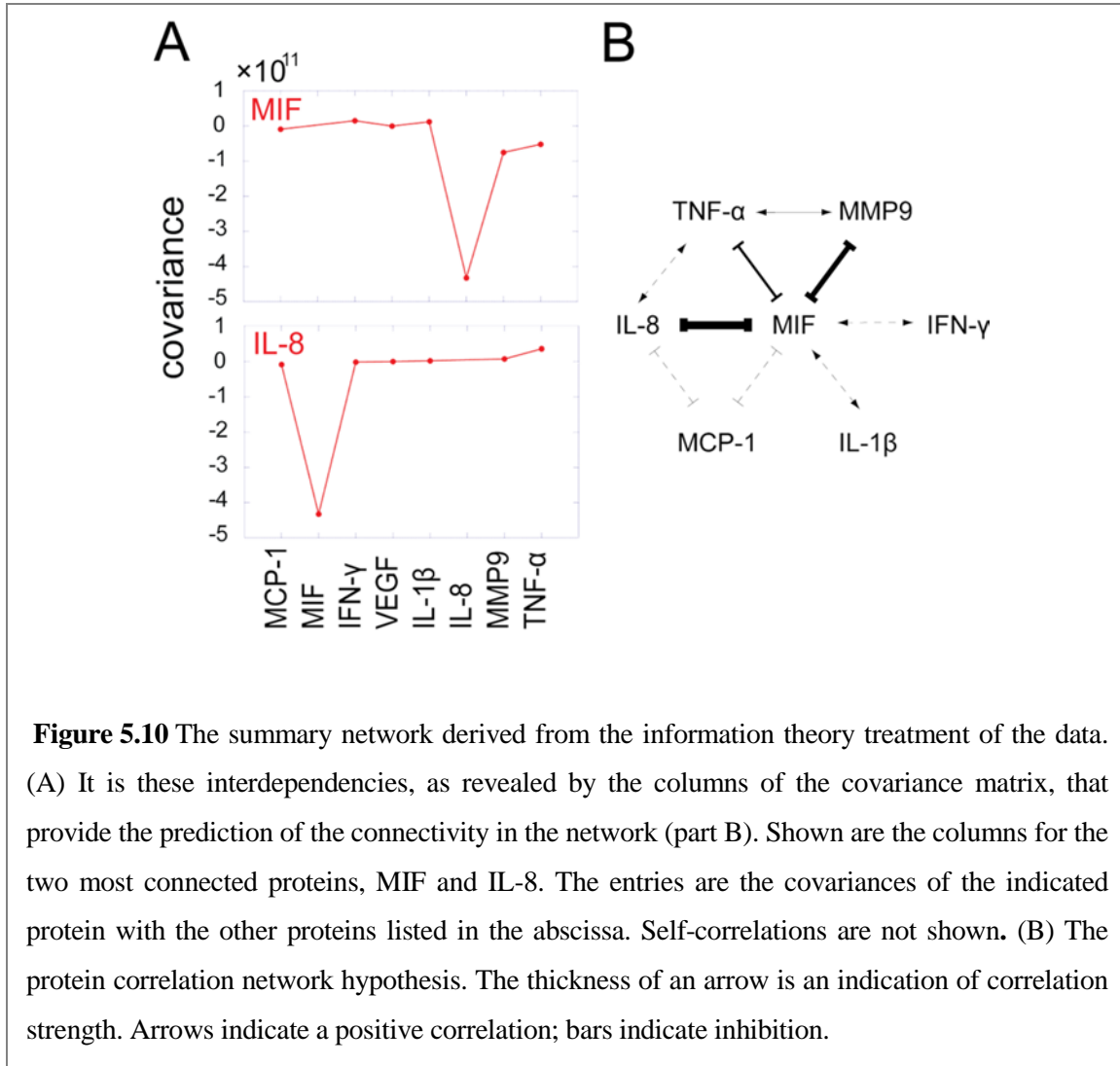
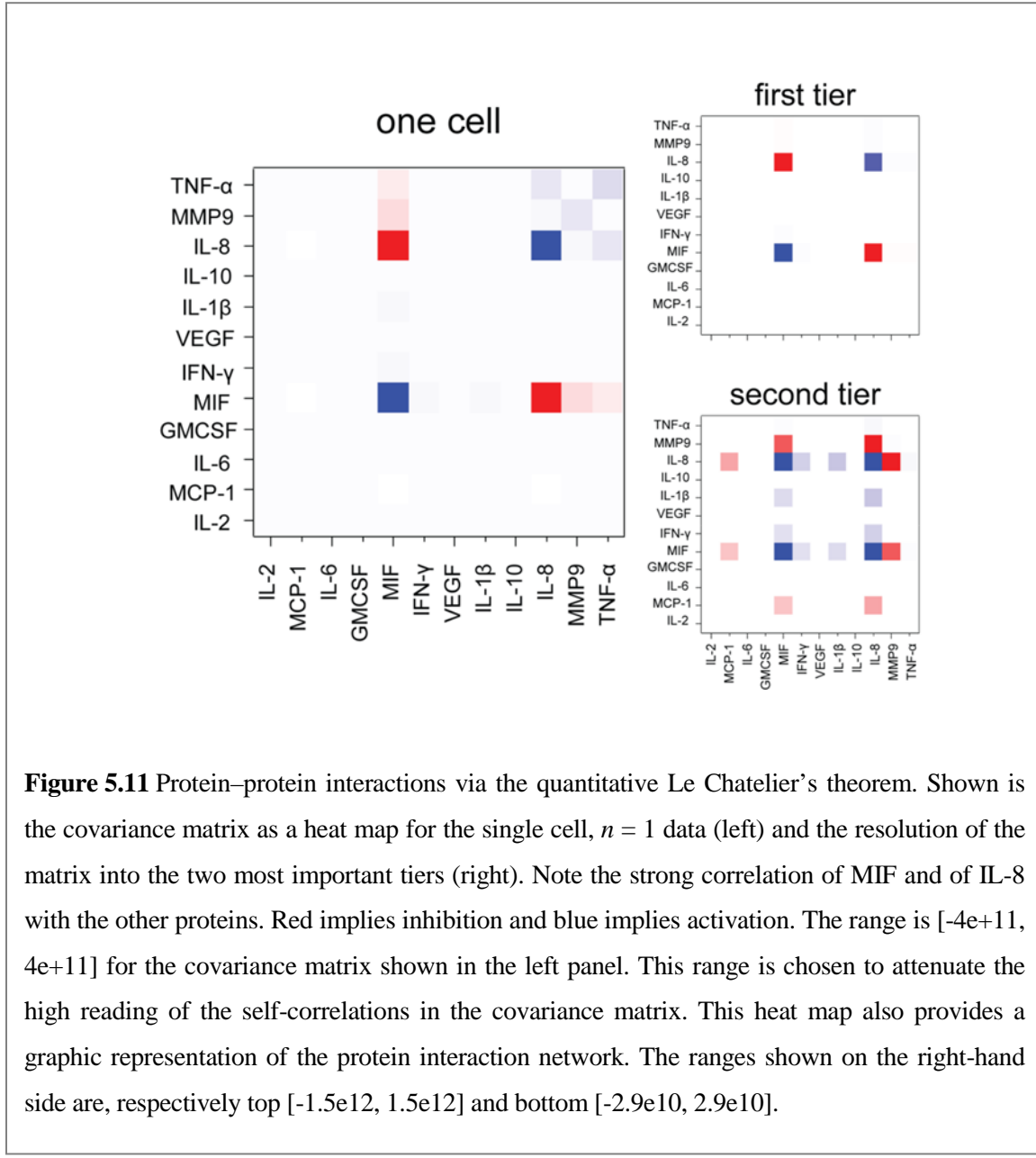


Figure 5.10 The summary network derived from the information theory treatment of the data. (A) It is these interdependencies, as revealed by the columns of the covariance matrix, that provide the prediction of the connectivity in the network (part B). Shown are the columns for the two most connected proteins, MIF and IL-8. The entries are the covariances of the indicated protein with the other proteins listed in the abscissa. Self-correlations are not shown. (B) The protein correlation network hypothesis. The thickness of an arrow is an indication of correlation strength. Arrows indicate a positive correlation; bars indicate inhibition.

is symmetrical, so that protein i is correlated with protein j just as much as protein j is correlated with protein i , $\Sigma_{ij} = \Sigma_{ji}$. This means that although both positive and inhibitory couplings can be extracted from the network, the direction of those couplings (i.e., protein i inhibits protein j , rather than vice-versa) is not resolved. The results for the overall network are shown in Fig. 5.10. Panel A is the raw data for plotting the network and panel B is the network itself. The protein most strongly coupled to all others is MIF, and it is primarily anti-correlated with the other proteins. Next in strength of coupling is IL-8. Note that the symmetry between any two proteins is limited; proteins 1 and 2 may be coupled to each



other, but protein 1 may be coupled to protein 3, while proteins 2 and 3 are uncorrelated.

Mathematically this is possible because the total coupling strength of protein i , sum of Σ_{ij}

over all j , can be quite different from the total coupling strength of protein j that is given as the sum of Σ_{ji} over all possible proteins i .

The covariance matrix shows the quantitative extent to which the fluctuations in any two proteins i and j are covarying. As discussed, about 14% of the value is due to noise. In

the network we want to compare the relative importance of the covariance of proteins i and j to the covariance of proteins l and m . We take it that the covariance of proteins l and m should not be regarded as comparable to the covariance of i and j when the measured covariance of l and m is below the uncertainty due to noise of the covariance of i and j . We construct a graphical global summary of the interaction network by retaining only those proteins that are covarying with one or more other proteins above the noise level of the highest covarying pair of proteins. Below we discuss the components of the covariance matrix. Thereby we will have a measure of uncertainty for the entire matrix. It turns out that the criterion we use above is consistent with this measure.

The largest covariance, 4×10^{11} is between MIF and IL-8. This sets a boundary of 6×10^{10} on the covariances of pairs that we show as connected in the network. The large and positive magnitude of the covariance of MIF and IL-8 is shown as a double-headed arrow. The arrow is double headed to denote the joint activation of one by the other. In the diagram, inhibition is indicated, as usual, by a bar at the end of the connector. The dashed line correlations of MIF with IFN- γ are of magnitude 2×10^{10} , and so may be corrupted by noise. The dashed line correlations between MIF and both MCP-1 and IL-1 β are even weaker (about 10^{10}). The more refined analysis presented in Fig. 5.11 shows, however, that these two correlations are likely real and above the noise level.

Macrophages are an important source of IL-8 and MIF,^{32–34} and IL-8 is secreted by the macrophages without LPS stimulation, while MIF is secreted upon LPS stimulation (Fig. 5.4A). Our derived network model indicates the MIF is inhibited by IL-8, and MIF, in turn, inhibits three other proteins, including TNF- α , while it promotes the production of IL-1 β . These predictions are consistent with the time-dependent measurements of secreted

proteins (Fig. 5.4B). From those measurements, we find that the levels of three proteins (MIF, TNF- α , and IL-1 β) that are secreted upon LPS stimulation, exhibit fluctuations over time. The MIF and TNF- α temporal fluctuations are anti-correlated, consistent with the network hypothesis. A detailed elucidation of the underlying mechanism for these dynamics will require additional experiments. However, it is encouraging that a network hypothesis derived from single-time-point, single-cell data does provide consistent insight into the dynamical responses of the macrophages to stimulation.

5.3.3 The composite networks

In the second stage in our analysis of the covariance matrix we aim to show a more resolved structure and thereby note features that are glossed over in the global network of Fig. 5.10B. We will show that there are several independent networks operating together to globally represent Fig. 5.10B. The detailed analysis also provides a more robust error estimate. To resolve independent inherent structures within the covariance matrix we consider what is known in matrix algebra as the spectral representation (See Section 5.7.6 and 5.7.7 for more details). Technically this is a ranking of the eigenvectors as also carried out in principal component analysis. We suggest, however, that for our system specifically this ranking allows an examination of tiers in the cell–cell signaling. The tiers are independent, meaning that they govern independent fluctuations. The proteins that are members of a given tier respond collectively to a perturbation.

The spectral theorem ²⁹ allows us to rank the contributions according to the decreasing magnitude of the eigenvalues. At the bottom are the smallest eigenvalues and these are attributed to experimental noise rather than to real biological information. For the single

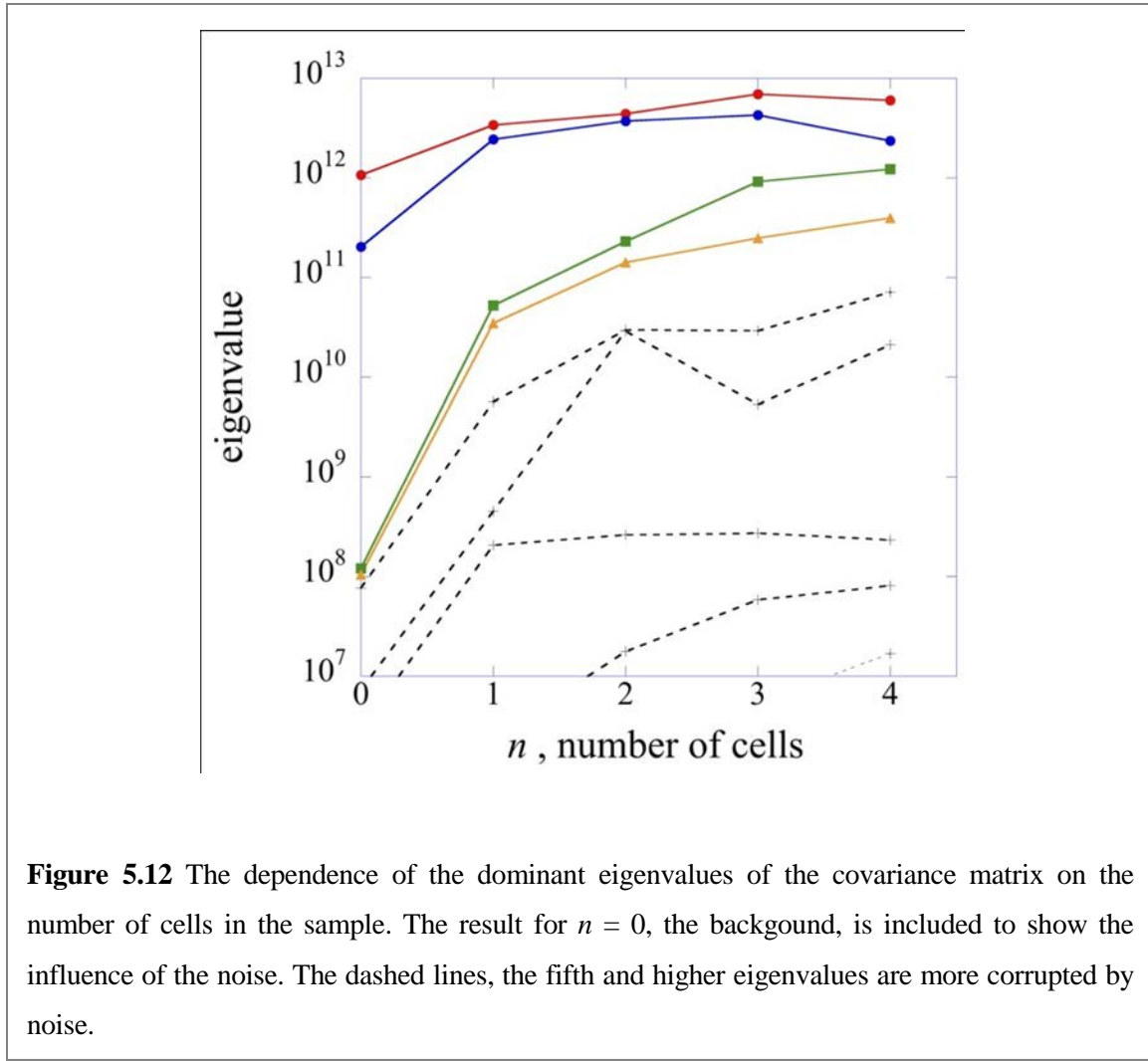


Figure 5.12 The dependence of the dominant eigenvalues of the covariance matrix on the number of cells in the sample. The result for $n = 0$, the background, is included to show the influence of the noise. The dashed lines, the fifth and higher eigenvalues are more corrupted by noise.

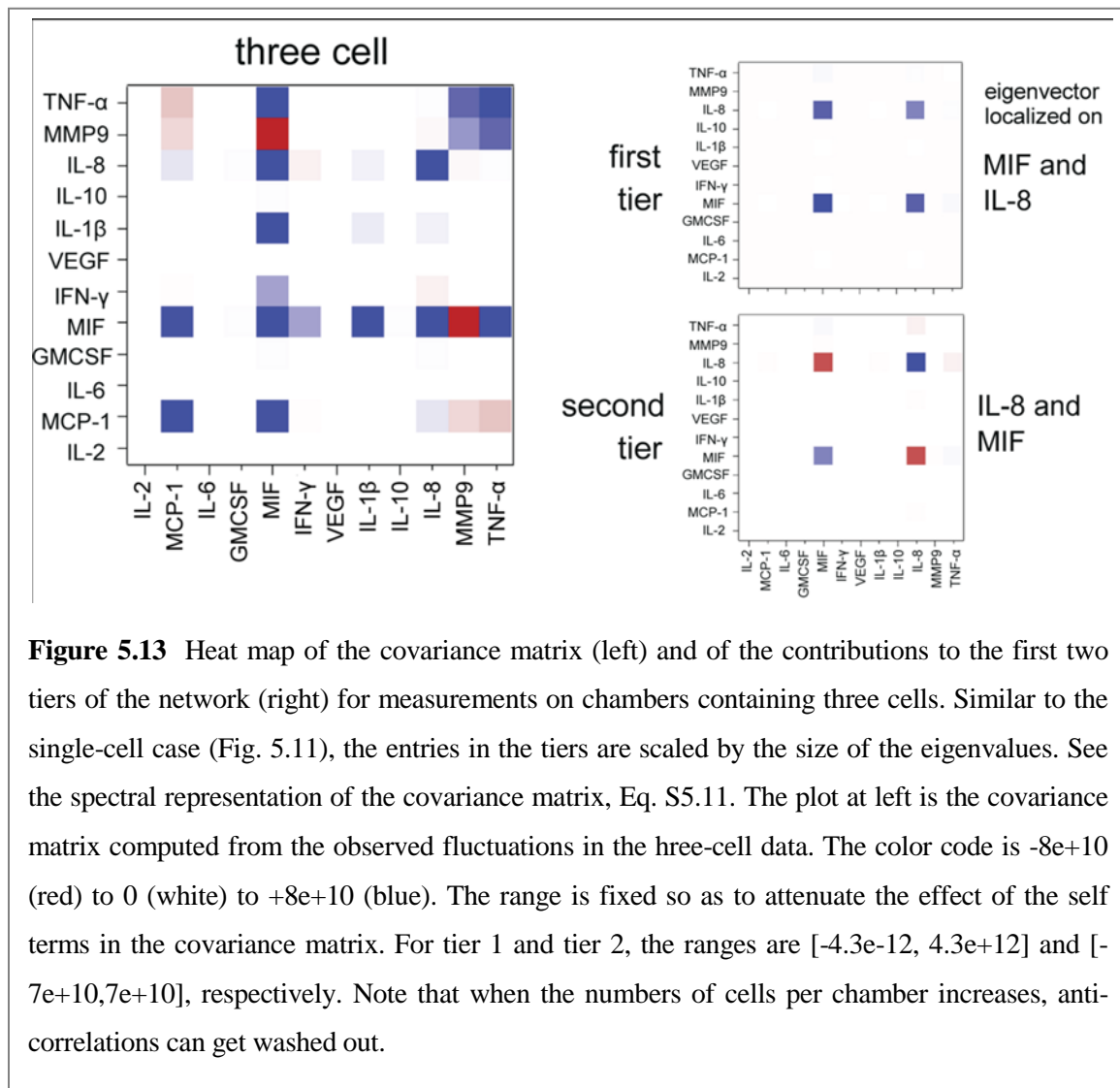
cell in the compartment we find, as expected for the linear regime, that the dominant eigenvectors are each localized around a particular protein. As shown in Fig. 5.11, the two largest are localized on MIF and IL-8. The leading eigenvalue = tier 1, is only about 30% bigger than the second one, $m = 2$. The third eigenvalue (not shown) is smaller by almost two orders of magnitude. Fig. 5.12 is a plot on a logarithmic scale of all non-zero eigenvalues. There are only two eigenvectors that, judging by the value of their corresponding eigenvalues, are definitely above the noise.

In drawing Fig. 5.10B we could not state definitely that the correlations of MIF with IFN- γ , MCP-1, and IL-1 β , are above the noise level. The more refined spectral analysis

shows that all these correlations are clearly evident in the second tier (Fig. 5.11) and so are secure. The Fig. 5.11 results are the fluctuations measured for single-cell experiments. (See Fig. 5.13 for similar results but for $n = 3$ cells per microchamber).

5.3.4 The number-based network

The network presented in Figs. 5.10 and 5.11 is based upon experimental measurements in which raw fluorescence intensities are converted into numbers of molecules. We do this conversion because it is the numbers of molecules that are secreted



by the cells, or to which the cells respond, that ultimately reflects the true biology. However, this conversion seemingly introduces an additional source of noise, especially when the measured fluorescence intensity is away from the linear regime of the calibration curves. However, this conversion yields an accurate reflection of the true measurements, and the accruing benefit is worthwhile. Specifically, the number of secreted proteins is independent of the very complicated experimental response function that depends upon the fluorescence detection methods, the various capture and detection antibodies used, and the fluorescence vs. concentration profiles that characterize calibration assays. We are thus able to apply the fundamental theory to quantitative molecular measurements, and so the resultant network is a more secure representation of the true cell biology, even if the accompanying experimental uncertainties are large relative to what would be estimated from pure fluorescence measurements.

Antibody Perturbations. We performed an inter-cellular signaling perturbation study by adding neutralizing antibodies to eliminate specific secreted cytokines. For these experiments, four groups of microchambers within each SCBC chip were operated independently. Three neutralizing antibodies (anti-VEGF, anti-IL-8, and anti-TNF- α) were added to the cells, with one antibody per microchamber group. A control experiment was performed without any neutralizing antibody. As shown in Fig. 5.14, the removal of IL-8 markedly increased the production of MIF, slightly increased IL-1 β , and slightly decreased TNF- α . The results are in agreement with the network hypothesis, Fig. 5.10B.

Using the theorem of Le Chatelier we quantitatively predict the effect of the antibody perturbations using eq. 5.2. Here, the input for the prediction is the covariance matrix for

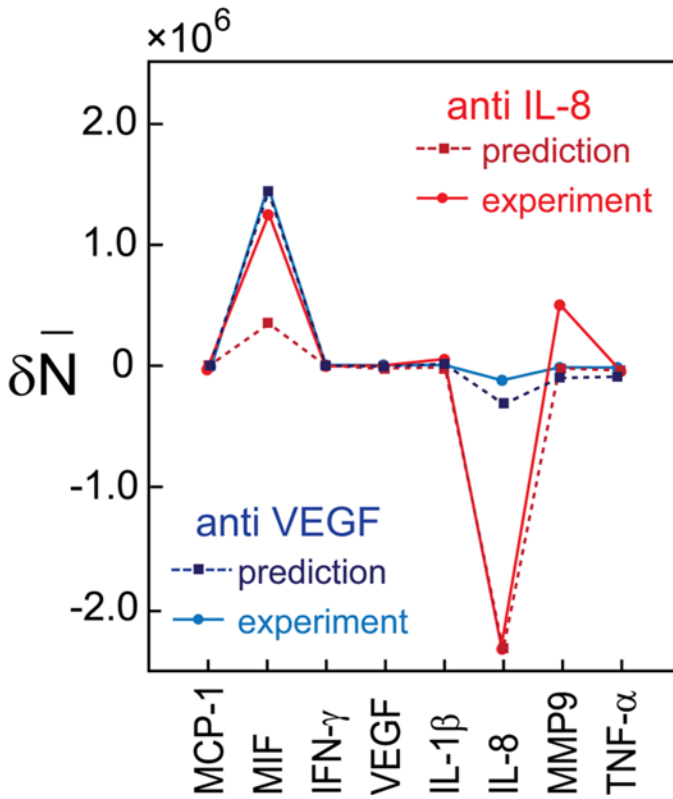


Figure 5.14 Perturbation of protein networks using neutralizing antibodies. The measured change in the mean number of eight proteins is compared against the predicted change, as computed from the fluctuations observed in the unperturbed single-cell data.

the unperturbed cells. To compute the predicted mean number of protein i after an antibody for protein j is applied we need to know the change in chemical potential of protein j . We take it that an antibody for a protein lowers its chemical potential. We determine the magnitude of that reduction by requiring that the decrease in the copy number of the directly perturbed protein is reproduced. Additional details are provided in section 5.7.9. The quality of the prediction in the perturbation experiments of IL-8 and VEGF is excellent, as shown in Fig. 5.14. The prediction of the results for the perturbation by anti-TNF- α is not in accord, likely because the change in the mean copy number of the proteins is smaller by about an order of magnitude, and so is close to the noise level.

5.4 Conclusions

The multiplexed measurements of secreted proteins by single cells and defined, few-cell colonies provide a unique opportunity to capture the fluctuations of individual cells. An information theoretic, maximal entropy analysis can be applied to reproduce the observed fluctuations in the levels of the different assayed proteins. The theoretical analysis can also account for why for some proteins exhibit broad fluctuations, while others exhibit narrow fluctuations. The experimental approach permits observations of the covariance in the fluctuations of different proteins, and how those fluctuations evolve as a single cell is perturbed by the presence of 1, 2, 3, etc., other cells. Again, with the information theory, these covariances can be analyzed to extract hypotheses about the network of interacting proteins. Measuring the role of antibodies for specific proteins provides a test of that network hypothesis, and demonstrates that the theory is able to quantitatively *predict* the results of the molecular perturbation experiments using only data obtained for the unperturbed cells. This demonstration of the Le Chatelier's principle appears to be general, and we are currently exploring how it can be applied towards understanding the role of other perturbations (such as hypoxia, genetic modifications, etc.). The long-term goal is to extend this approach towards understanding the various protein-signaling networks that operate within complex microenvironments, such as tumors.

5.5 References

1. Lin, W. W.; Karin, M., A cytokine-mediated link between innate immunity, inflammation, and cancer. *Journal of Clinical Investigation* **2007**, 117, (5), 1175–1183.
2. Gnechi, M.; He, H. M.; Liang, O. D.; Melo, L. G.; Morello, F.; Mu, H.; Noiseux, N.; Zhang, L. N.; Pratt, R. E.; Ingwall, J. S.; Dzau, V. J., Paracrine action accounts for marked protection of ischemic heart by Akt-modified mesenchymal stem cells. *Nature Medicine* **2005**, 11, (4), 367–368.
3. Croci, D. O.; Fluck, M. F. Z.; Rico, M. J.; Matar, P.; Rabinovich, G. A.; Scharovsky, O. G., Dynamic cross-talk between tumor and immune cells in orchestrating the immunosuppressive network at the tumor microenvironment. *Cancer Immunology Immunotherapy* **2007**, 56, (11), 1687–1700.
4. Seruga, B.; Zhang, H. B.; Bernstein, L. J.; Tannock, I. F., Cytokines and their relationship to the symptoms and outcome of cancer. *Nature Reviews Cancer* **2008**, 8, (11), 887–899.
5. Polyak, K.; Weinberg, R. A., Transitions between epithelial and mesenchymal states: acquisition of malignant and stem cell traits. *Nature Reviews Cancer* **2009**, 9, (4), 265–273.
6. Ariztia, E. V.; Lee, C. J.; Gogoi, R.; Fishman, D. A., The tumor microenvironment: Key to early detection. *Critical Reviews in Clinical Laboratory Sciences* **2006**, 43, (5–6), 393–425.

7. Sachs, K.; Perez, O.; Pe'er, D.; Lauffenburger, D. A.; Nolan, G. P., Causal protein-signaling networks derived from multiparameter single-cell data. *Science* **2005**, 308, (5721), 523–529.
8. Nomura, L.; Maino, V. C.; Maecker, H. T., Standardization and Optimization of Multiparameter Intracellular Cytokine Staining. *Cytometry Part A* **2008**, 73A, (11), 984–991.
9. Lamoreaux, L.; Roederer, M.; Koup, R., Intracellular cytokine optimization and standard operating procedure. *Nature Protocols* **2006**, 1, (3), 1507–1516.
10. Cox, J. H.; Ferrari, G.; Janetzki, S., Measurement of cytokine release at the single cell level using the ELISPOT assay. *Methods* **2006**, 38, (4), 274–282.
11. Nguyen, D. T.; Deforge, L. E.; Malak, T. A.; Remick, D. G., PGE2 Suppression of TNF α , IL-1, IL-6, and IL-8 in LPS-stimulated THP-1 cells. *Faseb Journal* **1992**, 6, (5), A1897–A1897.
12. Song, M. C.; Phelps, D. S., Comparison of SP-A and LPS effects on the THP-1 monocytic cell line. *American Journal of Physiology—Lung Cellular and Molecular Physiology* **2000**, 279, (1), L110–L117.
13. Quake, S. R.; Scherer, A., From micro- to nanofabrication with soft materials. *Science* **2000**, 290, (5496), 1536–1540.
14. Shin, Y. S.; Ahmad, H.; Shi, Q.; Kim, H.; Pascal, T. A.; Fan, R.; Goddard, W. A., 3rd; Heath, J. R., Chemistries for patterning robust DNA microbarcodes enable multiplex assays of cytoplasm proteins from single cancer cells. *Chemphyschem* **2010**, 11, (14), 3063–3069.

15. Bailey, R. C.; Kwong, G. A.; Radu, C. G.; Witte, O. N.; Heath, J. R., DNA-encoded antibody libraries: A unified platform for multiplexed cell sorting and detection of genes and proteins. *Journal of the American Chemical Society* **2007**, 129, (7), 1959–1967.
16. Wacker, R.; Niemeyer, C. M., DDI-mu FIA—A readily configurable microarray-fluorescence immunoassay based on DNA-directed immobilization of proteins. *Chembiochem* **2004**, 5, (4), 453–59.
17. Aderem, A.; Ulevitch, R. J., Toll-like receptors in the induction of the innate immune response. *Nature* **2000**, 406, (6797), 782–787.
18. Fan, J.; Malik, A. B., Toll-like receptor-4 (TLR4) signaling augments chemokine-induced neutrophil migration by modulating cell surface expression of chemokine receptors. *Nature Medicine* **2003**, 9, (3), 315–321.
19. Millet, L. J.; Stewart, M. E.; Sweedler, J. V.; Nuzzo, R. G.; Gillette, M. U., Microfluidic devices for culturing primary mammalian neurons at low densities. *Lab on a Chip* **2007**, 7, (8), 987–994.
20. Altschuler, S. J.; Wu, L. F., Cellular heterogeneity: do differences make a difference? *Cell* **2010**, 141, (4), 559–63.
21. Wang, J.; Ahmad, H.; Ma, C.; Shi, Q.; Vermesh, O.; Vermesh, U.; Heath, J., A self-powered, one-step chip for rapid, quantitative and multiplexed detection of proteins from pinpricks of whole blood. *Lab on a Chip* **2010**, 10, (22), 3157–62.
22. Findlay, J. W.; Dillard, R. F., Appropriate calibration curve fitting in ligand binding assays. *AAPS J* **2007**, 9, (2), E260–E267.
23. Levine, R. D., Information Theory Approach to Molecular Reaction Dynamics. *Annual Review of Physical Chemistry* **1978**, 29, 59.

24. Levine, R. D., Information Theoretical Approach to Inversion Problems. *Journal of Physics A—Mathematical and General* **1980**, 13, (1), 91–108.
25. Remacle, F.; Levine, R. D., The Elimination of Redundant Constraints in Surprisal Analysis of Unimolecular Dissociation and Other Endothermic Processes. *Journal of Physical Chemistry A* **2009**, 113, (16), 4658–4664.
26. Jaynes, E. T., *Probability Theory: The Logic of Science*. Cambridge University Press: Cambridge, 2004.
27. Mayer, J. E.; Mayer, M. G., *Statistical mechanics*. Wiley: New York, 1966.
28. Lotka, A. J., Note on Moving Equilibra. *Proceedings of the National Academy of Sciences of the United States of America* **1921**, 7, (6), 168–172.
29. Bellman, R., *Introduction to Matrix Analysis*. McGraw-Hill: New York, **1970**.
30. Wall, M. E.; Rechtsteiner, A.; Rochas, L. M., Singular value decomposition and principal component analysis. In *A Practical Approach to Microarray Data Analysis*, Berrar, D. P.; Dubitzky, W.; Granzow, M., Eds. Kluwer: Norwell, 2003; pp 91-109.
31. Jolliffe, I. T., *Principal Component Analysis*. Springer: New York, 2002.
32. Roger, T.; David, J.; Glauser, M. P.; Calandra, T., MIF regulates innate immune responses through modulation of Toll-like receptor 4. *Nature* **2001**, 414, (6866), 920–924.
33. Calandra, T.; Bernhagen, J.; Mitchell, R. A.; Bucala, R., Macrophage Is an Important and Previously Unrecognized Source of Macrophage-Migration Inhibitory Factor. *Journal of Experimental Medicine* **1994**, 179, (6), 1895–1902.
34. Janeway, C.; Murphy, K. P.; Travers, P.; Walport, M., *Janeway's immuno biology*. Garland Science: New York, **2008**.

35. Fan, R.; Vermesh, O.; Srivastava, A.; Yen, B. K. H.; Qin, L. D.; Ahmad, H.; Kwong, G. A.; Liu, C. C.; Gould, J.; Hood, L.; Heath, J. R., Integrated barcode chips for rapid, multiplexed analysis of proteins in microliter quantities of blood. *Nature Biotechnology* **2008**, *26*, (12), 1373–1378.
36. Lee, J. N.; Park, C.; Whitesides, G. M., Solvent compatibility of poly(dimethylsiloxane)-based microfluidic devices. *Analytical Chemistry* **2003**, *75*, (23), 6544–6554.
37. Levine, R. D., How large is 'large' for a thermodynamic-like behavior. *Physica E* **2001**, *9*, (3), 591–599.
38. Callen, H. B., *Thermodynamics and an Introduction to Thermostatics*. Wiley: NY, **1985**.
39. Alhassid, Y.; Levine, R. D., Experimental and Inherent Uncertainties in the Information Theoretic Approach. *Chemical Physics Letters* **1980**, *73*, (1), 16–20.
40. Han, Q.; Bradshaw, E. M.; Nilsson, B.; Hafler, D. A.; Love, J. C., Multidimensional analysis of the frequencies and rates of cytokine secretion from single cells by quantitative microengraving. *Lab on a Chip* **2010**, *10*, (11), 1391–1400.

5.6 Appendix A: Supplementary Experimental Methods (SI.I)

5.6.1 Experimental procedure

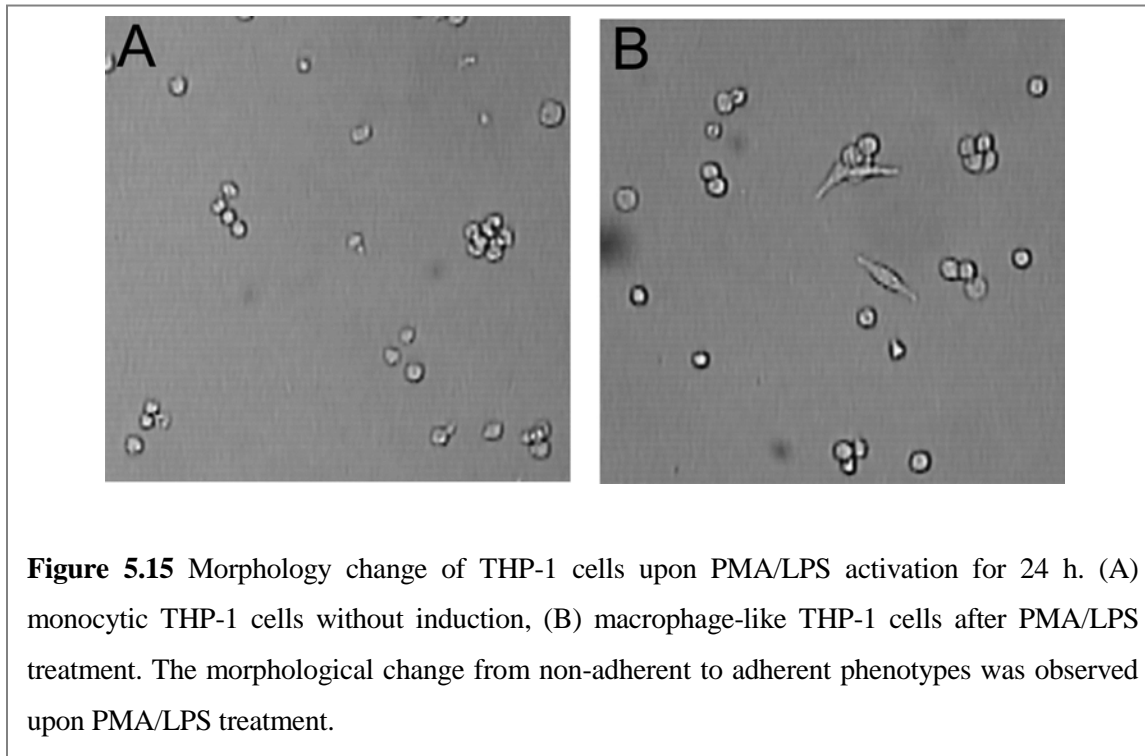
Microchip Fabrication. The SCBCs were assembled from a DNA barcode microarray glass slide and a PDMS slab containing a microfluidic circuit.^{14, 35} The DNA barcode array was created with microchannel-guided flow patterning technique.¹⁴ Each barcode was

comprised of thirteen stripes of uniquely designed ssDNA molecules. The PDMS microfluidic chip was fabricated using a two-layer soft lithography approach.¹³ The control layer was molded from a SU8 2010 negative photoresist (~ 20 μm in thickness) silicon master using a mixture of GE RTV 615 PDMS prepolymer part A and part B (5:1). The flow layer was fabricated by spin-casting the pre-polymer of GE RTV 615 PDMS part A and part B (20:1) onto a SPR 220 positive photoresist master at ~ 2000 rpm for 1 min. The SPR 220 mold was ~ 18 μm in height after rounding via thermal treatment. The control layer PDMS chip was then carefully aligned and placed onto the flow layer, which was still situated on its silicon master mold, and an additional 60 min thermal treatment at 80°C was performed to enable bonding. Afterward, this two-layer PDMS chip was cut off and access holes drilled. In order to improve the biocompatibility of PDMS, we performed a solvent extraction step, which removes uncrosslinked oligomers, solvent, and residues of the curing agent through serial extractions/washes of PDMS with several solvents.^{19, 36} We noticed that this step significantly improves the biocompatibility and the reproducible protein detection. Finally, the microfluidic-containing PDMS slab was thermally bonded onto the barcode-patterned glass slide to give a fully assembled microchip.

Barcode Arrays. The barcode array initially consists of 13 uniquely designed DNA strands labeled in order as A through M. Prior to loading cells, a cocktail containing all capture antibodies conjugated to different complementary DNA strands (A'-L') is flowed through the chambers, thus transforming, via DNA-hybridization, the DNA barcode into an antibody array. These dozen proteins that comprised the panel used here were encoded by the DNA strands A through L, respectively. Calibration and cross reactivity curves for each

protein assay are in Fig. 5.3: The DNA oligomer sequences and the antibody pairs used are listed in Tables 5.1 and 5.2.

Culture and Stimulation of THP-1 Cells. We cultured human monocyte THP-1 cells (clone TIB 202) in RPMI-1640 (ATCC) medium supplemented with 10% fetal bovine serum and 10 µM 2-mercaptoethanol. Cells grown close to the maximum density (0.8×10^6 cells/mL) were chosen for the experiment. Cells were first treated with 100 ng/mL phorbol 12-myristate 13-acetate (PMA) for 12 h during which a characteristic morphological change was noticed as an indication of the induction to the macrophages (Fig. 5.15). Cells were washed with fresh media and resuspended in media with PMA (100 ng/mL) and lipopolysaccharide (LPS, 200 ng/mL) at 0.5×10^6 cells/mL for the further differentiation and the TLR-4 activation.



On-chip Secretion Profiling. Prior to loading cells on the chip, the DNA barcode array was transformed into an antibody microarray through the following steps. First, 1% bovine serum albumin (BSA) in phosphate buffered saline (PBS) was flowed and dead-end filled into the chip to block non-specific binding. Second, a 200 μ l cocktail containing all 12 DNA-antibody conjugates at 1.25 μ g/mL in 1% BSA/PBS buffer was flowed through all microfluidic channels for a period of 1 h. Then, 100 μ l of fresh buffer was flowed into the device to replace DNA conjugated primary antibody solutions. The chip was then ready for use. Cells stimulated with PMA/LPS were loaded into the SCBC chip within 10 min in order to minimize pre-loading secretion. Then, the pneumatic valves were pressed down by applying 15–20 psi constant pressure to divide 80 microfluidic channels into 960 isolated microchambers. Next, the cells in every microchamber were imaged under a Nikon LV100 microscope and their numbers were counted. Afterwards the chip was placed in a cell incubator ($\sim 37^{\circ}\text{C}$ and 5% CO_2) for 24 h to perform on chip secretion. The chip was removed from the incubator and a 200 μ l cocktail containing all detection antibodies (each at 0.5 μ g/mL concentration) tagged with biotin was flowed through the microchannels by releasing the valves. Then, 200 μ l of the fluorescent probe solution (1 μ g/ml Cy5-labeled streptavidin and 25 nM Cy3-labeled M' ssDNA) was flowed through to complete the immuno-sandwich assay. Finally, the PDMS slab was peeled off and the microarray slide was rinsed with 1 \times PBS, 0.5 \times PBS, and DI water twice, sequentially, and spin-dried.

Bulk Secretion Profiling. Bulk measurements on the same panel of secreted proteins as were assessed within the SCBC microchambers were also carried out for the THP-1 cells with no stimulation, PMA stimulation, and PMA+LPS stimulation. Cells were cultured at

0.3×10^6 cells/mL, a comparable density to a single cell in a chamber. The media were collected after 24 h and the secreted proteins were detected as described below. For the PMA+LPS stimulation condition, the media were collected at multiple time points (2, 4, 6, 8, and 10 h) for the time-dependent analysis. For the bulk test, a SCBC chip was utilized without using valves for the microchannel to microchamber conversion. The same conditions as for the on-chip secretion profiling were applied except for the cell incubation step. Instead, the collected media was introduced to the channel sets and incubated for 3 h in the incubator.

Quantification and Statistics. All the barcode array slides used for quantification were scanned using an Axon Genepix 4400A two-color laser microarray scanner at the same instrumental settings—50% and 15% for the laser power of 635 nm and 532 nm, respectively. Optical gains were 500 and 450 for 635 nm and 532 nm fluorescence signals, respectively. The brightness and contrast were set at 90 and 93. The averaged fluorescence intensities for all barcodes in each chamber were obtained and matched to the cell number by custom-developed MATLAB (The MathWorks, Natick, MA) codes. Heat maps were generated using Cluster 3.0 and Java treeview (<http://rana.lbl.gov/EisenSoftware.htm>).

5.6.2 Experimental data analysis methods

Conversion to the Number of Molecules. The collected raw data is based on the fluorescence. In order to convert the fluorescence to the number of protein molecules, we used the calibration curves (Fig. 5.3). We used the four-parameter logistic model which is

commonly used for fitting an ELISA calibration curve. The fitting parameters can be found in Table 5.5.

Signal-to-Noise Calculations. Since the signal range highly depends on the activities of the antibodies as well as the cell biology, it is necessary to decide if the signal is real and reliable. Certain assayed proteins were identified as positively detected from single cells based upon signal-to-noise ratio (S/N), which was measured as follows: For each microchamber, the averaged fluorescence from the two barcode stripes used to capture and detect a given protein and the averaged fluorescence from the barcode stripes designed to capture and detect IL-2 were obtained. The ratio of the averaged values over all single-cell experiments (specific protein to IL-2) yields a S/N value. An S/N of 4 was utilized as a minimum for positive detection. Eight secreted proteins were thus identified from the single-cell measurements. Those proteins were (with S/N included in the parenthesis after the protein name): MCP-1 (4.65), MIF (1381.13), IFN- γ (4.33), VEGF (77.32), IL-1 β (94.70), IL-8 (2622.40), MMP9 (119.50), and TNF- α (410.74).

Analysis of Experimental and Biological Variation from SCBC-Based Single Cell Measurement. One of the major characteristics of SCBC analysis is the heterogeneous cellular behavior at the single-cell level. The experimental variation of the SCBC platform which reflects the system error as well as the biological variation due to the cellular heterogeneity is contributing to the fluctuation of the total signal. Thus, we need to check whether the heterogeneous signal responses are from the cells or the device itself.

The experimental error mainly includes the variation from non-uniform DNA barcode patterns and the variation due to the randomly distributed cell location in the chamber. The former can be estimated by the histogram of the fluorescence intensity from the calibration experiment with recombinant proteins. Since the recombinant protein has fixed concentration over the entire channel, it represents a uniform protein level without any heterogeneity or location dependence. As a result, the distribution of the fluorescence intensity of a specific recombinant reflects the detection profile of the DNA barcode.

Fig. 5.6A shows a representative histogram of signal derived from recombinant MIF protein at 5 ng/ml. The histogram shows a nice Gaussian distribution with a coefficient of variation (CV) around 7%. In the calibration experiment, basically the intensities of all the recombinant proteins at detectable concentrations follow a Gaussian distribution with CVs typically lower than 10%.

The cell location is another important factor for system error. Even though the chamber size is small, it is still big for a single cell. So the protein signal is dependent on diffusion and that is why the cell location can be a source of the variation. In order to minimize this effect, we utilized two sets of barcodes in a chamber and used the averaged signal intensity from two barcodes as the final signal value. However, the barcode close to the cell will undergo a higher local protein concentration than its counterpart and the different intensities of two sets of barcodes are amplified during the long incubation time. The diffusion process will lead the system close to the equilibrium but the cell that keeps secreting proteins with different kinetics makes it difficult for the chamber to reach its full equilibrium. In that sense, the randomly located cells can add an extra uncertainty to the SCBC system.

Because it is difficult to isolate the system error (especially for the cell location effect) from the heterogeneous cell response experimentally, we performed a Monte Carlo simulation by R (R Foundation for Statistical Computing, version 2.10.1). First of all, we investigated MIF as a representative case. We assumed one chamber had two sets of 13 barcodes such that each of them has MIF antibodies. By randomly positioning a cell with a fixed protein secretion rate and getting the protein concentration at specific barcode positions, we can find out what variation depends purely on the cell location and barcode non-uniformity. The total amount of secreted MIF during 24 h was estimated based on our experimental result. The secretion rate was 4.84 pg/mL per min from the SCBC (used for the simulation) and 11 pg/mL per min from the bulk condition. The corresponding secretion rate of a single cell, back-calculated based on the chamber and cell size ($10 \mu\text{m}^3$), was 0.065 nM/min. Values of parameters used in simulation can be found in Table 5.6. 5000 data sets for the protein concentration distributions from randomly located single cells were generated by solving a diffusion equation with a custom made MATLAB code and the results were analyzed with R. The parameters used in the simulation are exactly the same as our experimental environment. The chamber is 2000 μm in length and 100 μm in width with two sets of DNA barcodes M-A and A-M from left to right. Each barcode is 20 μm in width and 50 μm in pitch (30 μm gap between barcodes). The detection variation of the MIF protein due to the DNA uniformity obtained from the histogram of the calibration data set was incorporated to the analysis. Fig. 5.2C shows the histogram of the average fluorescence intensity from DNA sequence E (corresponding to MIF in the actual experiment) for 5000 single-cell cases. For the barcode variability, the actual value of 7.3%

was used. The final system error was 5.1% which is much smaller than the assay error from the experimental data sets, 55.2 %.

In order to consider the worst case, we used a barcode variability of 10% for the rest of the analysis. If the cell location effect is significant, we are supposed to see different errors on different barcode positions. Fig. 5.7 illustrates the histograms of average intensities from multiple barcode locations. The blue curves are line profiles of Gaussian distribution fitted with the mean and the standard deviation obtained from the corresponding simulation. The nice fitting between the Gaussian curves and the histogram indicates that the average intensity per chamber follows a Gaussian distribution with a predictable mean and CV. The CVs from this simulation represent the distribution of our measurements for single-cell chambers without considering the cellular heterogeneity, i.e., the system error. The experimental CVs for different barcode locations based on the system error were quite similar to one another (~ 7%).

We can define CV_{system} as the system error estimated by the simulation. We can also calculate the assay error from our experimental data set such that CV_{assay} refers to the total CV of our experimental data. Consequently, the biological variation for a single-cell experiment can be quantitatively estimated by the formula below:

$$CV_{\text{assay}} = (CV_{\text{system}}^2 + CV_{\text{biological}}^2)^{1/2}.$$

An estimation of biological variations of proteins for different barcode locations are shown in Table 5.7. It can be seen that the biological variation is dominant in the total error of the assay. This analysis verifies that the signal fluctuation that we can see from the single-cell experiment is a better representation for the single-cell heterogeneity than the systemic error from our platform.

5.7 Appendix B: Supplementary Theory Methods (SI.II)

5.7.1 Introduction to theoretical supplementary methods

We show how to characterize protein–protein interactions. Specifically we show that the different tiers of a signaling network can be quantitatively determined from the measured fluctuations in the concentrations of signaling proteins, and that the measured fluctuations in the concentrations of signaling proteins for the unperturbed cell can be used to predict the effect of introducing perturbations such as neutralizing antibodies. The approach is developed from an information theoretic perspective and it is related to the specification of the direction of change when a system responds to a perturbation, known as the principle of Le Chatelier. The corresponding result here is that we predict the sequence of tiers in the network (see Fig. 5.10). In addition we specify which signaling proteins are at a given tier of the network and their mutual influence, including inhibition (see Fig. 5.11). Experimental measurements of the fluctuation of concentrations in samples with nanoliter volume containing n cells, $n = 0,1,2,\dots$ (see Fig. 5.12 below) are used to validate the signaling protein network. Finally we use the protein-protein interaction as determined for the unperturbed cell to quantitatively predict (Fig. 5.14) the effect of perturbations.

The approach we propose provides an analogue and an extension of the statement that heat is transferred from a warmer to a colder body. We can understand this statement as a statement about the direction of a process between two equilibrium states, meaning that it is a static principle. We can also think of it as a statement about dynamics, meaning that it specifies the rate of change. We will here develop the formalism for the static interpretation.

The explicit introduction of time is possible and we have the required formalism at hand, but it requires a more elaborate theoretical foundation and so will be given elsewhere.

5.7.2 The ensemble: A basis for making predictions

The system we consider is many independent replicas of a compartment containing a single cell in a nutrient solution at thermal equilibrium. Because the system is not large, different replicas of it can differ in the number, N_i , of secreted proteins of kind i . We seek to represent these fluctuations by taking the different replicas as different samples from an ensemble of single-cell compartments where the mean number \bar{N}_i of proteins of kind i over the ensemble is given. Another given quantity is energy (and volume, which we do not indicate explicitly). We now seek the most probable distribution of protein numbers in different compartments. The solution is well known because if many compartments are measured then the required distribution is the one whose entropy is maximal. In textbooks of statistical mechanics this search for the most probable distribution is sometime called the Boltzmann approach. It is possible to show³⁷ that this approach does not require the system to be macroscopic in size. It is sufficient if we measure enough replicas so that the distribution of proteins does not significantly change as we add more measurements. If each replica is macroscopic, the fluctuations will be small and rare. Repeated measurements will give the same results. If each replica is small we can observe the fluctuations, which is the experiment described in the main text.

The key point is that even if the fluctuations are not small it is possible to make predictions. We discuss three types of predictions in the paper, with more details given in this section. We predict the distribution of fluctuations, we predict the tiers in the network,

and, in particular and as shown in Fig. 5.14 of the main text, we predict the response of a system to a perturbation. For these first and last predictions, we compare directly with experimental results. We emphasize that the prediction is made strictly independently of the experiment to which it is compared.

The probability of a system in a particular composition can be shown to be given by

$$P(N_1, N_2, \dots) = \exp\left\{\beta\left(\sum_i \mu_i N_i - E\right)\right\} / \Xi \quad (\text{S5.1})$$

This straightforward result is perhaps misleading in its simplicity. It is most directly derived by the method of Lagrange undetermined multipliers. The numerical value of these multipliers is determined at the final stage by imposing the condition that the distribution (Eq. S5.1) reproduces the given values of the means. There are as many multipliers as conditions.

β is the Lagrange multiplier that is determined by the mean value of the energy and, as usual, is related to the temperature T as $\beta = 1/kT$, where k is Boltzmann's constant. The μ_i 's are the chemical potentials as introduced in the thermodynamics of systems of more than one component.^{27, 38} The Lagrange multipliers that correspond to the given (mean) number of species i are known as the Planck potentials and denoted as α_i . It is often more convenient to work with $\mu_i, \alpha_i = \beta \mu_i$. If our system were macroscopic in size we would call μ_i 'the chemical potential of protein i '. For convenience we retain the designation 'potential' because, as we shall show, μ_i retains essential properties of the chemical potential even when fluctuations are finite. Ξ is a function of all the Lagrange multipliers and its role is to insure that the sum of the probability over all possible compositions yields one.

There are at least two points where important details are not revealed by the notation used in eq. S5.1. Both are relevant in what follows. First is the condition that the numerical values of the chemical potentials are determined by the given mean numbers, the \bar{N}_i s, of the proteins. Strictly speaking, we should write the chemical potentials as functions of the \bar{N}_i s. The other point arises when we want to treat the actual numbers \bar{N}_i s of the different proteins as continuous variables. This is needed, for example, to compute averages, normalize the distribution (eq. S5.1), etc. The integration for each protein is over $dN/N!$ where $N!$, the factorial of N , arises to account for the Gibb's paradox. Therefore, as a function of the continuous variable N the distribution for, say, one protein is

$$P(N) \propto \left(Q^N / N! \right) \exp(-\beta\mu N) \quad (\text{S5.2})$$

Here Q is the factor that arises by summing over all the internal states of the protein that are occupied at the temperature T . This result is used in the main text to fit the observed distribution for a single protein (Fig. 5.9).

5.7.3 Fluctuations describe the response to small perturbations

We show that by measuring the fluctuations in the unperturbed system we can predict how the system responds to *small* perturbations.³⁸ Proof: Say that we make a small change in the value of the chemical potential μ_i from its current equilibrium value to some new value $\mu_i + \delta\mu_i$. We do so isothermally. This change in μ_i potentially changes the equilibrium mean concentration of all species from \bar{N}_j to $\bar{N}_j + \delta\bar{N}_j$, for all j . To compute the change in concentrations we need to consider the change in the ensemble as represented

by Eq. S5.1. In the algebraic developments in eq. S5.4 below we make use of the definition of the mean concentration

$$\bar{N}_j = \sum N_j P(N_1, N_2, \dots) . \quad (\text{S5.3})$$

The summation in eq. S5.3 is over all the possible compositions, each weighted by its probability $P(N_1, N_2, \dots)$ computed as the distribution of maximal entropy. The same meaning for the summation is used also in eq. S5.4 below. We denote this averaging by an overbar. From eq. S5.1, the variation of the distribution that occurs when a particular chemical potential is changed by a small amount is $\delta P(N_1, N_2, \dots) = \beta \delta \mu_i N_i P(N_1, N_2, \dots)$. Note that it is in using this lowest term in the Taylor series that we assume that the change is small. It follows that on the average the proteins respond to the change as:

$$\begin{aligned} \delta \bar{N}_j &= \sum N_j \delta P(N_1, N_2, \dots) \\ &= \sum (N_j - \bar{N}_j) \delta P(N_1, N_2, \dots) \\ &= \beta \delta \mu_i \sum (N_j - \bar{N}_j) N_i P(N_1, N_2, \dots) \\ &= \beta \delta \mu_i \sum (N_j - \bar{N}_j) (N_i - \bar{N}_i) P(N_1, N_2, \dots) \\ &= \beta \delta \mu_i \overline{(N_j - \bar{N}_j)(N_i - \bar{N}_i)} . \end{aligned} \quad (\text{S5.4})$$

Note that the conservation of normalization implies that the average change in the probability must be zero, $0 = \sum \delta P(N_1, N_2, \dots)$, and we have used this result in the derivation above. In the last line in eq. S5.4 we have avoided writing the summation over all compositions by the use of the over bar to designate an average over the probability $P(N_1, N_2, \dots)$, which is the notation introduced in eq. S5.3.

Taylor theorem states that, in the leading order, the change of a function is the sum of the changes. Therefore the expression for an isothermal variation in all the chemical potentials leads to a change of the distribution of the form:

$$\delta P(N_1, N_2, \dots) = \beta \sum_i N_i P(N_1, N_2, \dots) \delta \mu_i. \quad (\text{S5.5})$$

The summation in eq. S5.5 is an ordinary sum over the finite number S of signaling proteins, $i = 1, 2, \dots, S$. Then we have the general equation of change that is an extended form of eq. S5.4 valid for all possible small isothermal changes in the chemical potentials

$$\delta \bar{N}_j = \beta \sum_i \overline{(N_j - \bar{N}_j)(N_i - \bar{N}_i)} \delta \mu_i. \quad (\text{S5.6})$$

This is the result that we use in this paper.

5.7.4 The principle of Le Chatelier

The principle in its simplistic statement claims that the system responds to a perturbation in a direction that restores equilibrium. For example, when the temperature of a heat bath is increased the mean energy of an immersed system goes up so that the distribution remains canonical. The proof for our case starts from eq. S5.3. When the chemical potential of protein i is changed, for an ensemble at maximal entropy the mean value of protein j changes by

$$\frac{\partial \bar{N}_j}{\partial \mu_i} = \sum N_j \frac{\partial P(N_1, N_2, \dots)}{\partial \mu_i}. \quad (\text{S5.7})$$

where, as emphasized in eq. S5.3, the distribution $P(N_1, N_2, \dots)$ is not arbitrary but is the one of maximal entropy as exhibited in eq. S5.1. Eq. S5.4 is recovered when the derivative in eq. S5.7 is evaluated. The reader may feel that this is a triviality but it is not without

meaning. What we have proven is that computing a small change in the distribution $P(N_1, N_2, \dots)$ when a particular chemical potential is changed from the value μ_i to a new value $\mu_i + \delta\mu_i$ is the same as computing the derivative of the distribution $P(N_1, N_2, \dots)$ at the point where the value of the chemical potential is μ_i . Then the change in the distribution is $(\partial P(N_1, N_2, \dots)/\partial\mu_i)\delta\mu_i$. Of course, this is what differential calculus is about. Yet the result is not pure mathematics. It shows that the new distribution is a distribution of maximal entropy of the functional form eq. S5.1, as otherwise the result will not hold. It says that a small change in the chemical potential μ_i , and no other change, leads to a new distribution which is also one of maximal entropy.

Typically we do not see the theorem of Le Chatelier stated as in eq. S5.6. This is because of the practical point that the number fluctuations are typically not easy to observe in a macroscopic system. Here however we deal with secretion of proteins by a single cell and, as shown in the main text and particularly in the histogram in Fig. 5.9, the distribution is clearly observed and the covariance can be computed from the experimental data as long as the number of replicas is not small.

5.7.5 The equation for the direction of change

The (symmetric) square matrix $\overline{(N_j - \bar{N}_j)(N_i - \bar{N}_i)}$ is the covariance matrix of the (equilibrium) fluctuations in the (equilibrium) concentrations, the \bar{N}_j s. It is an equilibrium average because, as explicitly shown in eq. S5.4, it is an expectation over the equilibrium distribution as given in eq. S5.3. The covariance matrix has the dimensions of S by S where S is the number of signaling molecules that take part. In practice we have to compromise on

this definition, meaning that S is the number of signaling molecules that can be detected. If an important protein is not detected then the network that we infer will be incomplete.

A covariance matrix can be shown to be a non-negative matrix, also called semipositive definite, meaning that its eigenvalues are zero or positive. If the concentrations of the signaling proteins can in principle be varied independently, which is definitely not necessarily the case, then the covariance matrix $\overline{(N_j - \bar{N}_j)(N_i - \bar{N}_i)}$ is a positive matrix with positive eigenvalues. We will discuss below why it will often be the case that for reasons of both principle and practice (e.g., experimental noise) there will be eigenvalues that are effectively zero. In that case, technically, the covariance matrix is positive semidefinite.³⁹

Eq. S5.6 specifies how the concentration of the j th signaling molecule varies when the i th chemical potential is changed. In general the correlation coefficient $\overline{(N_j - \bar{N}_j)(N_i - \bar{N}_i)}$ between the signaling molecules i and j can be either positive or negative. Therefore, in general the change $\delta\bar{N}_j / \delta\mu_i$ is not necessarily of the same direction for all proteins j . This obvious result will be important for us below. Using the observation that the covariance matrix is semipositive definite, it is however possible to determine the direction of change by first diagonalizing the covariance matrix. This means that we can determine S distinct linear combinations of signaling molecules, where (a) each such set of molecules changes in a given direction *and* (b) we can order the different sets in terms of the extent of their response such that the first set is the most changing, the second set changes to a lesser extent, etc. In the time-dependent formalism, not presented here, we can outright say that the first set is the fastest changing and therefore it is the first to change.

Then there follow changes in the second set, etc. It is clearly our intention to identify each set of signaling molecules as the set of molecules in a given tier in the network.

5.7.6 Tiers of the network are eigenvectors of the correlation matrix

Our next purpose is to define the tiers of the network. The set of proteins that participate in the m'th tier is determined as follows. Let \mathbf{S}_m designate the m'th eigenvector of the covariance matrix where the eigenvectors are listed in order of decreasing magnitude of the corresponding eigenvalue. The largest eigenvalue is m =1. Each eigenvector \mathbf{S}_m is a (column) vector of S components and it is determined by the matrix equation

$$\Sigma \mathbf{S}_m = \sigma_m^2 \mathbf{S}_m \quad , \quad m = 1, 2, . \quad (\text{S5.8})$$

where Σ is the S-by-S symmetric covariance matrix whose elements are $\Sigma_{ij} = \overline{(N_j - \bar{N}_j)(N_i - \bar{N}_i)}$, and we explicitly indicated that the eigenvalues are positive or zero but not negative (which defines a positive semidefinite matrix). The eigenvectors of the symmetric covariance matrix are orthogonal to one another and can be chosen to be normalized

$$\mathbf{S}_{m'}^T \cdot \mathbf{S}_m = \begin{cases} 0, & m' \neq m \\ 1, & m' = m \end{cases} \quad (\text{S5.9})$$

Here the superscript T designates the transpose so that $\mathbf{S}_{m'}^T$ is a row vector and eq. S5.9 is the scalar product.

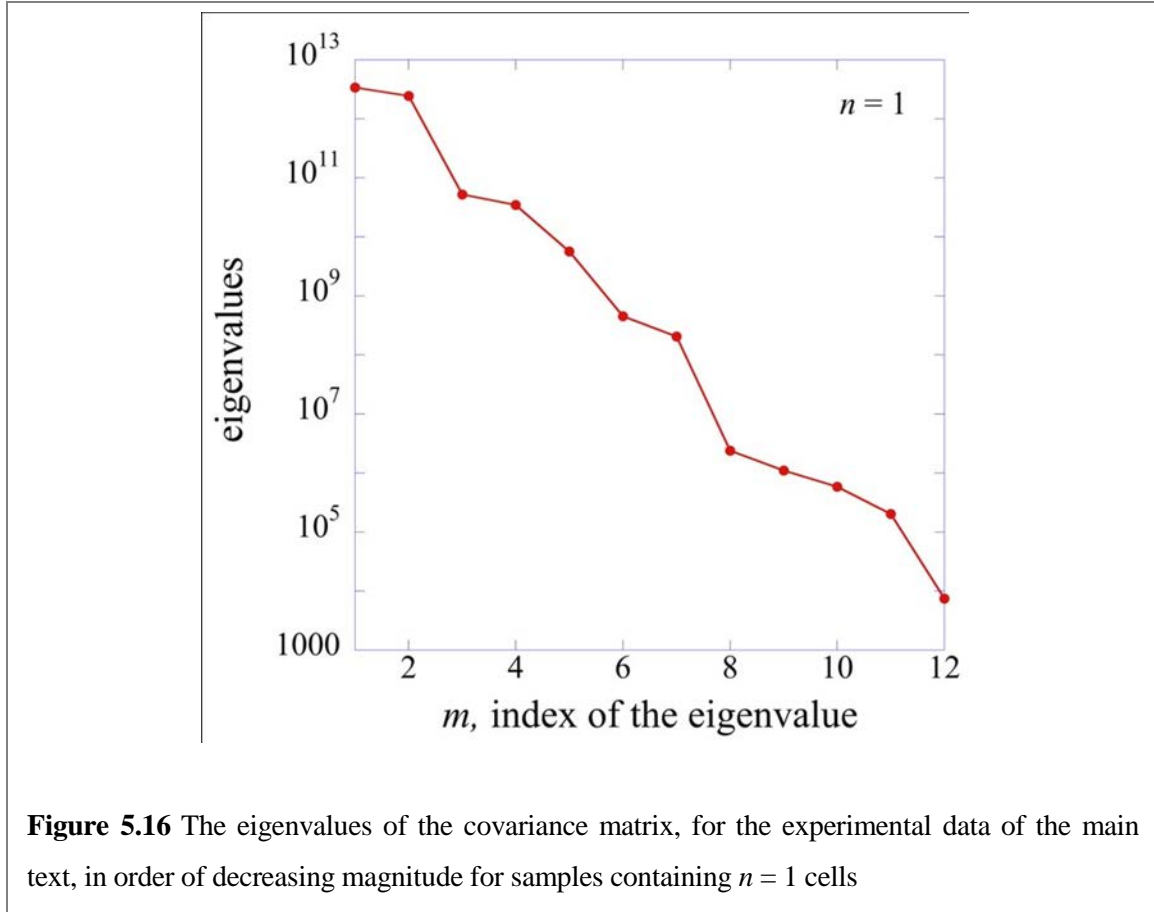


Figure 5.16 The eigenvalues of the covariance matrix, for the experimental data of the main text, in order of decreasing magnitude for samples containing $n = 1$ cells

For each value of the number of cells, n , in the compartment the eigenvalues are arranged in order of decreasing magnitude, the largest eigenvalue being labeled as $m = 1$ and the smallest as $m = 12$, and the results are shown for $n = 1$ in Fig. 5.16. See Fig. 5.12 for the dependence of the largest eigenvalues vs. cell number.

5.7.7 The spectral representation of the covariance matrix

Fig. 5.11 of the text shows the covariance matrix computed for experiments with one cell in the compartment. Table 5.8 is a digital representation of the same matrix.

Also shown in Fig. 5.11 is the resolution of the covariance matrix into tiers defined as follows: From each eigenvector \mathbf{S}_m we can define an S by S symmetric matrix \mathbf{P}_m as follows

$$\mathbf{P}_m = \mathbf{S}_m \cdot \mathbf{S}_m^T \quad (\text{S5.10})$$

The spectral theorem ²⁹ is the result that the covariance matrix Σ can be resolved into tiers as

$$\Sigma = \sum_m \sigma_m^2 \mathbf{P}_m \quad (\text{S5.11})$$

The eigenvalues σ_m^2 are arranged in a decreasing order so that each subsequent tier makes a smaller contribution. Fig. 5.16 shows that the eigenvalues decrease quite rapidly with increasing value of m . The very dominant contribution is from $m = 1$. The leading eigenvalue = tier 1, is only about 30% bigger than the second one, $m = 2$. The third eigenvalue is smaller by almost two orders of magnitude. Fig. 5.12 is a plot on a logarithmic scale of all non-zero eigenvalues. There are only two eigenvectors that, judging by the value of their corresponding eigenvalues are definitely above the noise. The dominant ($m = 1$) and the $m = 2$ eigenvectors for single cell measurements are shown in Fig. 5.11 of the text and for three cells in Fig. 5.13.

5.7.8 The role of the number of cells in the sample

It was possible to make repeated measurements of the protein concentrations for different values of the number of cells in the sample. In this section we argue that the direction of increasing n can be semi-quantitatively regarded as a direction of increasing time. Therefore by examining how the eigenvectors of the covariance matrix change with n

we have an independent determination of the direction of the *dynamic* response of the system.

Fig. 5.12 shows the largest eigenvalues for $n = 0, 1, 2, 3$ and 4 cells.

To interpret Fig. 5.12 within the point of view used in this paper we argue as follows: A single cell secretes a number of different signaling proteins and therefore even the data measured for a single cell can show the role of protein–protein interactions. If two cells are in the sample these interactions increase in importance. If we think of n as a measure of concentrations of proteins then $\bar{N} \propto n$, but to compute the covariance we need to divide by the number of protein molecules. So for both paracrine and endocrine signaling we expect the covariance to increase with n . When n becomes high there may be three or more cells interacting and the simple considerations break down.

5.7.9 Antibody perturbations

Fig. 5.14 shows a quantitative comparison of the measured results as compared to the purely theoretical *prediction* when neutralizing antibodies for specific proteins are added. We emphasize that it is a prediction because the results shown are based on using eq. S5.4 that we repeat here:

$$\delta \bar{N}_j = \beta \overline{(N_j - \bar{N}_j)(N_i - \bar{N}_i)} \delta \mu_i = \beta \Sigma_{ji} \delta \mu_i$$

The addition of a neutralizing antibody for protein i means that $\delta \mu_i$ is negative. The entries for the matrix Σ are given in Table 5.3. This matrix is computed for the *unperturbed* data. It is the matrix given in the table above that gives rise to the theoretical results shown in Fig. 5.14. We emphasize that the experimental results shown in Fig. 5.14 are for single

cells in the compartment. This means (see Fig. 5.12) that the largest eigenvalue, $\sigma_{m=1}^2$, of the covariance matrix is large indeed. Then, from eq. S5.11, the contribution from the first tier dominates. It is the two proteins in this tier that are shown in the panel. There are bigger discrepancies between theory and experiment for tiers 2 or 3 for which the experimental signal is weak.

5.8 Appendix C: Supplementary Tables

Table 5.1 Sequences and terminal functionalization of oligonucleotides*

Name	Sequence
A	5'- AAA AAA AAA AAA AGT CCT CGC TTC GTC TAT GAG-3'
A'	5' NH3-AAA AAA AAA ACT CAT AGA CGA AGC GAG GAC-3'
B	5'-AAA AAA AAA AAA AGC CTC ATT GAA TCA TGC CTA -3'
B'	5' NH3-AAA AAA AAA ATA GGC ATG ATT CAA TGA GGC -3'
C	5'- AAA AAA AAA AAA AGC ACT CGT CTA CTA TCG CTA -3'
C'	5' NH3-AAA AAA AAA ATA GCG ATA GTA GAC GAG TGC -3'
D	5'-AAA AAA AAA AAA AAT GGT CGA GAT GTC AGA GTA -3'
D'	5' NH3-AAA AAA AAA ATA CTC TGA CAT CTC GAC CAT -3'
E	5'-AAA AAA AAA AAA AAT GTG AAG TGG CAG TAT CTA -3'
E'	5' NH3-AAA AAA AAA ATA GAT ACT GCC ACT TCA CAT -3'
F	5'-AAA AAA AAA AAA AAT CAG GTA AGG TTC ACG GTA -3'
F'	5' NH3-AAA AAA AAA ATA CCG TGA ACC TTA CCT GAT -3'
G	5'-AAA AAA AAA AGA GTA GCC TTC CCG AGC ATT-3'
G'	5' NH3-AAA AAA AAA AAA TGC TCG GGA AGG CTA CTC-3'
H	5'-AAA AAA AAA AAT TGA CCA AAC TGC GGT GCG-3'
H'	5' NH3-AAA AAA AAA ACG CAC CGC AGT TTG GTC AAT-3'
I	5'-AAA AAA AAA ATG CCC TAT TGT TGC GTC GGA-3'
I'	5' NH3-AAA AAA AAA ATC CGA CGC AAC AAT AGG GCA-3'
J	5'-AAA AAA AAA ATC TTC TAG TTG TCG AGC AGG-3'
J'	5' NH3-AAA AAA AAA ACC TGC TCG ACA ACT AGA AGA-3'
K	5'-AAA AAA AAA ATA ATC TAA TTC TGG TCG CGG-3'
K'	5' NH3-AAA AAA AAA ACC GCG ACC AGA ATT AGA TTA-3'
L	5'-AAA AAA AAA AGT GAT TAA GTC TGC TTC GGC-3'
L'	5' NH3-AAA AAA AAA AGC CGA AGC AGA CTT AAT CAC-3'
M	5'-AAA AAA AAA AGT CGA GGA TTC TGA ACC TGT-3'
M'	5' Cy3-AAA AAA AAA AAC AGG TTC AGA ATC CTC GAC-3'

* All oligonucleotides were synthesized by Integrated DNA Technology (IDT) and purified via high-performance liquid chromatography (HPLC).

Table 5.2 Summary of antibodies used for macrophage experiments

DNA label	primary antibody (vendor)	secondary antibody (vendor)
A'	mouse anti-hu IL-2 (BD Biosciences)	biotin-labeled mouse anti-hu IL-2 (BD Biosciences)
B'	mouse anti-hu MCP-1 (eBioscience)	biotin-labeled armenian hamster anti-hu MCP-1 (eBioscience)
C'	rat anti-hu IL-6 (eBioscience)	biotin-labeled rat anti-hu IL-6 (eBioscience)
D'	rat anti-hu GMCSF (Biolegend)	biotin-labeled rat anti-hu GMCSF (Biolegend)
E'	goat anti-hu MIF (R&D systems)	biotin-labeled goat anti-hu MIF (R&D systems)
F'	mouse anti-hu IFN-γ (eBioscience)	biotin-labeled mouse anti-hu IFN-γ (eBioscience)
G'	mouse anti-hu VEGF (R&D systems)	biotin-labeled goat anti-hu VEGF (R&D systems)
H'	mouse anti-hu IL-1β (eBioscience)	biotin-labeled mouse anti-hu IL-1β (eBioscience)
I'	rat anti-hu IL-10 (eBioscience)	biotin-labeled rat anti-hu IL-10 (eBioscience)
J'	mouse anti-hu IL-8 (R&D systems)	biotin-labeled mouse anti-hu IL-8 (R&D systems)
K'	mouse anti-hu MMP9 (R&D systems)	biotin-labeled goat anti-hu MMP9 (R&D systems)
L'	mouse anti-hu TNF-α (eBioscience)	biotin-labeled mouse anti-hu TNF-α (eBioscience)

Table 5.3 Digital data for the fluctuation in protein copy numbers for experiments with single cell in the chamber

IL-2	MCP-1	IL-6	GMCSF	MIF	IFN-γ	VEGF	IL-1β	IL-10	IL-8	MMP9	TNF-α
3735.412	217395.9	13953.23	557.1622	3809515	13624.74	201.4036	8376.421	0	1454177	3205.591	152586.1
1665.362	27307.83	104.8926	1517.076	2820595	53647.16	22.99382	30393.38	2225.058	1549870	8513.336	139044.8
0	0	5.688741	983.9779	2039581	51073.18	5.659558	397.6828	1712.567	1556202	75864.65	105209.4
0	0	4.782456	0	442693.6	0	0.336728	0	0	341176.1	10460.81	39.82124
0	0	4.782456	0	394608.6	7158.123	0.336728	83.72112	0	1049468	5786.696	112.4533
0	9036.275	4.782456	315.5414	1182371	15521.45	2510.404	164.3377	0	2078531	530.3467	98.55574
0	8562.464	22.67125	1973.092	2340711	50886.57	0	8659.165	386.6576	1825752	3484.746	225206
972.853	5136.066	45.69175	0	2903862	30000.8	1.655758	1627.437	678.766	1357052	1609.678	487.7715
0	4625.892	5.688741	162.2633	515603.5	12411.14	258.1623	2951.517	1069.252	2085364	18909.8	95984.22
1115.354	5639.942	25.6359	0	3794851	59631.05	5.955249	75.74618	644.1138	829791.9	1197.849	9267.078
367.32	8562.464	0.620442	0	404940.8	0	5342.374	170.0894	425.4534	4964304	181518.4	2001.962
0	40152.21	47.5241	1517.076	3743529	8249.956	643.5375	2935.413	1281.727	5149720	38060.09	1084.421
876.3752	20185.95	28.71536	1658.653	665589.7	17294.07	4591.031	732.1417	1221.906	4543300	36619.56	127154.3
0	0	0	0	638485.4	0	0	2173.854	0	2932515	408789.6	64138.92
1068.126	0	13.28018	632.2731	438114.6	0	119.5423	102.6353	0	1034324	592.5651	4161.334

1575.52	19329.17	47.5241	961.4889	1217737	21180.92	2.07053	5.38982	813.5973	1055366	2244.563	1780.287
827.633	26895.82	175.1502	2258.346	5831647	64318.4	2721.671	3362.146	4140.063	3606621	5461.672	75502.9
0	4625.892	4.782456	256.7672	6562935	0	1.756733	8524.752	0	174775	2301.694	98.55574
0	0	18.45094	286.4852	359371.4	0	572.8267	52.38082	0	3107306	65788.63	25235.97
0	5136.066	0	371.9954	5772999	7715.093	0.919755	952.1023	125.4948	589949.5	3484.746	8.587119
577.7165	27307.83	7.645797	256.7672	481179.4	11991.4	5.082496	91.7772	1221.906	954720.5	1434.076	159.007
0	11362.51	218.9126	681.2702	3668936	35507.47	4.254203	3813.608	4117.263	2589890	42622.04	86305.23
474.0248	21038.24	6.64407	505.8466	396657.3	7715.093	1.859546	205.0206	0	8685444	1667.948	155173.2
0	0	336.0215	0	365278.4	0	0.606097	1608.84	174.4034	2065560	1138.365	3733.989
0	0	0	0	328035.4	7715.093	159.1543	138.7292	425.4534	1067345	3484.746	95.81771
0	0	58.9922	961.4889	300360.2	34353.44	0	54.93063	746.8858	1817495	2358.739	23134.31
0	0	4.782456	0	425186.2	7715.093	613.1612	99.90882	386.6576	4683202	3037.413	46.89755
0	0	3.928359	0	445991.3	7715.093	402.2585	0	975.2311	523909.4	6326.138	1054.297
2236.04	33403.67	476.1208	870.3418	435981.4	74992.86	23.9095	3930.914	1986.093	11697012	9358.114	8317287
0	8085.346	36.88775	453.3645	332604.1	11991.4	86.2306	113.6166	1370.279	1559706	7130.545	1958.179
1620.52	9974.818	0	286.4852	362920.9	7158.123	0.336728	42.31677	713.014	1569342	22053.76	23001.06
198.7022	28129.56	104.8926	582.4318	5431280	38632.32	0.534271	503.3473	746.8858	1414076	3818.009	82.34883
0	0	13.28018	0	294489.8	0	278.2761	39.8375	0	96873.01	181570.6	0
0	15851.76	13.28018	0	569708.6	11125.54	2369.121	328.8863	386.6576	1292647	23316.12	12607.48
1843.259	8562.464	86.41712	194.848	775007.6	19615.08	0.336728	4396.839	0	2386454	56608.75	570.4367
474.0248	16291.26	84.19013	870.3418	3567046	57034.26	44.96208	112244.6	1130.88	3238520	3707.119	85922.27
0	12275.83	14.52122	681.2702	446942.7	8249.956	3059.87	44.81139	425.4534	3127064	270629.6	16913.92
0	5639.942	65.01849	0	362459.2	0	0	16.1095	0	2971267	3429.024	115.2728
0	34605.82	175.1502	286.4852	499008.3	18309.28	152.4368	184.5588	425.4534	1011213	135792.6	1097.382
526.1976	584810	13.28018	0	308498.5	9264.625	483.3776	0	0	1509316	1052286	49352.54
421.1059	4625.892	0	531.6397	277526.7	17636.16	295.7684	824.1178	1684.681	1979177	42077.15	14565.16
924.7744	12275.83	114.5543	479.7625	451511.5	25255.09	1990.09	196.223	573.4616	2977232	121849.1	29473.5
0	0	5.688741	286.4852	1616413	24415.08	53.64644	21718.77	0	1961863	5948.816	16.0508
0	1935.839	22.67125	162.2633	537180.3	0	1.556662	426.2234	678.766	1662376	3928.711	1846405
4097.416	15410.74	6.64407	916.1621	627149.3	15153.07	950.0875	661.5037	911.38	4734071	15793.97	633893.1
0	5639.942	18.45094	0	3734680	19933.81	71.75808	611.5641	1877.786	1963379	160882.2	12793.76
0	0	45.69175	286.4852	472151	7715.093	188.2966	86.39776	0	2563383	70281.5	27115.65
138.713	12729.29	27.16157	128.1625	510521.3	9748.657	0.534271	363.1055	713.014	7637057	22154.85	306664.8
526.1976	14077.98	47.5241	753.3682	385982.2	17636.16	9497.397	81.05349	713.014	1650511	36569.86	69227.5
0	0	3.928359	505.8466	4597800	21486.18	55.44104	378.7795	0	4705311	1492.748	4042.245
474.0248	8562.464	13.28018	286.4852	415863.4	7158.123	0	304.2398	1656.69	6712149	124417.6	104764.8
0	4625.892	49.37952	870.3418	3610659	11125.54	308.8587	335.0802	1543.606	1731368	67269.56	273.0328
0	0	0	0	497690.4	12411.14	1.964157	57.49294	0	1609086	450905.5	109102.7
2149.562	10439.91	5.688741	286.4852	493432.2	0	95.38698	800.1525	0	2319845	933080.9	468816.9
0	2499.366	0	0	1938229	11563.1	15.08493	167.2109	1486.351	1882943	6809.424	1024.341
421.1059	260961.8	27.16157	1028.626	631535.9	0	297.85	213.8589	537.3803	1335228	1018.815	12.21319

0	7604.672	47.5241	194.848	414552.4	20562.75	3358.884	267.679	1656.69	4826026	12493.18	65787.75
778.5221	27307.83	339.5008	1638.592	3964841	84043.16	10.19566	170693.7	3082.111	4250173	17635.86	346394
0	4625.892	0	315.5414	480143.5	15521.45	401.1044	196.223	2225.058	3515798	580887	11928.38
0	8562.464	18.45094	286.4852	658884.1	7158.123	1.179999	150.0535	537.3803	1652656	454906.5	113008.1
474.0248	48688.48	15.79737	777.063	479056.9	15153.07	11.81997	621.5163	2039.74	4603005	201019.8	340191.5
474.0248	20612.64	6.64407	286.4852	436080.6	0	1.859546	234.6332	2012.957	6917958	11296.85	215980.3
0	0	768.0874	286.4852	373315	26079.52	1437.645	199.1509	678.766	2261670	2130.037	10466.12
0	0	0	0	426020.1	7158.123	2.743952	161.4698	0	3933389	4369.751	49058.97
0	0	189.3848	557.1622	494271.9	15521.45	494.498	127.5026	71.49773	3800164	477015.4	103268.1
1068.126	42500.29	5.688741	0	443142.7	0	2610.429	135.9132	220.2761	2342101	688400.6	12.21319
0	6631.472	19.82653	0	574020.6	12822.93	10.3724	175.8619	879.0676	4074696	105807.8	1513.189
972.853	10439.91	10.90809	729.5097	284256.4	18640.59	2235.697	133.1033	0	1470217	53399.89	4002.718
0	0	13.28018	0	597667.5	0	2019.485	264.6556	306.1297	1194410	29141.91	480.3807
0	51365.65	145.1361	1246.065	405806.5	32699.9	856.1518	113.1666	1959.145	1258039	183346.9	1417.034
0	729.7022	0	256.7672	602511.6	31733.5	0	234.6332	0	1122269	898.3988	400.546
1485.024	41719.38	139.8782	453.3645	444591	7158.123	885.0224	138.7292	1628.589	2793823	3540.416	27481.96
526.1976	6138.223	27.16157	0	465292.2	14400.48	1403.802	102.6353	746.8858	1844275	18451.63	97125.55
2192.854	60050.81	285.2598	557.1622	3976269	52552.65	235.1851	12868.12	1486.351	2056078	6272.314	6856.5
0	10439.91	0	128.1625	5629496	8249.956	0.399418	1762.11	678.766	813978.6	163717.2	92940.02
2535.544	14523.91	114.5543	344.0223	1484329	26621.01	8678.123	8057.573	2661.458	1986914	525123.6	889781.5
0	4108.532	0	557.1622	443841.6	7715.093	1.179999	216.8138	1281.727	1438747	72010.22	3496.753
421.1059	4625.892	55.08115	453.3645	533679.1	45692.16	1450.532	385.0693	463.4456	1859549	8089.271	175397.8
924.7744	0	27.16157	681.2702	2819971	22977.18	25.30396	258.6201	2836.369	2894811	40590.36	774.8536
1439.516	5136.066	47.5241	0	2087753	52000.61	0.399418	7422.418	879.0676	3000134	5786.696	97961.85
526.1976	0	0	162.2633	528450.2	11991.4	59.08624	22.98716	463.4456	1749215	3596.034	624.2794
577.7165	9506.996	49.37952	0	503131.4	15521.45	116.0933	837.8488	220.2761	1903608	164594.6	2006.839
577.7165	0	5.688741	453.3645	6660777	58080.71	120.3132	404.0062	0	1578115	1078.692	323.6175
0	11362.51	0	128.1625	440302	9264.625	114.9509	273.7368	813.5973	1578115	12129.72	1040989
1575.52	19329.17	325.6539	1638.592	4924300	64154.29	340.5053	1318.723	2861.155	2672000	23366.56	306.578
0	0	24.13892	0	6851805	53465.61	5.513485	638.1433	0	1028638	127948.9	12200.28
474.0248	9036.275	221.941	286.4852	458783.7	20873.14	49.24328	322.7051	1850.488	2457942	22811.51	822556.8
3613.793	57047.96	172.3469	938.885	406672.9	47264.38	865.9889	1690.864	2172.481	3502255	843555.9	353763.6
0	22308.79	60.97992	0	369312.3	19933.81	814.9924	119.1506	975.2311	2229100	92908.36	75331.28
2062.643	5639.942	0	194.848	828096.2	7715.093	3451.146	105.3695	463.4456	2062203	2529.389	49.30233
0	4625.892	150.4565	194.848	606027.9	15521.45	48.08955	732.1417	644.1138	2205137	44305.43	112117.4
876.3752	109736.4	15.79737	656.8714	4333366	13227.3	9.498279	3109.17	2910.581	1557792	40044.93	8399.296
474.0248	14077.98	58.9922	1050.792	4158207	40779.49	0.837598	2139.122	713.014	1602325	18247.85	13988.05
0	4625.892	9.77966	938.885	427984.9	28984.83	2539.309	133.1033	813.5973	3538045	6056.756	99712.96
474.0248	15851.76	97.82923	315.5414	3058525	52552.65	5.224942	344.3945	678.766	1596288	1434.076	17010.92
1620.52	30983.19	164.0253	2444.257	3783288	27421.74	8.150933	20591.01	713.014	1238515	126636.5	294604.8
0	5639.942	6.64407	0	4829314	14779.51	0	438.9771	0	8394607	1375.257	12.21319

0	9036.275	86.41712	1718.527	699222.5	0	0	8090.773	0	946538.8	1018.815	246.7378
421.1059	29356.69	57.02586	656.8714	427051.1	49758.73	5895.509	7.430834	713.014	855150.1	715.8439	12943.31
972.853	16729.29	124.4873	557.1622	3157311	24131.41	26.96196	2270.716	125.4948	1429803	10251.26	2675.917
474.0248	0	27.16157	344.0223	421026.8	33885.67	0.336728	158.6074	813.5973	4493846	3205.591	4785.501
0	0	4.782456	0	1735160	0	0	1064.458	1600.377	491041.6	56904.9	28.54088
924.7744	21462.78	329.098	1797.669	10572470	36640.69	87.27182	951072.8	2012.957	717967.5	5786.696	50463.01
1255.571	16729.29	36.88775	916.1621	387730.2	35507.47	12.37785	172.9731	943.4302	3107306	9305.439	99116.28
0	3047.191	0	0	601108.5	0	1098.532	62.65337	346.9365	1429264	2015.138	0
827.633	1935.839	22.67125	0	609026.5	16243.7	3776.053	49.844	644.1138	2839583	5948.816	10466.12
0	0	45.69175	0	529102.3	7715.093	148.7002	164.3377	0	2739500	135792.6	454.6833
0	5639.942	19.82653	800.6015	399905.3	11125.54	61.55719	99.90882	1069.252	3152475	3484.746	192.6131
1975.261	17165.9	322.2216	1203.28	10565748	90563.8	9.155434	41511.63	2959.817	2157535	136249.1	5338.093
0	0	18.45094	1246.065	476216.6	0	0.399418	1553.213	0	1844720	82939.55	2389.394
0	0	17.10759	531.6397	3728800	39283.39	2566.026	1008.095	0	747662.7	1667.948	230.5624
628.6544	9974.818	15.79737	426.6258	488669.7	30997.64	130.4801	65.2507	1038.132	4037787	39400.11	71229.18
924.7744	0	5.688741	0	1560874	36640.69	4.801319	54.93063	0	1778135	8724.937	77056.37
0	0	27.16157	0	382589.2	5961.002	1493.194	347.5054	0	1500979	607501.3	327.046
972.853	0	0	226.2736	441546.9	7715.093	786.2589	110.8603	678.766	7130236	167126.3	55851.67
526.1976	11362.51	3.130261	1203.28	1356636	21180.92	2759.997	3129.465	975.2311	2758719	3818.009	146319.6
577.7165	6631.472	19.82653	2201.941	5878268	13624.74	3241.913	37543.28	1221.906	1173170	13477.1	220.957
0	11362.51	0	315.5414	486844	27948.27	0	255.6081	463.4456	1388172	522389.9	78625.91
0	635058.1	6.64407	0	545876.8	7715.093	1100.19	190.3813	0	1518652	28391.09	109.6469
256.4187	46379.67	53.15834	729.5097	3301742	32699.9	4.389042	359.9795	1006.795	1864545	5353.088	227.3521
577.7165	13630.28	14.52122	2107.237	3806473	22683.47	121.4725	96650.04	1543.606	1174095	9252.748	26620.53
924.7744	10439.91	47.5241	453.3645	3281029	44088.98	0.016533	477.4821	346.9365	1063941	2812.305	447.3908
5587.157	5136.066	24.13892	681.2702	3016496	29240.69	47.22998	5719.854	425.4534	105126.8	6056.756	0
474.0248	8562.464	36.88775	1895.558	4112702	22683.47	3.224364	87695.31	644.1138	3622850	18094.94	112883.1
2955.955	18035.05	57.02586	2088.188	3559334	27421.74	17.95405	37266.68	1656.69	2244932	5786.696	952.3013
5355.51	8562.464	0	0	2892800	14015.67	128.5041	1271.685	0	1603673	9884.013	30912.89
0	0	14.52122	52.05951	831973.3	8249.956	518.8942	141.5514	0	1042440	1609.678	306814.1
0	4625.892	67.06888	557.1622	3166646	20249.67	2.288425	18257.35	71.49773	462439.1	2130.037	187929.7
5970.693	18035.05	90.92703	1160.163	2856820	31244.01	23.67953	522.8445	1795.612	215604.4	14560.51	4241.145

Table 5.4 Signal-to-noise ratio (S/N) for single cells in SCBC measurements

IL-2	MCP-1	IL-6	GMCSF	MIF	IFN-γ	VEGF	IL-1β	IL-10	IL-8	MMP9	TNF-α
1.0	4.7	3.6	1.4	1381.1	4.3	77.3	94.7	1.8	2622.4	119.5	410.7

Table 5.5 Parameters utilized for the protein assay calibration curve

$$y = \frac{A_1 - A_2}{1 + (x / x_0)^p} + A_2$$

	A1		A2		x0		p		Statistics	
	Value	Error	Value	Error	Value	Error	Value	Error	Reduced Chi-Sqr	Adj. R-Square
IL-2	0	0	256	0	7659.58168	973.0838	1.12824	0.16788	91.39131	0.99224
MCP-1	0	0	256	0	65733.51686	4770.5	1.12607	0.09607	29.62623	0.99578
IL-6	0	0	256	0	16231.59942	4515.94	0.67887	0.12265	243.09932	0.95697
GMCSF	0	0	256	0	2451.99685	295.3281	1.2195	0.13013	72.59138	0.99458
MIF	0	0	256	0	7892.74068	483.8218	1.14428	0.07578	20.31714	0.99821
IFN-γ	0	0	256	0	14549.5316	2773.804	1.57222	0.26181	172.2368	0.98713
VEGF	0	0	256	0	1687.9445	225.4782	0.69008	0.05631	58.49911	0.99513
IL-1β	0	0	256	0	2137.44388	208.9672	0.89593	0.07185	41.21361	0.99694
IL-10	0	0	256	0	3961.03661	328.4038	1.23209	0.08611	33.93572	0.99669
IL-8	0	0	256	0	1255.89317	225.9207	1.23262	0.19534	161.8703	0.98686
MMP9	0	0	256	0	70537.40022	1584.696	1.062	0.02495	2.60945	0.99961
TNF-α	0	0	256	0	4126.15703	661.2747	0.81683	0.09483	99.72583	0.99185

Table 5.6 Values of parameters used in simulation

Chamber size	2000 μm × 100 μm × 18 μm
Cell diameter	10 μm
Diffusion coefficient	10 ⁻⁶ cm ² /sec
Protein secretion rate (MIF)	0.065 nM/min
Molecular weight	12500 Da

Table 5.7 The coefficients of variation for each of the assayed proteins from single-cell experiments. The experimental CVs are estimated from the Monte Carlo simulations. The biological CVs, which clearly dominate the experiment, are calculated from $CV_{\text{assay}} = (CV_{\text{system}}^2 + CV_{\text{biological}}^2)^{1/2}$.

Barcode/Protein	Experimental CV (%)	Assay CV (%)	Biological CV (%)
B / MCP-1	7.12	380.4	380.3
E / MIF	7.05	55.2	54.7

F / IFN- γ	7.04	131.5	131.3
G / VEGF	7.03	149.7	149.5
H / IL-1 β	7.02	300.6	300.5
J / IL-8	7.00	14.4	12.6
K / MMP9	6.98	192.6	192.5
L / TNF- α	6.97	132.9	132.7

Table 5.8 Digital representation of the covariance matrix for single cell measurements

COV	IL-2	MCP-1	IL-6	GMCSF	MIF	IFN- γ	VEGF	IL-1 β	IL-10	IL-8	MMP9	TNF- α
IL-2	1.18E+06	-27830	7966.7	1.34E+05	2.30E+08	4.10E+06	85756	1.27E+06	1.60E+05	-1.06E+08	1.50E+07	2.31E+07
MCP-1	-27830	6.34E+09	-1.83E+05	-1.14E+06	-9.54E+09	-9.51E+07	6.10E+05	-3.31E+07	-2.52E+06	-8.51E+09	4.21E+09	-7.34E+08
IL-6	7966.7	-1.83E+05	9050.5	11507	1.56E+07	5.89E+05	734.25	4.20E+05	24714	-81623	-7.38E+05	1.04E+06
GMCSF	1.34E+05	-1.14E+06	11507	3.39E+05	3.75E+08	3.97E+06	53462	5.71E+06	2.07E+05	1.05E+07	-1.66E+07	1.75E+06
MIF	2.30E+08	-9.54E+09	1.56E+07	3.75E+08	3.12E+12	1.48E+10	-4.32E+08	1.19E+10	3.35E+08	-4.33E+11	-7.53E+10	-5.22E+10
IFN- γ	4.10E+06	-9.51E+07	5.89E+05	3.97E+06	1.48E+10	3.09E+08	-2.28E+05	1.40E+08	5.83E+06	-1.70E+09	-5.01E+08	-1.00E+08
VEGF	85756	6.10E+05	734.25	53462	-4.32E+08	-2.28E+05	2.48E+06	-2.65E+06	1.04E+05	9.34E+07	2.92E+07	2.59E+07
IL-1 β	1.27E+06	-3.31E+07	4.20E+05	5.71E+06	1.19E+10	1.40E+08	-2.65E+06	4.78E+08	4.46E+06	1.86E+09	-4.08E+08	3.16E+08
IL-10	1.60E+05	-2.52E+06	24714	2.07E+05	3.35E+08	5.83E+06	1.04E+05	4.46E+06	7.39E+05	2.20E+08	-5.64E+06	2.92E+07
IL-8	-1.06E+08	-8.51E+09	-81623	1.05E+07	-4.33E+11	-1.70E+09	9.34E+07	1.86E+09	2.20E+08	2.73E+12	7.05E+09	3.56E+10
MMP9	1.50E+07	4.21E+09	-7.38E+05	-1.66E+07	-7.53E+10	-5.01E+08	2.92E+07	-4.08E+08	-5.64E+06	7.05E+09	3.70E+10	5.25E+09
TNF- α	2.31E+07	-7.34E+08	1.04E+06	1.75E+06	-5.22E+10	-1.00E+08	2.59E+07	3.16E+08	2.92E+07	3.56E+10	5.25E+09	5.26E+10

Chapter 6

Probing Chemical and Physical Property Changes of Pulmonary Phospholipid Surfactants by Interfacial Ozone Reactions with Field-Induced Droplet Ionization Mass Spectrometry and Microfluidic-Based Bubble Analysis

6.1 Introduction

Lung disease is the third leading cause of death in the United States and lung disease death rates are still increasing.¹ A unique feature of the lungs is that they are constantly exposed to airborne environmental insults. Both short- and long-term exposure of lungs to pathogens, air pollutants, and other irritants can be a major cause of acute distress and contribute to chronic injuries such as cardiopulmonary mortality and lung cancer.^{1–3} Recently, Jerret et al. reported a significant increase in the risk of death from respiratory causes in association with air pollution which includes an increase in ozone (O_3) concentration.⁴

Pulmonary surfactant (PS) is a lipid-protein mixture that lines the air-liquid interface of alveolae.^{5, 6} The pulmonary surfactant comprises ~ 90% phospholipids and ~ 10% apoproteins by mass.⁶ Dipalmitoylphosphatidylcholine (DPPC) is the principal phospholipid component, which achieves very low surface tension (~ 0 mN/m) upon compression.^{7, 8} However, it adsorbs and spreads at the air-liquid interface very slowly (0.5

$\mu\text{m}^2/\text{s}$) at the physiological temperature (37°C), which is below the temperature (T_m) for its gel-to-liquid crystalline phase transition (41°C).^{7, 8} Unsaturated phospholipids, owing to their higher fluidity, improve adsorption and spreading properties of surfactant at the air-liquid interface.^{8, 9} However, they cannot produce sufficiently low surface tensions when surfactant layers are compressed.^{8, 10}

An increasing number of studies have focused on the heterogeneous chemistry of small molecules at the air-liquid interface, mainly using mass spectrometric¹¹ and spectroscopic¹² techniques, as well as theoretical methods.¹³ Recently, real-time monitoring of surface activity of fatty acids has been reported by two research groups.^{12, 14} Voss et al. have reported competitive air/liquid interfacial activities involving palmitic acid and oleic acid utilizing broad-bandwidth, sum frequency generation spectroscopy.¹² They observed that a mixed monolayer of the fatty acids was dominated by oleic acid, with palmitic acid becoming predominant when exposure to ozone results in oxidation of the oleic acid to more hydrophilic products. Using a single droplet, Gonzalez-Labrada et al. also reported a decrease in air liquid interface activity of oleic acid after exposure to a monolayer to ozone.¹⁴ Related studies of biologically relevant systems have only just begun, despite their importance. For example, Colussi and co-workers recently reported heterogeneous reactions of O_3 with ascorbic acid¹⁵ and uric acid,¹⁶ which are components of the pulmonary epithelial lining fluid, using ESI mass spectrometry.

Field-induced droplet ionization mass spectrometry (FIDI-MS) comprises a soft ionization method to sample ions from the surface of microliter droplets. FIDI-MS subjects neutral droplets to a strong electric field, leading to formation of dual Taylor cones in which streams of positively and negatively charged submicron droplets are emitted in

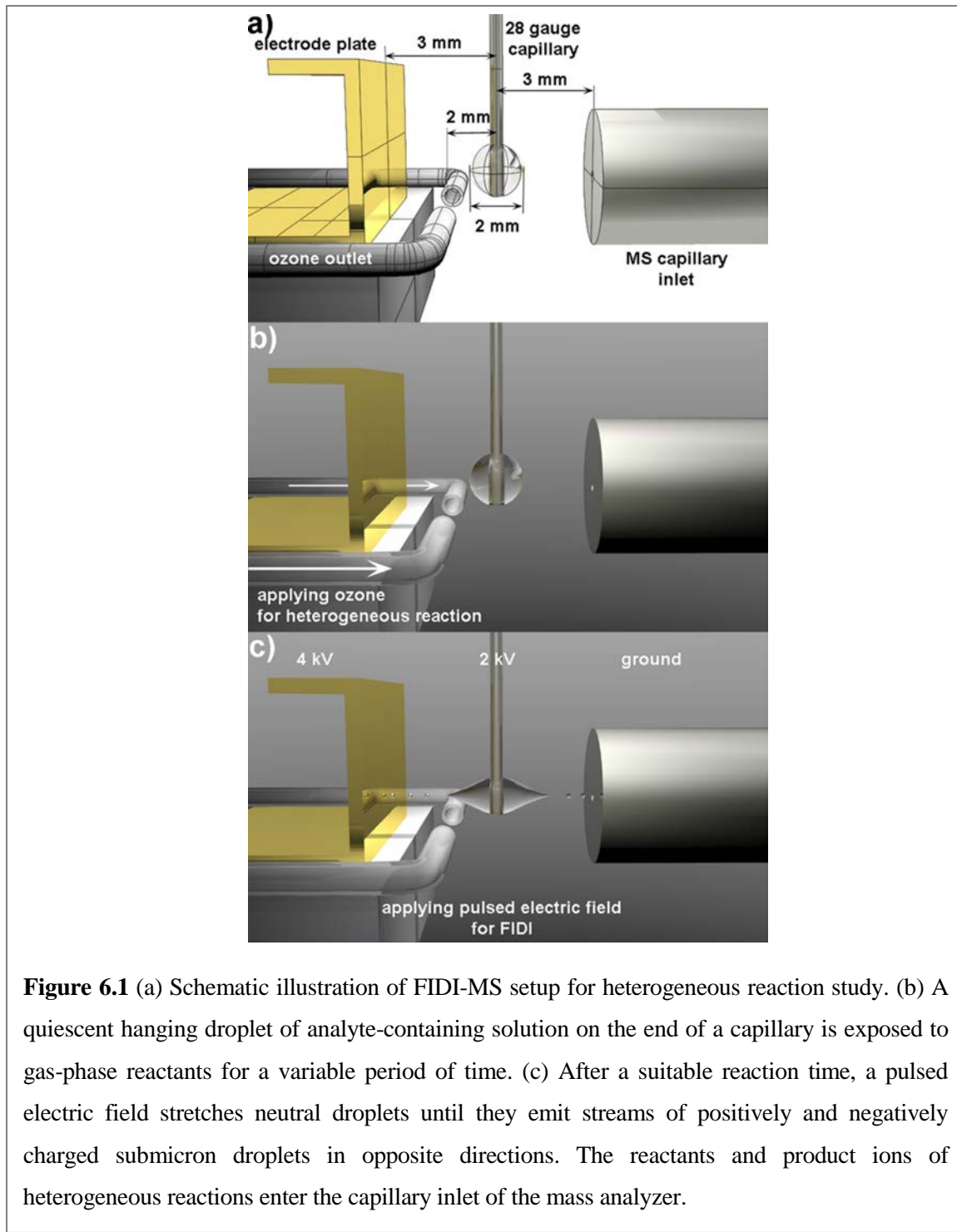
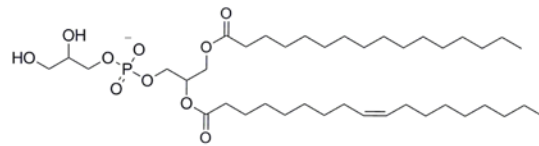


Figure 6.1 (a) Schematic illustration of FIDI-MS setup for heterogeneous reaction study. (b) A quiescent hanging droplet of analyte-containing solution on the end of a capillary is exposed to gas-phase reactants for a variable period of time. (c) After a suitable reaction time, a pulsed electric field stretches neutral droplets until they emit streams of positively and negatively charged submicron droplets in opposite directions. The reactants and product ions of heterogeneous reactions enter the capillary inlet of the mass analyzer.

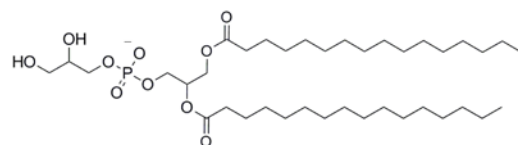
opposite directions, forming what is essentially a dual electrospray ion source.^{11, 17–19} It is ideally suited to monitor time-dependent heterogeneous reactions at the air-liquid interface. Previously, we demonstrated probing time-resolved ozonolysis of oleic acid and oleoyl-L-

α -lysophosphatidic acid using FIDI-MS.¹¹ In practice, a quiescent hanging droplet is formed on the end of a capillary and then exposed to gas-phase reactants for a variable period of time, followed by FIDI-MS sampling of molecular species present in the interfacial layer (Fig. 6.1).

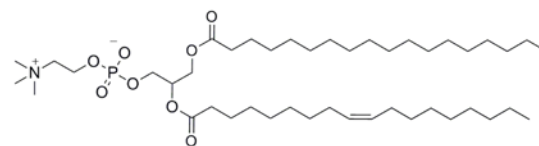
In this study, we utilize FIDI-MS for probing air-liquid interfacial oxidation by O₃ of 1-palmitoyl-2-oleoyl-*sn*-phosphatidylglycerol (POPG), representative of the major unsaturated anionic lipids in lung surfactant. Sampling droplets with an interfacial layer of POPG exposed to O₃ gas over a range of reaction times reveals the progress of distinct air-liquid interfacial chemistry. The competition of phospholipids subjected to a heterogeneous ozonolysis at the air-liquid interface is also studied using FIDI-MS. A mixture of the saturated phospholipid 1,2-dipalmitoyl-*sn*-phosphatidylglycerol (DPPG) and unsaturated POPG is investigated in negative ion mode using FIDI-MS. A mixture of 1,2-dipalmitoyl-*sn*-phosphatidylcholine (DPPC) and 1-stearoyl-2-oleoyl-*sn*-phosphatidylcholine (SOPC) surfactant is also studied to understand the air-liquid interfacial competition of phospholipids with different polar head groups in positive ion mode. Our results demonstrate that the relatively more hydrophilic products formed by oxidation of the unsaturated phospholipid dissolve back in the aqueous phase, leaving only saturated lipids at the interface. A detailed picture of the interfacial oxidation of unsaturated lipids by O₃ is provided by molecular dynamic (MD) simulations to support our interpretation of the experimental results. Solvation energetics of reactants and products are also evaluated by means of computational modeling. Structures of phospholipids investigated in this study are shown in Scheme 6.1.



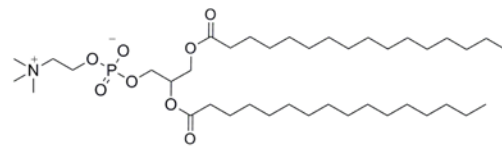
**1-Palmitoyl-2-oleoyl-*sn*-phosphatidylglycerol
(POPG)**



**1,2-Dipalmitoyl-*sn*-phosphatidylglycerol
(DPPG)**



**1-Stearoyl-2-oleoyl-*sn*-phosphatidylcholine
(SOPC)**



**1,2-Dipalmitoyl-*sn*-phosphatidylcholine
(DPPC)**

Scheme 6.1 Structures of POPG, DPPG, SOPC, and DPPC investigated in this study

Since the chemical modifications in those components will introduce a significant change in the physical characteristics of PS, it is necessary to understand how physical properties at the air-liquid interface will be altered by the chemical changes.

The above-mentioned investigations focused on molecular transformations that occur as a result of oxidative stress. Such molecular transformations can have a strong influence on the physical properties of the PS system (i.e., the surface tension and elasticity of the PS

interface), and so understanding how chemical transformations influence such physical properties can provide key insights into how the PS system responds to environmental challenges. Thus, in the second part of this chapter, we propose to utilize microbubbles as model system for investigating the physical transformations of the PS system when exposed to environmental challenges. Microbubbles have a potential for the interfacial physics study. They have the air-liquid interface and the composition of the interface can be easily modified by utilizing different components in solvent and gas. Interfacial dynamics can be further analyzed in microfluidic systems owing to their small characteristic size and high controllability.²⁰⁻²³ Especially, the breakup process of bubbles has been intensively studied with various flow parameters and compositions of gas as well as liquid. Prakash et al. showed another feasibility of bubbles in microfluidics by reporting on microfluidic bubble logic.²⁴ Their results indicate that the bubbles in microfluidic channel can deliver information based on a simplified dynamic flow resistance model. As demonstrated in previous studies, microbubbles in microfluidics impose rich information in their formation process and their behavior in a fluidic channel, which can provide us a comprehensive understanding of the interfacial physics.

In Section 6.3.2, we demonstrate an application of the bubble generation process in microfluidic system to the physical property analysis of lipid surfactant layer at the air-liquid interface as a model of alveolar sacs under oxidative stress condition. As characteristic analysis parameters, size and oscillatory behavior are studied under different conditions: normal air and air with ~ 20 ppm ozone exposures are used. Chemical composition change in a lipid monolayer under ozone exposure is observed by monitoring fluorescence-labeled unsaturated phospholipids at the air-liquid interface. This chemical

composition change, along with physical property change, induces altered bubble size and oscillatory behavior which can provide an improved understanding of the physics of the PS system when it is subjected to oxidative stress.

6.2 Experimental Methods

6.2.1 Chemicals and reagents

Sodium salts of DPPC, DPPG, POPG, SOPC, and NBD-PG (1-oleoyl-2-[12-[(7-nitro-2-1,3-benzoxadiazol-4-yl)amino]dodecanoyl]-sn-glycerol-3-[phospho-rac-(1-glycerol)]) were purchased from Avanti Polar Lipid (Alabaster, AL). All solvents (water and methanol) were purchased from EMD Chemicals, Inc. (Gibbstown, NJ).

6.2.2 Online FIDI-MS technique and heterogeneous oxidation by O₃

The FIDI-MS instrument used in this investigation was based on the design previously described by Grimm et al.¹¹ An ~ 2 mm o.d. droplet of analyte solution is suspended from the end of a 28 gauge stainless steel capillary (Small Parts, Inc.), which is located between the atmospheric sampling inlet of a Thermo Finnigan LCQ Deca mass spectrometer and a parallel plate electrode. The droplet is centered between the plate electrode and the MS inlet, which are separated by 6 mm. A flow of air containing O₃ is directed at both sides of the droplet by paired ~ 1.6 mm (0.063") id pyrex tubes located 1 mm from the droplet. Ozonolysis reactions occur between 0 and 30 s after a quiescent droplet is achieved (~ 1–2 s). Sampling is affected by pulsed voltages of 4 kV and 2 kV applied to the parallel plate electrode and supporting capillary, respectively. These voltages are tuned to be just above

threshold for initiating FIDI. The high-voltage initiates FIDI and directs submicron-sized charged progeny droplets into the LCQ for mass analysis. POPG and DPPG are monitored in negative ion mode and DPPC and SOPC are monitored in positive ion mode. The FIDI-MS spectra reported in this study were obtained by averaging five to ten individually acquired spectra from separately prepared droplets.

A pencil-style UV calibration lamp (model 6035, Oriel) generates ~ 20 ppm O_3 , measured spectrophotometrically using an absorption cell with 10 cm path length and calculated with Beer's Law using the molar absorption coefficient of $1.15 \times 10^{-17} \text{ cm}^2 \text{ molecule}^{-1}$, in air that continually bathes the droplet at 1500 mL min^{-1} . $100 \mu\text{M}$ POPG or mixtures of $50 \mu\text{M}$ unsaturated phospholipid (POPG or SOPC) and $50 \mu\text{M}$ saturated phospholipid (DPPG or DPPC) in 1:1 (by volume) water and methanol feed the droplet source. A recent study of DPPC monolayer on the surface of a water-methanol mixture reported a decrease of the lipid density in the monolayer due to the gradual incorporation of methanol molecules in the monolayer without significant difference of structural and electrical property of the monolayer.²⁵ In our study, we assume that the structures of the lipid surfactant layers on water-methanol mixtures are similar to their structures on water by itself.

6.2.3 Computational modeling

The MD simulations were performed with the all-atom CHARMM PARAM27²⁶ force field using the LAMMPS (Large-scale Atomic/Molecular Massively Parallel Simulator) code.²⁷ To describe water, we used a flexible TIP3P potential, which incorporates additional Hooke's constants, K, of $900 \text{ kcal/mol}/\text{\AA}^2$ for the OH bond and 110

kcal/mol/rad² for the HOH angle to improve the three site rigid TIP3P model.²⁶ The particle–particle particle–mesh method²⁸ was employed to compute the electrostatic interactions using an accuracy criterion of 10⁻⁴.

The initial structures for the lipid monolayer-water systems were prepared with 48 hexagonally-packed lipids on the 3168, 3264, 3744, and 4464 water molecules for the 55, 60, 65, and 70 Å²/Lipid surface densities, respectively. A potential of the form, $E = \epsilon[2/15(\sigma/r)^9 - (\sigma/r)^3]$, where $\epsilon = 0.1521$ kcal/mol and $\sigma = 3.1538$ Å with cut-off distance of 2.7071 Å, was applied at z = 0 to prevent water from diffusing in the negative z-direction. The dimensions of the simulation cells used were (55.21 × 47.82 × 200.0 Å) for the 55 Å²/Lipid, (57.67 × 49.94 × 200.0 Å) for the 60 Å²/Lipid, (60.02 × 51.98 × 200.0 Å) for the 65 Å²/Lipid, and (62.28 × 53.94 × 200.0 Å) for the 70 Å²/Lipid surface densities. The systems were equilibrated for 0.5 ns using 300 K NVT MD simulations by applying Nose-Hoover thermostat with a temperature damping relaxation time of 0.1 ps. Then, 2.0 ns NVT MD simulations were performed, and these trajectories were employed for the analysis of the atomic profiles.

The solvation energy, ΔE_{solv} , of the DPPG, POPG, and oxidative products of POPG (aldehyde and carboxylic acid) were evaluated using the Poisson-Boltzmann model,^{29, 30} which is implemented in the Jaguar V 7.5 package (Schrödinger, Inc., Portland, OR). In order to simplify considerations of the effect of functional groups on the solvation energies, analogous extended conformations of all species were employed for the calculations. DFT calculations were performed with the Becke three-parameter functional (B3)³¹ combined with the correlation functional of Lee, Yang, and Parr (LYP),³² using the 6-31G** basis set.

In order to describe the water solvation, solvent probe radius and solvent dielectric constant were set as 1.4 Å and 80.4, respectively.

6.2.4 Design and fabrication of microfluidic device

The microfluidic device was fabricated with PDMS (polydimethylsiloxane, Silgard 184, Dow Chemical, MI, USA) by standard soft lithography.³³ Standard photolithography techniques were utilized to create patterns in SU-8 (MicroChem, MA, USA) photoresist, supported on a Si wafer. The patterned SU-8 film was then used as a mold to cast a PDMS microfluidics chip. The design of the microfluidics was based on a flow focusing device (FFD),³⁴ combined with a straight microchannel oriented perpendicular to the bubble formation component. The height and width of the main channel was 200 µm, while the height and width of the narrower (bubble generation) channel was 60 µm. Detailed design parameters can be found in Fig. 6.2. The patterned, elastomeric PDMS layer was treated in oxygen plasma, and then bonded to a bare glass slide to form a closed microfluidic channel. Such plasma treatments make the PDMS surface hydropilic and that hydrophilicity was maintained by filling the microchannels with water immediately after the chip was assembled.³⁴

6.2.5 Bubble formation tests and analysis

The lipid sample was prepared by mixing 20 µM DPPC and 20 µM POPG in 1×PBS solution. The condition for the bubble generation was optimized for the air condition. The lipid sample flowed at a constant flow rate, 7 µl/min by a syringe pump and either air or ozone was injected at a constant pressure, 0.42 psi. Ozone was generated by a pencil-style

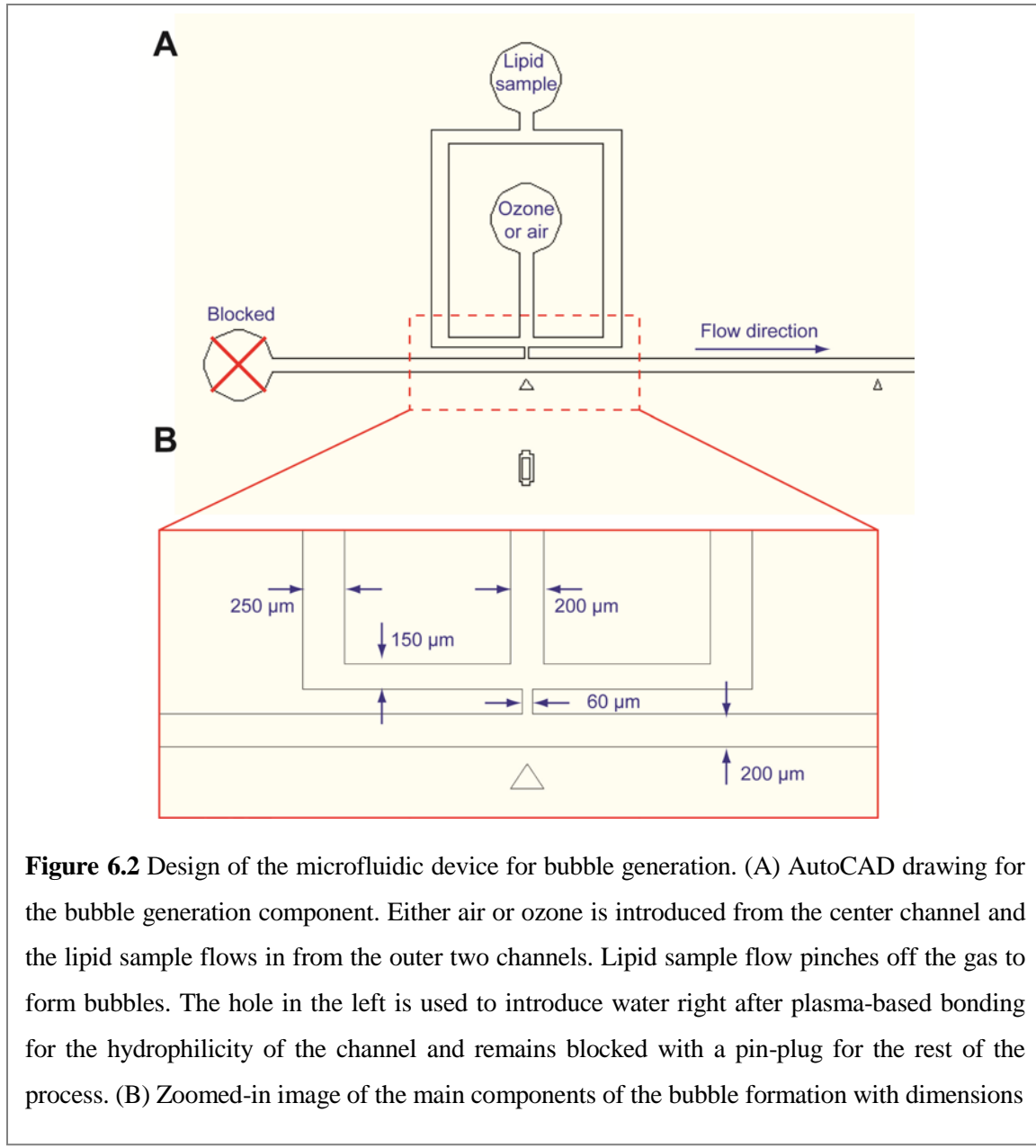


Figure 6.2 Design of the microfluidic device for bubble generation. (A) AutoCAD drawing for the bubble generation component. Either air or ozone is introduced from the center channel and the lipid sample flows in from the outer two channels. Lipid sample flow pinches off the gas to form bubbles. The hole in the left is used to introduce water right after plasma-based bonding for the hydrophilicity of the channel and remains blocked with a pin-plug for the rest of the process. (B) Zoomed-in image of the main components of the bubble formation with dimensions

UV calibration lamp (model 6035, Oriel) that was placed upstream of the pressure regulator. By turning on the UV lamp, air flow was converted to ozone flow. Ozone concentration was measured spectrophotometrically and maintained as 20 ppm.

The bubble formation process was monitored by a microscope throughout the experiments and recorded as a movie at 30 frames/sec by a CCD camera. All the images were extracted from the movie by DVDDVideoSoft (DVDDVideoSoft.com) and analyzed

with ImageJ (NIH) for the size and the generation time for the bubbles. The formation times for the first thirteen bubbles were measured for the analysis. For the bubble size analysis, the lengths of twenty bubbles were measured and 10% sample trimmed mean was obtained for the analysis.

6.2.6. Analysis and imaging of the ozone effect

To visualize the ozone effect at the interface, fluorescence-labeled PG lipid was added to the lipid sample. The lipid sample composition was 20 μM DPPC, 10 μM POPG, and 10 μM NBD-PG in 1 \times PBS solution. The same flow condition as for the bubble formation test was used while monitoring the fluorescence. Fluorescence images were taken by a fluorescence confocal microscopy for the air as well as the ozone conditions. 10 frames averaged image with the exposure of 7.2 μs and the gain of 7.7 was taken for visualization. Gray value intensity was measured with ImageJ.

6.3 Results and Discussion

6.3.1 Probing chemical property changes by FIDI

Interfacial Reaction of POPG with O₃. The *cis*-double bond of an unsaturated phospholipid reacts with O₃, yielding aldehyde and carboxylic acid products directly from primary ozonide (POZ) or through energetic Criegee intermediates (CI), while saturated phospholipids such as DPPG and DPPC remain intact. In this study we have investigated the heterogeneous reaction of O₃ with POPG as a representative unsaturated phospholipid in the PS system.

The negative ion FIDI-MS spectra for ozonolysis of POPG in a water/methanol (1:1 by volume) droplet are shown in Figure 6.3. Singly deprotonated POPG, observed at m/z 747, is seen as a dominant species in the FIDI-MS spectrum before O₃ application. Products resulting from ozonolysis of POPG appear at least as early as 5 s after exposing the droplet to O₃. The aldehyde and carboxylic acid products are observed at m/z 637 and m/z 653, respectively. In addition, hydroxyhydroperoxide (HHP), methoxyhydroperoxide (MHP), and what we assume to be the secondary ozonide (SOZ) are also observed as products of POPG ozonolysis at m/z 671, m/z 685, and m/z 795, respectively. The relative abundance of the reactant POPG decreases dramatically after 15 s of exposure, and the FIDI-MS spectrum is dominated by ozonolysis products after 30 s.

The formation of primary ozonide (POZ), which is the first step in the ozonolysis of POPG at the air-liquid interface, is described as



The ozone concentration is assumed to be constant during the reaction, which allows calculating the reaction rate using the pseudo-first-order rate constant k₂ = k₁[O₃], where k₁ = 4.5 × 10⁻¹⁶ cm³ molecule⁻¹ s⁻¹ adopted from ozonolysis of OPPC on NaCl.³⁵ The applied ozone concentration is ~ 5 × 10¹⁴ molecule cm⁻³ (20 ppm). The reaction rate is expressed as

$$-\frac{d[POPG]_{surf}}{dt} = k_2 [POPG]_{surf,0} \quad (6.2)$$

Solving eq. 6.2 gives

$$\frac{[POPG]_{surf}}{[POPG]_{surf,0}} = e^{-k_2 t} \quad (6.3)$$

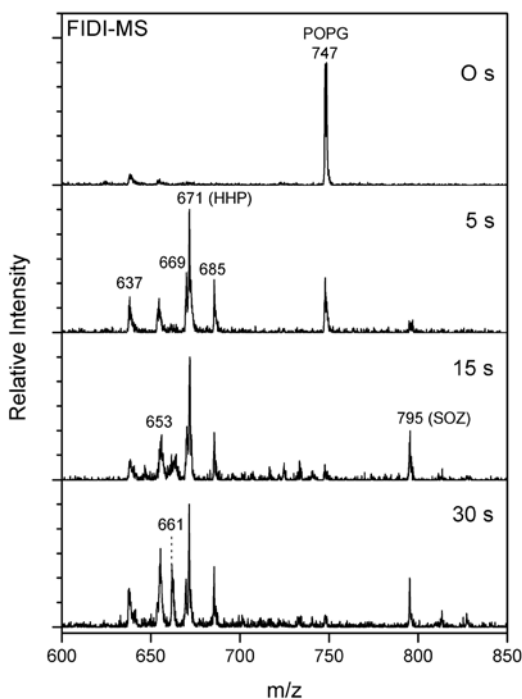
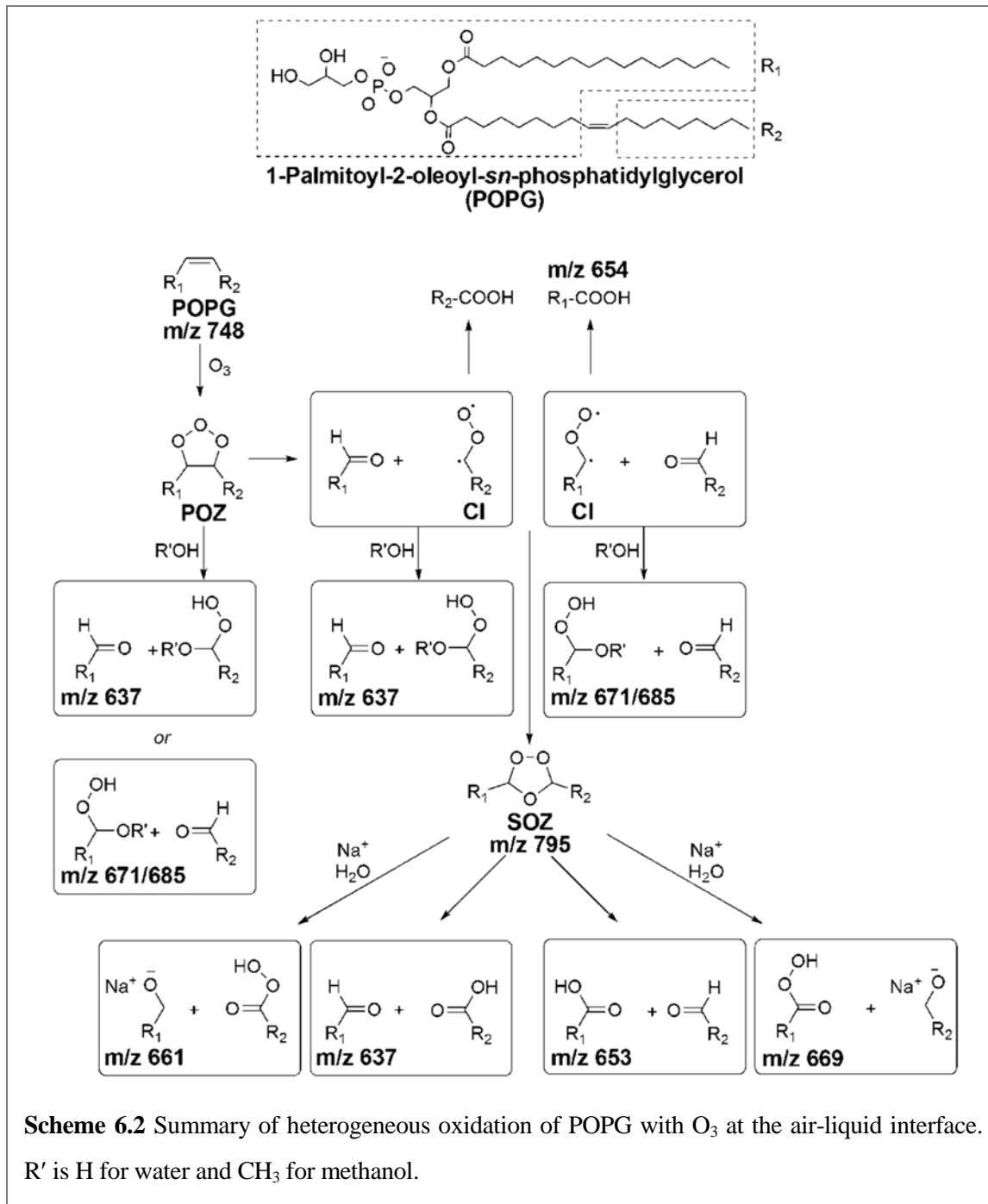


Figure 6.3 Heterogeneous reaction of POPG with O_3 as a function of time. In the absence of ozone, the negative ion FIDI-MS spectrum of POPG is dominated by the singly deprotonated POPG peak at m/z 747. POPG is depleted after 15 s of exposure, and oxidation products are dominated by deprotonated HHP at m/z 671. The aldehyde, carboxylic acid, and methoxyhydroperoxide products are observed at m/z 637, m/z 653, and m/z 685, respectively. The SOZ and sodiated alcohol products show up in the spectra at m/z 795 and m/z 661, respectively. The structure of each product is shown in Scheme 6.2.

For 90% and 99% depletion of POPG at the air-liquid interface, it takes ~ 10 s and ~ 20 s, respectively. This agrees well with the experimental observation of this study.

It is noteworthy that hydroxyhydroperoxide (HHP), methoxyhydroperoxide (MHP), and the SOZ, which are known to be metastable species in the bulk phase, are observed as major products of POPG ozonolysis in the FIDI-MS spectra (Figure 6.3).³⁵ In order to yield HHP, a Criegee intermediate (CI) or a POZ is required to react with a water molecule.^{35, 36} Rapid decomposition of HHP through proton transfers from water molecules yields



ROS,³⁶ which makes it difficult to observe HHP directly in the bulk-phase. The water density at the air-liquid interfacial region is significantly lower than in the bulk-phase.³⁷ In addition, water molecules in a lipid layer at the air-liquid interface are observed to be localized within the lipid head group region due to the strong interactions with polar head

groups.³⁸ These conditions allow HHP to be abundant in the lipid layer at the air-liquid interface, which is a characteristic of the heterogeneous reaction of POPG compared to the homogeneous reaction.³⁶ The observed MHP originates from the reaction of a CI or POZ with a methanol molecule in the droplet. The proposed reaction mechanisms are shown in Scheme 6.2.

A significant abundance of SOZ is observed in the FIDI-MS spectra after exposing the droplet to O₃ for 15 s. The structure of SOZ (m/z 795) is confirmed by low-energy-collision induced dissociation (CID), which yields the aldehyde (m/z 637) and carboxylic acid (m/z 653) fragments (Fig. 6.4). The peak corresponding to SOZ continues to build up

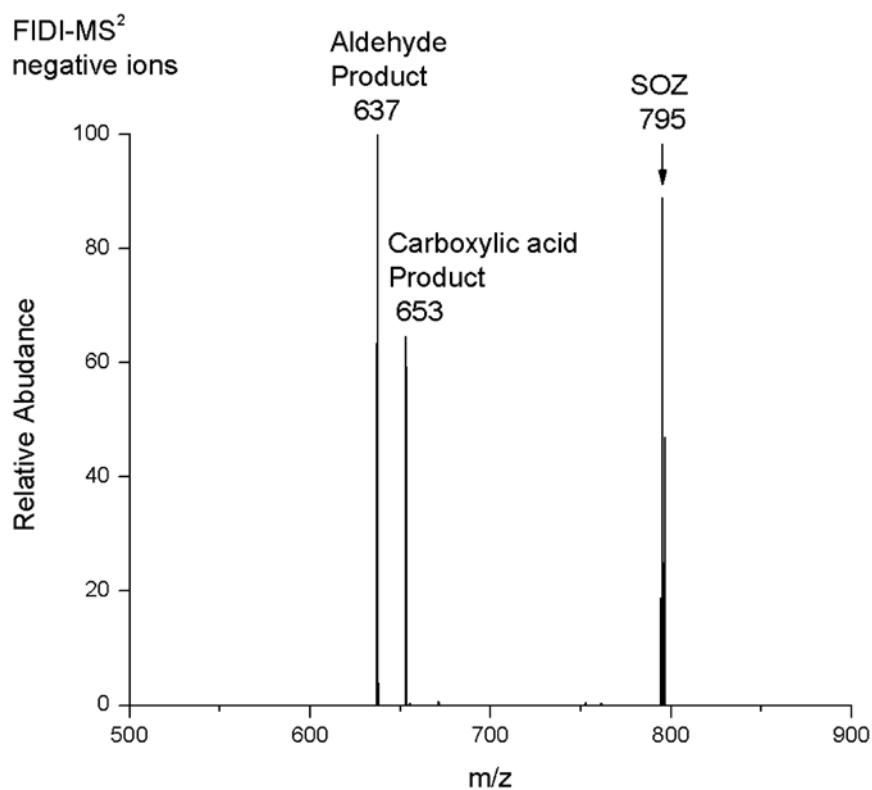


Figure 6.4 The FIDI-MS² spectrum of SOZ at m/z 795 showing two competitive products at m/z 637 and at m/z 653, which correspond to the aldehyde and carboxylic acid fragments, respectively

in the spectrum as the POPG lipid is depleted. We infer that the observed SOZ is not formed by direct rearrangement of POZ but rather by recombination of the CI with aldehydes (Scheme 6.2).^{35, 39} In the bulk-phase, however, faster reaction with water molecules prevents the CI from reacting with aldehyde to form SOZ.⁴⁰ A significant amount of the sodiated alcohol product (m/z 661) is observed after exposing the droplet to O_3 for 30 s. This product is due to the dissociation of SOZ followed by the association with sodium cation. This suggests that after SOZ is produced in an anhydrous environment, the newly formed hydrophilic molecule interacts with sodium cation in the liquid-phase to yield the sodiated alcohol product. These SOZ and sodiated alcohol products are characteristic of specific air-liquid interface chemistry during POPG ozonolysis.

Interfacial Reaction of a POPG and DPPG Mixture with O_3 . Figure 6.5 shows negative ion FIDI-MS spectra for the heterogeneous ozonolysis at several reaction times of a mixture of DPPG and POPG at the air-liquid interface. Conditions employed are identical to those used to obtain the data shown in Figure 6.3. Singly deprotonated DPPG and POPG, observed at m/z 721 and m/z 747, respectively, dominate the FIDI-MS spectrum before O_3 application, suggesting that the pulmonary surfactants DPPG and POPG form a mixed interfacial layer. The products resulting from the ozonolysis of POPG appear at least as early as 5 s after exposing the droplet to O_3 . All products, including aldehyde (m/z 637), carboxylic acid (m/z 653), HHP (m/z 671), and MHP (m/z 685), are observed to result from ozonolysis of POPG in the mixed surfactant system. The relative abundance of the reactant POPG decreases by half after 15 s of exposure, while the product abundance continues to increase after up to 30 s of exposure. The FIDI-MS spectrum is dominated by DPPG after 45 s.

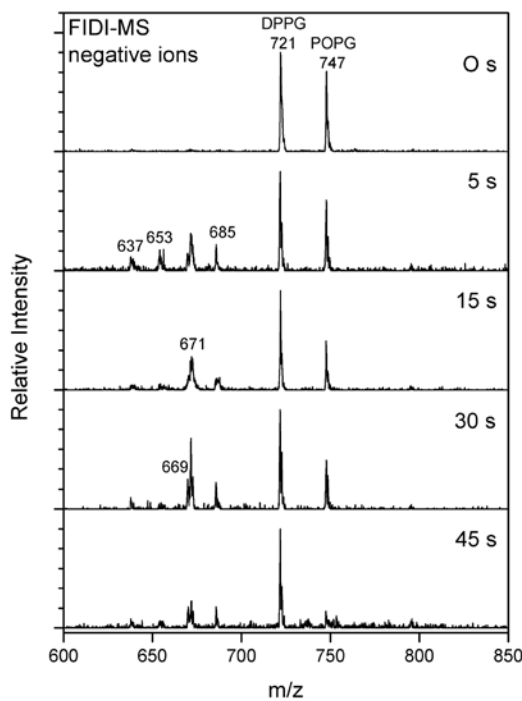


Figure 6.5 Heterogeneous reaction of a 1:1 mixture of POPG and DPPG with O_3 as a function of time. In the absence of ozone, the negative ion FIDI-MS spectrum is dominated by singly deprotonated POPG and DPPG at m/z 747 and m/z 721, respectively. The oxidation products of POPG—including aldehyde (m/z 637), carboxylic acid (m/z 653), HHP (m/z 671), and MHP (m/z 685)—are observed after 5 s of O_3 exposure. Singly deprotonated DPPG dominates the FIDI-MS spectrum after 45 s.

The absence of any ozonolysis products from the saturated lipid DPPG indicates that only the unsaturated lipid POPG reacts with ozone. Several differences are observed from the heterogeneous ozonolysis of the DPPG and POPG mixture compared to the ozonolysis of POPG alone. First, with extensive ozonolysis, the products disappear from the surface of the droplet, leaving only DPPG at the interface. The ozonolysis products of POPG are expected to be more hydrophilic than the precursor (Scheme 6.2). The data in Fig. 6.5 suggest that these hydrophilic products diffuse into the aqueous droplet, leaving only hydrophobic DPPG in the interfacial surfactant layer. Comparison of the results in Figs. 6.3

and 6.5 indicate that the overall ozonolysis reaction of POPG, including the depletion of POPG on the surface of the droplet, is slower in a mixture with DPPG.

The lipid tails of DPPG adopt a highly ordered arrangement in a surfactant monolayer.⁴¹ In the mixture of a DPPG and POPG, the saturated acyl chains of DPPG may act to shield POPG, limiting the approach of O₃ to the unsaturated carbons of POPG, with a corresponding slower reaction compared to POPG alone. Note also that a significant abundance of SOZ is not observed in the FIDI-MS spectrum of a mixture of DPPG and POPG (Fig. 6.5). As discussed earlier, SOZ is formed by the recombination of the CI with aldehyde under an anhydrous environment (Scheme 6.2).^{35,39} In the mixed surfactant layer, competition on the droplet surface is expected between hydrophobic DPPG and the relatively hydrophilic nascent products of POPG ozonolysis. This accounts for the observed predominance of DPPG in the FIDI-MS data at long times.

Interfacial Reaction of a SOPC and DPPC Mixture with O₃. We also investigated the heterogeneous reaction of O₃ with a mixture of saturated and unsaturated lipids using SOPC and DPPC in the positive ion mode (Fig. 6.6). In contrast to phosphatidylglycerol (PG), the positive ion mode FIDI-MS spectra of phosphatidylcholine (PC) show additional dimeric complexes along with monomers as sodiated species. The sodiated DPPC and SOPC monomers are observed at m/z 756 and m/z 810, respectively. The sodiated complexes at m/z 1489 and m/z 1597 are DPPC dimer and SOPC dimer, respectively. The heterogeneous dimeric complex of DPPC and SOPC is observed at m/z 1543. The measured intensity of the homogeneous and heterogeneous dimeric complexes are not very different from the statistical ratio (1:2:1) indicating that DPPC and SOPC form a well-mixed interfacial layer. The FIDI-MS spectrum reveals the ozonolysis products after 5 s of

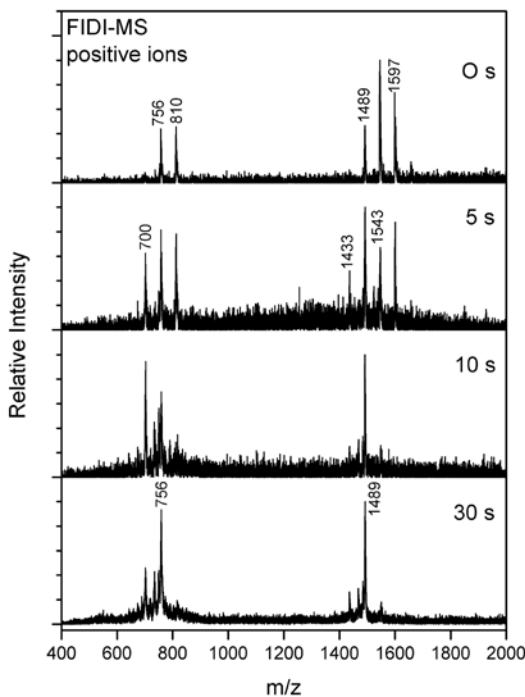


Figure 6.6 Heterogeneous reaction of a 1:1 mixture of SOPC and DPPC with O_3 as a function of time. In the absence of ozone, the positive ion FIDI-MS spectrum shows the singly charged sodiated DPPC and SOPC monomers at m/z 756 and m/z 810, respectively. The singly charged mono-sodiated DPPC and SOPC homodimers are observed at m/z 1489 and m/z 1597, respectively. The singly sodiated heterogeneous dimer of DPPC and SOPC appears at m/z 1543. The oxidation products of SOPC, including monomeric aldehyde product (m/z 700) and the complex of DPPC and aldehyde product (m/z 1433), are observed after 5 s of O_3 exposure. Sodiated DPPC monomers and dimmers of DPPC dominate the FIDI-MS spectrum after 30 s.

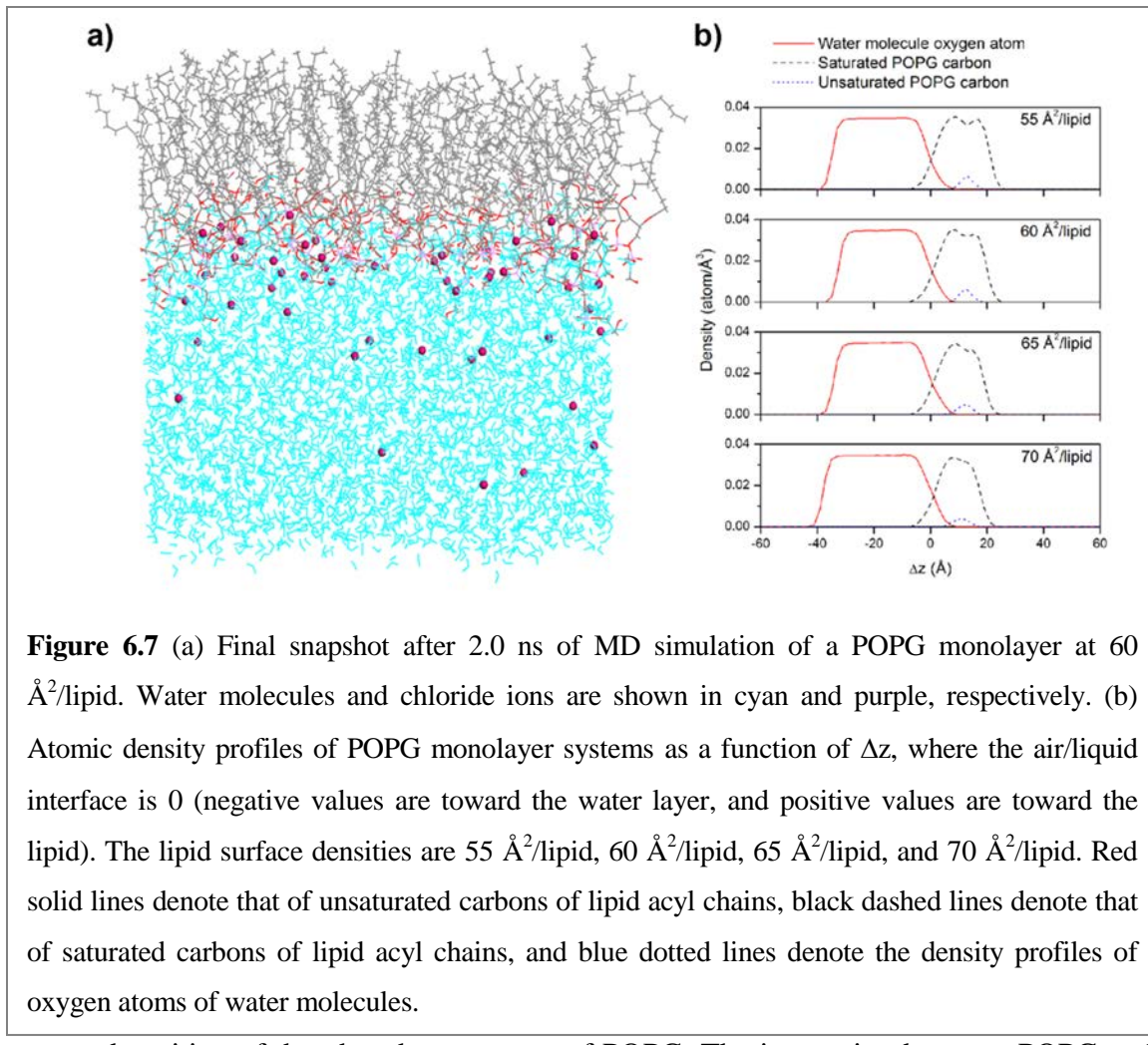
O_3 exposure. The product at m/z 700 corresponds to the sodiated aldehyde product of SOPC. The sodiated complex of intact SOPC and the aldehyde product of SOPC are observed at m/z 1543. With extensive ozonolysis (15 s), SOPC is depleted, and eventually the aldehyde products also disappear from the spectrum, suggesting that only DPPC remains in the surfactant layer.

In contrast to the negative FIDI-MS spectra of POPG, only aldehyde products are observed from the ozonolysis of SOPC. The only significant difference between the two

lipids is the nature of the polar head group, which is acidic in the case of the phosphatidylglycerol lipid and amphoteric (zwitterionic) in the case of the phosphatidylcholine lipid. However, it is not obvious how this might influence the observed difference in ozonolysis products. The two mixtures are similar in that at long times the more hydrophilic oxidation products disappear from the spectra as they are dissolved into the aqueous phase.

Note also that depletion of SOPC oxidation products occurs more rapidly from ozonolysis of the mixture of SOPC and DPPC compared to ozonolysis of the POPG and DPPG mixture. In forming a surfactant layer the fatty acid chains of the saturated phospholipid DPPC exhibit less-orderly packing compared to those of DPPG.⁴¹ More random orientation of DPPC fatty acid chains may cover unsaturated carbons of SOPC less effectively compared to DPPG, allowing SOPC to react with ozone more easily.

Water Density at the Position of Unsaturated Carbons in a Lipid Monolayer. As discussed above, the unique low water density environment of the air-liquid interface may allow us to observe metastable HHP and POZ in the heterogeneous ozonolysis of POPG. In order to develop a more detailed picture of the interfacial environmental, we carried out MD simulations for the POPG monolayer in a water box for 2.0 ns with four different surface densities (55, 60, 65, and 70 Å²/lipid). These surface densities are reported as a proper density range for pulmonary surfactant function from previous theoretical studies.^{41–43} The final snapshot in Fig. 6.7a shows the POPG monolayer at the air-liquid interface monolayer with 60 Å²/lipid surface density as a representative case. Fig. 6.7b shows the atomic density profiles of oxygen atoms of water molecules, saturated carbon atoms, and unsaturated carbon atoms of lipid acyl chains along ±Δz, which is z-direction relative to the



averaged position of the phosphorous atom of POPG. The interaction between POPG and water occurs in the region of overlapping density. The lipid head group is solvated, reflecting the strong ion-dipole interactions between the POPG phosphate group and water molecules. However, the water density at the double bond of POPG (5–20 \AA) is $\sim 0.0005 \text{ atom}/\text{\AA}^3$, which is ~ 70 times less dense than in the bulk-phase ($\sim 0.035 \text{ atom}/\text{\AA}^3$) when the POPG monolayer has 60 $\text{\AA}^2/\text{lipid}$ surface density. This indicates that a limited number of water molecules are involved when ozone interacts with the double bond of POPG. A single water molecule is required to form a HHP from a CI or a POZ.^{35,36} Further reactions with water molecules result in formation of ROS (Scheme 6.2).³⁶ The low water

concentrations around the double bond allow HHP to survive sufficiently long to be observed in the FIDI-MS spectra. It is noteworthy that SOZ appears after POPG is depleted on the surface of the droplet (Fig. 6.3). The fast reaction with water inhibits formation of SOZ from CI when water molecules are accessible.⁴⁰ Depletion of the limited number of water molecules in the hydrophobic portion of the ordered lipid allows SOZ to form and accumulate in the surfactant layer.

Solvation Energy of Phospholipids and Ozonolysis Products. We observe composition changes in the lipid surfactant layer resulting from ozonolysis of saturated and unsaturated phospholipid mixtures using time-resolved FIDI-MS (Fig. 6.5 and 6.6). To understand the surface activity of phospholipids and their oxidized products, DFT calculations were performed to compute the solvation energy, ΔE_{solv} , for DPPG, POPG, and two products (carboxylate and aldehyde) from the ozonolysis of POPG. The calculated ΔE_{solv} indicates the energy difference between the gas phase and the solution phase. Lower values of ΔE_{solv} would be expected to correlate with higher surface activity of molecules at the air-liquid interface. In addition, ΔE_{solv} provides a measure of the relative hydrophobicities of similar molecules. These results provide a reasonable explanation of the observed disappearance of the ozonolysis products from the surface of the droplet over time. Calculations were performed for both neutral and anionic states of the phosphatidylglycerol group. Table 6.1 lists the calculated ΔE_{solv} values of DPPG, POPG, and the ozonolysis products of POPG. The solvation of a singly charged anion is energetically favored compared to the corresponding neutral lipid by ~ 58 kcal/mol. Both anionic and neutral DPPG and POPG exhibit similar stability in the solution phase. This supports our hypothesis, based on the observed lipid distribution in the FIDI-MS spectrum

shown in Fig. 6.5, that both DPPG and POPG are co-located at the surface of the droplet. Carboxylic acid products are more stable in the solution phase compared to intact DPPG and POPG by ~ 8 kcal/mol. Once the carboxylic acid dissolves in the solution phase, further stability can be achieved by deprotonation of carboxyl group. The ΔE_{solv} of an aldehyde product is calculated as ~ 4.5 kcal/mol less than that of an intact POPG. However, it is ~ 3.7 kcal/mol higher than the ΔE_{solv} of a carboxylic acid product. This indicates that aldehyde products have higher surface activity than carboxylic acid products at the surface of the droplet. This agrees well with the positive ion mode FIDI-MS spectra, in which aldehyde is the predominant observed product from the ozonolysis of unsaturated phospholipids (Fig.6.6).

Table 6.1 Calculated solvation energies of phospholipids and ozonolysis products

Lipid	Solvation Energy (kcal/mol)	
	Neutral	Anionic
DPPG	-32.9	-91.5 ^a
POPG	-33.6	-91.7 ^a
Aldehyde product	-38.3	-96.2 ^a
Carboxylate product	-41.8	-100 ^a , -184 ^b

^aSingly charged anion with deprotonated phosphatidylglycerol group. ^bDoubly charged anion with deprotonated phosphatidylglycerol and carboxylate groups

6.3.2 Probing physical property changes by microfluidic bubble generator

Bubble Formation in a Microfluidic Device. The size of bubbles and the frequency of bubble generation were monitored to study physical characteristics induced by the change

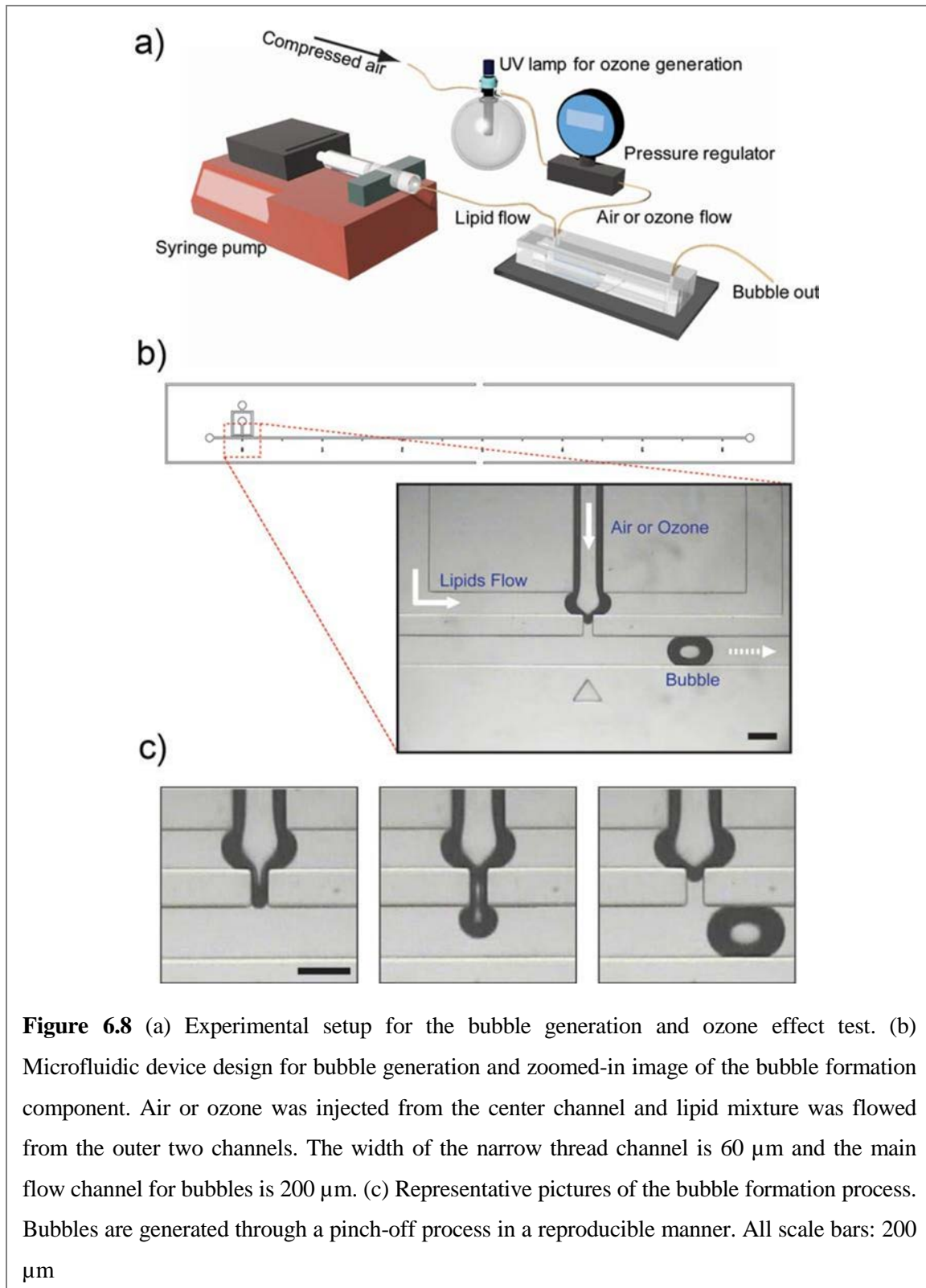


Figure 6.8 (a) Experimental setup for the bubble generation and ozone effect test. (b) Microfluidic device design for bubble generation and zoomed-in image of the bubble formation component. Air or ozone was injected from the center channel and lipid mixture was flowed from the outer two channels. The width of the narrow thread channel is 60 μm and the main flow channel for bubbles is 200 μm . (c) Representative pictures of the bubble formation process. Bubbles are generated through a pinch-off process in a reproducible manner. All scale bars: 200 μm

of chemical properties in the lipid layer. The experimental setup, device designs and bubble formation process are shown in Fig. 6.8. The bubble generation device comprises three

Table 6.2 Bubble size (in pixel) and the polydispersity index

	Air	Ozone
Average	64.43244	61.72388
Standard deviation	0.672664	1.125165
Polydispersity Index	1.043983	1.8229

$$\text{polydispersity index} = \frac{\text{standard deviation}}{\text{average}} \times 100$$

inlet channels: a center channel supplying gas and two outer channels supplying lipid mixture in solution. There is a constant inflow of lipids mixture and gas-generated bubbles in a highly reproducible manner through a pinch-off process (Fig. 6.8c). Bubbles were

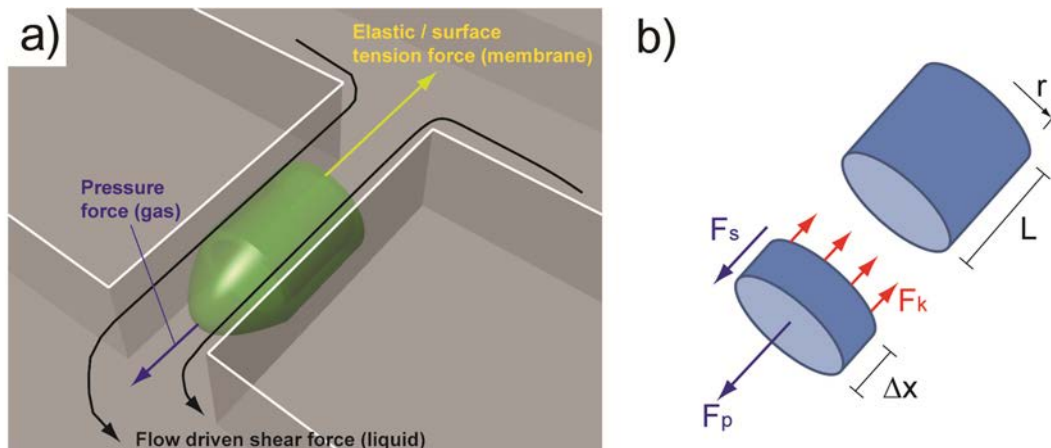


Figure 6.9 (a) Major force components for bubble generation on the lipid monolayer in the narrow channel region. Elastic force of the phospholipid monolayer at the air-liquid interface counteract the pressure force from the gas and the shear force from the bulk lipid flow. Since the pressure for the gas and the flow rate for the bulk lipid flow are fixed, the physical characteristics of the lipid monolayer plays a major role in the bubble formation process. (b) Free body diagram for the force balance. The interface in the thread (the narrow channel region) is assumed to be a cylinder.

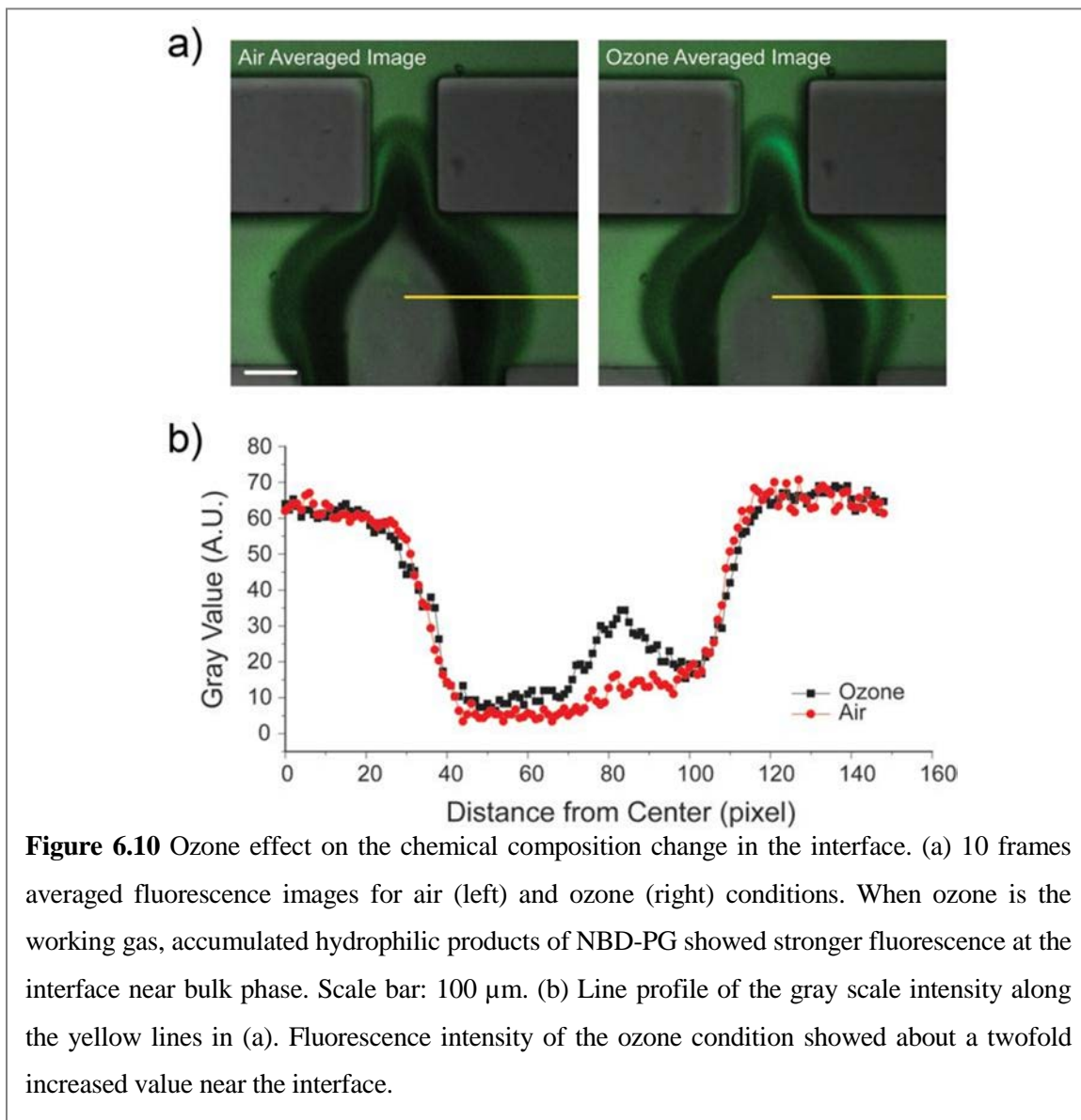
generated with a polydispersity index of ~ 1% (Table 6.2). The polydispersity index is defined as the standard deviation of the length of the bubble divided by the mean length of the bubble in percentage. Low polydispersity index indicates that our device enables making uniform bubbles, which leads to a statistically meaningful analysis on the interface.

Most commonly used microfluidic devices for bubble generation are based on two geometries: T junction^{22, 44} and FFD.^{23, 34} Our design is mostly based on FFD but also has a T-junction-like characteristic due to the perpendicular main flow channel to the bubble formation components. Thus, we can think of three major factors dominant for the bubble formation: pressure force from gas, shear stress induced by flow, and the elastic property of the monolayer thin film (Fig. 6.9).⁴⁵ Since we fix the pressure of gas and the flow rate, the characteristic change in the bubble is induced by a physical property change of the lipid monolayer, such as the interfacial tension or elasticity that will be discussed below.

Ozone Effect on the Air-Liquid Interface. In previous section (6.3.1), we demonstrated the heterogeneous ozonolysis of a mixture of saturated and unsaturated phospholipids at the air-liquid interface by field-induced droplet ionization mass spectrometry (FIDI-MS).⁴⁶ We found that only the unsaturated phospholipids react with ozone and form relatively hydrophilic products such as aldehyde and carboxylic acid which dissolve into the bulk phase leaving only saturated phospholipid on the surface of the droplet at ~ 30 s of time scale. In order to visualize this chemistry in our system, we used fluorescence-labeled unsaturated lipids, NBD-PG. NBD-PG has the same structure as POPG except for the fluorescence tag on the saturated acyl chain. Constant flow of lipid mixture of DPPC, POPG, and NBD-PG was maintained and either air or ozone was

introduced to generate bubbles. Stronger fluorescence was observed at the interface near liquid phase when ozone was introduced (Fig. 6.10). The stronger fluorescence is induced by the hydrophilic products (aldehyde and carboxylate) of NBD-PG that are dissolved into the bulk phase and accumulated near the interface. This indicates that we can visually detect the chemical change of the unsaturated lipid components induced by ozonolysis, which further supports our previous finding.⁴⁶

Since DPPC and POPG represent major components of saturated and unsaturated



phospholipds, respectively, in our lung pulmonary surfactant system, it is interesting to see physical as well as chemical property change of the air-liquid interface induced by environmental stress such as ozone. Especially, DPPC is known as the principal phospholipid component with very low surface tension upon compression^{8,47} and POPG is known to improve the adsorption and spreading of surfactant owing to its higher fluidity.⁴⁸ Thus, dissolving POPG into the bulk solution from the interface can change the physical characteristics of the interface, which relates to lung physiology and disease. It is also notable that the increase in ozone concentration is associated with the high risk of death from respiratory causes.⁴ In that sense, it is necessary to study the physical characteristics of our lung surfactant system under the environmental challenge, and microbubble can be a good model for a more in-depth understanding of the system owing to its air-liquid interface nature and similar size to the alveoli (100–300 μm).

Elastic Property of the Lipid Monolayer. We investigated the change of bubble formation processes caused by the chemical compostion alteration in a mixed lipid surfactant layer of DPPC and POPG due to the oxidative stress by ozone. In both cases, the tip of the interface near the bubble formation region oscillated significantly until the bubble was ejected to the flow (Fig. 6.11a and b). However, a significant difference was observed in a bubble formation process with ozone compared to air. In Fig. 6.11b we plotted the time-lapsed trajectories of the lower tip of the interface until bubbles were formed. Stronger oscillation was observed for the case of air compared to the case of ozone. The oscillatory characteristic indicates that the elastic property of the interface is different between air and ozone conditions. To further analyze this, we can consider the effective elastic modulus (E_{eff}) defined as

$$E_{eff} = \frac{\text{stress}}{\text{strain}}. \quad (6.4)$$

Under the assumption that the interface near the bubble formation region (in the thread) can be simplified as a cylinder (Fig. 6.9), we can expect the following force balance at equilibrium based on the free body diagram (Fig. 6.9b),

$$F_p + F_s = F_k. \quad (6.5)$$

where F_p , F_s , and F_k are pressure force, shear force and restoring elastic force, respectively.

By using $F_p = p\pi r^2$ and $F_k = k\Delta x$, eq. 6.5 becomes,

$$F_s = k\Delta x - p\pi r^2. \quad (6.6)$$

where k is the spring constant of the monolayer, Δx is transverse displacement, p is the applied pressure, and r is the radius of the cylinder. Then,

$$E_{eff} = \frac{\text{stress}}{\text{strain}} = \frac{p + F_s/2\pi rL}{\Delta x/L}. \quad (6.7)$$

where L is the initial length of the cylinder in the thread. In equilibrium condition, we can assume a harmonic oscillatory motion and the harmonic approximation leads to $F_k = k\Delta x = m(2\pi f)^2 \Delta x$, where m is the mass of the oscillating body, and f is the oscillation frequency.

From eqs. (6.6) and (6.7), the effective elastic modulus can be expressed as

$$E_{eff} = \frac{PL}{\Delta x} \left(1 - \frac{r}{2L}\right) + \frac{2\pi mf^2}{r}. \quad (6.8)$$

Assuming that low concentration of ozone (~ 20 ppm) does not change the density of working gas, E_{eff} becomes a function of the oscillation amplitude and the frequency. Analysis on our data in Fig. 6.11b shows that E_{eff} at the interface when ozone is applied is $\sim 28\%$ higher compared to the case of air. Numerical values used for the calculation can be found in Table 6.3. As discussed earlier, once the mixture is exposed to the ozone, POPG reacts with ozone and the products dissolve into the bulk phase: This leads to the higher

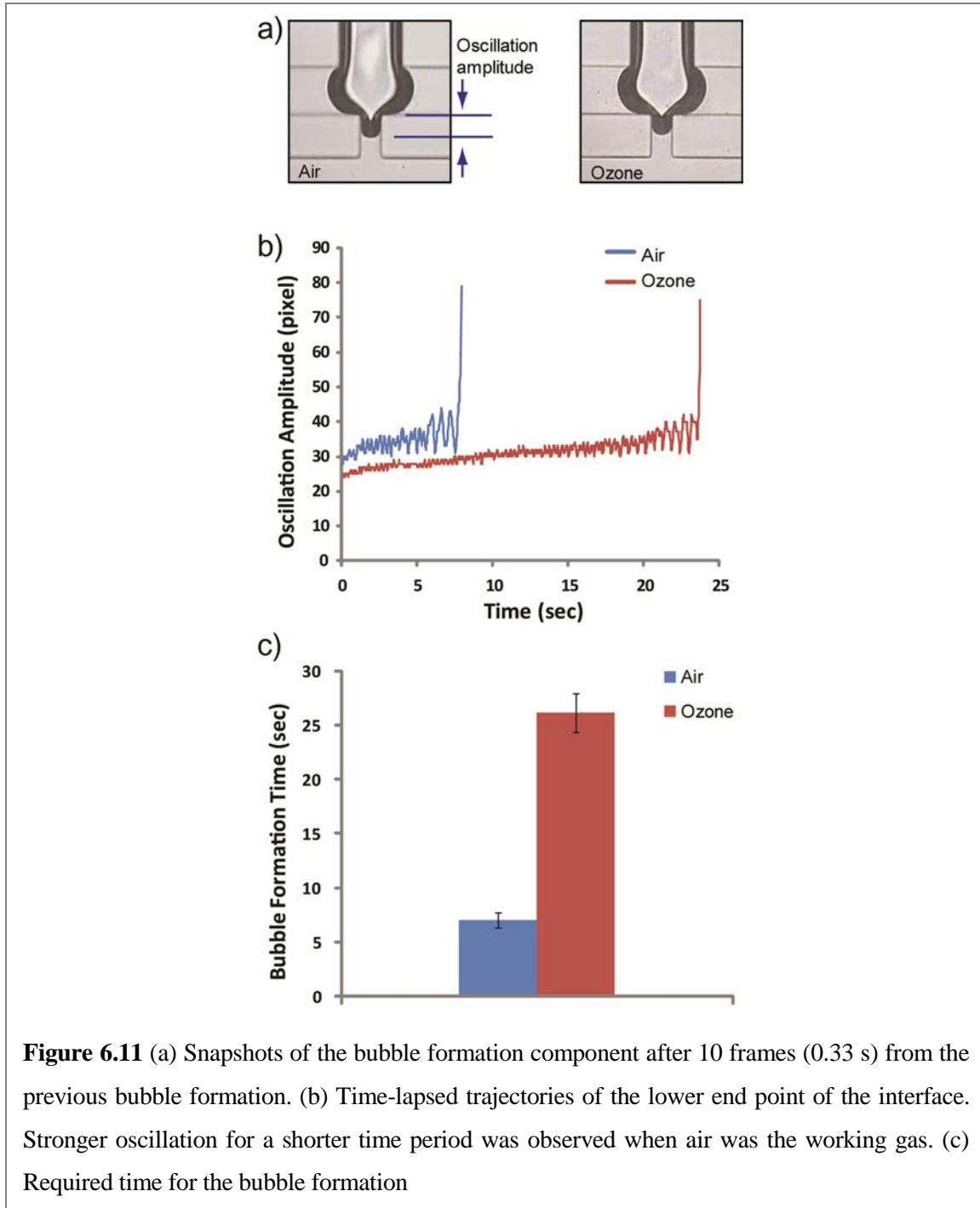


Figure 6.11 (a) Snapshots of the bubble formation component after 10 frames (0.33 s) from the previous bubble formation. (b) Time-lapsed trajectories of the lower end point of the interface. Stronger oscillation for a shorter time period was observed when air was the working gas. (c) Required time for the bubble formation

concentration of DPPC at the interfacial surfactant layer, which yields a more elastic interface (primarily due to less fluidity of the saturated lipids compared to the unsaturated ones).

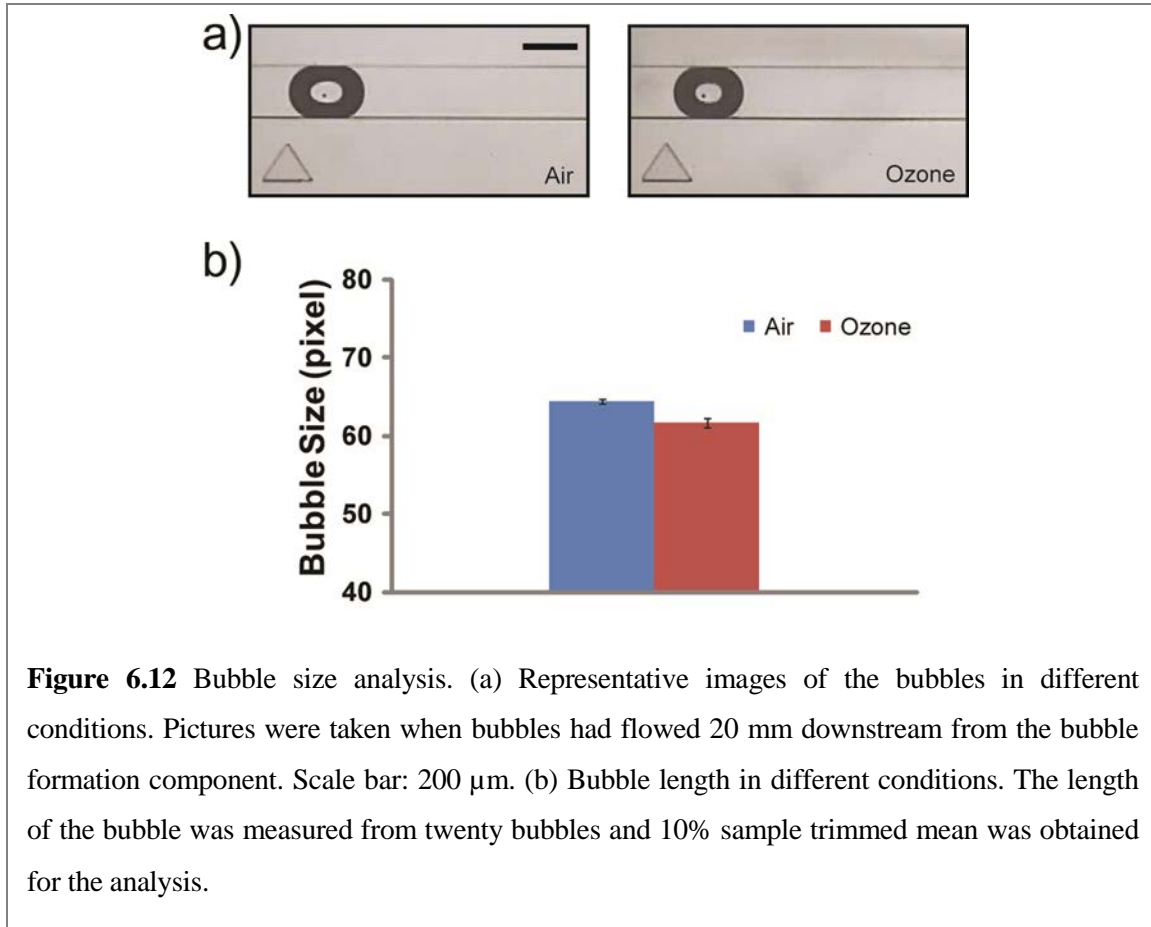
Another interesting factor to look at is the time required for the bubble formation (Fig. 6.11c). Obviously longer time was required for a bubble to be generated in the ozone condition. In our cylinder-shaped harmonic oscillator model, we can use an analogy between the bubble formation process and a deformation process of a material under increasing tensile stress. Assuming that the yield strain is similar for both air and ozone cases, the longer bubble formation time (i.e., higher yield stress) means that the system is more elastic (i.e., steeper slope in the stress-strain curve). Thus, the observed longer bubble formation time when ozone is introduced also indicates the higher E_{eff} value resulted from the low POPG content at the interface.

Table 6.3 Parameters for the effective elastic modulus calculation

	Air	Ozone
p	0.42 psi	
L	75 μm	
r	30 μm	
Δx	4.575 μm	3.575 μm
f^*	3.48 Hz	3.52 Hz
m	$1.68 \times 10^{-14} \text{ kg}$	$1.31 \times 10^{-14} \text{ kg}$
E_{eff}	37973.5 Pa	48595.5 Pa

* Frequency was obtained from the stable region in oscillation: for the air condition, 1.25 ~ 3.55 s and for the ozone condition, 13.75 ~ 17.30 sec regions were chosen to obtain the frequency.

Ozone Effect on Bubble Size. Bubble size is another metric for the physical property of the lipid surfactant layer. In Fig. 6.12, representative pictures of bubbles (a) and the averaged bubble sizes (b) are presented. The bubble size is smaller when ozone is the working gas. We can think of a simple scaling of the bubble size as Garstecki et al. has reported previously ^{34, 45}: $V_b \propto q_g \tau$, where V_b is the volume of bubble, q_g is the rate of inflow gas, and τ is the time that the thread stays open until bubble is ejected to the flow.



Since τ is inversely proportional to the elasticity, we can expect that high elasticity induces a shorter τ that reduces the volume of the bubble. This agrees well with our observation of increased E_{eff} and reduced size resulting from the increase of DPPC mole fraction in the surfactant layer following the heterogeneous ozonolysis of POPG. In addition to the effect of the elasticity of the surfactant layer, we can also examine the dynamic viscosity of the interface when the surfactant composition changes. The Hagen-Poiseuille relation, $q_g \propto p/\mu$ and $\tau \propto 1/q$, leads to $V_b \propto p/q\mu$, where μ is the dynamic viscosity and q is the volume flow rate of the solution. Since p and q are fixed in our experiment, we can compare the dynamic viscosity for both conditions simply by measuring bubble size. From the measured bubble scale, we found that the dynamic viscosity of the surfactant layer was increased by $\sim 4.4\%$ when ozone was used compared to pure air for bubble formation. We

found that the bubble formation process is very sensitive to the alterations of the lipid compositions in the surfactant layers and has a potential for being an analytical tool for studying interface physics.

6.4 Conclusions

The FIDI-MS technique is well suited to analyze chemical reactions of phospholipids at the air-liquid interface. In FIDI-MS spectra, ozonolysis products distinct from those formed in both the bulk-phase and the gas-phase are observed from an interfacial phospholipid surfactant layer. MD simulations correlate well with experimental observations and provide additional insights into the interactions between lipids and water molecules in the interfacial region. In these simulations the low water density around unsaturated carbons of the lipid acyl chain provides a rationalization for the experimental observation of metastable products resulting from ozonolysis of unsaturated phospholipids.

In the lung, oxidation of pulmonary surfactant causes surfactant dysfunction in adsorption and resspreading process, as well as reduction of surface tension.^{49, 50} Once O₃ traverses the air-liquid interface, it decays rapidly concomitant with the formation of ROS in regions with high water densities.⁵¹ However, due to the high reactivity with PS at the interface, it has been thought that little or none of the O₃ can penetrate the PS monolayer to attack the epithelium cells below.⁵² Instead of direct attack by O₃ and its derivative ROS, secondary oxidized products of PS, such as HHP, have been expected to yield cellular damage.⁵² Our FIDI-MS data indicate that more than 60% of the heterogeneous oxidation products of POPG by O₃ are peroxides. These products, which are more water soluble than

the lipid precursors, eventually dissolve into the bulk liquid where they form ROS³⁶ that can lead to cellular damage.

These findings provide mechanistic details for the reaction of ozone with unsaturated phospholipids, leading to possible damage of the pulmonary system by ROS or direct ozone exposure. Further studies with more elaborate model systems comprising surfactant proteins and various lipids could further clarify the effect of environmental exposures on the lung surfactant system. We have reported one such study, demonstrating that phospholipid surfactants have a profound effect in moderating the reactions of the important surfactant protein B with ozone.¹⁹

We also have developed a microfluidic bubble generator that enables the analysis of physical property changes in a model pulmonary surfactant layer at the air-liquid interface under oxidative stress condition. The bubble formation process was very sensitive to the surfactant composition. Chemical composition change of the phospholipid mixture under oxidative stress in the air-liquid interface was identified visually through fluorescence monitoring. Our platform was further validated for its potential use in studying the physical characteristics of the interface resulting from chemical reactions at the interface. Heterogeneous reactions followed by chemical composition changes have been studied as important parameters on the physics of the lipid surfactant, and we were able to observe their effects in terms of the bubble size and the formation process, especially oscillatory behavior. Owing to the sensitive response, reproducibility for good statistics, and the ease of manipulation/analysis, we believe that microbubbles in microfluidics have potential in understanding the interfacial physics as well as chemistry of the various surfactant systems.

6.5 References

1. Stansfield, A. D.; Jump, Z.; Sodlosky, S.; Rappaport, S.; Edelman, N.; Haldorsen, J.; Javed, T.; Martin, C.; Margulies, E. *Lung disease data: 2008*; American Lung Association National Headquarters. New York, 2008.
2. Anseth, J. W.; Goffin, A. J.; Fuller, G. G.; Ghio, A. J.; Kao, P. N.; Upadhyay, D., Lung surfactant gelation induced by epithelial cells exposed to air pollution or oxidative stress. *American Journal of Respiratory Cell and Molecular Biology* **2005**, 33, (2), 161–168.
3. Halliwell, B.; Gutteridge, J. M. C., Oxygen-toxicity, oxygen radicals, transition-metals and disease. *Biochemical Journal* **1984**, 219, (1), 1–14.
4. Jerrett, M.; Burnett, R. T.; Pope, C. A.; Ito, K.; Thurston, G.; Krewski, D.; Shi, Y. L.; Calle, E.; Thun, M., Long-Term Ozone Exposure and Mortality. *New England Journal of Medicine* **2009**, 360, (11), 1085–1095.
5. Perez-Gil, J.; Keough, K. M. W., Interfacial properties of surfactant proteins. *Biochimica Et Biophysica Acta—Molecular Basis of Disease* **1998**, 1408, (2–3), 203–217.
6. Lambert, M. G.; Vangolde, L. M. G.; Batenburg, J. J.; Robertson, B., The pulmonary surfactant system—biochemical aspects and functional significance. *Physiological Reviews* **1988**, 68, (2), 374–455.
7. Schram, V.; Hall, S. B., SP-13 and SP-C alter diffusion in Bilayers of pulmonary surfactant. *Biophysical Journal* **2004**, 86, (6), 3734–3743.

8. Hawco, M. W.; Davis, P. J.; Keough, K. M. W., Lipid Fluidity in Lung Surfactant—Monolayers of Saturated and Unsaturated Lecithins. *Journal of Applied Physiology* **1981**, 51, (2), 509–515.
9. Diemel, R. V.; Snel, M. M. E.; Waring, A. J.; Walther, F. J.; van Golde, L. M. G.; Putz, G.; Haagsman, H. P.; Batenburg, J. J., Multilayer formation upon compression of surfactant monolayers depends on protein concentration as well as lipid composition—An atomic force microscopy study. *Journal of Biological Chemistry* **2002**, 277, (24), 21179–21188.
10. Perez-Gil, J., Molecular interactions in pulmonary surfactant films. *Biology of the Neonate* **2002**, 81, 6–15.
11. Grimm, R. L.; Hodyss, R.; Beauchamp, J. L., Probing interfacial chemistry of single droplets with field-induced droplet ionization mass spectrometry: Physical adsorption of polycyclic aromatic hydrocarbons and ozonolysis of oleic acid and related compounds. *Analytical Chemistry* **2006**, 78, (11), 3800–3806.
12. Voss, L. F.; Hadad, C. M.; Allen, H. C., Competition between atmospherically relevant fatty acid monolayers at the air/water interface. *Journal of Physical Chemistry B* **2006**, 110, (39), 19487–19490.
13. Mundy, C. J.; Kuo, I. F. W., First-principles approaches to the structure and reactivity of atmospherically relevant aqueous interfaces. *Chemical Reviews* **2006**, 106, (4), 1282–1304.
14. Gonzalez-Labrada, E.; Schmidt, R.; DeWolf, C. E., Kinetic analysis of the ozone processing of an unsaturated organic monolayer as a model of an aerosol surface. *Physical Chemistry Chemical Physics* **2007**, 9, (43), 5814–5821.

15. Enami, S.; Hoffmann, M. R.; Colussi, A. J., Acidity enhances the formation of a persistent ozonide at aqueous ascorbate/ozone gas interfaces. *Proceedings of the National Academy of Sciences of the United States of America* **2008**, 105, (21), 7365–7369.
16. Enami, S.; Hoffmann, M. R.; Colussi, A. J., Ozonolysis of uric acid at the air/water interface. *Journal of Physical Chemistry B* **2008**, 112, (14), 4153–4156.
17. Grimm, R. L.; Beauchamp, J. L., Field-induced droplet ionization mass spectrometry. *Journal of Physical Chemistry B* **2003**, 107, (51), 14161–14163.
18. Grimm, R. L.; Beauchamp, J. L., Dynamics of field-induced droplet ionization: Time-resolved studies of distortion, jetting, and progeny formation from charged and neutral methanol droplets exposed to strong electric fields. *Journal of Physical Chemistry B* **2005**, 109, (16), 8244–8250.
19. Kim, H. I.; Kim, H. J.; Shin, Y. S.; Beegle, L. W.; Jang, S. S.; Neidholdt, E. L.; Goddard, W. A.; Heath, J. R.; Kanik, I.; Beauchamp, J. L., Interfacial Reactions of Ozone with Surfactant Protein B in a Model Lung Surfactant System. *Journal of the American Chemical Society* **2010**, 132, (7), 2254–2263.
20. Hashimoto, M.; Shevkoplyas, S. S.; Zasonska, B.; Szymborski, T.; Garstecki, P.; Whitesides, G. M., Formation of Bubbles and Droplets in Parallel, Coupled Flow-Focusing Geometries. *Small* **2008**, 4, (10), 1795–1805.
21. Garstecki, P.; Fuerstman, M. J.; Whitesides, G. M., Oscillations with uniquely long periods in a microfluidic bubble generator. *Nature Physics* **2005**, 1, (3), 168–171.

22. Garstecki, P.; Fuerstman, M. J.; Stone, H. A.; Whitesides, G. M., Formation of droplets and bubbles in a microfluidic T-junction-scaling and mechanism of break-up. *Lab on a Chip* **2006**, *6*, (3), 437–446.
23. Anna, S. L.; Bontoux, N.; Stone, H. A., Formation of dispersions using "flow focusing" in microchannels. *Applied Physics Letters* **2003**, *82*, (3), 364–366.
24. Prakash, M.; Gershenfeld, N., Microfluidic bubble logic. *Science* **2007**, *315*, (5813), 832–835.
25. Weis, M.; Kopani, M.; Jakubovsky, J.; Danihel, L., Ethanol and methanol induced changes in phospholipid monolayer. *Applied Surface Science* **2006**, *253*, (5), 2425–2431.
26. MacKerell, A. D.; Bashford, D.; Bellott, M.; Dunbrack, R. L.; Evanseck, J. D.; Field, M. J.; Fischer, S.; Gao, J.; Guo, H.; Ha, S.; Joseph-McCarthy, D.; Kuchnir, L.; Kuczera, K.; Lau, F. T. K.; Mattos, C.; Michnick, S.; Ngo, T.; Nguyen, D. T.; Prodhom, B.; Reiher, W. E.; Roux, B.; Schlenkrich, M.; Smith, J. C.; Stote, R.; Straub, J.; Watanabe, M.; Wiorkiewicz-Kuczera, J.; Yin, D.; Karplus, M., All-atom empirical potential for molecular modeling and dynamics studies of proteins. *Journal of Physical Chemistry B* **1998**, *102*, (18), 3586–3616.
27. Plimpton, S., Fast Parallel Algorithms for Short-range Molecular-Dynamics. *Journal of Computational Physics* **1995**, *117*, (1), 1–19.
28. Hockney, R. W.; Eastwood, J. W., *Computer simulation using particles*. McGraw-Hill: New York, 1981.
29. Tannor, D. J.; Marten, B.; Murphy, R.; Friesner, R. A.; Sitkoff, D.; Nicholls, A.; Ringnalda, M.; Goddard, W. A.; Honig, B., Accurate First Principles Calculation of Molecular Charge-distributions and Solvation Energies from Ab-Initio Quantum-

- Mechanics and Continuum Dielectric Theory. *Journal of the American Chemical Society* **1994**, 116, (26), 11875–11882.
30. Marten, B.; Kim, K.; Cortis, C.; Friesner, R. A.; Murphy, R. B.; Ringnalda, M. N.; Sitkoff, D.; Honig, B., New model for calculation of solvation free energies: Correction of self-consistent reaction field continuum dielectric theory for short-range hydrogen-bonding effects. *Journal of Physical Chemistry* **1996**, 100, (28), 11775–11788.
31. Becke, A. D., Density-Functional Thermochemistry .3. the Role of Exact Exchange. *Journal of Chemical Physics* **1993**, 98, (7), 5648–5652.
32. Lee, C. T.; Yang, W. T.; Parr, R. G., Development of the Colle-Salvetti Correlation-Energy Formula into a Functional of the Electron-Density. *Physical Review B* **1988**, 37, (2), 785–789.
33. Duffy, D. C.; McDonald, J. C.; Schueller, O. J. A.; Whitesides, G. M., Rapid Prototyping of Microfluidic Systems in Poly(dimethylsiloxane). *Analytical Chemistry* **1998**, 70, (23), 4974–4984.
34. Garstecki, P.; Gitlin, I.; DiLuzio, W.; Whitesides, G. M.; Kumacheva, E.; Stone, H. A., Formation of monodisperse bubbles in a microfluidic flow-focusing device. *Applied Physics Letters* **2004**, 85, (13), 2649–2651.
35. Karagulian, F.; Lea, A. S.; Dilbeck, C. W.; Finlayson-Pitts, B. J., A new mechanism for ozonolysis of unsaturated organics on solids: phosphocholines on NaCl as a model for sea salt particles. *Physical Chemistry Chemical Physics* **2008**, 10, (4), 528–541.
36. Santrock, J.; Gorski, R. A.; Ogara, J. F., Products and Mechanism of the Reaction of Ozone with Phospholipids in Unilamellar Phospholipid-Vesicles. *Chemical Research in Toxicology* **1992**, 5, (1), 134–141.

37. Rivera, J. L.; Starr, F. W.; Paricaud, P.; Cummings, P. T., Polarizable contributions to the surface tension of liquid water. *Journal of Chemical Physics* **2006**, 125, (9), 8.
38. Ghosh, A.; Smits, M.; Bredenbeck, J.; Bonn, M., Membrane-bound water is energetically decoupled from nearby bulk water: An ultrafast surface-specific investigation. *Journal of the American Chemical Society* **2007**, 129, (31), 9608–9609.
39. Lai, C. C.; Yang, S. H.; Finlaysonpitts, B. J., Interactions of Monolayers of Unsaturated Phosphocholines with Ozone at the Air-Water-Interface. *Langmuir* **1994**, 10, (12), 4637–4644.
40. Pryor, W. A., Can Vitamin-E Protect Humans Against the Pathological Effects of Ozone in Smog. *American Journal of Clinical Nutrition* **1991**, 53, (3), 702–722.
41. Kaznessis, Y. N.; Kim, S. T.; Larson, R. G., Simulations of zwitterionic and anionic phospholipid monolayers. *Biophysical Journal* **2002**, 82, (4), 1731–1742.
42. Kaznessis, Y. N.; Kim, S.; Larson, R. G., Specific mode of interaction between components of model pulmonary surfactants using computer simulations. *Journal of Molecular Biology* **2002**, 322, (3), 569–582.
43. Baoukina, S.; Monticelli, L.; Risselada, H. J.; Marrink, S. J.; Tieleman, D. P., The molecular mechanism of lipid monolayer collapse. *Proceedings of the National Academy of Sciences of the United States of America* **2008**, 105, (31), 10803–10808.
44. Thorsen, T.; Roberts, R. W.; Arnold, F. H.; Quake, S. R., Dynamic pattern formation in a vesicle-generating microfluidic device. *Physical Review Letters* **2001**, 86, (18), 4163–4166.

45. Garstecki, P.; Stone, H. A.; Whitesides, G. M., Mechanism for flow-rate controlled breakup in confined geometries: a route to monodisperse emulsions. *Physical Review Letters* **2005**, 94, (16), 164501.
46. Kim, H. I.; Kim, H.; Shin, Y. S.; Beegle, L. W.; Goddard, W. A.; Heath, J. R.; Kanik, I.; Beauchamp, J. L., Time Resolved Studies of Interfacial Reactions of Ozone with Pulmonary Phospholipid Surfactants Using Field Induced Droplet Ionization Mass Spectrometry. *The Journal of Physical Chemistry B* **2010**, 114, (29), 9496–9503.
47. Wang, Z. D.; Hall, S. B.; Notter, R. H., Dynamic Surface-Activity of Films of Lung Surfactant Phospholipids, Hydrophobic Proteins, and Neutral Lipids. *Journal of Lipid Research* **1995**, 36, (6), 1283–1293.
48. Gopal, A.; Lee, K. Y. C., Morphology and collapse transitions in binary phospholipid monolayers. *Journal of Physical Chemistry B* **2001**, 105, (42), 10348–10354.
49. Gilliard, N.; Heldt, G. P.; Loredo, J.; Gasser, H.; Redl, H.; Merritt, T. A.; Spragg, R. G., Exposure of the Hydrophobic Components of Porcine Lung Surfactant to Oxidant Stress Alters Surface-Tension Properties. *Journal of Clinical Investigation* **1994**, 93, (6), 2608–2615.
50. Rodriguez-Capote, K.; Manzanares, D.; Haines, T.; Possmayer, F., Reactive oxygen species inactivation of surfactant involves structural and functional alterations to surfactant proteins SP-B and SP-C. *Biophysical Journal* **2006**, 90, (8), 2808–2821.
51. von Gunten, U., Ozonation of drinking water: Part I. Oxidation kinetics and product formation. *Water Research* **2003**, 37, (7), 1443–1467.
52. Pryor, W. A., How Far Does Ozone Penetrate into the Pulmonary Air Tissue Boundary Before It Reacts. *Free Radical Biology and Medicine* **1992**, 12, (1), 83–88.